Search for New Heavy Gauge Bosons in $\sqrt{s} = 13$ TeV pp Collisions with ATLAS

A thesis submitted in accordance with the requirements of
the University of Liverpool for the degree of Doctor of Philosophy
by

Ellis Kay

Under the supervision of

Uta Klein & Carl Gwilliam

Department of Physics,
Oliver Lodge Laboratory
University of Liverpool

May 2018

Abstract

In this thesis, the search for a new heavy charged gauge boson, namely the W', in the contect of the Sequential Standard Model is described. The study presented here focuses on the electron channel, where the W' decays to an electron and a neutrino. The analysis utilises 36.1 fb^{-1} of $\sqrt{s}$ = 13 TeV pp collison data recorded using the ATLAS detector over the 2015+2016 data taking period at the Large Hadron Collider at CERN. The transverse mass, m_T, is used as the search variable and is analysed over the region $150 < m_T < 6000$ GeV. The m_T spectrum for selected W' candidates is compared to the Standard Model expectation, which is quantified using a combination of Monte Carlo and data-driven methods. No significant excess is observed above the Standard Model, therefore statistical techniques are adopted to obtain limits on the production and decay of this new gauge boson. Newly developed frequentist tools are used to set a 95% C.L lower limit on the W' transverse mass of 5.12 TeV.

A reinterpretation of $W' \to \ell\ell$ and $Z' \to \ell\nu$ results in the context of a Heavy Vector Triplet model is also presented. Combined $V' \to \ell\ell/\ell\nu$ resonances with masses below 4.67 TeV are excluded at 95% CL. A full combination of results obtained from these searches, as well as those obtained from searches for diboson resonances ($VV + VH$), is described, with final two-dimensional limits set in two coupling planes (based on couplings to fermions and Higgs). The resulting limits are compared to indirect limits from various EW fits (including LEP), proving to give more stringent constraints over the majority of the tested parmeter space.

Declaration

This thesis is the result of my own work, except where explicit reference is made to the work of others, and has not been submitted for another qualification to this, or any other, university. This thesis does not exceed the word limit for the respective Degree Committee.

Ellis Kay

Acknowledgements

Thanks everyone.

Contents

Introduction

The Standard Model (SM) of particle physics, which describes the nature of all known elementary particles and non-gravitational interactions, has proven to be a tremendously successful description of nature so far. Developed during the 20$^{\text{th}}$ century, this Quantum Field Theory (QFT) has stood the test of time, corroborated by countless subsequent experimental observations culimating in the discovery of the last of its predicted particles, the Higgs boson, in 2012 [1–4]. This historic measurement was achieved through analysis of $\sqrt{s} = 7$ TeV and 8 TeV proton-proton collisions at the Large Hadron Collider (LHC), measured by the general-purpose ATLAS (A Large Toroidal LHC ApparatuS) and CMS (Compact Muon Solenoid) detectors stationed at opposing sides of its 27 km ring.

Despite the SM's unmitigated success in describing the majority of our observations in particle physics thus far, many gaps in our understanding of nature remain, motivating us to seek solutions beyond the Standard Model (BSM). With the wide variety of outstanding physics questions, concerning topics from the hierarchy problem to matter-antimatter asymmetry and the origin of dark matter, the hunt for BSM physics involves a comprehensive collection of analyses spanning many theories and kinematic ranges. The LHC, now colliding protons at $\sqrt{s} = 13$ TeV with a luminosity of the order 10^{34} cm^{-2}s^{-1}, affords us with the potential to probe rare processes associated with these theories occuring at the hitherto uncharted TeV-scale. Searches for new heavy gauge boson resonances such as the W' and Z', which appear in a plethora of BSM theories, have clean and well understood final state signatures, making them *golden channels* for seeking the first hints of new physics. Such searches require a deep understanding of the proton structure, which is driven by theory in the absence of existing data at the high energy frontier. This thesis focuses on the search for W' bosons decaying to final states with an electron. Many BSM searches in ATLAS seek similar final states which can arise in shared BSM models, making their results compatible and open to various reinterpretations. The combination of complementary results from different searches may offer an increased sensitivity to an expanded paramter space which is not fully accessible to the individual participating analyses. The virtues of combination efforts are explored in this thesis, with the description of a novel effort to combine both the leptonically decaying W' and Z' searches with results of searches for diboson resonances.

The structure of this thesis is as follows:

Part I introduces the theoretical framework of particle physics, starting with a brief outline of the SM and the phenomenology of proton-proton collisions. Outstanding physics questions and problems with the SM are discussed, leading to a summary of W' phenomenology, where various models which seek to address these issues are introduced.

Part II gives a brief overview of the LHC and the ATLAS detector. The key concepts of Monte Carlo (MC) simulation of proton-proton collisions are explained as well as the methods employed by ATLAS to reconstruct the physics objects pertinent to the work presented in this thesis.

Part III describes and quantifies the theoretical uncertainties associated with lack of knowledge of the partonic structure of protons which are relevant to heavy boson searches.

Part IV presents the search for new heavy charged W' bosons with the ATLAS detector, complete with results obtained using 36.1 fb^{-1} of $\sqrt{s} = 13$ TeV LHC data.

Part V summarises the novel combination of the results of the ATLAS searches for $W' \to \ell\nu$, $Z' \to \ell\ell$ and diboson resonances.

Part VI closes with a synopsis of the results presented in the preceding sections with comments on the outlook of these analyses. Auxiliary material is also provided here.

Part I

Theory & Motivation

Chapter 1

The Standard Model of Particle Physics

The Standard Model of particle physics is a relativistic Quantum Field Theory (QFT) describing the properties of the fundamental constituents of matter and the non-gravitational interactions between them. It has been proven to be a highly robust and accurate theory through many high precision measurements [5] - as an example, the predicted magnetic dipole moment for the electron agrees with the measured value within 10 parts per billion. In this chapter, the elmentary particles and forces of the SM are introduced. The strong, electroweak and Higgs interactions are outlined based on content from various books and lectures [6–10], to which the reader is referred for further details.

1.1 Overview of the Standard Model

The SM is a non-abelian gauge theory based on a $SU(3)_C \times SU(2)_L \times U(1)_Y$ gauge group*, describing the strong (QCD) (section 1.2) and electroweak (section 1.3) interactions, respectively. As a consequence of Noether's theorem [11], stipulating that for every continuous symmetry there is a corresponding conservation law, each gauge

*The theory is non-abelian since the transformations of the $SU(3)_C$ and $SU(2)_L$ symmetry groups do not commute.

group in this theory has an associated conserved quantity. These are denoted by the indices C, L and Y, which represent *colour* (strong interaction), *weak isospin*[†] and *weak hypercharge* (both electroweak interaction), respectively. The conserved quantity in Quantum Electrodynamics (QED) is the *electric charge*, Q, which is convolved in the weak isospin and hypercharge (see section 1.3). The conservation of these quantities under gauge invariance is what leads to the fundamental forces associated with each gauge group.

The SM consists of 12 matter particles known as $fermions$, outlined in table 1.1, which have intrinsic spin, s, of $\frac{1}{2}$ (in natural units of $\hbar = \frac{h}{2}$ where h is Planck's constant). They are split into two categories: quarks, which interact via the strong force, and leptons, which do not. The quarks and leptons are further subdivided in three *generations* based on their flavour and mass. Each of these generations contains two types of quarks/leptons which have contrasting electromagnetic charge (fractional for for quarks and integer for leptons). For each of the quarks and leptons there exists a corresponding antiparticle with opposite-signed charge quantum numbers. The charged leptons interact via the electromagnetic and weak forces, while the electromagnetically neutral neutrinos only interact via the weak force. All quarks possess electromagnetic charge and can therefore interact with the electromagnetic force. Their ability to interact via the strong force is based on their possession of colour charge, of which there are three possible states: blue, red and green (and their corresponding anti-states).

[†]The L here indicates that the weak interaction only acts on left-chiral fermions - a feature which will be discussed later.

Quarks					
Generation	Particle		Electric Charge, Q [e]	Weak Isospin, T_3	Mass [GeV]
I	u	up	$+\frac{2}{3}$	$+\frac{1}{2}$	0.0023
	d	down	$-\frac{1}{3}$	$-\frac{1}{2}$	0.0048
II	c	charm	$+\frac{2}{3}$	$+\frac{1}{2}$	1.275
	s	strange	$-\frac{1}{3}$	$-\frac{1}{2}$	0.095
III	t	top	$+\frac{2}{3}$	$+\frac{1}{2}$	173.5
	b	bottom	$-\frac{1}{3}$	$-\frac{1}{2}$	4.18
Leptons					
Generation	Particle		Electric Charge, Q [e]	Weak Isospin, T_3	Mass [GeV]
I	e	electron	-1	$-\frac{1}{2}$	0.000511
	ν_e	electron neutrino	0	$+\frac{1}{2}$	$< 2e^{-9}$
II	μ	muon	-1	$-\frac{1}{2}$	0.105
	ν_μ	muon neutrino	0	$+\frac{1}{2}$	< 0.00019
III	τ	tau lepton	-1	$-\frac{1}{2}$	1.777
	ν_τ	tau neutrino	0	$+\frac{1}{2}$	< 0.0182

TABLE 1.1: Fermions of the Standard Model [12].

The quanta of the gauge invariant fields of the SM, and mediators of the associated forces, are the *gauge bosons*, outlined in table 1.2. They are all spin-1 particles and are therefore referred to as *vector bosons*. The electromagnetic force has an effectively infinite range. It is mediated by the massless photon, γ, which posseses no charge and can therefore not interact with the electromagnetic field (i.e. they cannot self-interact). The weak interaction is mediated by W and Z bosons, which have masses of 91.1876 ± 0.0021 GeV and 80.385 ± 0.015 GeV, respectively [12]. Given the Heisenberg uncertainty principle [13] and these masses, the effective range R_{eff} of the weak force is estimated as:

$$R_{eff} \approx c\Delta t \approx \frac{\hbar}{2mc} \tag{1.1}$$

where m is the mass of the exchange particle, giving an effective range of $\sim 10^{-18}$ m. The W bosons only couple to left-handed fermions since the weak interaction is *parity violating* - these fermions form isospin doublets under $SU(2)_L$ while their opposite-handed counterparts form singlets. Since W bosons possess electric charge, they can also couple to photons. They also enjoy self-interactions and can couple to the Z boson, since both electroweak bosons have weak isospin $T_3 = \pm 1$. The interactions between the γ, W and Z are summarised in figure 1.1. The strong force is mediated by the gluon, g. Though it is not explicitly stated in table 1.2, there are eight different types of gluon. This is due to the fact that gluons carry both colour and anticolour, which can form eight different combinations[‡]. Since QCD is a non-abelian gauge theory and gluons possess colour charge, gluon self-interactions are possible (up to 4-gluon vertices). Although the gluon is massless, the strong interaction has a restricted range. This is a consequence of the confinement property of QCD (discussed in section 1.2), dictating that colour charged degrees of freedom must bind together to form neutral hadrons. As a result, the strong force only has a direct effect at small distances of the order of the size of a hadron, at a range of $\sim 10^{-17}$ m. However, the force also has a residual effect, referred to as the *strong nuclear force*, which acts between hadrons due to their colour-charged constituents. Gluons are transmitted from the hadrons and subsequently form mesons, which act as the force carriers. The intensity of this force diminishes with distance in the form of a *Yukawa potential* [14]. These mesons have masses ranging from ~ 135 MeV (pions π) - ~ 7 GeV (rho meson ρ), giving the residual effects of the strong force an effective range of $\sim 10^{-15}$ m.

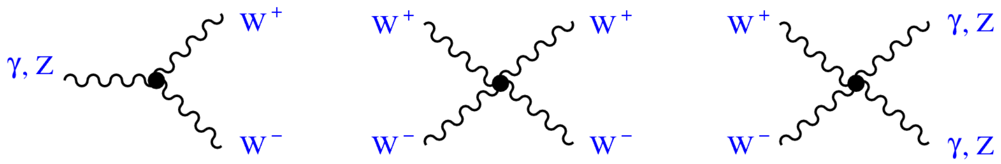

FIGURE 1.1: The self-interactions of the electroweak bosons. Taken from [9].

[‡]Although intuitively the three possible colours would lead to 9 different combinations, combinations of $r\bar{r} + b\bar{b} + g\bar{g}$ give colour singlet states which gluons cannot take.

Interaction	Boson		Mass [GeV]	Charge [e]	Effective Range [m]
EM	γ	photon	0	0	∞
Weak	W	W-boson	80.385	± 1	$\sim 10^{-18}$
	Z	Z-boson	91.1876	0	
Strong	g	gluon	0	0	$< 10^{-15}$

TABLE 1.2: Summary of the fundamental forces included in the Standard Model and the gauge bosons which mediate them [12].

1.2 The Strong Interaction

As mentioned above, QCD is the theory of the the strong interaction acting between quarks. The QCD Lagrangian can be constructed in a similar manner to that of QED (for which the reader is directed to sources such as [8]), though many experimental observations have informed the current picture of this gauge theory. The colour charge was introduced by Greenberg [15], Han and Nambu [16] as an $SU(3)$ degree of freedom - giving the gauge group of QCD. The motivation behind this was to provide an explanation for observations of spin $\pm\frac{3}{2}$ hadrons composed of same-flavour quarks, such as Δ^{++} (uuu), Δ^{-} (ddd) and Ω^{-} (sss), which would otherwise violate Pauli's exclusion principle. Based on this symmetry, the QCD Lagrangian can be constructed from a $SU(3)$ non-abelian Yang-Mills theory [17] resulting in:

$$\mathcal{L} = -\frac{1}{4}F^{a}_{\mu\nu}F^{\mu\nu}_{a} + \sum_{f}\bar{\psi}^{f}_{i}\left(i\gamma_{\mu}D^{\mu}_{ij} - m_{f}\delta_{ij}\right)\psi^{f}_{j}, \tag{1.2}$$

summed over all flavours, f, and all charges, a for Dirac field ψ with mass m. Here, γ_{μ} denotes the Dirac matrices while δ_{ij} denotes the Kronecker delta function§ The covariant derivative is given by:

$$D^{\mu}_{ij} = \partial^{\mu}\delta_{ij} + ig_{S}t^{a}_{ij}A^{\mu}_{a}, \tag{1.3}$$

§Which takes the value 1 if $i = j$ and 0 if $i \neq j$ and corresponds to the identity matrix $\left(\begin{smallmatrix}1 & 0\\ 0 & 1\end{smallmatrix}\right)$.

and the field strength tensor is given by:

$$F^a_{\mu\nu} = \partial_\mu A^a_\nu - \partial_\nu A^a_\mu - g_S f_{abc} A^b_\mu A^c_\nu, \tag{1.4}$$

where where ∂^μ denotes the derivative $\partial^\mu = \left(\frac{\partial}{\partial t}, -\vec{\nabla}\right)$, the gauge coupling term, g_S, represents the strength of the interaction and the colour matrices, t^a_{ij}, are the generators of $SU(3)$. The f_{abc} term corresponds to the structure constants of $SU(3)$ while $A_{\nu,\mu}$ denote the gauge (gluon) fields. The indices $a,\ b,\ c$ run over the 8 colour degrees of freedom. The third term in this tensor is what distinguishes QCD from QED, giving rise to high order gluon self-interactions and asymptotic freedom.

In QCD, g_S is related to the momentum transfer of a process, Q^2 via:

$$g^2_S(Q^2) = \frac{4\pi}{\beta_0 \ln\left(\frac{Q^2}{\Lambda^2_{QCD}}\right)}, \tag{1.5}$$

and is known as the *running coupling* (the motivation for which is explored in section 2.1), where the strong coupling $\alpha_S = \frac{g^2_S}{4\pi}$. In quantum field theory, calculation of a physical observable R as a perturbative series in the coupling (α_S) requires *renormalisation* in order to remove ultraviolet divergences. This introduces an additional energy scale μ, corresponding to the point at which subtractions are performed to remove divergences. The observable R then depends on the ratio $\frac{Q}{\mu}$ and the renomalised α_S depends on μ[¶] - this latter dependence is encoded in the *beta function*, denoted here as β_0. In the asymptotic limit ($Q^2 \to \infty$) the strong coupling tends to zero and gluons and quarks behave like "free" particles (again, see section 2.1). This is the regime of *perturbative QCD* (pQCD). At low energies, $Q^2 \to \Lambda^2_{QCD}$ (where the scale of QCD, Λ_{QCD} is known as the *hadronisation scale*), the strong coupling tends to infinity. As a result, colour charged quarks bind together to form colour neutral hadrons.

[¶] A renormalisation group equation is defined and solved by defining the running coupling $\alpha_S(Q)$.

1.3 Electroweak Physics

The current theory of electroweak interactions is the result of decades of postulates informed by experimentally established facts. In 1932, Fermi formulated a theory for β-decay of the neutron as a four fermion process. According to this theory, the weak interaction is parity conserving. However, evidence to the contrary was found in the Wu experiment [18], where electrons emerging from decays of ^{60}Co were found to be predominantly left-handed. The V-A (vector minus axial vector) theory, developed in 1958 [19, 20], modifies the Fermi theory to take chirality and parity into account. However, this theory still proves insufficient: it is not renormalisable, it behaves poorly at high energies‖ and it does not account for the discovery of neutral currents [21]. In order to address the high-energy problems, bosons acting as as mediators for the weak interactions (analogous to photons in QED) were postulated; two charged ($W^{\pm}$) and one neutral (Z^0) for the charged and neutral currents, respectively. The W [22] and Z [23] discoveries corroborated this theory in 1983.

These experimental developments demand a description of EW interactions with an elaborate structure; it requires several fermion flavours, different properties for left and right handed fields, massive gauge bosons W and Z as well as the massless photon A_μ. This is achieved through the Glashow, Weinberg, Salam (GSW) model [24–26], or Standard Model, of electroweak physics. The simplest group with doublet representations is $SU(2)$ and an additional $U(1)$ is required to include electromagnetic interactions. To describe the unified EW interaction, the direct product of these groups is used. It therefore follows that the considered symmetry group (G) is:

$$G \equiv SU(2)_L \otimes U(1)_Y. \tag{1.6}$$

The gauge field dynamics are given by the gauge part of the Lagrangian:

$$\mathcal{L}_g = -\frac{1}{4} B_{\mu\nu} B^{\mu\nu} - \frac{1}{4} F^i_{\mu\nu} F_i^{\mu\nu}, \tag{1.7}$$

‖For masses $\gtrsim$ 1 TeV scattering cross-sections violate the unitarity bound of $\sigma \leqslant \frac{4\pi}{s}$.

where the field strength tensors for $SU(2)_L$, $F^i_{\mu\nu}$ are given by:

$$F^i_{\mu\nu} = \partial_\nu W^i_\mu - \partial_\mu W^i_\nu + g\epsilon_{ijk} W^j_\mu W^k_\nu. \tag{1.8}$$

and for $U(1)_Y$, $B_{\mu\nu}$, by:

$$B_{\mu\nu} = \partial_\nu B_\mu - \partial_\mu B_\nu. \tag{1.9}$$

Here g is the $SU(2)$ gauge coupling, ϵ_{ijk} is the Levi-Civita or "permutation" symbol**, $W_{\nu\mu}$ and $B_{\nu\mu}$ are the $SU(2)$ and $U(1)$ gauge fields, respectively, and $i = 1...3$. The charges associated with $SU(2)$ and $U(1)$ are the weak isospin, T and weak hypercharge, Y, respectively. These are related to electric charge via the Gell-Mann-Nishijima relation [27, 28]:

$$Q = T_3 + \frac{1}{2}Y, \tag{1.10}$$

where T_3 is the third component of the isospin.

The $SU(2)_L$ gauge group acts on weak isospin doublets such as:

$$\begin{pmatrix} \nu_e \\ e^- \end{pmatrix}_L = \frac{1}{2}(1-\gamma_5)\begin{pmatrix} \nu_e \\ e^- \end{pmatrix}, \tag{1.11}$$

where $\gamma^5 = i\gamma^0\gamma^1\gamma^2\gamma^3$ is defined by the Dirac matrices. The right-handed components of the leptons do not have right-handed neutrino partners and are singlets under weak isospin. Left-handed quarks also form weak iso-doublets:

$$\begin{pmatrix} u \\ d' \end{pmatrix}, \quad \begin{pmatrix} c \\ s' \end{pmatrix}, \quad \begin{pmatrix} t \\ b' \end{pmatrix}, \tag{1.12}$$

while their right-handed counterparts form singlets. Here, down-type quarks are denoted with a prime since their flavour eigenstates (d', s', b') are not equal to their mass eigenstates (d, s, b) but are related through the *Cabibo-Kobayashi-Maskawa* (CKM) matrix [29], V^{CKM}. In a similar manner, the neutrino mass and flavour eigenstates are related through the *Pontecorvo-Maki-Nakagawa-Sakata* (PMNS) matrix, V^{PMNS} [30].

**This is a tensor of rank 3 which is defined as 0 if any of the labels ijk are the same, 1 if i, j, k is an even permutation of 1,2,3 and -1 if i, j, k is an odd permutation of 1,2,3.

Focusing on leptons, the fermionic part of the EW Lagrangian takes the form:

$$\begin{aligned}\mathcal{L}_f = \overline{(\nu_e, e^-)_L}\, i\gamma^\mu \left(\partial_\mu + i\frac{g^{'}}{2} Y B_\mu + i\frac{g}{2}\tau_a W_\mu^a\right)\begin{pmatrix}\nu_e \\ e^-\end{pmatrix}_L \\ + \overline{e_{\bar{R}}} i\gamma^\mu \left(\partial_\mu + i\frac{g^{'}}{2} Y B_\mu\right) e_{\bar{R}} \\ + \text{same terms for } \mu \text{ and } \tau \text{ fields,}\end{aligned} \tag{1.13}$$

where $g^{'}$ is the $U(1)$ gauge coupling, Y is the generator for the $U(1)$ symmetry group and τ_a represents the generator for the $SU(2)$ symmetry group $\left(T_a = \frac{1}{2}\tau_a\right)$. The gauge fields written in these Lagrangian terms are not the ones observed in nature, but they mix to form them. The charged $W^{\pm}$ are the result of a complex linear combination of $SU(2)$ states:

$$W_\mu^\pm = \frac{W_\mu^1 \mp i W_\mu^2}{\sqrt{2}}, \tag{1.14}$$

while the neutral Z_μ and A_μ are given by a mixture of the W_μ^3 and B_μ fields:

$$\begin{pmatrix} Z_\mu \\ A_\mu \end{pmatrix} = \begin{pmatrix} \cos\theta_W & -\sin\theta_W \\ \sin\theta_W & \cos\theta_W \end{pmatrix}\begin{pmatrix} W_\mu^3 \\ B_\mu \end{pmatrix}, \tag{1.15}$$

where θ_W denotes the Weinberg mixing angle which is related to the $SU(2)$ and $U(1)$ coupling constants by:

$$\tan\theta_W = \frac{g^{'}}{g} \tag{1.16}$$

An outstanding issue which has not yet been explained here is the mass of the W and Z bosons. Measurements of these bosons, as well as the limited range of the weak force, indicate that, unlike the photon, they are massive. However, simply incorporating mass terms into the above Lagrangian would violate gauge invariance, making the theory non-renormalisable. In order to give these bosons masses, additional terms must be introduced. This is accomplished through the *Higgs Mechanism*.

1.4 The Higgs Mechanism

In the Higgs mechanism [31–35] the EW gauge symmetry is spontaneously broken to the electromagnetic subgroup:

$$SU(3)_C \times SU(2)_L \times U(1)_Y \xrightarrow{SSB} SU(3)_C \times U(1)_{QED}. \quad (1.17)$$

Spontaneous symmetry breaking (SSB) implies that the theory in question is still gauge invariant under a given symmetry, though the ground state is not. This is achieved through the introduction of a new complex scalar field, the *Higgs field*, ϕ. An $SU(2)_L$ doublet of complex scalar Higgs fields is introduced:

$$\phi = \begin{pmatrix} \phi^+ \\ \phi_- \end{pmatrix} = \frac{1}{\sqrt{2}} \begin{pmatrix} \phi_1 + i\phi_2 \\ \phi_3 + i\phi_4 \end{pmatrix}, \quad (1.18)$$

where the four real scalar fields, ϕ_i, correspond to four degrees of freedom (d.o.f). This doublet has weak isospin $T = \frac{1}{2}$ and hypercharge $Y = 1$ (leading to electromagnetic charges of +1,0 for the $T^3 = \pm\frac{1}{2}$ members of the doublet from equation 1.3), allowing interactions with the weak bosons.

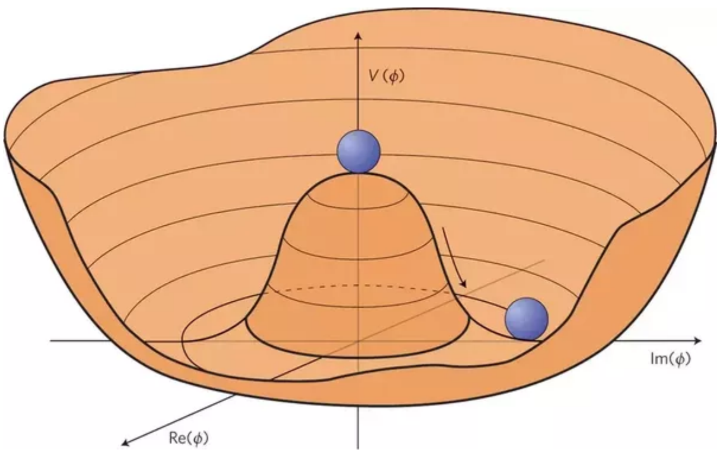

FIGURE 1.2: A graphical representation of the Higgs potential, $V(\phi)$. Taken from [36].

The covariant derivative of the Higgs field is given by:

$$D_\mu \phi = \left(\partial_\mu + i\frac{g'}{2} B_\mu + i\frac{g}{2}\tau_a W_\mu^a \right) \phi \quad (1.19)$$

and its Lagrangian is:

$$\mathcal{L}_H = (D_\mu \phi)^\dagger (D^\mu \phi) - \mu^2 \phi^\dagger \phi - \lambda (\phi^\dagger \phi)^2, \tag{1.20}$$

where μ and λ are free parameters. The last two terms in this Lagrangian represent the most general invariant and renormalisable Higgs potential, $V(\phi)$. The parameter λ must be > 0 in order to ensure an absolute minimum in the Lagrangian (i.e. give the potential a lower bound) and $\mu^2 < 0$ to give more than one minimum rather than just one at $\phi_i = 0$, enabling SSB.

Figure 1.2 shows the shape of the Higgs potential, which has infinite solutions for the minima at $\phi^\dagger \phi = \frac{-\mu^2}{2\lambda}$. Calculating the potential's minimum leads to the *vacuum expectation value* (vev), v. The vacuum state is chosen to be:

$$\phi_0 = \frac{1}{\sqrt{2}} \begin{pmatrix} 0 \\ v \end{pmatrix} \quad , \qquad v = \sqrt{\frac{-\mu^2}{\lambda}}. \tag{1.21}$$

This is chosen such that $Q\phi_0 = 0$ in order to guarantee that $U(1)$ (which is generated by Q) is unbroken by the Higgs mechanism and the photon remains massless.

In the absence of the gauge interactions, the four degrees of freedom from the complex scalar field give three massless (and non-physical) *Goldstone bosons* and a massive Higgs field. In the presence of the gauge fields, the fields are transformed into the *unitary gauge* and the Higgs field can be written as:

$$\phi(x) \to \frac{1}{\sqrt{2}} \begin{pmatrix} 0 \\ v + H \end{pmatrix}, \tag{1.22}$$

with scalar field H. The Goldstone bosons are absorbed by the weak gauge bosons in gauge transformations, leading to longitudinal polarisation components for the gauge bosons and consequently their mass terms. The covariant derivative of the Higgs field acts on the vacuum value as:

$$D_\mu \phi_0 = \frac{ig}{\sqrt{2}}(W_\mu^+ T_+ + W_\mu^- T_-)\phi_0 + \frac{ig}{\cos\theta_W} Z_\mu T_3 \phi_0 = \frac{ig}{2} W_\mu^+ \begin{pmatrix} v \\ 0 \end{pmatrix} - \frac{ig}{2\sqrt{2}\cos\theta_W} Z_\mu \begin{pmatrix} 0 \\ v \end{pmatrix}. \tag{1.23}$$

In the vacuum state, it follows that the kinetic term of the Higgs field is:

$$(D_\mu \phi_0)^\dagger (D^\mu \phi_0) = -\frac{g^2 v^2}{8}\big(2W_\mu^+ W^\mu + \frac{1}{\cos^2\theta_W} Z_\mu Z^\mu\big). \tag{1.24}$$

Using equation 1.15, the mass terms for the weak gauge bosons can therefore be calculated as:

$$M_Z = \frac{v}{2}\sqrt{g^2 + g'^2} = \frac{m_W}{\cos\theta_W}, \qquad M_W = \frac{gv}{2} = \frac{e_0 v}{2\cos\theta_W}, \tag{1.25}$$

where e_0 is the coupling constant of the photon $e_0 = \frac{gg'}{\sqrt{g^2+g'^2}} = g\sin\theta_W = g'\cos\theta_W$ (see [8]).

The Higgs field also gives rise to fermion masses by introducing Yukawa mass terms into the Lagrangian. These have the form:

$$g_f \bar{\psi}_L \phi \psi_R, \tag{1.26}$$

where g_f is the Yukawa coupling between the fermion and the Higgs field and the ψ_L, ψ_R terms represent the wavefunction of the fermion. Following SSB, at the vev of the Higgs potential, this becomes:

$$g_f \frac{v}{\sqrt{2}} \bar{\psi}_L \phi \psi_R, \tag{1.27}$$

leading to fermion mass terms, m_f:

$$m_f = \frac{g_f v}{\sqrt{2}}. \tag{1.28}$$

The Higgs mass, m_H arises from the Higgs potential and is given as:

$$m_H = \sqrt{2\lambda}\, v. \tag{1.29}$$

The vacuum expectation value can be related to the Fermi constant, G_F, via:

$$v = \frac{1}{\left(\sqrt{2}G_F\right)^{\frac{1}{2}}} \sim 246\text{GeV}, \tag{1.30}$$

hence the Higgs sector of the SM has only one free parameter which is chosen to be either λ or m_H. The Higgs couplings to the SM bosons, depicted in figure 1.3, are determined through the boson mass and v.

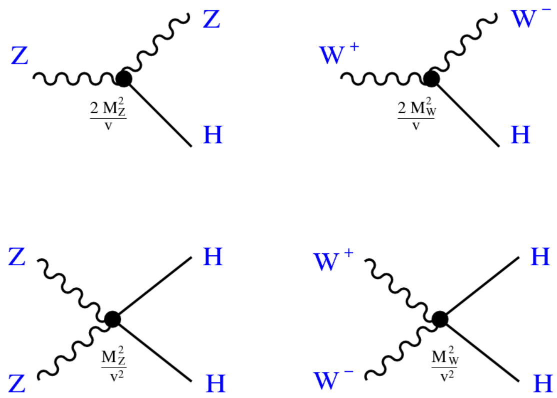

FIGURE 1.3: The Higgs couplings to the SM gauge bosons. Taken from [9].

In 2012, the Higgs boson was discovered with $m_H \sim 125.09$ GeV [1–4] by the ATLAS and CMS collaborations at CERN, completing the Standard Model. The discovered boson has been found to be compatible with the SM $J^P = O^+$ quantum numbers for the Higgs [3, 37]. Now work continues to measure more important properties, such as the Higgs self-coupling and branching ratios to other bosons, in order to probe the nature of electroweak symmetry breaking.

Chapter 2

The Phenomenology of Proton-Proton Collisions

The hadron-hadron scattering processes which occur at collider experiments such as the LHC can be classified as either *hard* or *soft*. Both processes are underpinned by QCD, though different approaches are required to understand the two cases. Hard processes, such as W and Z production, occur at high energy scales and therefore short distances, hence perturbative QCD can provide their cross sections with good precision using the *factorisation theorem*.

As outlined by Drell and Yan [38], the concept of the parton model of the proton developed for deep inelastic scattering (DIS) can be extended to hard scattering processes in hadron-hadron collisions [39]. This means that the cross sections of such processes can be *factorised* into long distance terms describing the distribution of partons contained in the incident hadrons and a short distance term describing the resulting hard scattering of the partons to produce final state particles [6]. In this chapter, the partonic structure of the proton is outlined and the process of cross section determination is summarised in the context of Drell-Yan processes in proton-proton collisions.

2.1 The Structure of the Proton

Hadrons do not only contain valence quarks (e.g. *uud* for the proton): they consist of a "sea" of gluons and virtual quark-antiquark pairs originating from many interactions. The knowledge of this structure, originating from early deep inelastic scattering (DIS) experiments, helped to shape the current understanding of QCD. Cross sections for inelastic Coulomb scattering from nuclei are characterised by two form factors [40], or *structure functions*, which at fixed lepton beam energy depend on the negative four-momentum transfer squared for the process, Q^2, and electron energy loss in the rest frame of the nucleon. SLAC scattering cross-section measurements [41] were found to exhibit scaling behaviour, showing Q-indepence: an observation which was predicted by Bjorken [42]. In the wake of the observations of this *Bjorken scaling*, the parton model was proposed by Richard Feynman [42–45]. In this model, the scaling behaviour is attributed to point-like elastic scattering of free "partons" within hadrons. Measurements made by Callan and Gross of virtual photon scattering cross sections [42] concluded that these partons must be spin $\frac{1}{2}$ fermions - these were subsequently accepted to be the quarks of the SM. This idea of free quarks was reconciled with the confinement property of QCD through the idea of a scale dependent coupling which was large at low energies (short distances) and small at high energies (long distances) [46, 47]. Measurements of the structure function at a range of x values made by the H1 [48] and ZEUS [49] collaborations as well as fixed target experiments [50, 51] showed that at increased resolution (i.e. higher Q^2) this Bjorken scaling breaks down and the proton appears to have more constituents - revealing the sea of partons which constitute hadronic matter.

2.2 Drell-Yan Processes in Proton-Proton Collisions

In high energy proton-proton collisions, the charged current (CC) and neutral current (NC) Drell-Yan (DY) processes (figure 2.1) are amongst the dominant production modes for W and Z bosons. In the Drell-Yan process, a quark and antiquark annihilate to form an intermediate boson which subsequently decays into two leptons (NC) or a lepton and a neutrino (CC). For the case of the neutral current, the intermediate boson can either be a Z boson or a virtual off-shell photon (γ^*) since these bosons have the same quantum numbers.

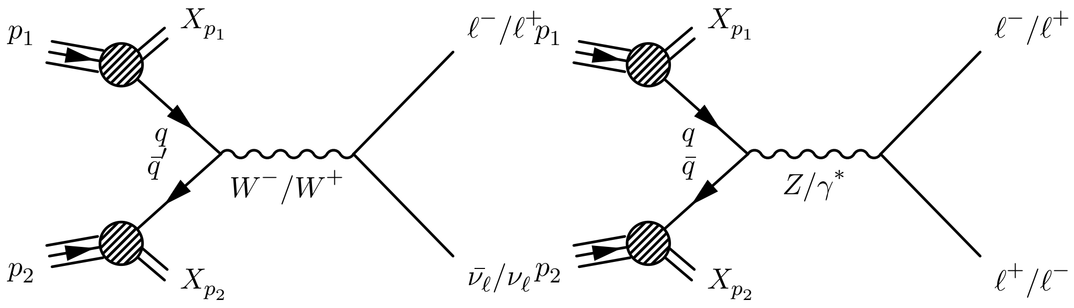

(a) Charged Current **(b)** Neutral Current

FIGURE 2.1: Feynman diagrams for the charged current and neutral current Drell-Yan processes. Here, $p_{1,2}$ represent the colliding protons and $X_{p1,2}$ represent the remaining partons from these protons which do not participate in this process.

For 2→2 processes such as Drell-Yan production, the Mandelstam variables [52] may be used to relate the participating particles' momenta. For processes with incoming particles with momenta p_A and p_B and outgoing particles with momenta k_A and k_B these are:

$$\begin{aligned}
\hat{s} &\equiv (p_A + p_B)^2 \equiv (k_A + k_B)^2\,; \\
\hat{t} &\equiv (p_A - k_A)^2 \equiv (k_B - p_B)^2\,; \\
\hat{u} &\equiv (p_A - k_B)^2 \equiv (k_A - p_B)^2\,,
\end{aligned} \tag{2.1}$$

where $\hat{s}$ is known as the square of the centre-of-mass (cms) energy of the incoming quark and antiquark, $\hat{t}$ is known as the square of the four-momentum transfer between incoming and outgoing particles and $\hat{u}$ is the square of the four-momentum transfer with a crossing symmetry (with aprticles k_A and k_B switched). The terms s-channel (space-channel), t-channel (time-channel) and u-channel are used to describe different possible scattering events whose four-momentum squared equals $\hat{s}$, $\hat{t}$ or $\hat{u}$. The particles in the DY scattering can therefore be described as:

$$\begin{aligned} &q(p_A, \sigma_A) + \bar{q}(p_B, \sigma_B) \to \ell^-(k_A, \tau_A) + \ell^+(k_B, \tau_B) \quad \text{and} \\ &q(p_A, \sigma_A) + \bar{q}(p_B, \sigma_B) \to \ell^{+/-}(k_A, \tau_A) + \nu_\ell/\bar{\nu}_\ell(k_B, \tau_B), \end{aligned} \tag{2.2}$$

for the neutral and charged current cases, respectively, with σ and τ describing the helicities of the incoming quarks and outgoing fermions, respectively.

As mentioned in the previous section, the proton contains a "sea" of quarks which contribute the antiquarks required for DY production. This is reflected in the cms energy of the $q\bar{q}$ system from a pp collision, defined as [53]:

$$\hat{s} = M^2 = x_1 x_2 s = x_1 x_2 \left(2P_{beam}\right)^2, \tag{2.3}$$

where s is the cms energy of the pp system, M is the mass of the produced resonance (W or Z), P_{beam} is the proton beam momentum and $x_{1,2}$ represent the fraction of the proton's momentum carried by each struck parton (also known as the Bjorken x). The partons participating in the DY process are not usually at rest in the reference frame of the hadrons (i.e. the lab frame for the collider). Rather, the partons receive a longitudinal boost in the direction of the beam axis which is dependent on $\frac{x_1}{x_2}$. This boost is more easily accounted for in terms of the rapidity, y_{cm}:

$$y_{cm} = \frac{1}{2} \ln \frac{x_1}{x_2} = \frac{1}{2} \ln \frac{E + p_z}{E - p_z}, \tag{2.4}$$

where E and p_z denote the energy and longitudinal momentum of the produced boson, which is at rest in the frame of the quark/antiquark system. Combining equations 2.3 and 2.4 yields the momentum fraction carried by each parton:

$$x_{1,2} = \sqrt{\frac{M^2}{s}} e^{\pm y_{cm}}. \tag{2.5}$$

The probability of struck parton with flavour q carrying a momentum fraction x of a collided hadron's momentum for a given *factorisation scale*, μ_F, (which can be defined as the scale which separates long-distance and short-distance phenomena*) is given by a *parton distribution function*, $F_q\left(x, \mu_F^2\right)$. The PDF comes into the overall cross section for the DY process $pp \to ij$ which is written as:

$$\sigma_{pp\to ij} = \int dx_1 dx_2 \sum_q \left(F_q\left(x_1, \mu_F^2\right) F_{\bar{q}}\left(x_2, \mu_F^2\right) + F_{\bar{q}}\left(x_1, \mu_F^2\right) F_q\left(x_2, \mu_F^2\right)\right) \sigma_{q\bar{q}\to ij}, \tag{2.6}$$

The partonic cross section $\sigma_{q\bar{q}\to ij}$, which is calculated using pQCD, depends on this factorisation scale and also (at higher order QCD) a *renormalisation scale*, μ_R, which describes the scale at which the strong coupling constant α_S is evaluated†. Typically these are chosen such that $\mu_R = \mu_F$ with a value that is around the energy scale, Q^2, of the process in question. In the DY case, $Q^2 = M^2$.

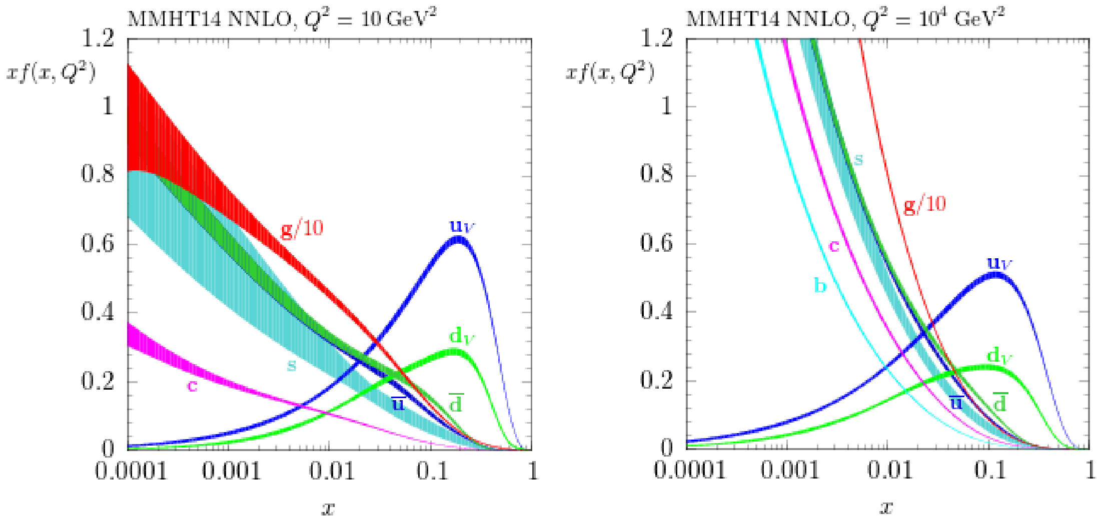

(a) $Q^2 = 10$ GeV^2 **(b)** $Q^2 = 10^4$ GeV^2

FIGURE 2.2: Plots showing a PDF set calculated for different Q^2 values. The coloured lines show the individual contributions from the quarks and gluons, with the latter scaled down by factor 10. Both from [54].

In the perturbative regime ($\alpha_S(Q^2) \ll 1$), the dependence of parton distributions on Q^2 can be calculated theoretically using evolution equations for parton densities known as

*This arbitrary separation is introduced in order to protect the cross section calculation from infrared (IR) divergences arising from massless particles.

†This scale is introduced to protect against ultraviolet (UV) divergences arising from higher order loops with large momentum.

DGLAP[‡] equations [58]. These equations are formulated for different levels of approximations relative to the power of $\alpha_S(Q^2)$ in the calculation, referred to as *leading-order* (LO), *next-to-leading-order* (NLO), *next-to-leading-order* (NNLO) and so on. However, the PDF's Bjorken x dependence cannot be calculated from first principles and must instead be extracted using experimental results. PDFs are obtained by fitting available cross section data points from various experiments in a grid of Q^2 and x values. A variety of such fits exist which are produced by different groups - these are referred to as 'PDF sets'. The most valuable inputs for this purpose come from DIS (lepton-nucleon scattering) experiments, since the leptons involved in the collisions can act as probes to measure the partonic structure of hadrons. Generally, the dependence of the distributions for different partons on x is parametrised at a low value of Q^2 (Q_0^2) and then evolved up in Q^2 using the DGLAP equations. Figure 2.2 gives an example of a PDF set calculated at two different Q^2 values using *ep* data collected by the H1 and ZEUS collaborations [54]. The data from these experiments have endured as the most important inputs for the PDFs used at the LHC since they cover the lowest, and therefore most relevant (see figure 2.3), range of Bjorken x values. While Q^2 is fixed for a given x for measurements made by the *pp* experiments, both of these parameters may be varied simultaneously for DIS experiments, giving the Q^2 lever arm which is necessary for precise PDF measurements. There are experimental and theoretical uncertainties associated with PDFs which must be taken into account for the analyses which use them. Details of the calculation and application of such uncertainties for the analysis outlined in this thesis are given in part III.

2.2.1 Uncertainties for PDF Fits

Heavy quarks, especially the charm and bottom quarks, must have their masses taken into account for QCD calculations which are involved in global fits for parton distributions. Near the threshold $Q^2 \sim m_H^2$, massive quarks are created in the final state as opposed to being treated as constituents of the proton, while at scales much higher than this they are expected to behave like the other essentially 'massless' partons **??**.

[‡]Named as such due to the contributions from Gribov and Lipatov [55], Altarelli and Parisi [56] and Dokshitzer [57].

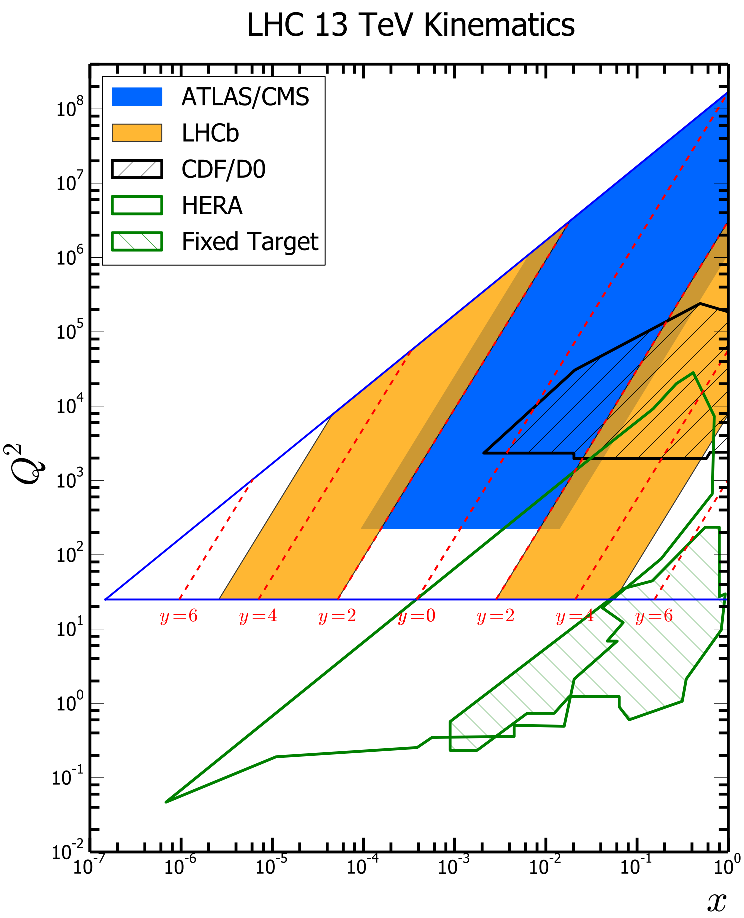

FIGURE 2.3: The (x, Q^2) plane which is probed by fixed target, HERA, CDF/D0 and various LHC experiments. Clearly H1 and ZEUS cover the lowest x range, which is relevant to the LHC. From [59].

As previously stated, PDF's are parametrised at a starting scale Q_0^2, which is generally chosen to be below the threshold of the charm mass. For this reason, the c and b quark masses often appear as model variations considered as uncertainties in PDF fits.

Another source of uncertainty is the *strangeness suppression factor*, which may take various values. This factor accounts for the suppression of strange quarks relative to up and down quarks observed in measurements of dimuon production in neutrino scattering [60–63].

Other uncertainties arise as a result of the parameters used for the fits of parton distributions. Gluon distributions xg, valence and anti-quark distributions xu_v, xd_v, $x\bar{u}$, $x\bar{d}$ $x\bar{s}$ are parametrised at the starting scale Q_0^2, evolved to the measurement scale and convolved with hard-scattering coefficients in order to give theoretical cross section predictions. A χ^2 function is used to compare these predictions to the data. The optimal functional form for the parametrisation of each parton distribution is then found using a parameter scan, generally of the form $A_i x^{B_i}(1-x)^{C_i}P_i(x)$ where $P_i(x) = (1 + D_i x + E_i x^2)e^{F_i x}$ for each flavour i. Experimental uncertainties from measured data may then be propagated to these fit parameters A_i, $B_i ... F_i$, leading to uncertainties on the PDF. Further details of these parametrisations may be found in [64].

Chapter 3

Physics Beyond the Standard Model

The Standard Model of particle physics has proven to be a tremendously successful description of our observations so far. However, there are many shortcomings where the model fails to provide answers to important open questions. In order to put these to rest, we seek solutions in new physics beyond the Standard Model (BSM). Many extensions of the SM predict new heavy gauge bosons; the detection of such particles could therefore provide evidence of new physics and guide us towards solutions to some of the unsolved puzzles in nature. This thesis focuses on searches for W' and Z' bosons, which are heavy counterparts of the SM W and Z bosons. These bosons are considered as “golden channels” for probing BSM physics thanks to their relatively clean and well-understood final states.

In this chapter, some of the outstanding questions motivating BSM searches are outlined. Additionally, the phenomenology of W' bosons (with a lesser focus on Z') is summarised.

3.1 Motivation to Look Beyond the Standard Model

The Hierarchy Problem

A hierarchy problem occurs when the measured value of a physical parameter greatly differs from its fundamental value, necessitating an 'unnatural' level of correction to reconcile the two. There are two well-known hierarchy problems in particle physics. The first is the large difference between the electroweak ($\sim$ 100 GeV) and Planck ($\sim 10^{18}$ GeV) scales; there is no consensus on why the weak force should be so much stronger than gravity. The second is related to the mass of the Higgs boson; though the Higgs mass has been measured at the electroweak scale (125 GeV), the bare mass m_0* is at the Planck scale. This is due to the contributions from one-loop diagrams of virtual particles, of which there could be an infinite number. This means that the corrections to the bare mass are quadratically divergent, up to the cut-off of our understanding; the Planck scale, λ. In order to counter these corrections and give the measured Higgs mass, the bare mass must be finely tuned to the level of 1×10^{16} GeV. It is this level of fine-tuning which motivates the existance of TeV scale physics which could serve to cancel some of the quadratically divergent corrections.

Neutrino Masses

Though the SM includes neutrinos as massless (Weyl) spinors, observations of neutrino-oscillations have proven that neutrinos do possess mass. Only left-handed neutrinos have been observed in nature so far, and the SM does not include right-handed neutrinos. All of the other massive elementary fermions in the SM come in pairs of opposite chirality which form Dirac spinors. Neutrino mass could indicate that they are in fact Dirac particles, requiring the introduction of right-handed neutrino spinors in the SM. Another theory is that neutrinos could be Majorana fermions, that is, fermions which serve as their own antiparticles. The pursuit of answers as to whether or not right-handed neutrinos exist and why the right-handed neutrinos we observe have such small masses motivates looking beyond the SM.

*The bare mass is defined as the limit of an elementary particle's mass at a distance approaching zero, or at a collision energy approaching infinity. The experimentally observed mass m of a particle is calculated as $m = m_0 + \delta_m$, where δ_m is the additional mass contribution arising from interactions of the particle with fields.

Dark Matter & Dark Energy

Global fits to the cosmic microwave background (CMB) have indicated that the baryonic matter described by the Standard Model only constitutes around 5% of the total mass of the Universe [65–67]. Measurements of the rotation curves of galaxies and gravitational lensing [68] indicate the existence of dark matter (DM), which makes up for 27% of our Universe. Here, "dark" refers to the fact that this matter is electrically neutral and does not emit or interact with electromagnetic radiation. In most theories†, dark matter does not couple via the strong interaction, meaning the only possible DM candidate in the SM is the neutrino, which only interacts weakly. For reasons related to the fact that neutrinos have a very small mass [70], only a small fraction of (*hot*) dark matter can be attributed to these SM particles. The search for a more suitable dark matter candidate therefore extends into physics beyond the SM, such as supersymmetry (SUSY).

The remaining 68% of the Universe is composed of dark energy. This has been inferred through observations of acceleration of the expansion of the universe [71], which would require some additional energy source.

Three Families

We know that there are three generations of quarks and leptons in the SM, as all have been observed experimentally. However, the reason for there being no more than three is not known and leads to possible explanations which go beyond the SM.

Grand Unification

The unification of all of the fundamental forces is one of the primary goals of particle physics. In Grand Unified Theories (GUTs), the forces are all merged into one single force with a shared coupling constant in a simillar manner to the unification of the weak and electromagnetic forces. All interactions are then unified in a simple gauge group, with the simplest examples being $SU(5)$ or $SO(10)$. As shown in figure 3.1, there is no point in the SM where the running couplings of the three fundamental forces meet. In BSM theories, such as SUSY, the running of these couplings is altered in such a way that there is a point where they are equal and unification is achieved.

† There are theories which predict Strongly Interacting Massive Particles (SIMPs) [69].

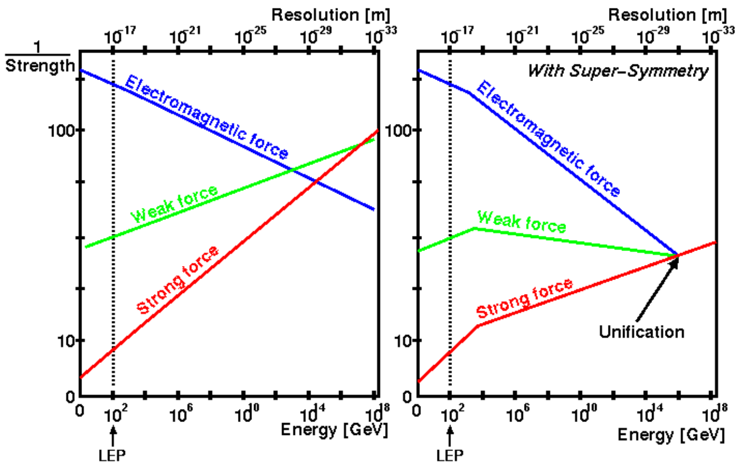

FIGURE 3.1: A sketch of the running of the strong, weak and electromagnetic couplings in the SM (left) and in a possible supersymmetric scenario (right). Taken from [72].

Matter-Antimatter Asymmetry

The Standard Model predicts that matter and antimatter should be produced at the same rate. If this were the case in the creation of the Universe, all of this matter and antimatter would have annihilated, leaving only energy. This is clearly not the case, indicating that there may be different physical laws for baryonic and antibaryonic matter. Several hypotheses as to the source of this imbalance lead to the Sakharov conditions [73] for baryogenesis, which state that matter and antimatter can be produced at different rates if an interaction is Baryon number violating, C and CP-symmetry violating and out of thermal equilibrium. Many BSM theories, such as GUTs and SUSY introduce new particles which interact in ways which satisfy all of these conditions in order to address this problem.

3.2 Phenomenology of W' Bosons

New heavy gauge bosons, W' and Z', are predicted in a plethora of BSM theories which seek to provide explanations for the aforementioned shortcomings of the SM. Generally, these new particles can be seen as heavier versions of their SM counterparts, though their couplings and spin can differ between models. New Z' bosons often arise from extensions of $U(1)$ symmetry, while W's (usually alongside Z') arise predominantly in extensions of electroweak symmetry with extra $SU(2)_N$ gauge groups. Since the main analysis in this thesis is a search for W' bosons, this section is focused on the phenomenology of these new particles. Examples of models in which W' bosons arise include:

The Sequential Standard Model

The Sequential Standard Model (SSM) [74] introduces two charged W's and a neutral Z'. In this model, these new bosons have the same quantum numbers and couplings to fermions as their SM counterparts but much larger (TeV-scale) masses and larger widths (approximately 3% of the pole mass). The SSM is not thought to be realistic - rather, it serves as a *standard candle* model, paving the way for more complex reinterpretations. In this thesis, the SSM is used without W-W' interference taken into account (as it normally would be in this model, see below), since such effects have a strong dependence on couplings and would therefore lead to a departure from the desired model-independence of this study.

W-W' Mixing

In many models, there can be interference between the W and W'x[75]. Interference is a reduction (or increase) in the differential cross section for a process due to another process with the same initial and final state. This is due to the fact that the calculated differential cross section depends on the absolute square of the sum of the Feynman amplitudes for all diagrams connecting these states. In the case of $W-W'$ interference, the matrix element squared for calculating the cross section becomes:

$$\begin{aligned} |\mathcal{M}| &= |\mathcal{M}_{SM} + \mathcal{M}_{BSM}|^2 \\ &= |\mathcal{M}_{SM}|^2 + |\mathcal{M}_{BSM}|^2 + 2\mathrm{Re}(\mathcal{M}^*_{SM} \cdot \mathcal{M}^*_{BSM}), \end{aligned} \tag{3.1}$$

where $\mathcal{M}_{SM}$ and $\mathcal{M}_{BSM}$ are the Feynman amplitudes for the SM (W) and BSM (W') Feynman diagrams, respectively. The first (SM) term represents the *irreducible background* in the search for new physics, while the last two terms form the BSM signal. The last term, which mixes SM and BSM contributions, is the *interference term.* A left-handed W'can interfere with its SM counterpart either constructively or destructively, depending on the relative sign of the W'coupling to quarks and leptons. For large interference effects, there must be $\mathcal{M}_{SM} >> 0$.

Left-Right Symmetric Models

Left Right Symmetric Models (LRSM) [76–86] are a class of GUT motivated theories which extend (potentially through breaking of $SO(10)$ or E_6) the gauge group of the SM to $SU(2)_L \times SU(2)_R \times U(1)_{B-L}$. As a result, these theories predict the existence of extra neutral Z_R and charged W_R gauge bosons. In these models, the W' boson is always lighter than the Z'; the ratio of their masses is:

$$\frac{M_{Z'}^2}{M_{W'}^2} = \frac{\kappa^2(1-x_W)\rho_R}{\kappa^2(1-x_W)-x_W} > 1, \tag{3.2}$$

where $\kappa \equiv \frac{g_L}{g_R}$ is the ratio of $SU(2)_{L,R}$ couplings, $x_W = \sin^2\theta_W$ where θ_W is the weak mixing angle and $\rho_R = 1$ or 2 depending on whether the symmetry is broken by a Higgs doublet or triplet, respectively.

The fact that these models would provide a natural scenario for the seesaw mechanism [87], whereby massive, right handed Majorana neutrinos are introduced to balance the diminutive masses of observed neutrinos, provides further motivation to seek W's in such a context.

Extra Dimensional Models

Some models [88] predict $W'$and Z' bosons which emerge as Kaluza-Klein excitations [89–91], that is, excitations in space with one or more additional compactified dimensions, of the SM gauge bosons, propagating in extra dimensions. Such models could lead to an explanation for the relative weakness of gravity compared to electromagnetism, as the gravitational force could be spread out across these additional dimensions.

The search for Z' bosons, a GUT model, formulated in 10 dimensions, in which the E_6 gauge group is broken into $SU(5)$ and two additional $U(1)$ groups **??**, leading to two new neutral gauge bosons Z'_ψ and Z'_χ. The lightest linear combination of these bosons is considered as the Z' candidate: $Z'\left(\theta_{E_6}\right) = Z'_\psi \cos\theta_{E_6} + Z'_\chi \sin\theta_{E_6}$, where $-\pi \leqslant \theta_{E_6} < \pi$ is the mixing angle between the bosons. Six different models [92, 93] each lead to a specific Z' state, named: Z'_ψ, Z'_N, Z'_η, Z'_I, Z'_S and Z'_χ.

Little Higgs Models

Little Higgs models [94] are non-GUT theories which aim to provide a solution for the heirarchy problem. This is achieved by introducing additional new gauge bosons, fermions and Higgses in order to cancel the quadratic divergencies which push the Higgs mass towards the Planck scale. Such theories (e.g. the *littlest Higgs* theory [95]) are based on an $SU(5)$ global symmetry and a locally gauged subgroup $[SU(2)_1 \times U(1)_1] \times [SU(2)_2 \times U(1)_2]$. The global symmetry is spontaneously broken down to $SO(5)$ with a vacuum expectation value of the order f, while the gauge symmetry $[SU(2) \times U(1)]^2$ is broken to the SM gauge group. As a result of the global symmetry breaking, 14 Goldstone bosons arise, including a real singlet and a real triplet, which become the longitudinal components of the new gauge bosons. These bosons have mass of the order f.

Technicolor Models

Technicolour theories [96–98] introduce a new gauge force coupled to new massless fermions (*technigluons* and *techniquarks*) in order to provide a mechanism for the breaking of electroweak gauge symmetry. *Extended Technicolour* (ETC) Models [99] introduce an extended gauge sector $SU(2)_{heavy} \times SU(2)_{light}$, where the first two generations experience the weaker $SU(2)_{light}$ and the third generation feels the stronger $SU(2)_{heavy}$. Both W' and Z' bosons are introduced in these extentions.

331 Models

W' bosons are predicted in 331 models [100–102] with $\beta = \pm\frac{1}{\sqrt{3}}$, where β is a parameter which identifies the type of 331 model considered. These models stand out from the others summarised here in that they do not involve the introduction of additional $SU(2)$ factors. The symmetry breaking $SU(3)_L \times U(1)_W \rightarrow SU(2)_W \times U(1)_\gamma$ leads to a pair of new W' bosons and three Z' bosons. Such models are strongly motivated by the fact that they could provide an answer as to why there are only three families of fermions through the introduction of a unique mechanism for gauge anomaly[‡] cancellation. In the SM, these gauge anomalies are cancelled separately within ach of the three quark families. In 331 models, the three families transform differently under the extended gauge group, meaning anomaly cancellation is achieved through the summation over all families, necessitating all three (though cancellation could also be possible for 6 families, 9 families and so on).

Minimal Supersymmetric Models

The Minimal Supersymmetric Standard Model (MSSM) [103] is the simplest supersymmetric extension of the SM, where the word “minimal” refers to the fact that it introduces the minimum number of new particles and interactions. In some extensions of the MSSM [104], additional $U(1)$ or $SU(2)$ gauge groups lead to new heavy gauge bosons such as W' and Z'.

The Heavy Vector Triplet Model

When searching for new resonances such as the W'or Z', there may be difficulties in determining which theory they arise from. Since each model comes with specific properties, many time consuming dedicated searches would be required to pinpoint the origin of these new particles. The Heavy Vector Triplet model [105, 106] seeks to expedite this process through the introduction of simplified phenomenological Lagrangians which

[‡]Gauge anomalies are processes which invalidate the gauge symmetry of the quantum field theory, for example one-loop diagrams of chiral fermions with n external gauge bosons where $n = 1 + \frac{D}{2}$ with D being the number of spacetime dimensions.

encompass various interpretations to more explicit models. As a consequence, results from searches conducted using this model may be reinterpreted in different theoretical contexts without the need for conducting separate analyses. This model generalises effective field theories with extended gauge sectors, where new particles can arise in multiplets of Lorentz and gauge quantum numbers. In the case of a heavy vector triplet $\mathcal{W}$, two charged W's and a neutral Z' are predicted. The Lagrangian for this triplet is:

$$\mathcal{W}^a_\mu \big[g_l \overline{l_L} \gamma^\mu \tau_a l_L + g_q \overline{q_L} \gamma^\mu \tau_a q_L + g_\phi \big(\phi^\dagger \tau_a i D^\mu \phi + h.c. \big) \big], \tag{3.3}$$

where g_l, g_f and g_ϕ (also denoted g_H) are the couplings to leptons, fermions and the Higgs, respectively. These couplings may also be expressed as:

$$g_f = g_q = g_l = \frac{g^2 c_f}{g_V} \quad g_H = c_H g_V, \tag{3.4}$$

where g is the SM $SU(2)_L$ gauge coupling, g_V parametrizes the interaction strength between the heavy vectors and $c_{f,H}$ are free parameters which are fixed in the explicit model.

In this thesis, two main examples of explicit models which are used to populate the parameter space of the HVT are referenced: HVT A and HVT B. In model A, the vector triplet arises from an extended gauge symmetry, with the symmetry breaking $SU(2)_1 \times SU(2)_2 \times U(1)_Y \rightarrow SU(2)_L \times U(1)_Y$ as described in [107]. In model B, which is a minimal composite Higgs model oulined in [108], the triplet arises in an $SO(5)/SO(4)$ global symmetry.

Part II

Experimental Setup

Chapter 4

The Large Hadron Collider

The Large Hadron Collider (LHC) is a hadron-hadron synchrotron built by the European Organisation for Nuclear Research (CERN) between 1998 an 2008 [109]. It lies in a tunnel 26.7 km in circumference, 45 – 170 m below the Franco-Swiss border, and is the largest particle physics experiment ever to be built. The counter-rotating hadronic beams which collide therein usually consist of protons, though heavy ions, such as lead nuclei, are used on a less frequent basis to extend CERN's physics program. This thesis focuses solely on proton-proton (pp) collisions.

4.1 Accelerator Complex

Figure 4.1 depicts a schematic of the LHC main ring and delivery system. The proton acceleration process begins with a simple bottle of hydrogen gas. The atoms it contains are stripped of their electrons in an electric field in order to yield protons. These protons are then injected into a linear accelerator (Linac 2) where they are accelerated to an energy of 50 MeV using a series of Radio-Frequency (RF) cavities. Next, they are injected into the Proton Synchrotron Booster (PSB), which accelerates them to 1.4 GeV, followed by the Proton Synchrotron (PS) which accelerates them to 25 GeV. The RF cavities of the Proton Synchrotron split the beam of protons into discrete packets known as "bunches". After this stage, these bunches are passed through the

Super Proton Synchrotron (SPS), where they are accelerated to 450 GeV before being injected into the two beam pipes comprising the main ring of the LHC.

The beam in one pipe circulates clockwise while the beam in the other circulates anti-clockwise. They are guided round the circumference of the accelerator by 1232 super-conducting dipole magnets and are accelerated by 8 RF cavities per ring until each beam reaches an energy of 6.5 TeV. There are four interaction points (IPs) where bunches cross and collisions take place, atop which the four main experiments are situated: ATLAS [110, 111], CMS [112, 113], LHCb [114] and ALICE [115].

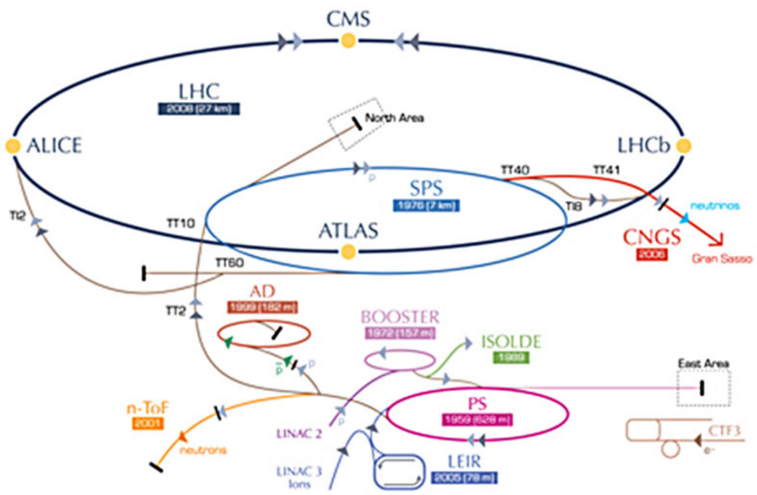

FIGURE 4.1: A schematic view of the CERN accelerator complex. The various accelerators used for the preparation of the hadron beams are shown, as well as the locations of the four main detectors [116].

4.2 Luminosity

The integrated luminosity, denoted by L, is the measure of the total number of collisions that occur over a period of time. It has units of cm^{-2}, though is usually quoted in units of barns, b, where 1 b = 10^{-24} cm^{-2}. The luminosity per second is known as the "instantaneous" luminosity, denoted by $\mathcal{L}$. The total number of events for a process X is given by:

$$N_{pp\to X} = \sigma_{pp\to X} L = \sigma_{pp\to X} \int \mathcal{L} dt = \frac{N_{tot}}{\sigma_{tot}}, \tag{4.1}$$

where σ is the cross-section for the process, N_{tot} is the number of collisions and σ_{tot} is the toal proton-proton collision cross-section. The instantaneous luminosity for a proton-proton collider is calculated as:

$$\mathcal{L} = \frac{N_b^2 n_b f_{rev} \gamma_r}{4\pi \epsilon_n \beta^*} \mathcal{F}. \tag{4.2}$$

Here, N_b is the number of protons per bunch, n_b is the number of bunches per beam, f_{rev} is the revolution frequency of the RF cavities, γ_r is the relativistic gamma factor, ϵ_n is the normalised transverse beam emission at the IP, β^* is the beta function describing the beam envelope at the IP. $\mathcal{F}$ is a geometric luminosity reduction factor caused by the crossing angle between the beams at the IP:

$$\mathcal{F} = \frac{1}{\sqrt{1 + \left(\frac{\sigma_s}{\sigma_{xing}} \frac{\alpha}{2} \right)^2}}, \tag{4.3}$$

where σ_s is the r.m.s bunch length, σ_{xing} is the transverse beam size[*] in the crossing plane and α is the full crossing angle. The beam parameters for the LHC in 2015 and 2016 are summarised in table 4.1.

Parameter Name	2015	2016
Energy [TeV]	6.5	6.5
Bunch Spacing [ns]	25	25
β^* [cm] (Crossing Angle [µrad])	80(290)	40(140)
Emittance ϵ^* [µm] (start of fill)	3.5	2.0
Max. Bunch Population [10^{11} p/bunch]	1.15	1.15
Max. # of Bunches Per Injected Train	144	96
Max. # of Bunches / Colliding Pairs IP1/5	2244/2232	2220/2208
Max. Stored Energy [MJ]	270	265
Peak Luminosity [10^{34} cm^{-2}s^{-1}]	~ 0.5	1.4

[*]The transverse beam size in plane x or y is defined as $\sigma_{x,y} = \sqrt{\beta^* \gamma^{-1} \epsilon_{x,y}}$, where $\epsilon_{x,y}$ are (normalised) transverse emittances, β^* is the β-function at the IP and γ is the relativistic factor [117].

Table 4.1: LHC beam parameters for 2015 and 2016. Here IP1 and IP5 refer to the interaction points at ATLAS and CMS, respectively. Taken from [118].

The total luminosity is calculated as a sum of instantaneous luminosity measured over a series of "luminosity blocks".

4.3 Pileup

In a given bunch crossing, there may be more than one inelastic *pp* interaction giving rise to final state particles. These are known as "pileup", or specifically "in-time-pileup", interactions. Another form of pileup known as "out-of-time pileup" can also arise when interactions from different bunches occur during the time taken by the detector to process a single event. The average number of pileup interactions per event, $\langle\mu\rangle$, is related to the centre of mass energy of the collision, the number of bunches in the beam and the characteristics of the beam, such as the number of protons per bunch and the beam size. The collision data collected at the beginning of Run 2 (2015) used a 50 ns bunch spacing, which has since been reduced to 25 ns - a number which is achieved when the accelerator is filled with 2808 bunches. This equates to a proton-proton collision frequency of 40 MHz. As the instantaneous luminosity achieved by the LHC increases, average pileup becomes larger and more measures must be taken to improve its modelling.

Chapter 5

A Large Toroidal LHC ApparatuS

The ATLAS detector, illustrated in figure 5.1, is one of the two nearly hermetic general purpose detectors at the LHC. It is designed to provide high quality measurements for a wide range of SM and BSM studies while handling the tremendous collision rates and radiation levels of the LHC beams. According to the letter of intent [119] for the detector, its basic design considerations are:

- Very good electromagnetic calorimetry for electron and photon identificaton and measurements, complemented by hermetic jet and missing transverse energy calorimetry.
- Efficient tracking at high luminosity for lepton momentum measumements and for enhanced electron and photon identificaton, and tau and heavy flavour tagging capabilities at lower luminosity.
- Precision muon momentum measurements with standalone capability at the highest luminosities.
- Large acceptance in pseudorapidity coverage.
- Triggering and measurements of particles at low thresholds.

Over 3000 scientists from 38 countries work together in the ATLAS collaboration, maintaining the detector and analysing the data which it records.

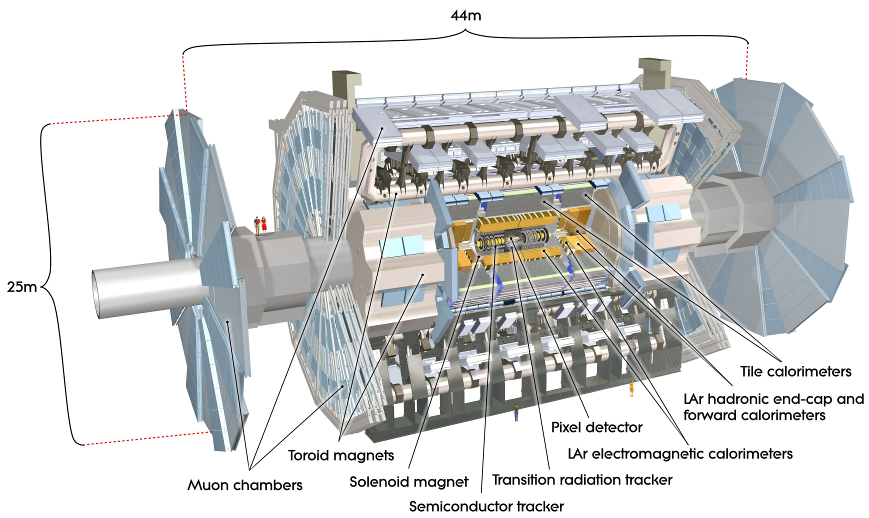

FIGURE 5.1: An overview of the ATLAS detector and its subdetectors [120].

5.1 The ATLAS Coordinate System

ATLAS uses a right handed coordinate system with the z-axis along the beam pipe and the origin at the nominal interaction point at the centre of the detector. The positive x axis points towards the centre of the ring, while the positive y axis points upwards towards the Earth's surface. Cylindrical coordinates (R,ϕ) are used in the transverse (xy) plane, where ϕ is the azimuthal angle around the beam pipe and R is a measure of the radial distance from the interaction point. The polar angle θ is the angle between the particle three-momentum $\mathbf{p}$ and the positive direction of the beam axis. The pseudorapidity η is defined in terms of θ as:

$$\eta = -\ln\tan\left(\frac{\theta}{2}\right), \tag{5.1}$$

hence η is zero when θ is perpendicular to the beam-axis. The angular separation (ΔR) between objects is defined as:

$$\Delta R = \sqrt{(\Delta\phi)^2 + (\Delta\eta)^2}. \tag{5.2}$$

The transverse component of any vector, such as the transverse momentum p_{T}, is defined as its projection in the xy plane. Since the boost along the z axis is so high, the energy and momentum of particles is often given in terms of this component.

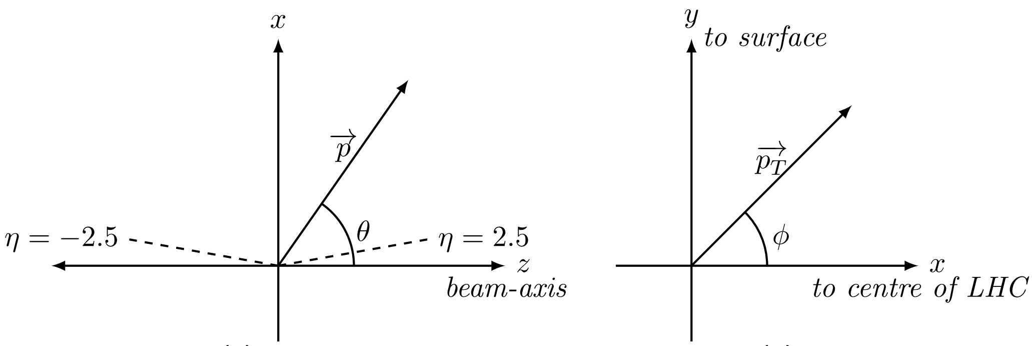

(a) xz-plane **(b)** xy-plane

FIGURE 5.2: An illustration of the ATLAS coordinate system showing (a) the xz-plane with the definition of θ and examples of η values and (b) the xy-plane showing the definition of ϕ.

Tracks detected in ATLAS are parametrized at the point of closest approach to the beam axis using the *perigee* parameters as illustrated in figure 5.3:

- The charge/momentum ratio of the particle in question, $\frac{q}{p}$.
- The angle between the particle's transverse momentum and the x-axis, ϕ_0.
- The angle between the particle's momentum and the z-axis in the Rz plane, θ_0.
- The signed distance of closest approach to the beam axis (also known as the *transverse impact parameter*), d_0. The quality of this measurement is often quantified using the d_0 significance $= \frac{|d_0|}{\left(\sigma(d_0)\right)^{\frac{1}{2}}}$, where $\sigma(d_0)$ is the uncertainty on d_0.
- The z-coordinate of the track at the point of closest approach to the beam axis, z_0.

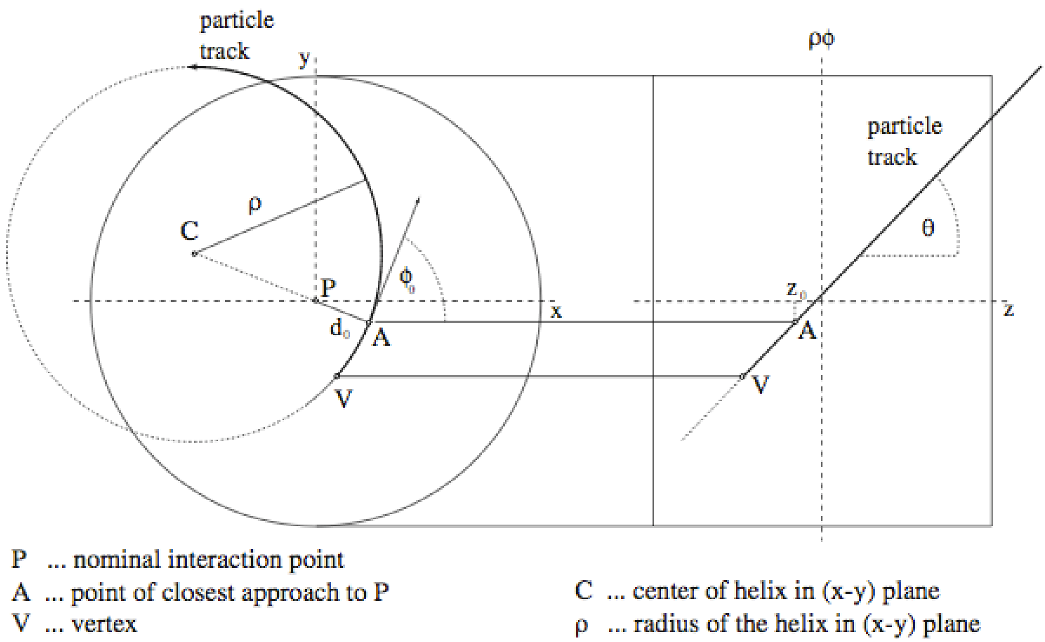

FIGURE 5.3: An illustration of the perigee parameters of a track in the ATLAS detector.

5.2 Detector Outline

The ATLAS detector is 46 metres long, 25 metres wide and weighs around 7000 tonnes. It is forward-back symmetric with respect to the beam interaction point and has full coverage in azimuthal angle. It consists of four major subsystems which are arranged in concentric cylindrical layers: the Inner Detector (ID), the Electromagnetic Calorimeter (ECAL), the Hadronic Calorimeter (HCAL) and the Muon Spectrometer (MS). The detector, and each of its subsystems, can be divided into three regions: the central barrel region and two endcap regions on either end. The ID [121, 122], described in more detail in section 5.3, is responsible for tracking and recognition of charged particles, while the calorimeters [123–125] outlined in section 5.5 measure the energies of electromagnetic and hadronic particles and aid in particle identification. The MS [126], detailed in section 5.6, provides precision momentum and position measurements of muons. The strong magnetic fields required for momentum measurements are provided by a system of magnets which are briefly described in sections 5.4 and 5.6.2.

In addition to these subsystems, the ATLAS detector boasts a series of complex trigger systems and luminosity detectors. The trigger system, responsible for reducing the raw data rate from ∼40 MHz to ∼200 Hz [127] so that it can be stored for analysis, is outlined in section 5.7. The luminosity detectors, which record soft collisions in the forward regions of the detector are described in 5.8.

5.3 The Inner Detector

The Inner Detector (see figure 5.4) is the closest subsystem to the IP, covering the range $3 < R < 120$ cm. It consists of two silicon detectors, the Pixel Detector [128] and Semiconductor Tracker (SCT), covering $|\eta| < 2.5$ and a straw tube gaseous detector, the transition radiation tracker (TRT), covering $|\eta| < 2.0$, all immersed in a homogeneous 2T magnetic field supplied by a superconducting solenoid magnet. The silicon detectors are cooled to around -20°C for optimal performance.

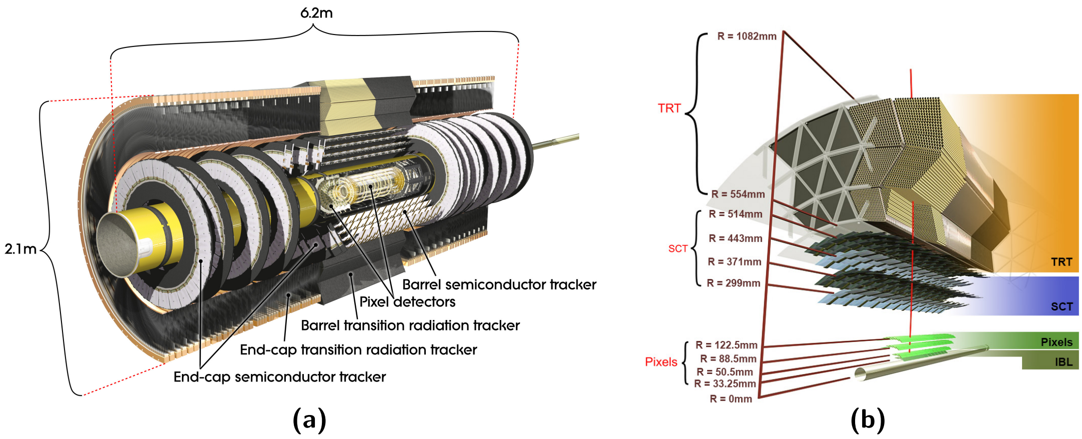

FIGURE 5.4: The layout of the ATLAS inner detector with its subsystems labelled. Figure (a) shows the longitudinal view [120] while (b) shows the cross-sectional view [129].

The Inner Detector's main purposes are to locate primary and secondary vertices, measure the momentum and position of charged particles and to identify electrons. A summary of the main attributes of the ID subsystems can be found in table 5.1.

Subdetector	Element Size [µm]	Intrinsic Resolution [µm]	Radius of the Barrel Layers [mm]
IBL	50 × 250	8 × 40	33.2
Pixel	50 × 400	10 × 115	50.5, 88.5, 122.5
SCT	80	17	299, 371, 443, 514
TRT	4000	130	554 – 1082

TABLE 5.1: Summary of the main characteristics of the ID subdetectors. The intrinsic resolution and sensor element size are reported in terms of $(R-\phi, z)$ for the pixel and IBL detectors and $(R-\phi)$ for the SCT and TRT. For the SCT and TRT the element sizes refer to the spacing of the readout strips and the diameter of the straw tubes, respectively. Taken from [130].

5.3.1 The Pixel Detector

The Pixel detector is the closest subdetector to the beam pipe. It is designed to take a very high granularity, high precision set of measurements as close as possible to the interaction point and is mainly responsible for impact parameter* measurements. It consists of 1744 silicon pixel modules; 1456 split into three barrel layers and 288 in three disks at each end. Each of the these modules contains 46080 pixels, giving ~ 80 million readout channels. Each pixel has a typical size of 50×400 µm^2 and thickness of 250 µm. The Pixel Detector was designed to work for instantaneous luminosities up to 1×10^{34} cm^{-2}s^{-1}. Since the LHC luminosity was upgraded to double this value for Run-2, this posed serious problems for the front-end electronics and performance of the subsystem - the original B-layer's expected lifetime without upgrade was the equivalent of $\sim$ 500 fb^{-1} [131]. The solution to this problem was to insert a new layer of pixels, known as the Inner B-Layer (IBL) [132], between the beam and the innermost layer of the detector in order to recover the reduced efficiency of the subdetector. The IBL consists of around 12 million pixels spread across 224 modules. In contrast to those in the original Pixel Detector, these have a size of 50×250 µm^2 and a thickness of 200 µm (60% of the original pixel size) [133]. The inclusion of this layer improves impact parameter resolution almost by a factor of two for tracks with low transverse

*Defined as the a track's distance of closest approach to the beam axis.

momentum [132], as well as providing an additional space point closer to the IP for enhanced pattern recognition.

5.3.2 The Semiconductor Tracker

Surrounding the Pixel Detector is the Semiconductor Tracker. It is designed to provide eight precision measurements per track and contributes to the measurements of charged particle momentum, impact parameter and vertex position. The SCT is a silicon strip detector comprised of 4088 modules arranged in a barrel of four cylinders and two endcaps each of nine disks. The 2112 barrel modules all follow the same rectangular design, while the endcap modules are split into four trapezoidal designs tailored to their radial location, as outlined in table 5.2.

Disk	0	1	2	3	4	5	6	7	8
Outer	52	52	52	52	52	52	52	52	52
Middle	40	40	40	40	40	40	40	-	-
Short Middle	-	-	-	-	-	-	-	40	-
Inner	-	40	40	40	40	40	-	-	-
Total	92	132	132	132	132	132	92	92	52

Table 5.2: Number of modules in each disk of an SCT endcap. Taken from [134].

Outer, middle and inner endcap modules are named based on their position on the endcap disk. All modules consist of two pairs of back-to-back 80 µm pitch sensors apart from the endcap inner and short-middle modules, which only contain one pair of silicon sensors due to their smaller size. All modules are split into 12 chips each of 128 silicon strips/channels. Six of these chips are on each side of the module, where the sides are referred to as “link0” (outer) and “link1” (inner). Link0 and link1 sensors are aligned with a stereo angle of 40 mrad to each other and are connected to binary signal readout chips, increasing accuracy of track measurement and enabling z-position measurements. The precision of the SCT modules is 17 µm in the R$-\phi$ coordinate and 580 µm for the z- coordinate.

5.3.3 The Transition Radiation Tracker

The outermost subsystem of the Inner Detector, located at 554 < R < 1082 mm, is the TRT. It is a straw tube tracker consisting of around 300,000 polyimide drift tubes each with a 4 mm diameter. Each of these tubes is inter-leaved with transition radiation material, filled with a Xenon-based or Argon-based gas mixture and has a 31 µm diameter gold-plated tungsten wire running through its core acting as an anode. When an ultra-relativistic charged particle with Lorentz factor γ passes through the dielectric boundaries of a straw, it emits transition radiation (comprising of soft X-rays) which ionises the gaseous mixture and produces a signal. The probability for a given particle to emit transition radiation is determined by its γ-factor, therefore measurement of this radiation is a powerful tool for particle identification. Since electrons generally have large γ-factors, they are likely to emit transition radiation photons which are easily distinguishable from those produced by the low energy backgrounds (predominantly pions). Figure 5.5 shows the probability of a TRT high-threshold (HT) hit as a function of the Lorentz factor for the barrel and endcap regions. The TRT is designed to exploit this, providing discrimination between electrons and pions over the range 1-200 GeV. This subdetector is therefore crucial to the electron selection process in ATLAS and subsequently the W' analysis outlined in this thesis.

As with the other ID subdetectors, the TRT is split into a barrel region and two endcap regions. The barrel straws are 144 cm long and run parallel to the beam line, covering from 560 to 1080 mm, $|z| < 720$ mm and $|\eta| < 1$. The endcap straws are 37 cm long and run perpendicular to the beamline (in a radial arrangement around the beam), covering 617 < R < 1106 mm, $827 < |z| < 2664$ mm and $1 < |\eta| < 2$. Each TRT straw has an intrinsic accuracy of 130 µm in R-ϕ. Since approximately 36 hits are expected for a charged particle traversing the TRT, it contributes substantial improvements to momentum measurements of these particles in tracks from the Pixel and SCT subsystems.

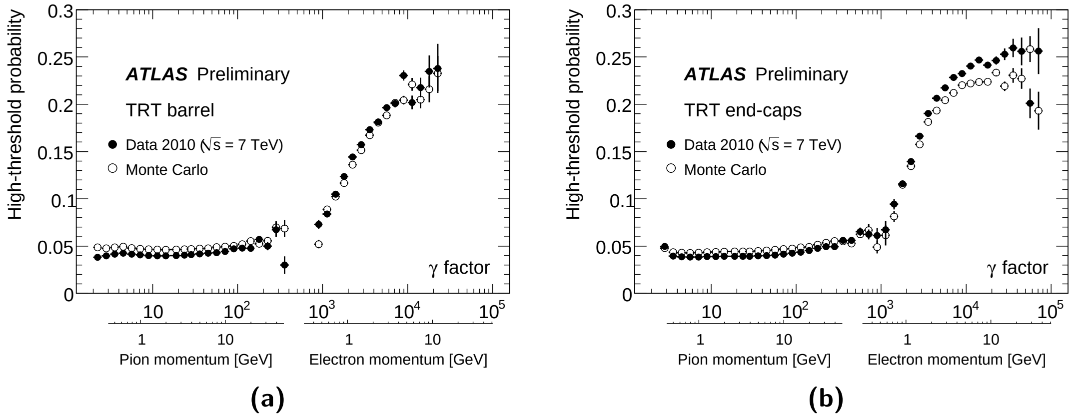

FIGURE 5.5: Plots of the probability of a TRT high-threshold hit as a function of the Lorentz γ factor for the barrel (a) and endcap (b) regions. Taken from [135].

5.4 The Solenoid Magnet

A superconducting solenoid magnet [136] provides a magnetic field of 2 T parallel to the beam axis in order to bend charged particles for momentum measurement. It is 5.3 m long, 2.4 m in diameter, 4.5 cm thick and weighs 5 tonnes. The magnet coil is positioned in front of the calorimeters and is therefore required to be as thin and transparent as possible. It consists of 9 km of aluminium-stabilised superconducting wire and operates at a nominal current of 7.73 kA and a temperature of 4.5 K.

5.5 The Calorimeters

The ATLAS calorimeters [123], which serve to measure the energy of incident particles, are illustrated in figure 5.6. They are split into two main systems: the Electromagnetic Calorimeters, which measure electromagnetically interacting particles, and the Hadroinic Calorimeters, which measure strongly interacting particles. These systems have three regions corresponding to the barrel and each endcap, providing measurements in the region $\eta < 4.9$ and complete coverage in ϕ. This coverage is necessary for the accurate reconstuction of missing energy; an important variable for many physics searches such as the one presented in part IV of this thesis. The depth of the calorimeters is chosen to maximise the containment of electromagnetic and hadronic showers,

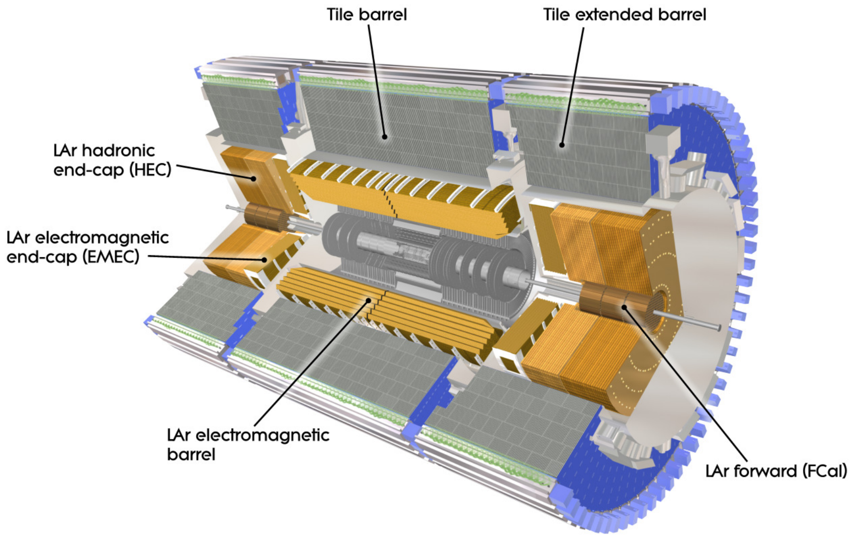

FIGURE 5.6: Cut-away view of the ATLAS calorimeter system. The components which use LAr as the active medium are shown in gold, encompassing all of the EM calorimeter systems and forward hadronic calorimeter systems. The components which use tile scintillators are shown in silver. Taken from [120].

limiting punch-through to the muon system which surrounds them. This thickness equates to 11 interaction lengths (λ), defined as the average distance required for the energy of a particle to reduce by a factor of $\frac{1}{e}$ via hadronic interactions. The system adopts two different calorimetry technologies: liquid Argon (LAr) [124] calorimeters and tile [125] calorimeters. The EM calorimeter is composed exclusively of the former, while the hadronic calorimeter is composed of a mixture of the two.

The energy resolution of the calorimeter systems is described by the function:

$$\frac{\sigma(E)}{E} = \frac{a}{\sqrt{E[\mathrm{GeV}]}} \oplus b, \tag{5.3}$$

where a is a stochastic term relating to the shower evolution and b is a constant term which quantifies calorimeter response. The energy resolution requirements for the various systems are outlined in table 5.3

Detector Component	Energy Resolution $\left(\frac{\sigma(E)}{E}\right)$
ECAL	$\frac{10\%}{\sqrt{E}} \oplus 0.7\%$
HCAL Barrel	$\frac{50\%}{\sqrt{E}} \oplus 3\%$
HCAL Endcap	$\frac{100\%}{\sqrt{E}} \oplus 10\%$

Table 5.3: The energy resolution of the various calorimeter systems. Taken from [120].

5.5.1 LAr Electromagnetic Calorimeters

The ECAL is responsible for measuring the energies of incoming photons and electrons and the electromagnetic component of incident jets. It makes use of lead absorbers surrounded by liquid Argon with kapton electrodes inbetween. In order to ensure that the Argon remains in liquid form, the calorimeter's barrel and endcap components are each housed in their own cryostat at -88°C.

The barrel region ($|\eta| < 1.475$) is split into two identical half-barrels separated by a 4 mm gap at $z = 0$, while the end caps are each split into an outer ($1.375 < |\eta| < 2.5$) and inner ($2.5 < |\eta| < 3.2$) wheel. The total thickness of a barrel module ranges from 22 to 33 radiation lengths, X_0, defined as the average distance required for a particle to lose $\frac{1}{e}$ of its electromagnetic energy. The "crack" region between $1.375 \leqslant |\eta| \leqslant 1.52$ is normally excluded from analyses which require precise electron measurements. This is due to the fact that there can be energy loss where gaps exist in the ECAL detector material, and successful measurements in this region are affected by additional non-active materials required to cool and instrument the inner detector. The modules consist of absorbers arranged in an accordion shape with individual cells segmented in $\eta - \phi$, as shown in figure 5.7(a). This ensures complete ϕ coverage without any cracks, as well as fast extraction of signals at the rear or front of the electrodes. The module structure is split into three layers of decreasing granularity. The first thin ($4.3X_0$) layer provides high precision positon measurements with a granularity of 4.69 mm ($\Delta\eta = 0.0031$); approximately $\frac{1}{8}$ of the granularity of the second layer, which is designed to contain the bulk of the electromagnetic shower (with its length of $16X_0$). The third layer contributes to measurements of the shower development and provides an estimate of any leakage into the HCAL. For the range $|\eta| < 1.8$, an additional presampler detector is placed in front of the first layer in order to correct for energy lost by electrons and photons upstream of the calorimeter. The high granularity of the ECAL leads to high p_T resolution and enables discrimination between jets, photons and leptons based on the shape of their showers (see chapter 7).

5.5.2 Hadronic Calorimeters

The Hadronic Calorimeters are responsible for measuring the strongly interacting component of incident jets and absorbing all detectable particles which have passed through the ECAL (except for muons). They are split into the tile calorimeter (HCAL), the LAr hadronic end-cap calorimeter (HEC) and the LAr forward calorimeter (FCal). The tile calorimeter sits directly outside the ECAL, coveringt he region $|\eta| < 1.7$. It is subdivided into a central barrel and two extended barrels. Its modules, or wedges, of size $\Delta\phi \sim 0.1$ are comprised of steel aborbers with scintillating tiles as the sampling medium. A sketch of their layout is shown in figure 5.7(b). Scintillators absorb the energy of incident charged particles and release photons which travel through fibre optic cables to readout photomultiplier tubes (PMTs). The Hadronic endcap calorimeters cover $1.5 < |\eta| < 3$. Similarly to the ECAL, they use LAr as a detection medium due to their exposure to high radiation in this region, but with copper absorbers. The Forward Calorimeters (FCal) provide coverage over $3.1 < |\eta| < 4.9$. Each FCal is split into 3 modules: an electromagnetic module (FCal1) and two hadronic modules (FCal2 and FCal3). FCal1 uses copper absorbers while FCal2 and FCal3 use Tungsten. Since the FCal modules are located at high η, around 4.7 m from the IP, they are exposed to very high particle fluxes. Their design is influenced by this, adopting very small LAr gaps in order to avoid ion-buildup problems and provide the highest possible detector density.

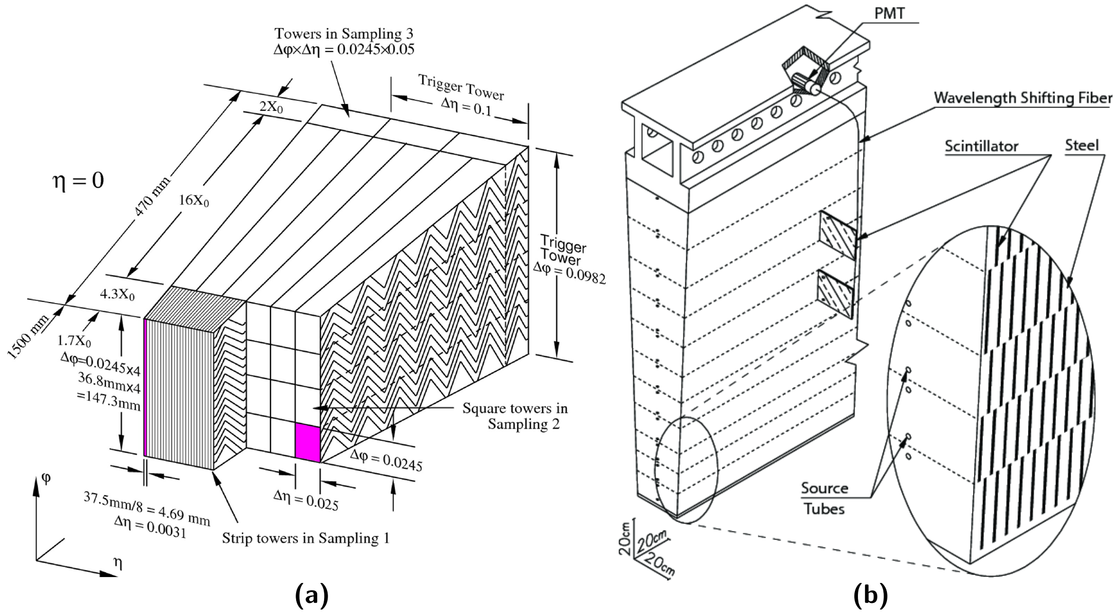

FIGURE 5.7: Figure (a) is a sketch of the structure of a LAr barrel module where the different layers are clearly visible. The granularity in η and ϕ of the cells of each of the layers and of the trigger towers is shown. Figure (b) is a sketch of the structure of a HCAL tile module, showing how the mechanical assembly and optical readout are integrated. The tiles fibres and photomultipliers of the optical readout are depicted. Both from [120].

5.6 The Muon System

The outermost and largest subdetector of ATLAS is the muon spectrometer (MS) (figure 5.8(a)). It is responsible for detecting and precisely measuring the momenta of muons; the only detectable particles from the pp collisions which are capable of escaping the calorimeters. Three large superconducting air-core toroid magnets (figure 5.8(b)) serve to bend the trajectories of muons passing through the spectrometer.

5.6.1 The Muon Spectrometer

The Muon Spectrometer adopts four different gaseous detector technologies: Monitored Drift Tubes (MDTs), Cathode Strip Chambers (CSCs), Resistive Plate Chambers (RPCs) and Thin Gap Chambers (TGCs). There are 1150 MDTs in the MS, providing tracking in both the barrel and endcap regions with a z resolution of 35 µm per MDT. In the first endcap layers corresponding to the region $2.0 < |\eta| < 2.7$, thanks to their

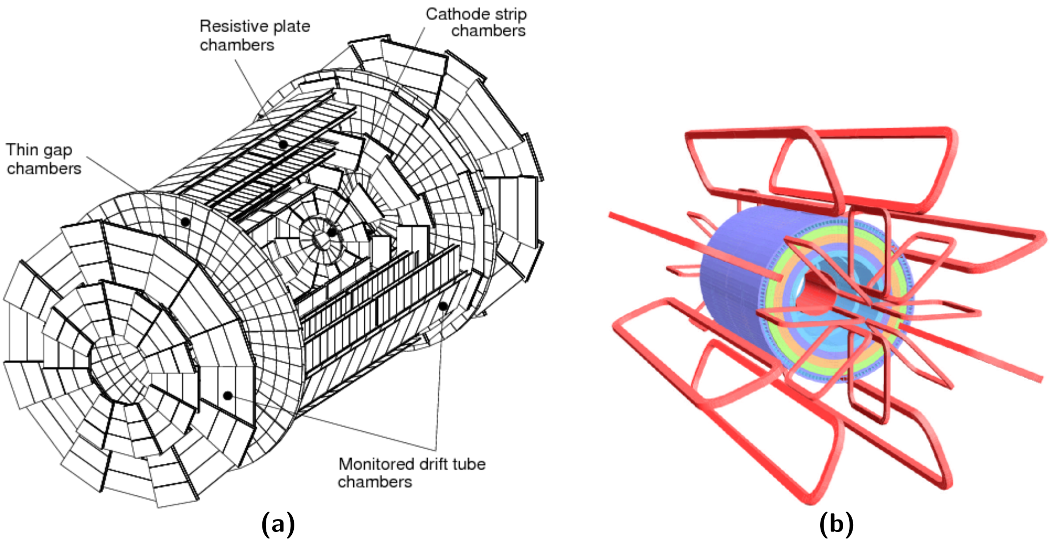

FIGURE 5.8: Diagrams of the ATLAS muon system. Figure (a) depicts the muon spectrometer with its various features labeled [110], while figure (b) shows the toroid (and central solenoid) magnet system [120].

higher granularity, CSCs provide extra precision tracking measurements where the expected muon rate is high. The CSCs have a resolution of 40 µm in R and 5 mm in ϕ. RPCs and TGCs are used to trigger on muon events in the barrel and endcap regions, respectively. These systems are optimised for time resolution over spatial resolution. The former measures the ϕ and z components of muons with a spatial resolution of 1 cm, while the latter provides measurements with resolution of 2–3 mm in R and 3–7 mm in ϕ. The temporal resolutions of these systems are 1 and 4 ns, respectively.

5.6.2 The Toroidal Magnet System

The magnetic field for the MS is generated by three large toroids. Each of these consists of eight coils with 120 (barrel) or 116 (endcap) turns assembled radially and symmetrically about the beam axis; a configuration which provides a field which is orthogonal to most muon trajectories. The coils operate at a nominal temperature of 4.6 K, achieved by liquid helium cryostats. In the range $|\eta| < 1.4$, a 0.5 T magnetic field is provided by the large barrel toroid, while the two endcap magnets provide 1 T in the range $1.6 < |\eta| < 2.7$. In the so called 'transition region' of $1.4 < |\eta| < 1.6$, a bending field is provided by both the barrel and endcap toroids. In this region the magnetic field is lower than eleswhere, varying up to $|\delta B| \approx 0.2$ T.

5.7 The Trigger System

The rare physics processes which we seek to detect at ATLAS occur at very low rates with respect to the total proton-proton inelastic scattering cross section. This means that, in order to produce a significant number of events containing these processes, a high luminosity is required. The LHC produces collisions every 25 ns (or at a rate of 40 MHz). However, the available data collection bandwidth and storage capacity of ATLAS is significantly smaller than what is required to process this event rate. It is therefore crucial to have an efficient trigger system to select the collision data which provides only high quality information for rare signals of interest.

The ATLAS Trigger and Data Acquisition (TDAQ) system consists of a hardware-based first level known as Level-1 [137] and a software-based Higher Level Trigger (HLT) [138]. The L1 trigger reduces the event rate to a maximum of 100 kHz with a decision time of less than 2.5 µs. It uses reduced granularity information from the muon trigger chambers and calorimeters in order to apply selections based on measurements of physics objects from early reconstruction. This level of the trigger also defines geometrical Regions of Interest (ROIs) in η and ϕ, outlining the localized regions of the detector where particle candidates are observed. If a ROI passes the criteria of one or more of the L1 triggers associated with the candidate, the trigger fires and passes the ROI information to the HLT. The HLT consists of the Level-2 (L2) trigger and Event Filter (EF), which were merged into one for Run-2. This trigger investigates the ROIs with full detector granularity (L2) and uses algorithms which are as close as possible to those used for offline event reconstruction (EF) in order to further accept or reject events. It reduces the event rate to 1 kHz with an average latency of 350 ms.

5.8 Luminosity Monitoring

ATLAS uses a series of purpose-built subdetectors in the very forward region in order to measure the LHC luminosity delivered to the experiment. These detectors are the LUminosity measurement using Cerenkov Integrating Detector (LUCID)[139], the Beam Conditions Monitor (BCM) [140] and the Absolute Luminosity For ATLAS (ALFA).

The LUCID detector is the main system responsible for luminosity monitoring. It consists of two detectors which sit close to the beam at $z = \pm 17$ m from the interaction point, covering $5.6 < |\eta| < 6$. Each of these detectors is comprised of 20 aluminium pipes filled with C_4F_{10} gas arranged around the beam pipe. Forward particles from inelastic *pp* scattering produce Cerenkov light as they hit these tubes, which is then measured by PMTs. The signal from these PMTs is read out at a rate which is faster than the bunch crossing rate, meaning the luminosity for each bunch crossing can be measured.

The BCM monitors the general conditions and quality of the beams, though it can also provide luminosity information to complement LUCID. It consists of two diamond sensors located at $z = \pm 1.84$ m from the interaction point, covering $|\eta| = 4.2$.

ALFA is located at $z = \pm 240$ m from the interaction point at only 1 mm from the beam. It uses scintillators with PMT readouts to measure elastic *pp* scattering rates, which can be used to calibrate the luminosity measurements made by the other detectors.

It is possible to monitor the luminosity using primary vertex counting from the Inner Detector. However, this counting becomes more difficult as pileup increases, leading to a less precise measurement. The Forward and Tile Calorimeters can also be used to provide average particle rates as a cross check for the dedicated luminosity subdetectors. However, these measurements are over longer time scales rather than per-bunch level.

The main technique for calculating the absolute luminosity involves calibrating the rate measurements made by these detectors using Van der Meer scans [141]. During these scans, the effective area of the beams is measured by sweeping the beams across each other in x and y independently. Using the convolved beam sizes in x and y, $\Sigma_x = \sqrt{\delta^2_{x,beam\,1} + \delta^2_{x,beam\,2}}$ and $\Sigma_y = \sqrt{\delta^2_{y,beam\,1} + \delta^2_{y,beam\,2}}$, the luminosity can be determined as:

$$L = \frac{n_b f_r n_1 n_2}{2\pi \Sigma_x \Sigma_y}, \tag{5.4}$$

where n_b is the number of proton bunches crossing at the IP, f_r is the LHC revolution frequency (11245.5 Hz) and n_1 and n_2 are the numbers of particles in each colliding bunch.

A possible way to measure (or monitor) the LHC luminosity is through measurements of well-known channels with large cross-sections and clean final state signatures. Standard "candle" channels such as Z bosons decaying to leptons are good examples. This involves measuring the rates of the chosen events with backgrounds subtracted in order to quantify the luminosity constraining the cross-section (σ) to its experiemental value using:

$$\sigma(L) = \frac{N_{sig+bg} - N_{bg}}{\epsilon \times L}, \tag{5.5}$$

where N_{sig+bg} is the measured data, N_{bg} is the number of expected background events taken from simulations and ϵ is an efficiency value encompassing detector effects, reconstruction and selection.

A total of 3212.96 pb^{-1} of 2015 data and 32861.60 pb^{-1} of 2016 data was recorded by ATLAS with a combined associated uncertainty of 3.2%†. This uncertainty is derived using a methodology similar to the one described in [143] from a preliminary calibration of the luminosity scale using Van der Meer scans which were performed in August 2015 and May 2016. As part of the luminosity monitoring, the average pileup per bunch crossing is also determined, as shown in figure 5.9. The average pileup has visibly increased from the 2015 to 2016 runs due to the increasing instantaneous luminosity.

†This is a preliminary value relevant to the data used for this analysis. The final luminosity uncertainty is 2.2% [142].

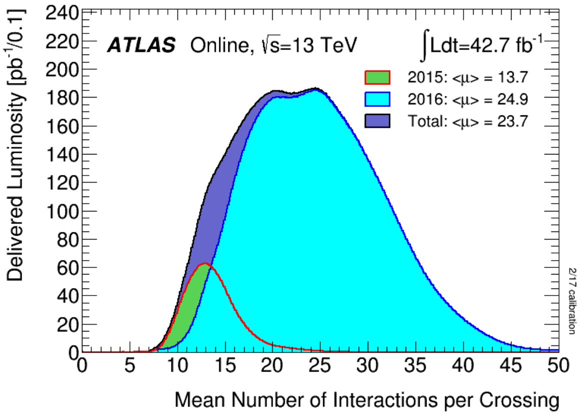

FIGURE 5.9: The luminosity-weighted distribution of the mean number of interactions per crossing for the 2015 and 2016 pp collision data at $\sqrt{s} = 13$ TeV. From [144].

5.9 ATLAS Performance

The ATLAS detector continues to collect data at an increasing rate. Figure 5.10 shows plots for the integrated luminosity delivered to and collected by ATLAS thus far. The results presented in this thesis use 3.2 fb^{-1} of 2015 $\sqrt{s} = 13$ TeV data and 32.9 fb^{-1} of 2016 $\sqrt{s} = 13$ TeV data, collected thanks to the consistently high performance of the subdetectors and data acquisition system. The detector continues to surpass its own records of recorded instantaneous luminosity in the ongoing 2017 data-taking period, though the work presented here does not include this dataset.

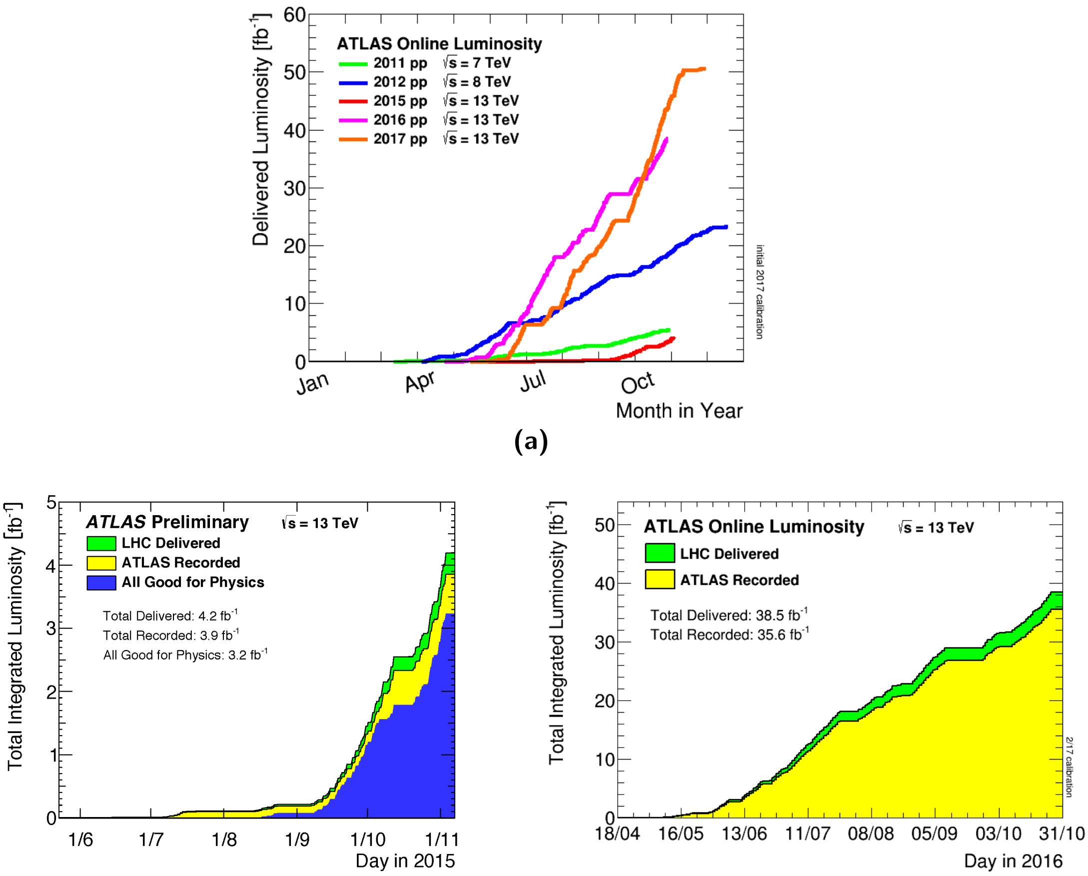

(a)

(b)

(c)

FIGURE 5.10: Figure (a) shows the cumulative luminosity versus day delivered to ATLAS during stable beams for high energy *pp* collisions. Lines corresponding to 2011, 2012, 2015, 2016 and 2017 data are shown. Figures (b) and (c) show the integrated luminosity versus time delivered to (green) and recorded by (yellow) ATLAS during stable beams for the 2015 and 2016 datasets, respectively. Figure (b) also shows the certified good quality data in blue. From [144].

Chapter 6

Modelling of Physics Processes

In the quest for new physics, the precise modelling of SM processes and BSM signal shapes is of the utmost importance. Monte Carlo (MC) simulations are utilised to model events of interest from the initial collision to the detector measurement. In order to provide realistic and reliable predictions, they must encapsulate decades of physics theory and measurements as well as detailed modelling of the ATLAS detector and its limitations. This is no simple task: the hadron-hadron collisions which take place at the centre of the ATLAS detector lead to non-trivial final states which arise from interactions between energetic partons. This means that simulations need to account for the poorly understood phase transitions of partons between the pertubative and non-perturbative regime of QCD. Four-vectors of each particle from the underlying physics process are produced using MC event generators before being processed through detailed simulations of the detector. MC event generators generally operate by splitting events up into stages according to characteristic energy scales. These stages typically include:

- Calculating the production of heavy/hard particles using Matrix Elements (MEs) at a given perturbative order.
- Considering the soft/collinear particles, resumming leading terms to all orders of QCD.

- Dressing these Matrix Elements with the contributions from soft emissions to represent the whole phase space.
- Modelling the hadronisation of partons as their energies decrease to the non-perturbative scale.
- Modelling any subsequent decays of unstable hadrons into long lived particles which go on interact with the detector.

In this chapter, some of these steps are explained, the Monte Carlo generators relevant to this thesis are introduced and a brief summary of the detector simulation is provided.

6.1 Additional Processes From the Proton-Proton Collision

As previously outlined in section 1.2, although pQCD treats the partons from the interacting protons as free particles, the colour confinement property of QCD dictates that at low energies they cannot be directly observed. Rather, they must combine to form the colourless hadrons which are measured in particle physics experiments. Such interactions lead to gluon emissions in either the initial or final state of a process. These emissions (as well as analogous QED processes) are referred to as *initial state radiation* (ISR) and *final state radiation* (FSR), respectively. The colour charged partons will emit QCD Bremsstrahlung when they are accelerated, leading to futher ISR and FSR and thus a *parton shower*. In addition to the main hard process of interest, where a parton from each of the colliding protons interacts, there are many softer interactions which the remaining partons participate in, collectively referred to as beam remnants. The partons from these radiative processes will eventually reach an energy scale where pQCD is not applicable and will subsequently hadronise. Figure 6.1 roughly depicts the processes which arise from the proton-proton collision which must be modelled by MC event generators. The incoming partons are depicted as three horizontal green lines coming from the left and right. The partons arising from the initial protons are shown in blue. One of these from each proton goes on to initiate a shower, each having one parton go on to contribute to the hard process which is depicted as a red circle. The outgoing partons from this process, shown in red, shower until they reach the hadronisation stage, forming colour-neutral states whoich are shown in green. The decay of short-lived particles is also shown in green. The evolution of the proton remnants which do not contribute to the hard process is shown in purple. These processes also lead to the colour-neutral states which would lead to signatures in the detector.

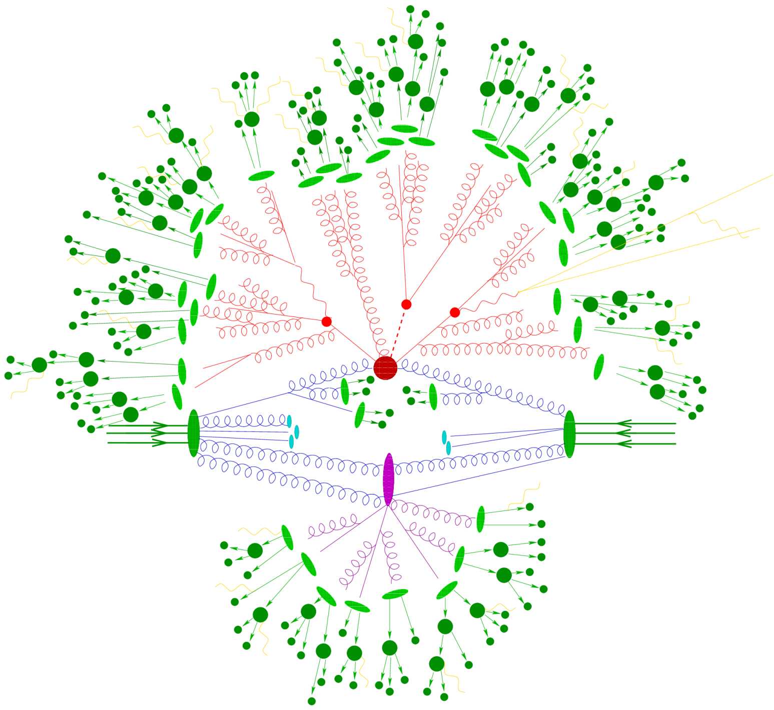

FIGURE 6.1: A schematic diagram of a hadron-hadron collision as it is simulated by a MC event generator. Gluons and quarks arising from the intial protons are shown in blue. The red circle at the centre represents the hard collision, with lines of the same colour emerging from it representing Bremsstrahlung as simulated by parton showers. The hadronisation stage is shown in green: the light green shapes show the parton-to-hadron transitions while the dark green shapes indicate hadron decays. Yellow lines are representative of soft photon radiation. The purple shape represents a secondary scattering event. From [145].

6.2 Monte Carlo Generators

Due to the complex nature of proton-proton collisions, modelling such processes is a challenging task. In order to provide an accurate description of the final states studied in physics analysis, MC generators must account for the various intermediate steps connecting the initial event to the long-lived final state particles. The process of modelling an event typically includes the following three stages:

Matrix Elements

The cross section for the hard scattering process $q\bar{q} \to ij$ can be calculated using the Feynman rules via the matrix element, $\mathcal{M}$, of the parton-parton cross-section. Generally, this can be interpreted as the sum over all Feynman diagrams participating in the process ($\mathcal{F}^{(a)}_{q\bar{q}\to ij}$):

$$\mathcal{M}_{q\bar{q}\to ij} = \sum_a \mathcal{F}^{(a)}_{ij\to F}. \tag{6.1}$$

Such calculations are performed at various levels of precision, equating to the relevant order of perturbation theory. At tree-level (LO) this is fairly straightforward and can be quickly calculated using MC generators. Higher order (HO) calculations, however, become more laborious due to the need to account for processees involving, for example, the radiation of additional hard partons. These effects can lead to singularities in the ME and must therefore be corrected for by the generator.

Parton Shower Algorithms

The ME calculation step above provides calculations for a fixed order of QCD, with only simple partonic final states. However, as discussed, we observe hadronic final states which result from a complicated series of scattering events. Modelling of the extraneous soft, collinear emissions from the scattering event, as well as the evolution of the partons, is handled by parton shower (PS) algorithms. Fundamentally, these algorithms involve sequentially calculating the probability for parton a to split into partons $b+c$, defined by a set of fragmentation equations, developing a full parton shower. These probabilities describe real parton emissions at each order in perturbation theory. In order to account for virtual (quantum loop) effects and restrict the probability of branching to $\leqslant 1$, the DGLAP equations are modified by adding the probability of *not* splitting during a given *evolution scale* (between energies Q_1 and Q_2), given by the *Sudakov form factor* [146]. The evolution of the shower may be described using different variables (e.g. ordering by p_T or angular variables); this choice distinguishes the various MC generators from one another. The inclusion of this factor also provides a link to the hadronisation process, since it introduces a cut-off to the shower evolution when the probability of branching reaches zero (at the scale of QCD (Λ_{QCD})). Showering algorithms become more complex when additional effects, such as ISR and FSR, are taken into account. In-depth details of the algorithms can be found in [147].

Matrix Element Matching

The ME gives an exact description of specific parton topologies where the partons are hard and separated at fixed order of perturbative series, but is computationally expensive and lacking in the description of additional contributions. On the other hand, the PS gives a sum of all collinear soft emissions, but fails to describe the hard emission at wide angles. In order to properly characterise the creation and evolution of jets from the initial event, the information from these sources must be merged. The combination itself brings complications - the fact that the ME is at fixed order while the PS is inclusive means that they are not directly compatible. Also, there could be double counting in certain regions of phase space which must be avoided. The methods for combination are typically referred to as “matching” and “merging”. Matching methods generate the whole phase space using the PS, but correct for the hardest emission using the ME, while merging methods introduce a *merging scale* above which partons are generated using the ME and below which they are generated using the PS. This is a very simplified overview of the procedures, of which there are many variations. Details of some of the different methods adopted by MC generators can be found in [148].

Tuning

Some observables which are modelled by event generators may be experimentally well measured, but explicitly sensitive to infrared physics. In such cases, formal factorasation theorems may not exist, leading to an incorrect description of the underlying event. Monte Carl is *tuned* to data in order to improve the modelling of parameters which are better described through measurement.

6.2.1 Monte Carlo Modelling Used

Drell Yan (DY) $W \to \ell\nu$ and $Z \to \ell\ell$ (where $\ell = e, \tau^*$)production processes are generated using Powheg-Box v2 [149] interfaced to the Pythia 8.186 [150] parton shower model. The CT10 PDF set [151] is used in the matrix element. The AZNLO set of tuned parameters [152] is used, with PDF set CTEQ6L1 [153], for the modelling of non-perturbative effects. The EvtGen 1.2.0 program [154] is used to describe the properties of b- and c-hadron decays. In DY production, the dominant component of HO EW corrections is QED FSR. This contribution is included using Photos++ 3.52 [155]. Additional HO EW processes are taken into account using corrections which are outlined in section 6.3.

For the generation of $t\bar{t}$ events, Powheg-Box v2 [149] is used with the CT10 PDF set [151] in the ME calculations. Electroweak t-channel and Wt-channel single top events are generated with Powheg-Box v1. This event generator uses the 4-flavour scheme for the NLO matrix element calculations together with the fixed four-flavour PDF set CT10f4. For all top processes, top-quark spin correlations are preserved (for t-channel, top quarks are decayed using MadSpin [156]). The PS, hadronisation, and the underlying event are simulated using Pythia 6.428 [157] with the CTEQ6L1 [153] PDF set and the corresponding Perugia 2012 set of tuned parameters (P2012) [158]. The top mass is set to 172.5 GeV. The EvtGen 1.2.0 program [154] is used for the properties of b- and c-hadron decays. The renormalisation and factorisation scales are set to:

- t-channel $= 4 * \sqrt{m_b^2 + p_{T,b}^2}$ where b denotes the spectator b-quark.
- $Wt = m_t$.
- $t\bar{t} = \sqrt{m_t^2 + p_{T,b}^2}$.

Diboson processes are simulated with the Sherpa 2.1.1 event generator [159]. MEs contain all diagrams with four electroweak vertices. They are calculated for up to 1 (4ℓ,

*Samples with decays to muons are not required in this electron channel analysis - the corresponding muon channel analysis uses μ and τ samples.

2ℓ+2ν) or 0 partons (3ℓ+1ν) at NLO and up to 3 partons at LO using Comix [160] and OpenLoops [161], and merged with the Sherpa parton shower [162] using the ME+PS@NLO prescription [163]. The CT10 PDF set [151] is used in conjunction with dedicated parton shower tuning developed by the Sherpa authors.

Cross sections for certain samples are scaled up to higher orders than those obtained from these generators using *k-factors* which are explained in more detail in section 6.3. An *event filter* is applied using ATLAS code in order to discard certain events and subsequently enrich samples with events of interest. The ratio of events which are kept (N_{MC}) to the total number of generated events (N_{tot}) is referred to the *filter efficiency*, $\epsilon_{filter} = \frac{N_{MC}}{N_{tot}}$. The integrated luminosity of a Monte Carlo sample with this efficiency taken into account is given by:

$$L_{MC} = \frac{N_{MC}}{\sigma_{tot}} = \frac{N_{MC}}{\sigma_{process} \times \epsilon_{filter}}, \tag{6.2}$$

where $\sigma_{process}$ is the cross section of the simulated process. This luminosity is further scaled to that of the analysed data for data/MC comparisons.

6.3 Higher Order Corrections

The theory calculations outlined in [164] allow for predictions of cross sections for the Drell Yan process at NNLO in QCD and NLO in electroweak effects, excluding the QED final state radiation (FSR) contribution, which is already modelled by PHOTOS. For the $W' \to \ell\nu$ and $Z' \to \ell\ell$ searches, mass-dependent k-factors constructed using these cross sections are used in order to correct predictions to the most current theory knowledge. In both cases, DY background processes are shifted to NNLO in QCD and NLO in EW while the signal processes are shifted only to NNLO in QCD. For the signals, the NLO EW contributions are neglected due to the fact that they are highly model dependent, therefore including them would be at odds with the attempts to create robust, model-independent searches.

For the Standard Model DY background processes, NLO EW corrections can be explictly calculated, since the couplings and masses are well known. In principle this is also possible for new gauge boson models, though this would mean masses (and the couplings for each of those masses) would all have to be set while maintaining gauge invariance. In making this choice, much of the flexibility of these searches would be lost and time-consuming calculations would have to be performed for each individual reinterpretation.

Two main methodologies exist for producing combined NNLO QCD and NLO EW cross sections: the *factorised* approach and the *additive* approach [164]. In the factorised approach the HO EW corrections are applied as a factor which is the same for all QCD orders (meaning the EW factor is dependent on LO QCD):

$$\sigma_{NNLO\_QCD+NLO\_EW} = k_{QCD} \times k_{EW} \times \sigma_{LO\_QCD},$$

where

$$k_{QCD} = \frac{\sigma_{NNLO\_QCD}}{\sigma_{LO\_QCD}} \quad \text{and} \quad k_{EW} = \frac{\sigma_{NLO\_EW,LO\_QCD}}{\sigma_{LO\_QCD}}. \tag{6.3}$$

In the additive approach, HO EW corrections are a constant additional σ to be added to each order of QCD (meaning that these EW factors are QCD independent of perturbative order):

$$\begin{aligned} \sigma_{NNLO\_QCD+NLO\_EW} &= \sigma_{NNLO\_QCD} + \Delta\sigma_{LO\_QCD+NLO\_EW} \\ &= \sigma_{NNLO\_QCD}\left(1 + \frac{\Delta\sigma_{LO\_QCD+NLO\_EW}}{\sigma_{NNLO\_QCD}}\right). \end{aligned} \tag{6.4}$$

The additive approach is chosen to be the nominal one for W' and Z' searches. It has already been used for run-1 ATLAS exotics searches (such as the dilepton search [165]). Figure 6.2 shows the difference in uncertainty values using the two approaches for each vector boson studied.

The magnitude of the NLO EW k-factors is $\sim$ 20% for the additive approach and $\sim$ 30% for the factorised approach at around 4 TeV. This spread is due to the unknown $\alpha_S \times \alpha_{em}$ mixed effects. This means that, for a mass of 4 TeV, NLO EW corrections

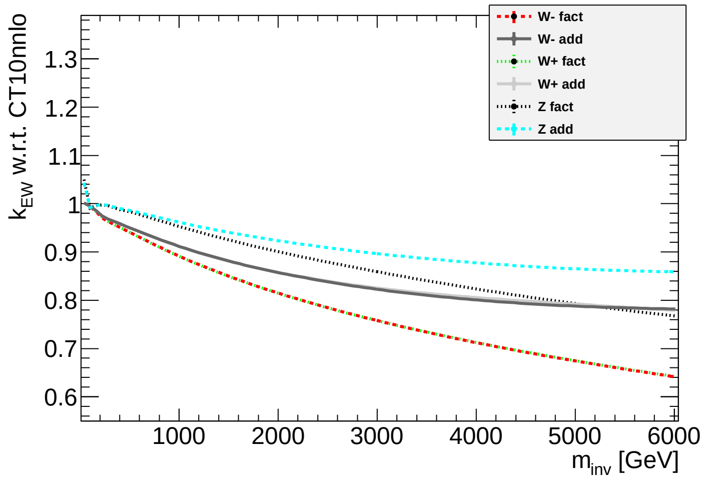

FIGURE 6.2: A comparison of the uncertainties for W'^{+}, W'^{-}, W and Z for the additive and factorised approaches to EW uncertainty treatment [166].

are 20% ± 10%, since the sign of the mixed terms is unknown. This uncertainty is symmetrised w.r.t the additive approach in order to give an uncertainty envelope. Other uncertainties associated with the applied higher order corrections are outlined in part III.

6.4 Detector Simulation

The information provided by the generators described above is not directly usable for physics analysis - an additional step of simulating the detector response is needed. For ATLAS, this is achieved using a C++ framework called ATHENA [167]. At this stage, interactions of final state particles with the detector are simulated, including displaced vertices for long-lived particles, shower evolution in the calorimeters and pile-up. Depending on time constraints or computer resources, analyses can choose to run a *full simulation* (FULLSIM) or a *fast simulation* (FASTSIM). The samples used for the analysis in part IV are produced using the full simulation. This is performed using GEANT4 [168], which is a toolkit used for the simulation of the passage of particles through matter. The tool uses a complete description of the detector and models individual particles' trajectories through it. The process of converting event generator output to something which resembles the ATLAS data which undergoes physics analysis is generally divided into three steps [169]:

1. Particle information passed from the relevant event generator is converted to hits (energy deposits) in each subdetector.
2. These deposits are digitised to emulate detector responses, or *digits*. Typically a digit is produced when the voltage or current on a readout channel exceeds a pre-defined threshold value within a given time window. Digits from each subdetector are written out as Raw Data Objects (RDOs).
3. The resultant digits are converted back to particles using the same reconstruction algorithms which are used for processing real data.

6.5 Pileup Reweighting

The MC samples used for analysis are enriched with pileup events using a flat distribution of expected $\langle\mu\rangle$ based on previous measurements [170]. In order to simulate the changing pileup conditions of the incoming data, this flat distribution is corrected to the latest distribution measured in data using a *pileup reweighting* (PRW) tool [171].

Chapter 7

Object Reconstruction

The elementary particles which physics analyses seek to measure are not directly observed in the ATLAS detector. They must therefore be reconstructed and identified based on their experimental signatures. In this chapter, the methods employed for reconstruction and identification of the pertinent physics objects for the analysis described in part IV are outlined.

7.1 Electrons

Electrons are reconstructed using a combination of information from the different subdetectors - predominantly the ID and ECAL. These systems provide tracks and energy deposits (clusters), respectively, which are combined in order to give the four vectors of electrons.

Electromagnetic clusters in the ECAL are reconstructed from seed clusters with $E_T >$ 2.5 GeV, which are found using a *sliding-window* algorithm [172]. This algorithm has a window size of 3×5 in units of 0.025×0.025, corresponding to the granularity of the EM Calorimeter's second layer* in $\Delta\eta \times \Delta\phi$ (see figure 5.7(a)). A *duplicate-removal* algorithm is also applied to nearby seed clusters. Once the clusters are identified, track reconstruction is performed.

*The majority of the EM shower is collected in this layer at high energy.

The inner detector track reconstruction software [173] adopts an event data model [174] with a full description of the detector design [175] to reconstruct tracks in three stages [127]:

1. A pre-processing stage, in which raw pixel and SCT data are converted into space points (where the SCT 3D coordinates are obtained by combining information from link0 and link1 of the silicon wafers which were outlined in section 5.3.2) and TRT raw timing information is converted into drift circles.

2. A track-finding stage, in which various algorithms optimised for different applications are used to build tracks. The default algorithm forms track seeds using hits from the pixel detector and the first SCT layer. These seeds are then extended through the remainder of the SCT, using additional hits to form track candidates. These candidates are then fitted and subjected to quality cuts in order to reject fake tracks. Surviving tracks are extended into the TRT so that drift-circles may be associated with them, resolving any left/right ambiguities in the process (there can be various possible paths which traverse all of the drift circles).

3. A post-processing stage, in which primary vertices are reconstructed using a dedicated vertex finder. This is proceeded by the reconstruction of photon conversions and secondary vertices using additional algorithms.

The algorithms used for the second stage use particle-specific hypotheses for the particle mass and probability to undergo Bremsstrahlung; namely the pion and electron hypotheses. The standard ATLAS pattern recognition [173] uses the pion hypothesis for energy loss in the detector. Since the 2012 data-taking period, track reconstruction for electrons has been significantly improved by adding additional electron-specific track reconstruction [176], where the electron hypothesis is used. If a track seed with $p_T > 1$ GeV falls within an EM cluster ROI[†] but cannot be attributed to a full track with at least seven hits using the pion hypothesis, a second attempt at pattern recognition is performed using the electron hypothesis. This involves using a *Gaussian Sum Filter* in order to account for large Bremsstrahlung effects [177]. Track candidates are then fitted using the relevant particle hypothesis using an ATLAS track fitter [178].

[†] A region of interest with a cone-size of $\Delta R = 0.3$ is defined around a seed cluster if it passes given shower shape requirements.

Again, if the pion hypothesis fails at this stage, the process is repeated using the electron hypothesis.

Obtained tracks are loosely matched to EM clusters using requirements [176] based on the distance in η and ϕ between the position of the extrapolated track in the middle layer of the calorimeter and the centre of the cluster. These requirements take into account energy loss due to Bremsstrahlung and number of hits in the silicon detector. An electron is reconstructed if at least one track is matched to the seed cluster. Although all tracks which are matched to the cluster are maintained for further analysis, the best-matched one is selected as the primary track, which describes the kinematics of the electron. The selection of this track is crucial to the electron reconstruction process. The best-matched track preferentially has hits in the pixel detector and is subject to requirements on the angular distance between its ID track and calorimeter seed cluster (more details can be found in [176]). The reconstruction chain outlined here is summarised in figure 7.1.

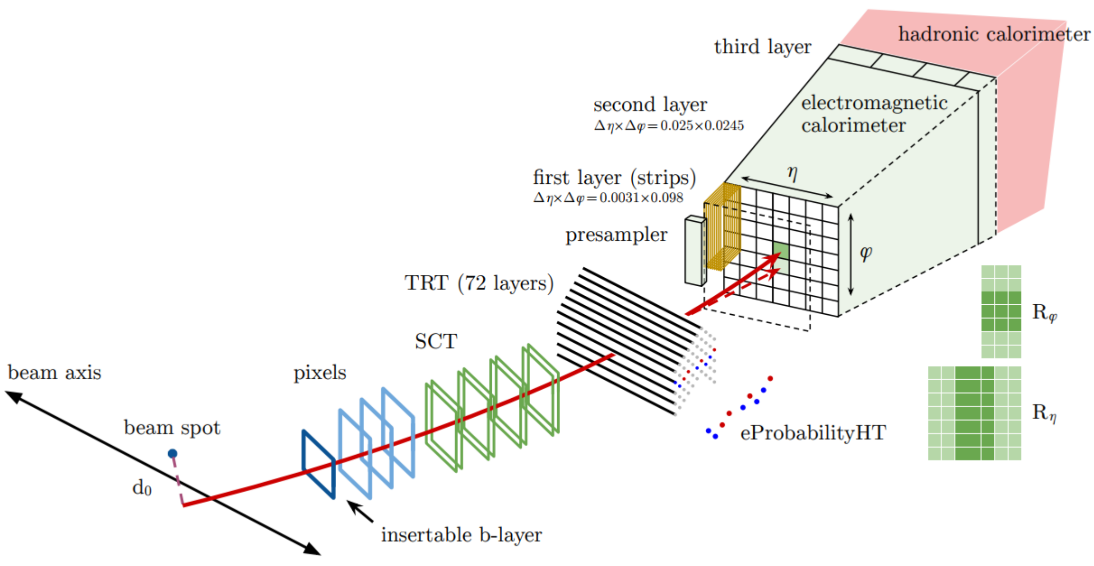

FIGURE 7.1: A schematic of the electron reconstruction process. From [179].

The overall reconstruction efficiency is quantified using a *tag-and-probe* method, which uses $Z \to ee$ and $J/\Psi \to ee$ events due to their large cross sections and clean di-electron final states. The low E_T range (around 7 - 20 GeV) is covered by the $J/\Psi \to ee$ events while measurements above 15 GeV use the $Z \to ee$ events. The method involves using one of the final state electrons which passes strict identification criteria (see below) to "tag" the event. A second "probe" electron is identified using a loose selection, then requirements on the di-electron invariant mass (and on lifetime information for the J/Ψ case) are applied to the tag-probe pair. Since the tag electron is almost certainly genuine, if the invariant mass/lifetime of the constructed pair is consistent with the true value, the probe is also considered to be authentic. The probe is subjected to further selections in order to eliminate the possibility of contamination from background objects (such as hadrons misidentified as electrons or electrons arising from photon conversions). The efficiency is then defined as the fraction of probe electrons which satisfy the tested criteria. As shown in figure 7.2, this efficiency is over 95% for the whole E_T range. The aforementioned improvement for the 2012 dataset onward is made apparent by this plot, which also shows the 2011 efficiency.

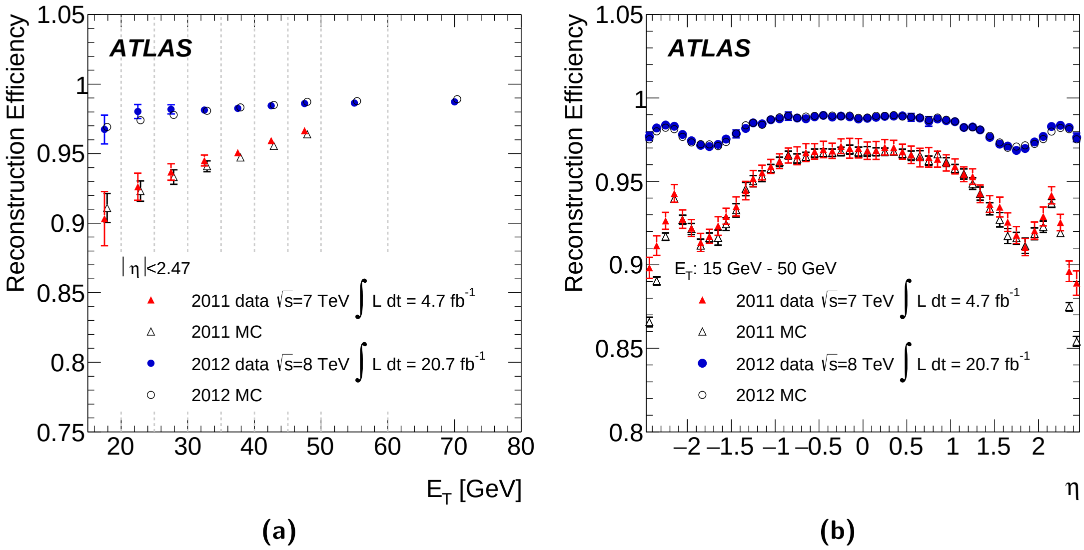

FIGURE 7.2: Measured reconstruction efficiencies as a function of E_T (a) integrated over the full pseudorapidity range and (b) as a function of η for 15 GeV $< E_T <$ 50 GeV for the 2011 (triangles) and the 2012 (circles) data sets. Both from [176].

Once the clusters have been built and attached to tracks, electron identification is applied in order to filter out background objects which can form clusters, such as hadronic jets and electrons from photon conversions. Genuine electrons are discriminated from backgrounds using a likelihood (LH) based method based on various variables describing shower and track properties, as detailed in [179]. Three levels of identification operating points are provided for electron ID, referred to (in order of increasing background rejection) as *Loose*, *Medium* and *Tight*. These operating points are designed in such a way that the samples selected by them are subsets of each other (i.e. Loose⊆Medium⊆Tight). Each uses a different set of selections which are described in detail in [180].

The *Loose* identification uses shower-shape variables in the first and second layers of the EM calorimeter along with hadronic-leakage information, that is, the ratio of energy in the ECAL to the energy deposited in the hadronic calorimeters. It also applies requirements on the electron track quality (minimum number of Pixel and SCT hits) and track-cluster matching.

The *Medium* identification tightens the requirements imposed by the *Loose* selection as well as introducting additional conditions. A hit is required in the innermost layer of the pixel detector in order to reject electrons arising from photon conversions. A selection requirement is also placed on the transverse impact parameter[‡] $|d_0|$ and on transition radiation in the TRT (in order to reject charged-hadron background).

The *Tight* identification tightens the requirements of the *Medium* selection further. Additional conditions include requirements on track quality in the presence of a track extension in the TRT and the ratio, $\frac{E}{p}$, of EM cluster energy to track momentum. A veto is also placed on electron clusters matching reconstructed photon conversion vertices.

The identification efficiency is also measured using the tag-and-probe method using electrons from $J/\Psi \rightarrow ee$ and $Z \rightarrow ee$ processes. Figure 7.3 shows the identification efficiency for each of the operating points. Though the more stringent requirements clearly lead to lower efficiencies, they also provide greater background rejection - this is why they are favoured for analyses such as the one presented in part IV.

In addition to identification requirements, electron isolation requirements defined by several working points are used in order to further reject hadronic jets which can be misidentified as electrons. The main two main variables used to inform these cuts are calorimeter-based isolation and track-based isolation criteria which are defined in **??**.

[‡]d_0 is the minimum distance between the object (in this case an electron track) and the primary vertex in the transverse plane.

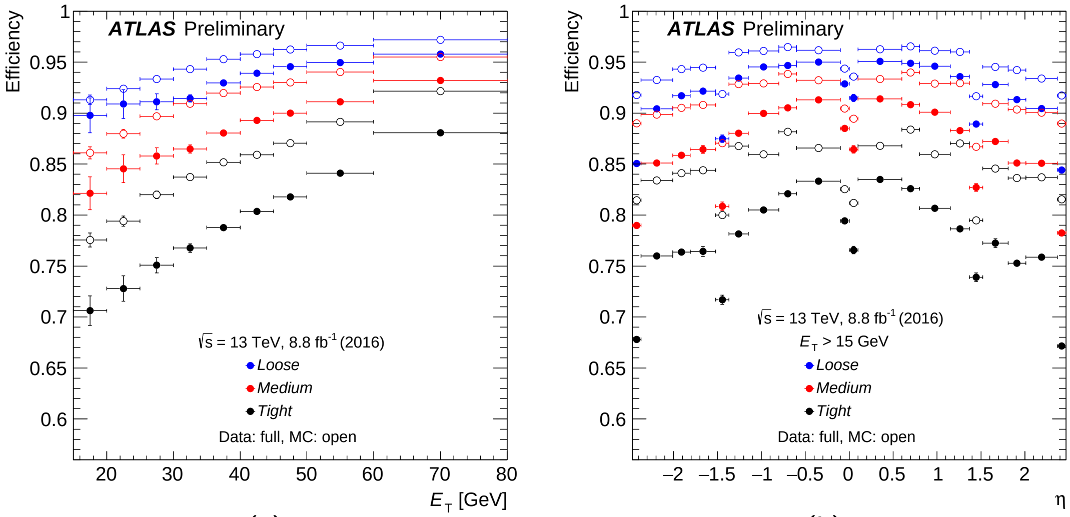

(a) **(b)**

FIGURE 7.3: Electron identification efficiencies in $Z \to ee$ events as a function of E_T integrated over the full pseudorapidity range 7.3(a) and as a function of η for electrons with $E_T > 15$ GeV 7.2(b) from 8.8 fb^{-1} of 2016 data. The lower efficiency in data w.r.t MC is understood to arise from mismodelling of calorimeter shapes and out-of-date modelling of TRT conditions. From [181].

For the W' analysis outlined in this thesis, in the interest of maintaining a high signal efficiency after tight likelihood requirements, only *Loose* isolation criteria are used.

Electrons selected for the analysis outlined in this thesis must satisfy the following criteria:

- $|\eta| < 2.47$, excluding $1.37 < |\eta| < 1.52$ crack.
- Not flagged as being from a bad calorimeter cluster.
- $p_T > 65$ GeV
- d_0 significance < 5 w.r.t. the beam line.
- Pass the likelihood *Tight* identification criteria.
- Fulfill the *Loose* isolation criteria.

7.2 Muons

Muon reconstruction is initially perfomed independently by the ID and MS, where tracks are expected. The ID reconstructs muons like any other charged particle (following the method outlined in section 7.1 without the electron-specific adaptations). The MS defines track "segments" in individual muon chambers based on hit patterns measured therein. These segments are reconstructed by performing a straight-line fit to the hits found in each layer. The MS identifies hits in each of the muon chambers which are aligned on a trajectory in the bending plane of the detector. Muon track candidates are then constructed by fitting hits from segments in different layers of the subdetector. Based on the information provided by these subsystems and several reconstruction criteria, four different muon "types" (outlined in [182]) are defined. For the analysis presented in part IV, *combined* (CB) muons, which are formed through the successful combination of an MS track with an ID track, are used. Efficient identification and reconstruction of combined muons is important to this analysis, since they are used for the construction of the missing transverse energy.

Isolation criteria are also applied for reconstructed muons in order to further reject fake candidates, especially those arising from b-decays. Various isolation working points defined using track-based and calorimeter-based isolation variables are are available, as defined in **??**. For the analysis presented here, the *LooseTrackOnly* working point (which solely uses track-based isolation as the discriminating variable) is adopted in the interest of keeping a high signal efficiency.

A high-p_{T} muon working point has been developed and optimised specifically for the W' and Z' searches **??**. This working point selects combined muons passing a *Medium* identification selection which are reconstructed with at least three hits in three stations in the MS. These requirements are chosen to improve the sagitta measurement (with a requirement of $\frac{q}{p}$ significance $>$ 7) and subsequently the p_{T} resolution. The working point also vetoes MS tracks which fall into poorly aligned chambers[§] based on their $\eta - \phi$ coordinates.

[§]Currently the excluded chambers are Barrel Inner Small (BIS) 7+8 and the overlap between the barrel and endcap at $1.01 < |\eta| < 1.1$.

Muons are selected for the anlaysis outlined in this thesis based on the following criteria:

- Pass the HLT_mu50 trigger.
- Resconstructed as a combined muon.
- $p_T > 55$ GeV.
- Pass the MCP high-p_{T} WP selection and bad muon veto.
- d_0 significance < 3 w.r.t. the beam line.
- $|z_0| \sin\theta < 0.5$ mm w.r.t. the primary vertex.
- Fulfill the *LooseTrackOnly* isolation criteria.

7.3 Jets

Collimated collections of particles resulting from the fragmentation and hadronization of quarks and gluons are referred to as jets. Jets are reconstructed from three-dimensional clusters of calorimeter cells known as *topo-clusters* [172], which attempt to encompass an entire particle shower. Topo-clusters are constructed using neighbouring calorimeter cells containing energy above a noise threshold which is estimated using measurements of electronic noise and simulated pile-up contributions. The cluster energy is the sum of all of the calorimeter cells contained in the cluster. These clusters are combined using jet algorithms, of which there are many [183] - the relevant one for the work presented in this thesis is the *anti-k_t* algorithm [184] with a distance parameter R = 0.4. Jets are reconstructed with this algorithm on the condition that they have an energy greater than 7 GeV. The measured jet energy is corrected to account for effects such as dead material in the detector, leakage of particles outside the calorimeter, particles which lie outside of the jet algorithm cone and particle reconstruction energy. This is achieved through the application of p_T and η dependent Jet Energy Scale (JES) corrections which are determined using Monte Carlo simulation [185].

Jets are used in the analysis outlined in this thesis for the construction of the missing energy. They are also important due to the fact that the analysis looks at a final state containing an electron, which could be "faked" by a jet.

7.4 Photons

Photons are expected to predominantly interact in the EM calorimeter, depositing all of their energy and producing a shower therein. However, it is also possible for them to first interact with the ID, producing tracks, before showering in the calorimeter in a similar manner to electrons (resulting in a level of ambiguity between the signatures of these physics objects). Photons are classified based on whether they interact with the detector via the former or latter scenario as "unconverted" and "converted", respectively.

Unconverted photons are reconstructed using an algorithm which builds clusters with a size based on the particle type and location (barrel or endcap) around a seed position [172].

Converted photons are reconstructed from conversion vertices (where the photon produces an e^+e^- pair) in the ID which are classified depending on the number of electron tracks assigned to them. These vertex candidates are transformed into converted photon objects if they can be matched to a reconstructed EM calorimeter cluster. Algorithms, described in detail in [186], are used to distinguish reconstructed converted photons from electrons.

Photons are used in the analysis described in part IV in order to reconstruct the missing transverse energy. The selected photons must pass a tight identification working point [187] and have $p_{\mathrm{T}} >$ 25 GeV and $|\eta| <$ @2.37, excluding the crack region.

7.5 Hadronic Taus

Hadronically decaying tau leptons are reconstructed using anti-$\mathrm{k_t}$ jets (with R=0.4) and clusters of calibrated calorimeter cells as inputs for a reconstruction algorithm as outlined in [188]. In the analysis outlined in part IV, taus are used for the reconstruction of the missing transverse energy - these leptons must pass a medium identification working point [189] and have $p_{\mathrm{T}} > 20$ GeV and $|\eta| < 2.5$, excluding the crack region.

7.6 Missing Transverse Energy

The missing transverse energy ($E_{\mathrm{T}}^{\mathrm{miss}}$) is a quantity which utilizes the law of conservation of 4-momentum to indirectly measure any particles which do not deposit any energy within the detector. In the standard model the only examples of such particles are the neutrinos $\nu_{e,\mu,\tau}$; since neutrinos are weakly interacting leptons, they do not undergo the strong or electromagnetic forces, meaning their interaction cross-section with the ATLAS detector is essentially non-existent. Since the initial energy of particles travelling transverse to the beam axis is zero, any net momentum in the transverse plane is indicative of “missing” energy. Their existence must therefore be inferred through the missing transverse energy. This variable is consequently vital to analyses such as the one presented in part IV, which have neutrinos in their final state. It is also an important quantity for general exotic searches, since any imbalance observed in the transverse plane could indicate the existence of an undiscovered unobservable object.

The transverse momenta (see section 5.1) of the colliding partons from the LHC are generally very small with respect to the energy scale of the collision. Using the uncertainty principle with the knowledge that these partons are confined within the proton diameter $\mathcal{O}(1)$ fm, the order of magnitude of the transverse momentum can be calculated:

$$\Delta p_T = \frac{\hbar}{\Delta x} \approx \frac{0.2\,\mathrm{GeVfm}}{1\mathrm{fm}} = 0.2\,\mathrm{GeV}. \tag{7.1}$$

This is negligible compared to the TeV scale of the collision, hence the sum of the transverse momenta of all of the visible final state particles is assumed to be zero.

This means that the existence of any particles which remain undetected can be inferred by a value of total measured transverse momentum which is non-zero:

$$\sum_{reconstructed} \vec{p}_T \; + \sum_{missing} \vec{p}_T = 0. \tag{7.2}$$

Therefore:

$$\sum_{missing} \vec{p}_T = -\sum_{reconstructed} \vec{p}_T, \tag{7.3}$$

where "reconstructed" refers to the particles which have been detected and "missing" refers which to those which have escaped detection. In general, masses are neglected in the definition of $E_{\mathrm{T}}^{\mathrm{miss}}$, so the missing transverse energy is defined by the magnitude of the missing transverse momentum:

$$E_{\mathrm{T}}^{\mathrm{miss}} = \left| \sum_{missing} \vec{p}_T \right| = \left| -\sum_{reconstructed} \vec{p}_T \right|. \tag{7.4}$$

The missing transverse energy is generally reconstructed using energy deposits in the calorimeters and muons reconstructed in the muon spectrometer, so this equation may be interpreted as:

$$E_{\mathrm{T}}^{\mathrm{miss}} = \left| -\sum_{reconstructed} \vec{p}_T \right| = \; -\sum_{calo} \vec{E}_T^{calo} - \sum_{MS} \vec{E}_T^{MS}, \tag{7.5}$$

where "calo" refers to the momentum measured in the calorimeter and "MS" refers to the momentum measured in the muon spectrometer. Since this constructed $E_{\mathrm{T}}^{\mathrm{miss}}$ measurement could include missing objects or "gaps" in the detector, reconstruction actually uses mesasurements of other physics objects in order to capitalize on their precise calibration. The calorimetric component is refined by associating calorimeter clusters to reconstructed objects using specialised overlap removal[¶]. For the purposes of the analysis described in part IV, the $E_{\mathrm{T}}^{\mathrm{miss}}$ is be defined as:

[¶]Calorimeter cells which are not associated with any object may still be included.

$$E_{\mathrm{T}}^{\mathrm{miss}} = \underbrace{\underbrace{-\sum_{\substack{\text{selected}\\ \text{electrons}}} \vec{p}_T^{\,e}}_{E_T^{miss,e}} \underbrace{-\sum_{\substack{\text{accepted}\\ \text{taus}}} \vec{p}_T^{\,\tau}}_{E_T^{miss,\tau}} \underbrace{-\sum_{\substack{\text{accepted}\\ \text{photons}}} \vec{p}_T^{\,\gamma}}_{E_T^{miss,\gamma}} \underbrace{-\sum_{\substack{\text{selected}\\ \text{muons}}} \vec{p}_T^{\,\mu}}_{E_T^{miss,\mu}} \underbrace{-\sum_{\substack{\text{accepted}\\ \text{jets}}} \vec{p}_T^{\,jets}}_{E_T^{miss,jet}}}_{\text{hard term}} \underbrace{\underbrace{-\sum_{\substack{\text{unused}\\ \text{tracks}}} \vec{p}_T^{\,track}}_{E_T^{miss,soft}}}_{\text{soft term}} . \tag{7.6}$$

Based on recommendations from the JetEtMiss group [190, 191], only electrons and muons which pass the signal selection for this analysis are used. Energy and momentum calibration corrections [192] are applied to these leptons as well as the jets. Photons (tight working point [187]) and taus (medium working point [189]) are subject to various p_T and η requirements which are implemented in the MET construction software before their inclusion. The $E_{\mathrm{T}}^{\mathrm{miss}}$ is constructed using the "METMaker" tool. After the electrons, taus, photons and muons are added to the estimate (in that order) with the necessary overlap removal, jets are added. The jets are required to have $p_T > 20$ GeV to be included. Additionally, if the jets have 20 GeV $< p_T <$ 60 GeV and $|\eta| < 2.4$, they are required to have a Jet Vertex Tagger (JVT) [193] variable > 0.59. This variable is designed to identify and suppress any pile-up jets. Tracks which belong to the primary vertex that have not been accounted for at this stage are added to the $E_{\mathrm{T}}^{\mathrm{miss}}$ soft term.

7.7 Event Cleaning

In order to ensure that the data used for analysis is of an acceptable quality, a set of cleaning requirements are imposed on the data and MC [194]. These selections are applied in an attempt to minimise the number of poorly measured events and spurious signals which make it into an analysis. For the analysis presented in part IV, the relevant event cleaning conditions are:

Good Run List (GRL)

The Good Run List catalogues all of the recorded luminosity blocks which pass a basic set of data quality requirements. Blocks which were recorded during prolonged periods of downtime for any subdetectors, for example, are omitted from this list. If a data event originated from a luminosity block which does not appear on this list, it is rejected. The luminosity quoted in section 5.9 is the value after this GRL is taken into account.

LAr and Tile Calorimeter Cleaning

It is possible that the calorimeters may experience "noise bursts" or record corrupted data, amongst other problems, during data taking. Events which have been flagged as being stricken by such issues are vetoed.

SCT Cleaning

The SCT modules are often recovered in order to address issues in recording data. After this happens there may be a delay in resyncing them, leading to "dead time" during which events cannot be properly recorded in the subdetector. Events which are affected by this issue are flagged and vetoed.

Primary Vertex Selection

Events are required to contain a Primary Vertex (PV). In the context of the analysis presented here, the PV is the vertex which has at least two tracks (with $p_{\mathrm{T}} > 0.4$ GeV) associated with it and the highest $\sum p_T^2$.

Part III

Theoretical Uncertainties in Heavy Boson Searches

Chapter 8

PDF Uncertainties

Searches for heavy gauge bosons, such as the W' and Z', probe previously uncharted kinematic regions as their mass predictions extend to the TeV scale. As these searches delve deeper into hitherto unexplored kinematic regions at the high energy frontier, detailed modelling of the relevant systematic uncertainties becomes increasingly important. In particular, uncertainties pertaining to knowledge of the partonic structure of the proton become progressively larger as the vector boson masses surpass the range where PDF data is informed by experiment. In order to account for these uncertainties, predictions must be shifted using the latest theory knowledge.

Uncertainties for all available modern NNLO QCD PDF sets are considered for the studies in this thesis, these include:

- CT14 [195]
- NNPDF 3.0 [196]
- PDF4LHC15 [197]
- HERA 2.0 [198]
- ABM16 [199]
- MMHT2014 [54]
- JR14 [200]
- ATLAS-epWZ16 [201]

These PDF sets require various prescriptions for quantifying their uncertainties, based on the manner in which the central values were calculated. In this chapter, the different calculation methods are described with results shown for each case. Uncertainties are evaluated for all three vector bosons (W^+, W^- and Z/γ^*), as well as for the combined W, where cross sections for the individual charged vector bosons are summed up before calculations are performed. In addition to calculating the uncertainties for each of these PDF sets, a PDF choice uncertainty is calculated by comparing the nominal set for the $W'$and Z' analyses (CT14 NNLO) to all other sets. All cross sections used for these studies were produced with VRAP 0.9 [202] using the methods outlined in [164] and supplied by [166].

8.1 Errors for Hessian PDF Sets

So called *Hessian* PDF sets are provided as a collection of mutually independent parameters formed by varying the central PDF values by their systematic uncertainties, reflecting experimental uncertainties of the data used for the PDF fit and model/-parametrisation uncertainties. These variations are treated in pairs and referred to as the "eigenvectors" of the PDF set in function space, as they can be varied in orthogonal directions in order to quantify the systematic uncertainties. In some cases, the errors calculated for such sets are asymmetric about the central value, while for others the errors are symmetric. In both cases, the PDF set is provided as a nominal value and a number of these shifted parameters for each mass point.

In the asymmetric case, upper and lower uncertainties are calculated as:

$$\Delta\sigma^+ = \sqrt{\sum_{i=1}^{N_{eig}} \left[\max\bigl(\sigma_i^+ - \sigma_0, \sigma_i^- - \sigma_0, 0\bigr)\right]^2}$$

and

$$\Delta\sigma^- = \sqrt{\sum_{i=1}^{N_{eig}} \left[\max\bigl(\sigma_0 - \sigma_i^+, \sigma_0 - \sigma_i^-, 0\bigr)\right]^2} \tag{8.1}$$

respectively, where N_{eig} is the number of PDF eigenvectors, σ_0 is the central value PDF, σ_i^+ is the higher value of the i$^{\text{th}}$ PDF eigenvector and σ_i^- is the lower value of the i$^{\text{th}}$ PDF eigenvector.

Symmetric uncertainties are also calculated as a cross-check for PDF sets with asymmetric errors. These are obtained through taking a simple average of the up and down uncertainties:

$$\Delta\sigma^{symm} = \frac{1}{2}\sqrt{\sum_{i=1}^{N_{eig}} \left[\sigma_i^+ - \sigma_i^-\right]^2}. \tag{8.2}$$

The nominal CT14 as well as MSTW 2008 and MMHT 2014 are examples of PDF sets comprised of asymmetric Hessian eigenvectors.

For the symmetric case, variations are not paired. Instead, the symmetric error for each “eigenvector” is simply taken as the difference between the variation and the nominal value:

$$\Delta\sigma^{symm} = \sqrt{\sum_{i=1}^{N_{eig}} \left[\sigma_i - \sigma_0\right]^2}. \tag{8.3}$$

Examples of symmetric Hessian PDF sets include ABM16, JR14 and PDF4LHC 15.

For limit setting in the heavy boson searches, total hessian up and down uncertainties would traditionally be provided as *nuisance parameters** used to apply the PDF uncertainty. However, these summed values inadequately describe the strong mass dependence exhibited by the individual eigenvectors for each set. Though this issue can be addressed by applying each individual eigenvector as a nuisance parameter, this can lead to time consuming limit setting for PDF sets with a larger number of variations. As a compromise, eigenvectors which display similar mass dependence may be summed up to form a set of “bundles”, each of which can be applied as a nuisance parameter. For $W'$and Z' searches this was the chosen method, until a reduced set of seven symmetric eigenvectors for the nominal CT14 set (which originally consisted of 28 eigenvectors) was constructed and provided by CT14 authors [203]. This set is

*These are defined as parameters which are not of immesiate interest in a statistical analysis, but which must be accounted for when analysing parameters of interest, e.g. systematic uncertainties. The role of such parameters is explained in chapter **??**.

favoured since the eigenvectors are orthogonal between W and Z: a crucial step towards a combined W'/Z' search (see part V). Figures 8.1 and 8.2 show the resulting eigenvectors for the W and Z boson, respectively. Dashed lines on these plots indicate a relative uncertainty of 3%, since eigenvectors with (absolute) maximum values below this threshold are considered negligible for the individual $W'$and Z' searches. Figure 8.3 shows the comparison of the summed eigenvectors for the full and reduced sets for W and Z.

This reduced set of eigenvectors is only valid for resonance masses of 120-6000 GeV for for the neutral current and 200-6000 GeV for the charged current.

8.2 Errors for Monte Carlo PDF sets

Some PDF sets are produced using the Monte Carlo methodology, whereby a number of pseudodata replicas are generated about the nominal value. For such PDF sets, a central curve is constructed by taking a simple mean of all of these replicas for each mass point. Error bands can be calculated at 90% confidence level (CL) and 68% CL by excluding the appropriate number of highest and lowest replicas and then taking the maximum and minimum of the remaining replicas for each mass bin.

The NNPDF 3.0 NNLO PDF set requires this treatment. Upon performing the calculations for this set, it was noted that for W^+, and subsequently combined W, the central value for some mass points was negative. This is symptomatic of the absence of PDF data at high Bjorken x, where cross sections are driven to extremely low values; as a result, many replicas produced by shifting these cross sections are negative. In order to amend this, it was suggested by NNPDF 3.0 authors that any negative replica values should be set to zero. Initially, a set of 100 replicas was tested, but this proved insufficient - around $\sim$ 50% of these replica values were negative and setting these to zero had a large impact on the calculated central values. It was concluded that a set of $\sim$ 1000 replicas (at least) is necessary in order to provide $\sim$ 500 positive replicas, which is enough to reduce any bias brought about to setting values to zero. The plots in figure 8.4 show the central curves for the W cross sections before and after setting

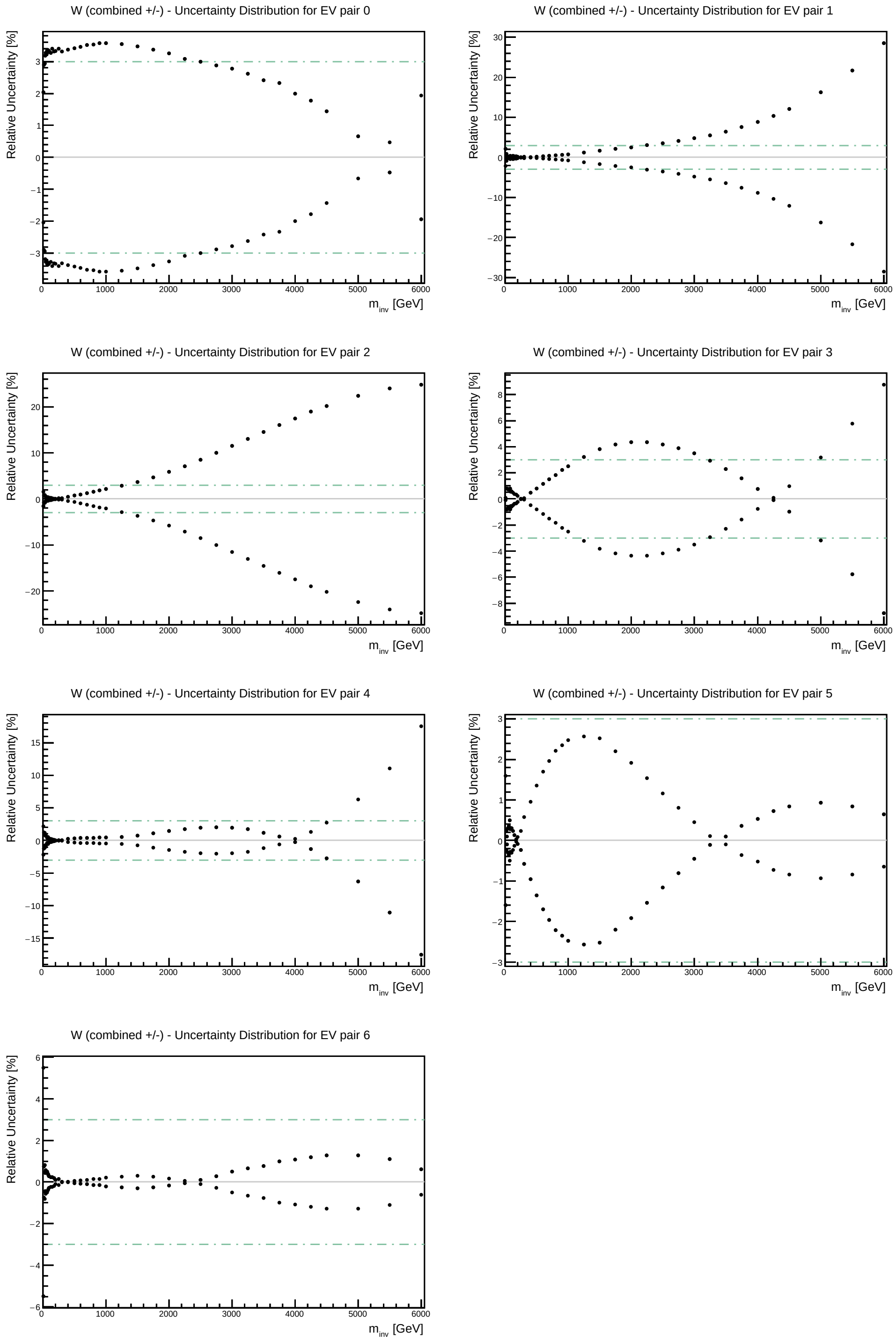

FIGURE 8.1: Distributions of the seven CT14 eigenvector bundles [203] for the charged current Drell-Yan process as a function of invariant mass of the W boson. The dashed lines indicate a relative uncertainty of 3%.

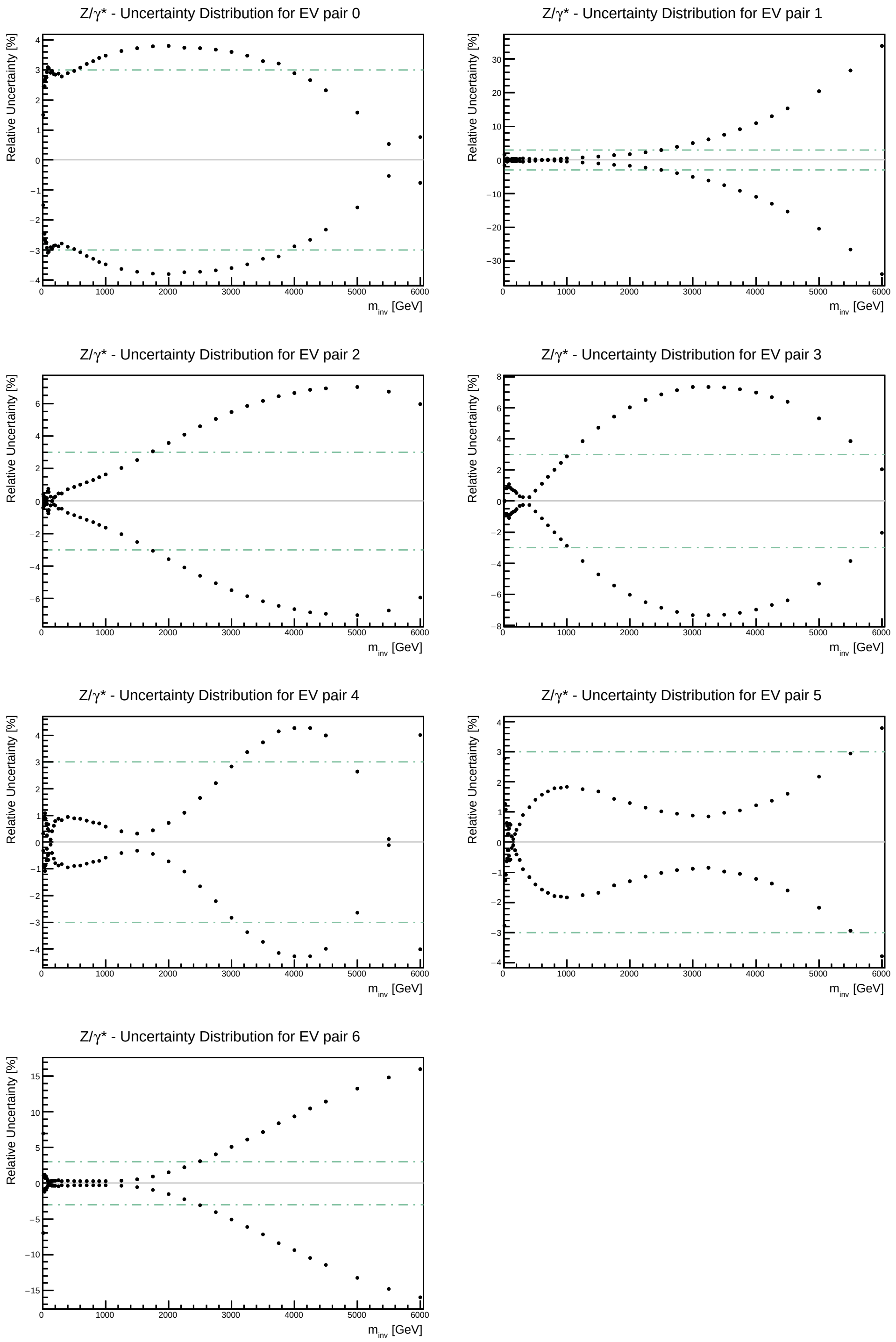

FIGURE 8.2: Distributions of the seven CT14 eigenvector bundles [203] for the neutral current Drell-Yan process as a function of invarant mass of the Z/γ^* boson. The dashed lines indicate a relative uncertainty of 3%.

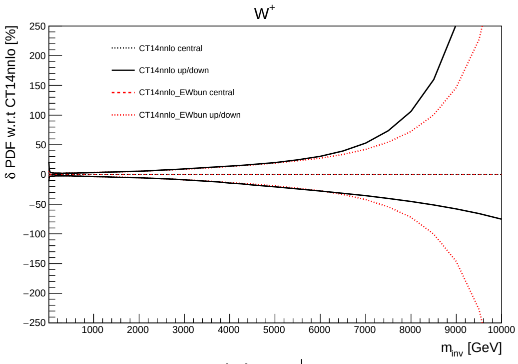

(a) W^+

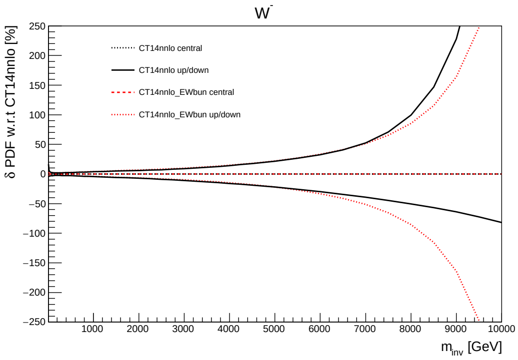

(b) W^-

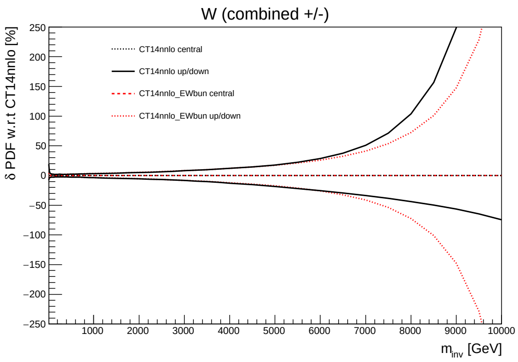

(c) W

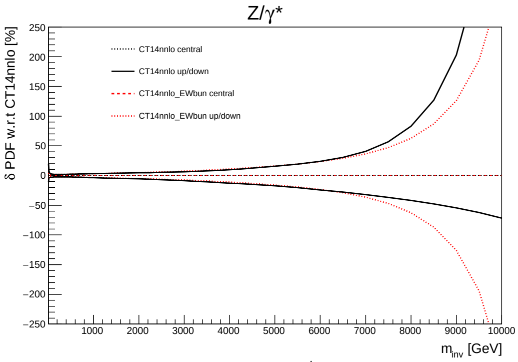

(d) Z/γ^*

FIGURE 8.3: Comparisons of the mass distributions for the sum of the original 28 CT14 eigenvectors to the sum of the reduced set of 7 for (a) W^+, (b) W^-, (c) combined W and (d) Z/γ^*. These are expressed as the ratio to the central value of the nominal CT14 - the three bands for each set correspond to the nominal value and the upper and lower uncertainy envelopes. The disagreement above the validity range of the reduced set (6000 GeV) is clearly visible).

the negative replicas for this set to zero. In this plot, two methods for calculating the central value are also shown - taking the mean and the median of the replicas.

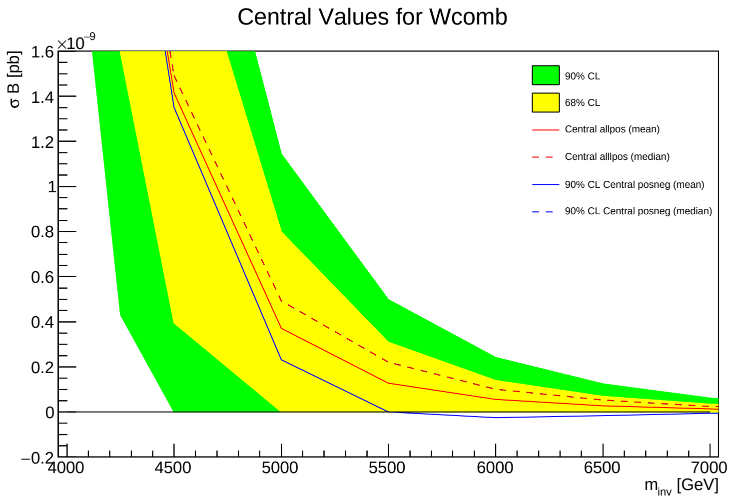

FIGURE 8.4: The plot of cross section times branching fraction as a function of boson invariant mass, showing the central values for W obtained for the 1000 replica NNPDF 3.0 set before (blue) and after (red) setting all negative replicas to zero. The dotted lines show a median value of the replicas excluding zeros while the complete lines show the mean. Green Yellow bands give the 90% and 68% upper and lower limits, respectively (after setting negative replicas to zero).

8.3 Treatment of HERA 2.0 Errors

The HERA 2.0 set is provided with two different error sets:

- An asymmetric Hessian set of 28 eigenvectors.
- A set of 13 additional variations, including 10 model variations, which must be paired, and an envelope of 3 maximal parametrisation variations. These variations are listed in table 8.1.

Upper and lower errors for the Hessian eigenvectors are calculated using the aforementioned equations 8.1. These are then added in quadrature to the 10 (paired) model variations and the envelope of the parametrisation variables in order to obtain the full upper and lower errors for this set. Figure 8.5 shows the mass distributions of the central values and uncertainty envelopes for each gauge boson, taken as a ratio to the nominal CT14 central values. In addition to the full uncertainty envelopes, the distributions for each of the individual sources of errors are shown in order to give a picture of where each contribution dominates the total uncertainty.

Variation no.	Name	Value(s)	Description
		Model Variations	
1	f_s	0.3	Strangeness suppression factor.
2	f_s	0.5	Strangeness suppression factor.
3	f_s	hermesfs-03	Strangeness suppression factor.
4	f_s	hermesfs-05	Strangeness suppression factor.
5	Q^2 cut	2.5 GeV^2	
6	Q^2 cut	5.0 GeV^2	
7	m_b	4.25 GeV	b quark running mass
8	m_b	4.75 GeV	b quark running mass
9	m_c	1.37 GeV	c quark running mass
10	m_c	1.49 GeV	c quark running mass
		Parametrisation Variations	
11	Q_0^2, m_c	1.6 GeV^2, 1.43 GeV	Evolution starting scale, c quark running mass.
12	Q_0^2, m_c	2.2 GeV^2, 1.49 GeV	Evolution starting scale, c quark running mass.
13	D_{u_v}	-	Parameter of PDF fit (section 2.2.1).

TABLE 8.1: The 13 additional variations used to calculate the erros for the HERA 2.0 PDF set. These are split into 10 model variations (1-10) and 3 parametrisation variables (11-13).

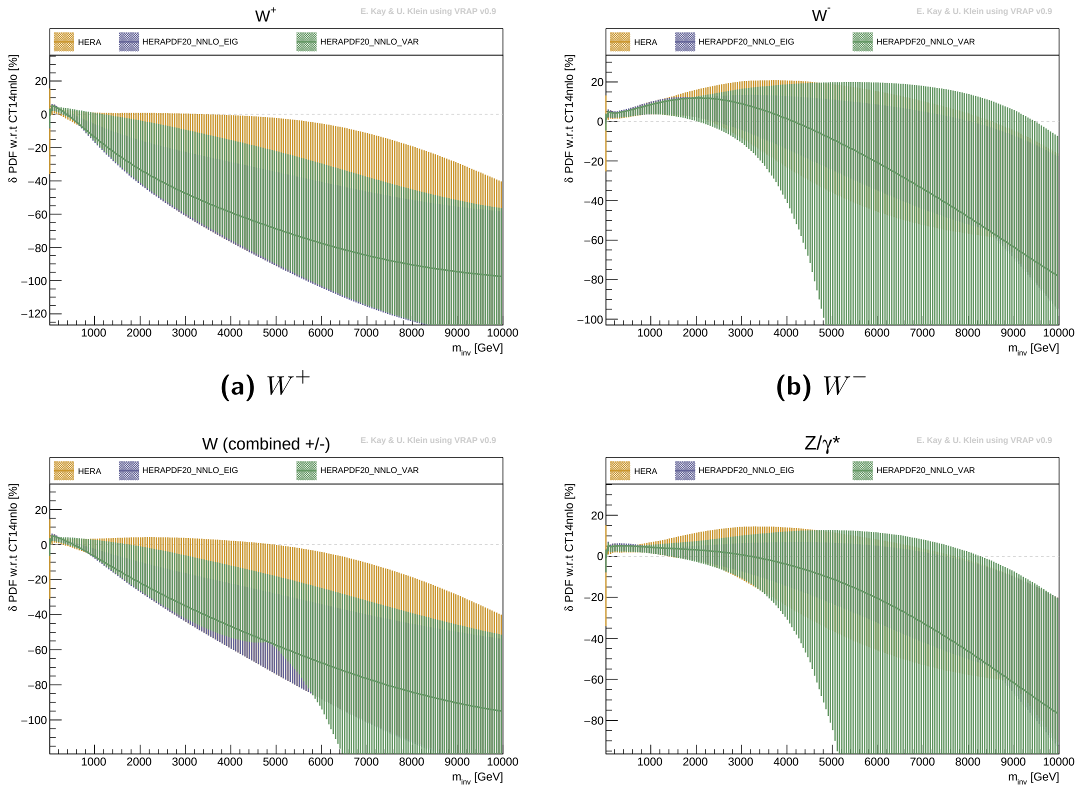

(a) W^+ **(b)** W^- **(c)** W **(d)** Z/γ^*

FIGURE 8.5: Plots showing the contributions to HERA 3.0 cross sections (presented as ratios to CT14) for (a) W^+, (b) W^-, (c) combined W and (d) Z/γ^*. The different colours correspond to the various error sets which contribute to the total uncertainty envelopes (yellow).

8.4 Treatment of ATLAS-epWZ16 Errors

The ATLAS-epWZ16 PDF set is processed in a similar manner to the HERA 2.0 set. A set of 30 asymmetric Hessian eigenvectors are supplemented by two additional sets of variations:

- A set of 15 additional variations consisting of 6 model variations (paired) and an envelope of 9 maximal parametrisation variations. These are listed in table 8.2.
- An envelope of 13 theoretical variations associated with the Drell Yan predictions, listed in table 8.3.

As with the HERA case, the upper and lower uncertainties for the Hessian eigenvectors are calculated using the equations 8.1. These are then added in quadrature to the upper and lower uncertainties obtained for the other two sets of variations. Figure 8.6 shows the mass distributions of the central values and uncertainty envelopes for each gauge boson, taken as a ratio to the nominal CT14 central values. As for the HERA case, in addition to the full uncertainty envelopes, the distributions for each of the individual sources of errors are shown in order to give a picture of where each contribution dominates the total uncertainty.

Member no.	Name	Value(s)	Description
		Model Variations	
1	m_b	4.25 GeV	b quark running mass
2	m_b	4.75 GeV	b quark running mass
3	Q^2_{min}	5 GeV^2	Minimum Q^2 of inclusive data in the fit.
4	Q^2_{min}	10 GeV^2	Minimum Q^2 of inclusive data in the fit.
5	Q^2_0, m_c	1.6 GeV^2, 1.37 GeV	Evolution starting scale, c quark running mass.
6	Q^2_0, m_c	2.2 GeV^2, 1.49 GeV	Evolution starting scale, c quark running mass.
		Parametrisation Variations	
7	$B_{\bar{s}}$	-	Parameter of PDF fit (section 2.2.1).
8	$D_{\bar{s}}$	-	Parameter of PDF fit (section 2.2.1).
9	$D_{\bar{u}}$	-	Parameter of PDF fit (section 2.2.1).
10	$D_{\bar{d}}$	-	Parameter of PDF fit (section 2.2.1).
11	D_{d_v}	-	Parameter of PDF fit (section 2.2.1).
12	D_{u_v}	-	Parameter of PDF fit (section 2.2.1).
13	D_g	-	Parameter of PDF fit (section 2.2.1).
14	F_{u_v}	-	Parameter of PDF fit (section 2.2.1).
15	F_{d_v}	-	Parameter of PDF fit (section 2.2.1).

Table 8.2: The 6 model (1-6) and 9 parametrisation (7-15) variations used to calculate the errors for the ATLAS-epWZ16 PDF set.

Member no.	Name	Value(s)	Description
1	Ep	-0.6%	Beam energy (down)
2	Ep	+0.6%	Beam energy (up)
3	NLO EW	-	NLO EW corrections down
4	NLO EW	-	NLO EW corrections up
5	FEWZ	-	FEWZ - DYNNLO difference
6	μ_r, μ_f	1/2, 1/2	Renormalisation & factorisation scale (relative to W or Z mass)
7	μ_r, μ_f	2, 2	Renormalisation & factorisation scale (relative to W or Z mass)
8	μ_r, μ_f	1, 1/2	Renormalisation & factorisation scale (relative to W or Z mass)
9	μ_r, μ_f	1, 2	Renormalisation & factorisation scale (relative to W or Z mass)
10	μ_r, μ_f	1/2, 1	Renormalisation & factorisation scale (relative to W or Z mass)
11	μ_r, μ_f	2, 1	Renormalisation & factorisation scale (relative to W or Z mass)
12	$\alpha_S(m_Z)$	0.116	Strong coupling
13	$\alpha_S(m_Z)$	0.120	Strong coupling

Table 8.3: The 13 theoretical variations used to calculate the errors for the ATLASep-WZ PDF set.

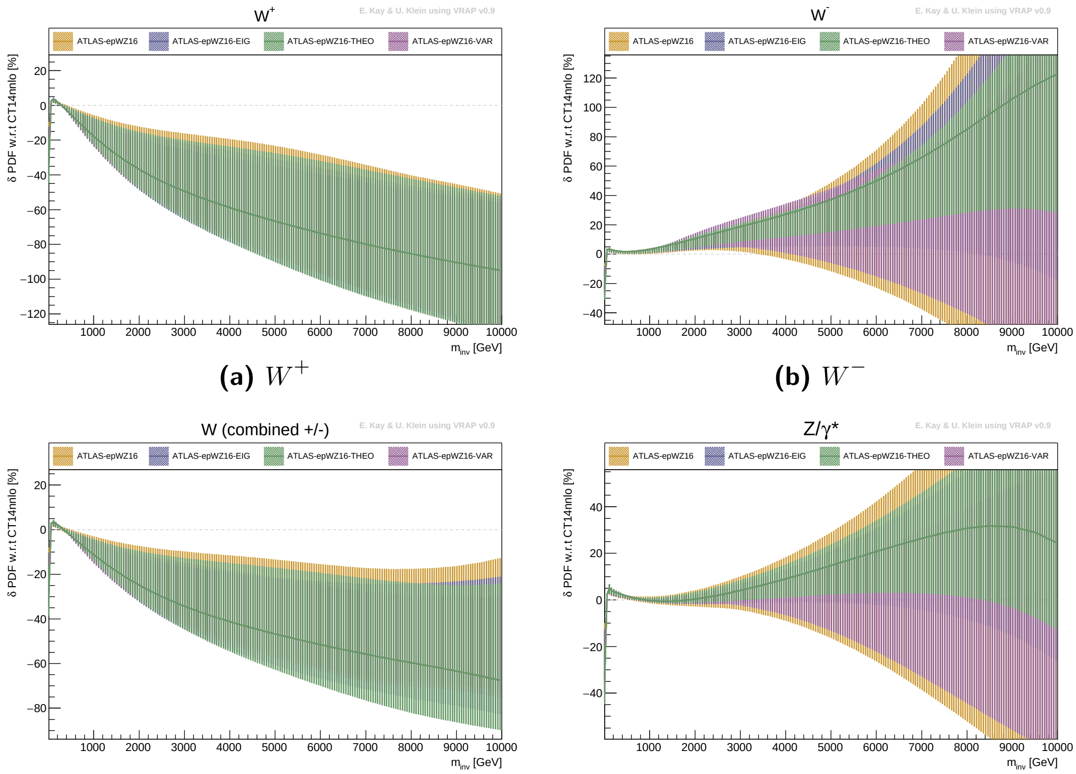

(a) W^+ **(b)** W^-

(c) W **(d)** Z/γ^*

FIGURE 8.6: Plots showing the contributions to ATLAS-epWZ16 cross sections (presented as ratios to CT14) for (a) W^+, (b) W^-, (c) combined W and (d) Z/γ^*. The different colours correspond to the various error sets which contribute to the total uncertainty envelopes (yellow).

8.5 PDF Choice Uncertainty

In order to model the uncertainty associated with the PDF choice, the ratio of each PDF set's central value and uncertainties with the central value for the nominal PDF set is calculated. Figure 8.7 shows the distributions of these ratios as a function of the invariant mass of the vector boson. Uncertainty envelopes for each PDF set are calculated by dividing the upper and lower error bands for the set by the nominal PDF's central value. In the case of MC generated PDF sets, such as NNPDF, bands for 68% C.L and 90% C.L can be constructed.

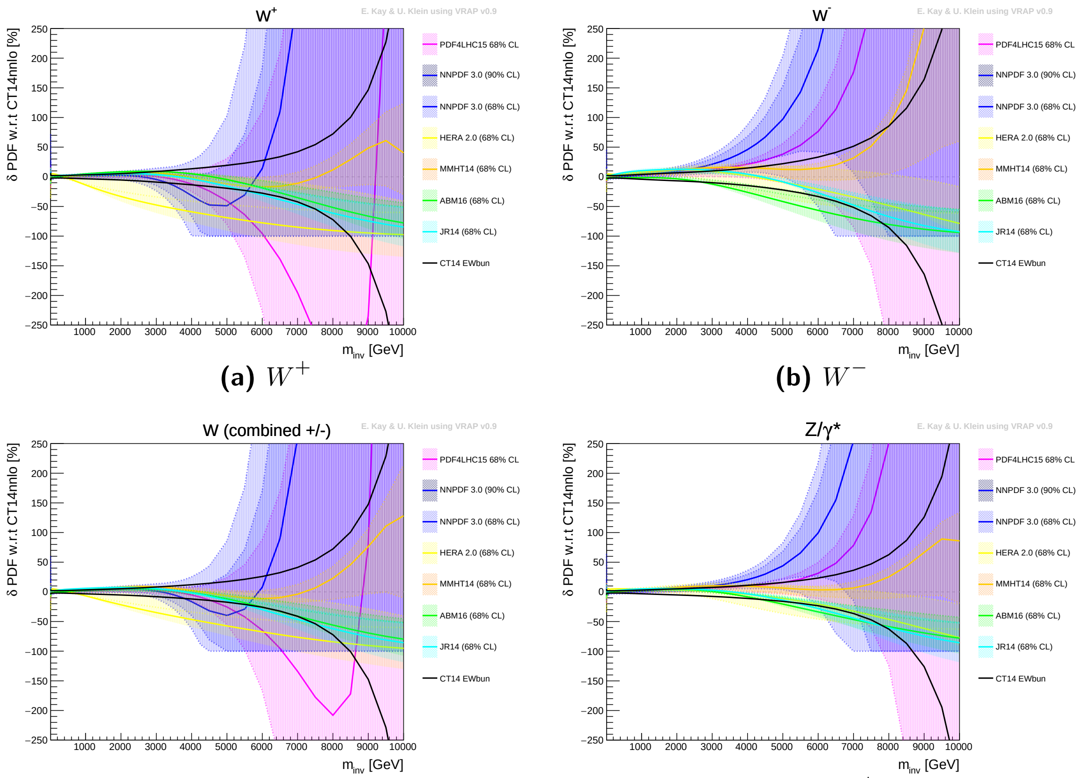

(a) W^+ **(b)** W^- **(c)** W **(d)** Z/γ^*

FIGURE 8.7: Plots showing the PDF uncertainties for all PDF sets studied w.r.t the nominal PDF set (CT14) for (a) W^+, (b) W^-, (c) combined W and (d) Z bosons. The ratios of upper and lower estimates to central CT14 are indicated by the shaded regions, while the lines represent the ratios for the central values. For NNPDF, both 68% and 90% C.L. errors are provided and illustrated with the lighter and darker shading, respectively.

At lower masses $\leqslant$ 3 TeV, the PDF sets are generally in good agreement, with most of the envelopes lying within the upper and lower CT14 errors. At higher masses they begin to diverge, with the envelopes for some PDF sets becoming very large. The NNPDF envelopes are large and cover the variations for most of the other PDF sets, motivating the use of this set for the PDF choice uncertainty for the W' and Z' searches. The visible truncation for NNPDF at the point where the replicas go negative is a result of the treatment which was outlined in 8.2. The PDF4LHC envelope reaches negative values at higher masses for all of the bosons, with the central value also going negative in the case of W^+ (and therefore the combined W). In order to address this in future, an approach similar to the one used for the NNPDF set may be adopted.

8.6 α_S Uncertainty

In addition to the general PDF uncertainties outlined here, the uncertainty in the value of the strong coupling is accounted for in the W' and Z' searches. The α_S values used in cross section calculations for the W' and Z' searches are provided in the NNLO PDF sets. The various PDF groups follow different strategies for obtaining α_S - in some cases it is a result of the PDF fit while in others the Particle Data Group (PDG) [12] value is used.

In the heavy boson searches, for the nominal CT14 NNLO PDF set, α_S uncertainty is considered as a nuisance parameter. The uncertainty due to variations in α_S is calculated through studying the effect of changing α_S by $\pm$ 0.003 (from the nominal 0.118) in the cross section calculation. This is a conservative 90% CL variation in accordance with the 68% CL recommendation of 0.0015 from PDF4LHC authors [197]. The maximum and minimum cross section deviation is identified per mass bin and the resulting positive and negative deviations are calculated for each vector boson.

Figure 8.8 shows the distributions of the α_S uncertainty calculated for each vector boson for the CT14 NNLO PDF set. For both the W and Z this uncertainty is small below masses of $\sim$ 6 TeV.

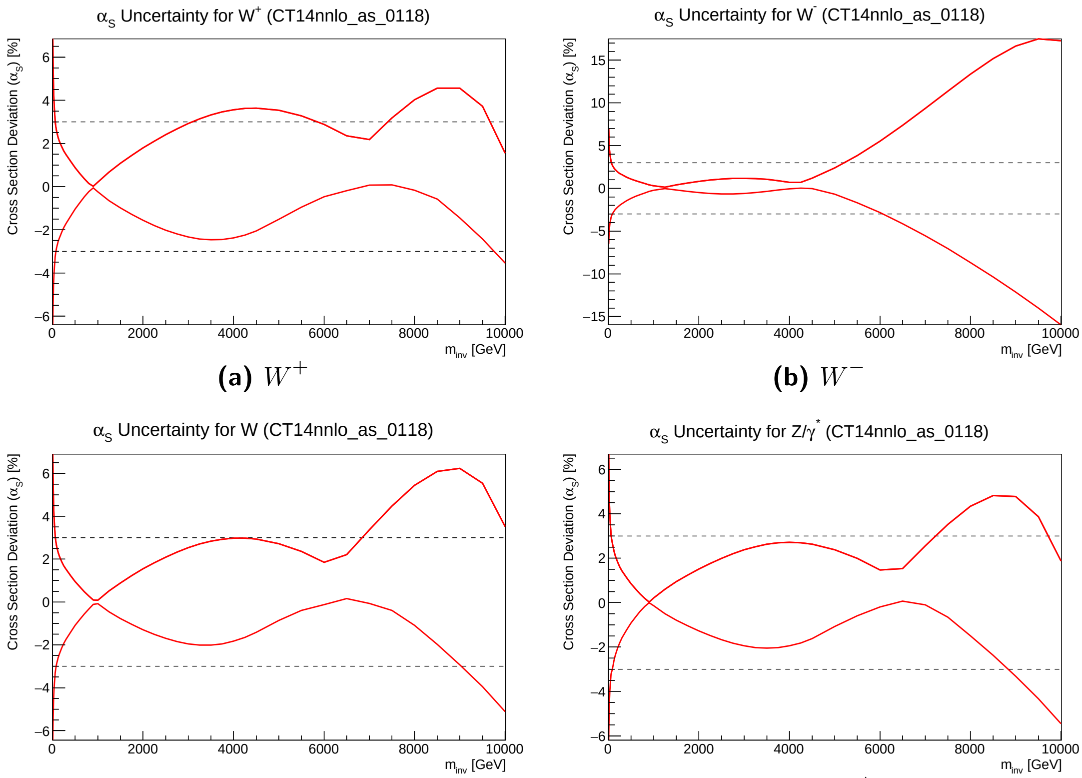

(a) W^+ **(b)** W^-

(c) W **(d)** Z/γ^*

FIGURE 8.8: Plots showing the up and down deviations due to α_S uncertainty for (a) W^+, (b) W^-, (c) combined W and (d) Z/γ^* for the CT14 NNLO PDF set. Black dotted lines indicate $\pm 3\%$ uncertainty, inside of which uncertainties are considered to be negligible.

Part IV

Search for a Heavy Charged Gauge Boson Decaying to an Electron and a Neutrino

Chapter 9

Analysis Strategy

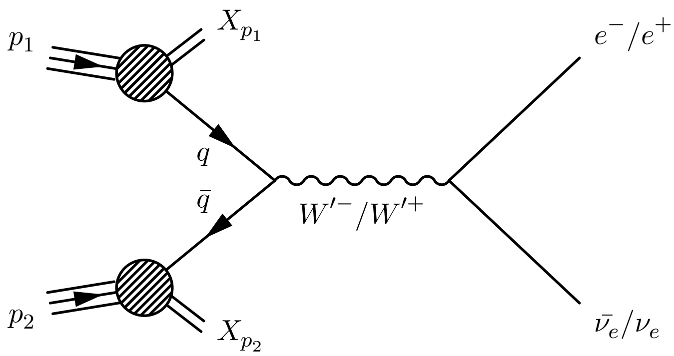

FIGURE 9.1: Feynman diagram for the s-channel production of a W' boson with a subsequent decay to an electron and a neutrino.

In this chapter, the analysis strategy for the search for a new heavy charged s-channel resonance (figure 9.1) decaying to an electron and a neutrino in the context of the SSM is outlined. In the interests of achieving model independence, interference effects between the SSM W' and the SM W and decays into other bosons are neglected. The analysis involves identifying events which have one high-p_{T} isolated, central electron and a large $E_{\mathrm{T}}^{\mathrm{miss}}$, then searching for deviations from the standard model using the *transverse mass*, m_T, defined as:

$$m_T = \sqrt{2 p_T E_{\mathrm{T}}^{\mathrm{miss}} \left(1 - \cos\phi_{\ell\nu}\right)}, \tag{9.1}$$

where p_T is the transverse momentum of the selected electron and $\phi_{\ell\nu}$ is the angle between the lepton and $E_{\mathrm{T}}^{\mathrm{miss}}$ in the transverse plane.

9.1 Event Selection

In order to isolate events of interest from the data recorded by ATLAS, selection criteria are applied to the data and Monte Carlo. These requirements, referred to as "cuts", are chosen such that they reject as much background as possible while minimising loss of W' candidates.

First a set of cleaning cuts, as described in section 7.7, are applied in order to remove data candidates if they are not in the GRL[*,†], are flagged as incomplete or do not belong to a primary vertex. Selected events must also pass at least one of the triggers corresponding to the relevant dataset (2015 or 2016), outlined in table 9.1. For the 2015 data, these triggers require either a medium likelihood electron with $p_{\mathrm{T}} > 25$ GeV, a medium likelihood electron with $p_{\mathrm{T}} > 60$ GeV or a loose likelihood electron with $p_{\mathrm{T}} > 120$ GeV. For the 2016 data, the triggers require either a medium likelihood electron with $p_{\mathrm{T}} > 60$ GeV or a loose likelihood electron with $p_{\mathrm{T}} > 140$ GeV. The 2016 triggers have a "nod0" tag, indicating that the electron likelihood identification was performed without using d_0 or d_0 significance as discriminating variables [204].

Run Periods	Trigger
276262–284484 (2015 data)	e24_lhmedium_L1EM20VH OR e60_lhmedium OR e120_lhloose
297730–311481 (2016 data)	e60_lhmedium_nod0 OR e140_lhloose_nod0

TABLE 9.1: Triggers for the $W' \to e\nu$ decay channel for the 2015 and 2016 datasets.

Electron candidates are selected based on the criteria outlined in section 7.1. Selected events must have exactly one electron passing these requirements and any events which

[*] 2015 GRL period: data15_13TeV.AllYear; defect: PHYS_StandardGRL_All_Good_25ns; defect tag: DetStatus-v79-repro20-02.

[†] 2016 GRL period: data16_13TeV.AllYear; defect: PHYS_StandardGRL_All_Good_25ns; defect tag: DetStatus-v88-pro20-21.

contain additional electrons which pass a loosened version of this selection (likelihood tight $\rightarrow$ medium, $p_T > 20$ GeV) are vetoed.

In order to construct the missing transverse energy, muons are also selected according to the criteria listed in section 7.2 and passed to the MET construction tool. Events are vetoed if they contain any additional muons which pass a loosened version of this selection (high-p_{T} working point $\rightarrow$ inclusive OR medium+high-p_{T}, $p_T > 20$ GeV). A veto is also applied to events which contain "bad" quality jets (using the "LooseBad" cut level [205]) which do not overlap with the electron candidate $(R > 0.2)^{\ddagger}$. Surviving events are then subject to a $E_{\mathrm{T}}^{\mathrm{miss}}$ cut of $E_{\mathrm{T}}^{\mathrm{miss}} > 65$ GeV and a m_T cut of $\mathrm{m}_T > 130$ GeV.

The selection is fully orthogonal to the one used in the dilepton (Z') search [206], facilitating combination of the results of these analyses (as is performed in part V of this thesis). Figure 9.2 shows the electron channel *yield*, defined as the number of selected events divided by the integrated luminosity $\frac{N_{\mathrm{selected}}}{L_{\mathrm{int}}}$, for each run of the 2015 and 2016 data after the full selection. The overall increase in yield observed in the 2016 data can be attributed to a correlation between yield and average pileup, μ, which is larger for the 2016 dataset (as previously shown in figure 5.9). To illustrate this, figure 9.3 shows a direct comparison of the yield and average pileup $\langle\mu\rangle$ for each run in the two datasets. More yield/$\langle\mu\rangle$ plots can be found in appendix A.

‡Jets which do coincide with selected electrons are considered as electron candidates and are therefore permitted to exhibit "bad" characteristics which are addressed by the electron quality cuts.

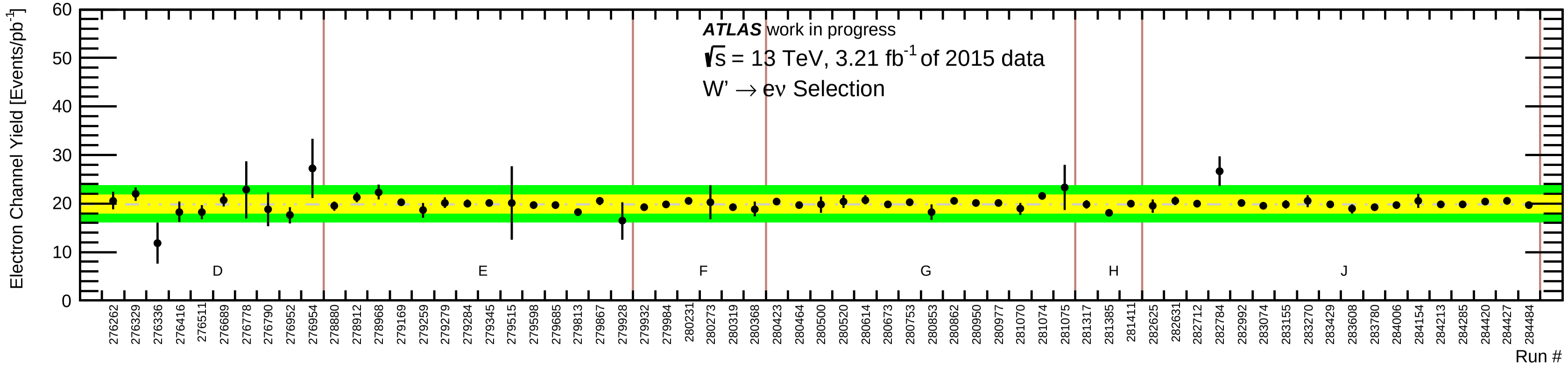

(a) 2015

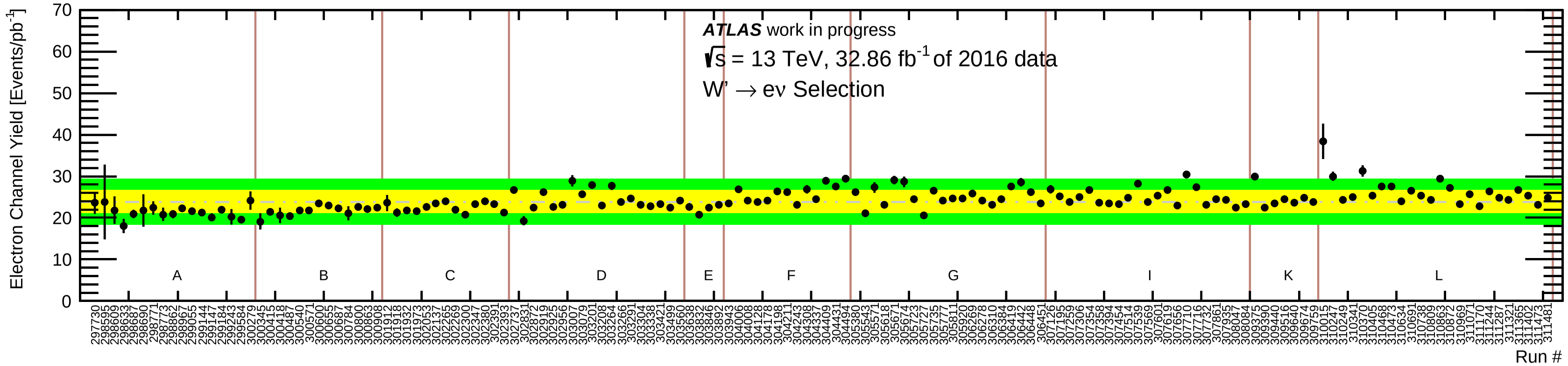

(b) 2016

FIGURE 9.2: Electron channel yields for each run (chronologically in the x-axis) of the (a) 2015 and (b) 2016 data with sigma bands indicating 1 and 2 standard deviations (σ) from the mean yield.

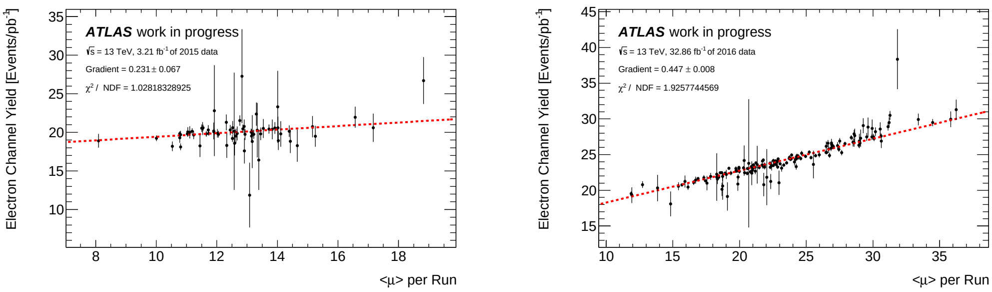

(a) 2015 **(b)** 2016

FIGURE 9.3: Electron channel yield vs. average pile-up $\langle \mu \rangle$ per run for (a) 2015 and (b) 2016 data. The gradients for the lines fitted to these points are quoted.

9.2 Signal Modelling

The sharply falling cross section σ as a function of invariant mass for the $W' \to e\nu$ process proves demanding for generation of MC signal samples. Though it is possible to generate dedicated samples for different W' pole masses (as was the case in previous iterations of this search [207]), this becomes computationally expensive when considering a large number of resonance masses which each require large quantities of generated events. In order to ensure statistics across the considered kinematic range for any given pole mass up to 7 TeV, a high statistics "flat" MC sample [208] with no resonance shape is generated and reweighted. Details of this sample are given in table 9.2. The total cross section for the $W' \to e\nu$ process is determined using Pythia 8 [209] using the NNPDF23 LO [210] PDF set, and corrected to NNLO through the application of an invariant-mass dependent NNLO QCD k-factor (as described in section 6.3). Higher order electroweak corrections are not applied to the signal cross sections due to the strong model dependence that this would introduce.

Process	Dataset ID	N_{evt} $[\times 10^3]$	Generator σB [nb]
$W' \to e\nu$ (Flat)	301533	1000	0.024960

TABLE 9.2: The Monte Carlo W' signal sample used for this analysis. The physics process, ATLAS MC run number, number of generated events and cross section times branching ratio σB are given.

This flat sample is produced by removing the Breit-Wigner [211] term from the PYTHIA event generation. Additionally, at the generation stage, the square of the matrix element is divided by a function of lepton-neutrino invariant mass ($m_{\ell\nu}$):

$$f(m_{\ell\nu}) = \exp\left(\frac{-p_1 m_{\ell\nu}}{\sqrt{s}}\right)\left(\frac{m_{\ell\nu}}{\sqrt{s}}\right)^{p_2}, \tag{9.2}$$

where p_1 and p_2 are constants determined from a fit and $\sqrt{s} = 13000$ GeV. This step is performed in order to avoid a fast drop in cross section as a function of invariant mass. The resulting flat mass spectrum can be reweighted to any desired resonance mass by applying a weight w on an event-by-event basis. Since the differential cross section has a strong mass dependence, additional weights along with the Breit-Wigner term are included in order to address this. These additional terms are the result of studies such as [212], which found a $\frac{1}{m_{\ell\nu}}$ shape to be optimal for the unweighted distribution in order to achieve the same uncertainty for all reweighting pole masses. The final weight is determined as:

$$w = \begin{cases} 10^{12} \times 102.77 \exp\left(-11.5\frac{m_{\ell\nu}}{\sqrt{s}}\right) \times W_{BW} & \text{if } m_{\ell\nu} < 299\,\text{GeV}, \\ 10^{12} \times \exp\left(-16.1\frac{m_{\ell\nu}}{\sqrt{s}}\right) \times \left(\frac{m_{\ell\nu}}{\sqrt{s}}\right)^{1.2} \times W_{BW} & \text{if } m_{\ell\nu} \geqslant 299\,\text{GeV}, m_{\ell\nu} < 3003\,\text{GeV}, \\ 10^{12} \times 1.8675 \exp\left(-31.7\frac{m_{\ell\nu}}{\sqrt{s}}\right) \times \left(\frac{m_{\ell\nu}}{\sqrt{s}}\right)^{4.6} \times W_{BW} & \text{if } m_{\ell\nu} \geqslant 3003\,\text{GeV}. \end{cases} \tag{9.3}$$

Here, the Breit-Wigner weight, W_{BW}, is defined as:

$$W_{BW} = \frac{1}{(m_{\ell\nu}^2 - M^2)^2 + (m_{\ell\nu}^2 \times \Gamma)^2}, \tag{9.4}$$

where M is the desired pole mass and the width, Γ, is calculated as:

$$\Gamma = \frac{1}{(\sin^2\Theta_W)^{-1} \times ((\alpha_{EM}(m_Z))^{-1} + 1.45\log(\frac{m_Z}{M}))} \times \frac{3 + (1 + \frac{rtW}{2}) \times (1 - rtW)^2}{4}. \tag{9.5}$$

In this equation, m_Z is the mass of the Z boson and rtW is defined as:

$$rtW = \left(\frac{m_t}{M}\right)^2, \tag{9.6}$$

where $m_t = 172.5$ GeV is the mass of the top quark. The fine structure constant at the scale of the Z mass $\alpha_{EM}(m_Z) = \frac{1}{127.918}$ and the weak mixing angle $\sin^2 \Theta_W = 0.2312$. The number 1.45 in the denominator corresponds to the coefficient of the running fine structure constant above the Z mass.

Figure 9.4 shows the distributions of the invariant and transverse mass for the flat sample before reweighting and after reweighting to various pole mass hypotheses. The W' signal shape is a Jacobian peak which falls sharply at high m_T. This shape becomes significantly more diffuse at higher pole masses ($\gtrsim 5$ TeV) as a result of steeply falling PDFs at high Bjorken x.

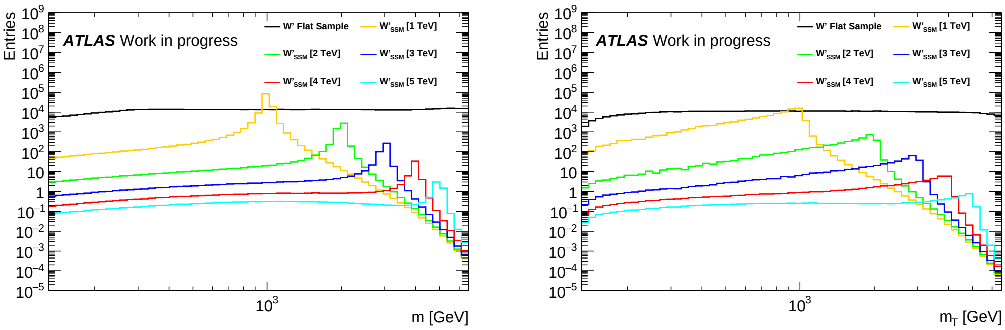

(a) (b)

FIGURE 9.4: Distributions of (a) the invariant mass and (b) the transverse mass for the flat $W' \rightarrow e\nu$ sample before (black) reweighting and after being weighted to example pole masses in the range 1-5 TeV.

9.3 Background Processes

In order to conduct the search for exotic resonances decaying to an electron and $E_{\mathrm{T}}^{\mathrm{miss}}$, we must consider the known SM processes which result in this same final state. These backgrounds must be fully understood in order to observe any excesses over SM predictions. The background processes considered in this search are described in the following.

Charged Current Drell-Yan (CCDY) Off-Shell Production

The CCDY s-channel production of the SM W boson (figure 2.1(a)) produces an electron and $E_{\mathrm{T}}^{\mathrm{miss}}$ final state predominantly in the Jacobian peak region around the W mass at $\sim$80 GeV. However, there is also a high mass off-shell production tail which covers the full kinematic range of the W' search. This is by far the dominant source of irreducible background in this study.

Similar decays of the SM W boson to τ leptons also provide a source of background, as W bosons arising from subsequent leptonic decays of the taus can decay to the $e+E_{\mathrm{T}}^{\mathrm{miss}}$ final state (as shown in figure 9.5).

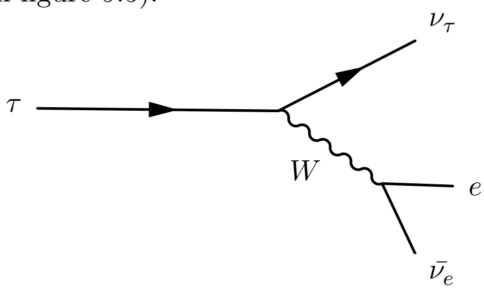

FIGURE 9.5: Feynman diagram for a τ decay resulting in a W boson which subsequently decays to an electron and a neutrino.

Neutral Current Drell-Yan (NCDY) Off-Shell Production

The NCDY production of the SM Z (or γ^*) boson (as previously shown in figure 2.1(b)) with a decay to the di-electron final state may be considered a background source if one of the produced electrons evades detection or is not properly reconstructed. The NCDY process where the Z decays to a pair of τ leptons is also a source of the background due to the τ decays mentioned above.

Top Backgrounds

Since the top quark is the heaviest particle of the SM, it leads to background processes for many high mass searches. As the top decays to a W boson and b meson, it is a relevant background source for the W' search, mainly in cases where the W boson subsequently decays leptonically[§]

Top quarks can be produced in pp collisions in pairs via the strong interaction (figure 9.6) or one at a time via the weak interaction (figure 9.7). In the case of top pair

[§]Decays of the W bosons to jets are taken into account in the multijet background (see below).

production, scenarios where a produced W boson decays leptonically and the other hadronically provide a background in the $e + E_{\mathrm{T}}^{\mathrm{miss}}$ channel. In the case of single top production, top quarks produced in association with a W boson are also considered. The s-channel single top production (figure 9.7) is a negligible source of background and therefore not included in this analysis. The different top backgrounds taken into account in this analysis are listed in table 9.7.

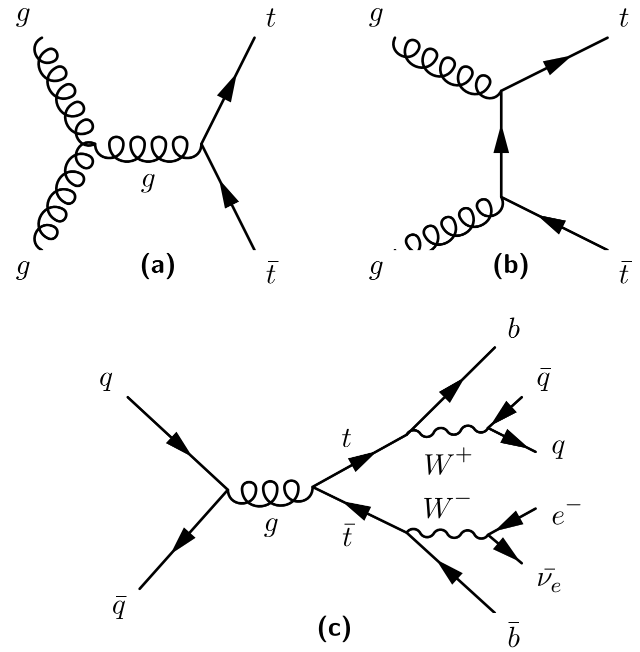

FIGURE 9.6: Feynman diagrams for processes contributing to the $t\bar{t}$ background, including (a) s- and (b) t-channel top quark pair producton. Figure (c) shows s-channel top pair production with subsequent decays leading to a final state with one electron.

Diboson Production

Events where two SM gauge bosons are produced in the hard scattering pp interaction are referred to as diboson events. Such events can produce $e + E_{\mathrm{T}}^{\mathrm{miss}}$ final states through various decays, some of which are depicted in figure 9.8. The dibson production processes taken into account for this analysis are listed in table 9.7.

Multijet Background

As previously discussed, pp collisions lead to an enormous amount of jets which arise from strong (QCD) interactions. As a result, they are a large source of background in many searches, including the one described here. Weak or electromagnetic decays of hadrons, such as pions within jets, can lead to electrons which may be mistaken

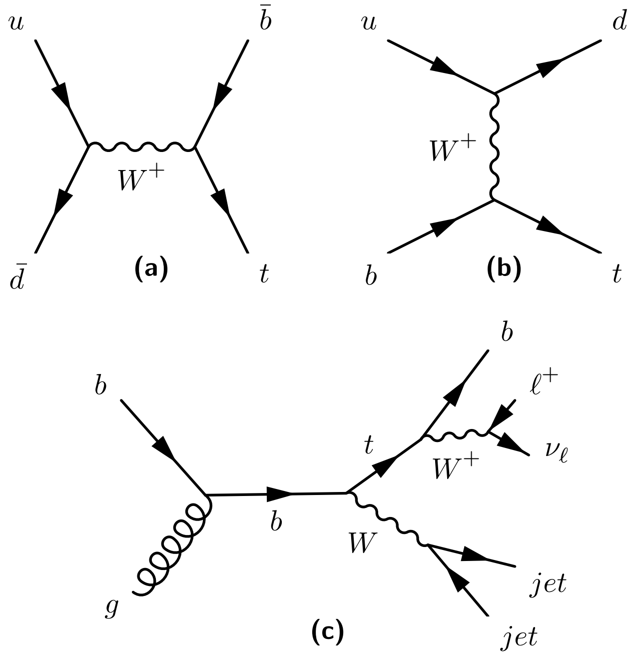

FIGURE 9.7: Feynman diagrams for processes contributing to the "single top" background, including (a) s- and (b) t-channel top producton and (c) associated Wt production with subsequent decays to W bosons.

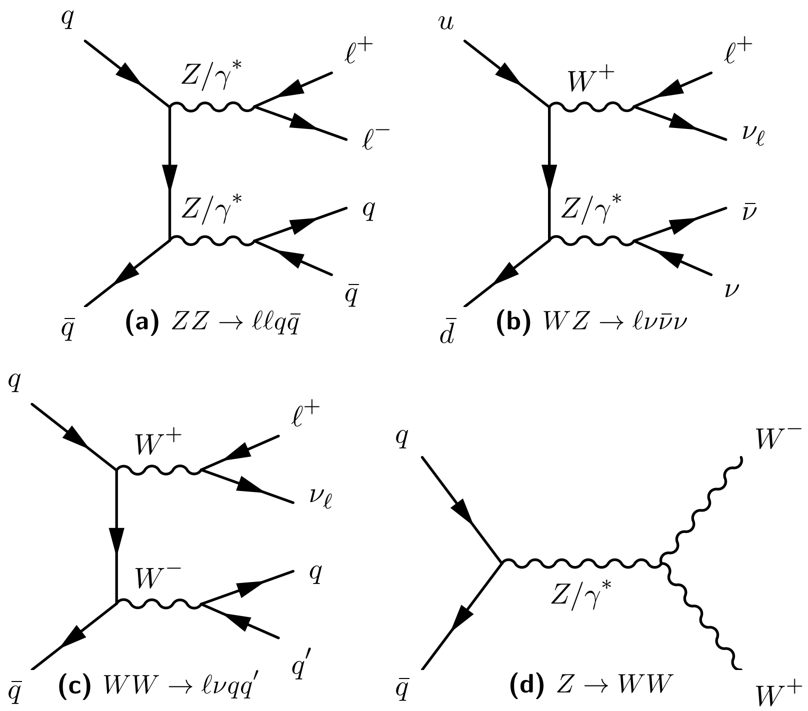

FIGURE 9.8: Feynman diagrams for various possible processes contributing to the diboson background.

for signal candidates. Additionally, jets can "fake" electrons when they leave deposits in the EM calorimeter where tracks are created by their constituent charged hadrons or photons from decays such as $\pi \to \gamma\gamma$. The total background resulting from such processes is referred to as the *multijet* background, which is described in more detail in section 9.4.

9.3.1 Modelling of MC Backgrounds

All backgrounds apart from QCD multijet are modelled using MC. Due to the fact that the large cross sections for production of jets arising from QCD processes prove demanding for MC, the associated background is modelled using data driven methods which are described in section 9.4. The high mass range of the W' search presents challenges for background modelling: steeply falling cross sections of the physics processes necessitate very high statistics for MC samples, while lack of data at high mass impacts the data driven multijet background estimate. Since sufficiently large MC samples are unavailable (as well as additional high mass data), various alternative measures are taken to address this issue.

Drell-Yan backgrounds (e and τ) are produced as a series of samples binned in invariant mass of the $\ell\nu/\ell\ell$ pair. High statistics "inclusive" samples are generated with a mass cut applied at 120 GeV in order to provide statistics at the Jacobian peak, while mass-binned samples are produced for masses greater than 120 GeV. Tables 9.3 and 9.4 list the CCDY electron and tau MC samples and tables 9.5 and 9.6 list the NCDY electron and tau MC samples. These inclusive and binned samples are then "stitched" together in order to form the total background. Figure 9.9 shows the transverse mass distributions for the charged and neutral current processes in the electron channels for each binned sample with the resultant total distributions overlayed. The MC generator cross sections for these processes are corrected to higher order by appling NNLO QCD and NLO EW k-factors, as outlined in section 6.3.

For top and diboson backgrounds only inclusive MC samples are generated, details of which are listed in table 9.7. The transverse mass distributions obtained from processing these samples are then fitted with functional forms and extrapolated to high mass. This fitting and extrapolation method is also applied to the multijet background estimate. An overview of the fitting method (with results shown) is given in section 9.6.

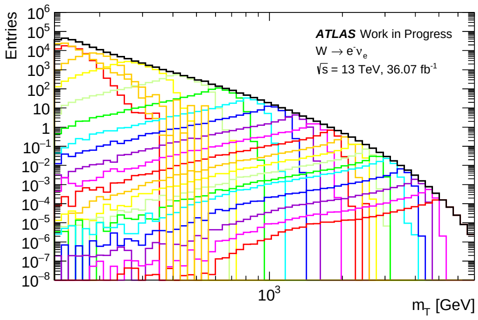

(a) $W^- \to e^- \bar{\nu}_e$

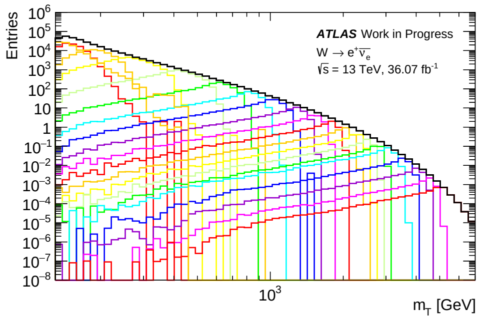

(b) $W^+ \to e^+ \nu_e$

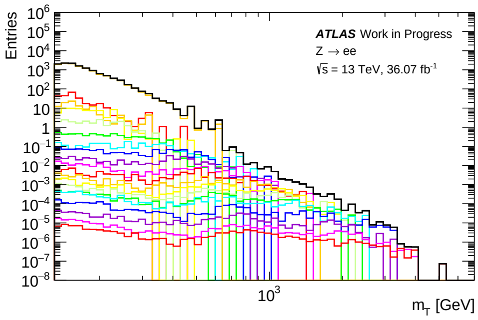

(c) $Z \to ee$

FIGURE 9.9: Transverse mass distributions for (a) $W \to e^- \bar{\nu}_e$, (b) $W \to e^+ \nu_e$ and (c) $Z \to ee$. The coloured lines represent the distributions for the individual mass-binned samples, while the black lines give the summed distributions which are used as backgrounds in the analysis.

Process	Dataset ID	N_{evt} [$\times 10^3$]	Generator σB [pb]	L_{int} [fb^{-1}]
Inclusive and mass binned $W \to e\nu_e$				
cu$W^+ \to e^+\nu_e$	361100	41415	1.1e+04	3.7
$W^- \to e^-\bar{\nu}_e$	361103	49904	8.3e+03	6
$W^+(120, 180) \to e^+\nu_e$	301060	500	32	16
$W^+(180, 250) \to e^+\nu_e$	301061	250	5	50
$W^+(250, 400) \to e^+\nu_e$	301062	140	1.8	80
$W^+(400, 600) \to e^+\nu_e$	301063	100	0.31	3.2e+02
$W^+(600, 800) \to e^+\nu_e$	301064	50	0.061	8.2e+02
$W^+(800, 1000) \to e^+\nu_e$	301065	50	0.018	2.8e+03
$W^+(1000, 1250) \to e^+\nu_e$	301066	50	0.0073	6.9e+03
$W^+(1250, 1500) \to e^+\nu_e$	301067	50	0.0025	2e+04
$W^+(1500, 1750) \to e^+\nu_e$	301068	50	0.00099	5.1e+04
$W^+(1750, 2000) \to e^+\nu_e$	301069	40	0.00042	9.4e+04
$W^+(2000, 2250) \to e^+\nu_e$	301070	47	0.00019	2.4e+05
$W^+(2250, 2500) \to e^+\nu_e$	301071	50	9.3e-05	5.4e+05
$W^+(2500, 2750) \to e^+\nu_e$	301072	50	4.6e-05	1.1e+06
$W^+(2750, 3000) \to e^+\nu_e$	301073	50	2.3e-05	2.1e+06
$W^+(3000, 3500) \to e^+\nu_e$	301074	50	1.8e-05	2.7e+06
$W^+(3500, 4000) \to e^+\nu_e$	301075	50	5.1e-06	9.8e+06
$W^+(4000, 4500) \to e^+\nu_e$	301076	50	1.4e-06	3.5e+07
$W^+(4500, 5000) \to e^+\nu_e$	301077	50	4e-07	1.2e+08
$W^+(> 5000) \to e^+\nu_e$	301078	50	1.5e-07	3.3e+08
$W^-(120, 180) \to e^-\bar{\nu}_e$	301080	500	22	23
$W^-(180, 250) \to e^-\bar{\nu}_e$	301081	250	3.3	76
$W^-(250, 400) \to e^-\bar{\nu}_e$	301082	150	1.1	1.4e+02
$W^-(400, 600) \to e^-\bar{\nu}_e$	301083	100	0.18	5.7e+02
$W^-(600, 800) \to e^-\bar{\nu}_e$	301084	50	0.031	1.6e+03
$W^-(800, 1000) \to e^-\bar{\nu}_e$	301085	50	0.0083	6e+03
$W^-(1000, 1250) \to e^-\bar{\nu}_e$	301086	50	0.0032	1.6e+04
$W^-(1250, 1500) \to e^-\bar{\nu}_e$	301087	50	0.001	5e+04
$W^-(1500, 1750) \to e^-\bar{\nu}_e$	301088	50	0.00037	1.4e+05
$W^-(1750, 2000) \to e^-\bar{\nu}_e$	301089	50	0.00015	3.3e+05
$W^-(2000, 2250) \to e^-\bar{\nu}_e$	301090	50	6.5e-05	7.7e+05
$W^-(2250, 2500) \to e^-\bar{\nu}_e$	301091	50	3e-05	1.7e+06
$W^-(2500, 2750) \to e^-\bar{\nu}_e$	301092	50	1.5e-05	3.4e+06
$W^-(2750, 3000) \to e^-\bar{\nu}_e$	301093	50	7.3e-06	6.9e+06
$W^-(3000, 3500) \to e^-\bar{\nu}_e$	301094	50	5.7e-06	8.8e+06
$W^-(3500, 4000) \to e^-\bar{\nu}_e$	301095	50	1.6e-06	3.1e+07
$W^-(4000, 4500) \to e^-\bar{\nu}_e$	301096	50	4.7e-07	1.1e+08
$W^-(4500, 5000) \to e^-\bar{\nu}_e$	301097	50	1.4e-07	3.5e+08
$W^-(> 5000) \to e^-\bar{\nu}_e$	301098	50	6.2e-08	8.1e+08

TABLE 9.3: The MC samples for the CCDY background. For each dataset, the physics process (including the mass range in GeV where appropriate), the ATLAS MC run number, the number of generated events, the cross section times branching ratio and the equivalent integrated luminosity ($L_{\text{int}} = \frac{N_{evt}}{\sigma B}$) are listed.

Process	Dataset ID	N_{evt} [$\times 10^3$]	Generator σB [pb]	L_{int} [fb^{-1}]
	Inclusive and mass binned $W \to \tau\nu_\tau$			
$W^+ \to \tau^+\nu_\tau$	361102	29982	1.1e+04	2.7
$W^- \to \tau^-\bar{\nu_\tau}$	361105	19955	8.3e+03	2.4
$W^+(120, 180) \to \tau^+\nu_\tau$	301140	500	32	16
$W^+(180, 250) \to \tau^+\nu_\tau$	301141	250	5	50
$W^+(250, 400) \to \tau^+\nu_\tau$	301142	150	1.8	86
$W^+(400, 600) \to \tau^+\nu_\tau$	301143	100	0.31	3.2e+02
$W^+(600, 800) \to \tau^+\nu_\tau$	301144	50	0.061	8.2e+02
$W^+(800, 1000) \to \tau^+\nu_\tau$	301145	50	0.018	2.8e+03
$W^+(1000, 1250) \to \tau^+\nu_\tau$	301146	50	0.0073	6.9e+03
$W^+(1250, 1500) \to \tau^+\nu_\tau$	301147	50	0.0025	2e+04
$W^+(1500, 1750) \to \tau^+\nu_\tau$	301148	50	0.00099	5.1e+04
$W^+(1750, 2000) \to \tau^+\nu_\tau$	301149	50	0.00042	1.2e+05
$W^+(2000, 2250) \to \tau^+\nu_\tau$	301150	50	0.00019	2.6e+05
$W^+(2250, 2500) \to \tau^+\nu_\tau$	301151	50	9.3e-05	5.4e+05
$W^+(2500, 2750) \to \tau^+\nu_\tau$	301152	50	4.6e-05	1.1e+06
$W^+(2750, 3000) \to \tau^+\nu_\tau$	301153	50	2.3e-05	2.1e+06
$W^+(3000, 3500) \to \tau^+\nu_\tau$	301154	50	1.8e-05	2.7e+06
$W^+(3500, 4000) \to \tau^+\nu_\tau$	301155	50	5.1e-06	9.8e+06
$W^+(4000, 4500) \to \tau^+\nu_\tau$	301156	50	1.4e-06	3.5e+07
$W^+(4500, 5000) \to \tau^+\nu_\tau$	301157	50	4e-07	1.2e+08
$W^+(> 5000) \to \tau^+\nu_\tau$	301158	50	1.5e-07	3.3e+08
$W^-(120, 180) \to \tau^-\bar{\nu_\tau}$	301160	500	22	23
$W^-(180, 250) \to \tau^-\bar{\nu_\tau}$	301161	250	3.3	76
$W^-(250, 400) \to \tau^-\bar{\nu_\tau}$	301162	150	1.1	1.4e+02
$W^-(400, 600) \to \tau^-\bar{\nu_\tau}$	301163	100	0.18	5.7e+02
$W^-(600, 800) \to \tau^-\bar{\nu_\tau}$	301164	50	0.031	1.6e+03
$W^-(800, 1000) \to \tau^-\bar{\nu_\tau}$	301165	50	0.0083	6e+03
$W^-(1000, 1250) \to \tau^-\bar{\nu_\tau}$	301166	46	0.0032	1.5e+04
$W^-(1250, 1500) \to \tau^-\bar{\nu_\tau}$	301167	50	0.001	5e+04
$W^-(1500, 1750) \to \tau^-\bar{\nu_\tau}$	301168	50	0.00037	1.4e+05
$W^-(1750, 2000) \to \tau^-\bar{\nu_\tau}$	301169	50	0.00015	3.3e+05
$W^-(2000, 2250) \to \tau^-\bar{\nu_\tau}$	301170	50	6.5e-05	7.7e+05
$W^-(2250, 2500) \to \tau^-\bar{\nu_\tau}$	301171	50	3e-05	1.7e+06
$W^-(2500, 2750) \to \tau^-\bar{\nu_\tau}$	301172	50	1.5e-05	3.4e+06
$W^-(2750, 3000) \to \tau^-\bar{\nu_\tau}$	301173	50	7.3e-06	6.9e+06
$W^-(3000, 3500) \to \tau^-\bar{\nu_\tau}$	301174	50	5.7e-06	8.8e+06
$W^-(3500, 4000) \to \tau^-\bar{\nu_\tau}$	301175	50	1.6e-06	3.1e+07
$W^-(4000, 4500) \to \tau^-\bar{\nu_\tau}$	301176	50	4.7e-07	1.1e+08
$W^-(4500, 5000) \to \tau^-\bar{\nu_\tau}$	301177	50	1.4e-07	3.5e+08
$W^-(> 5000) \to \tau^-\bar{\nu_\tau}$	301178	50	6.2e-08	8.1e+08

TABLE 9.4: The MC samples for the $W \to \tau\nu_\tau$ background. For each dataset, the physics process (including the mass range in GeV where appropriate), the ATLAS MC run number, the number of generated events, the cross section times branching ratio and the equivalent integrated luminosity ($L_{\text{int}} = \frac{N_{evt}}{\sigma B}$) are listed.

Process	Dataset ID	N_{evt} [$\times 10^3$]	Generator σB [pb]	L_{int} [fb^{-1}]
Inclusive and mass binned $Z \rightarrow e^+e^-$				
$Z \rightarrow e^+e^-$	361106	79942	1.9e+03	42
$Z(120, 180) \rightarrow e^+e^-$	301000	499	17	29
$Z(180, 250) \rightarrow e^+e^-$	301001	250	2.9	86
$Z(250, 400) \rightarrow e^+e^-$	301002	150	1.1	1.4e+02
$Z(400, 600) \rightarrow e^+e^-$	301003	100	0.2	5.1e+02
$Z(600, 800) \rightarrow e^+e^-$	301004	145	0.037	3.9e+03
$Z(800, 1000) \rightarrow e^+e^-$	301005	50	0.011	4.7e+03
$Z(1000, 1250) \rightarrow e^+e^-$	301006	50	0.0043	1.2e+04
$Z(1250, 1500) \rightarrow e^+e^-$	301007	50	0.0014	3.5e+04
$Z(1500, 1750) \rightarrow e^+e^-$	301008	50	0.00055	9.2e+04
$Z(1750, 2000) \rightarrow e^+e^-$	301009	100	0.00023	4.3e+05
$Z(2000, 2250) \rightarrow e^+e^-$	301010	50	0.0001	4.8e+05
$Z(2250, 2500) \rightarrow e^+e^-$	301011	50	4.9e-05	1e+06
$Z(2500, 2750) \rightarrow e^+e^-$	301012	50	2.4e-05	2e+06
$Z(2750, 3000) \rightarrow e^+e^-$	301013	50	1.2e-05	4e+06
$Z(3000, 3500) \rightarrow e^+e^-$	301014	10	1e-05	1e+06
$Z(3000, 3500) \rightarrow e^+e^-$	301014	10	1e-05	1e+06
$Z(3500, 4000) \rightarrow e^+e^-$	301015	50	2.9e-06	1.7e+07
$Z(4000, 4500) \rightarrow e^+e^-$	301016	50	9e-07	5.6e+07
$Z(4500, 5000) \rightarrow e^+e^-$	301017	50	2.8e-07	1.8e+08
$Z(> 5000) \rightarrow e^+e^-$	301018	50	1.3e-07	4e+08

TABLE 9.5: The MC samples for the NCDY background. For each dataset, the physics process (including the mass range in GeV where appropriate), the ATLAS MC run number, the number of generated events, the cross section times branching ratio and the equivalent integrated luminosity ($L_{\text{int}} = \frac{N_{evt}}{\sigma B}$) are listed.

Process	Dataset ID	N_{evt} [$\times 10^3$]	Generator σB [pb]	L_{int} [fb^{-1}]
		Inclusive and mass binned $Z \to \tau^+\tau^-$		
$Z \to \tau^+\tau^-$	361108	39495	1.9e+03	21
$Z(120, 180) \to \tau^+\tau^-$	301040	450	17	26
$Z(180, 250) \to \tau^+\tau^-$	301041	150	2.9	51
$Z(250, 400) \to \tau^+\tau^-$	301042	444	1.1	4.1e+02
$Z(400, 600) \to \tau^+\tau^-$	301043	150	0.2	7.7e+02
$Z(600, 800) \to \tau^+\tau^-$	301044	450	0.037	1.2e+04
$Z(800, 1000) \to \tau^+\tau^-$	301045	450	0.011	4.2e+04
$Z(1000, 1250) \to \tau^+\tau^-$	301046	450	0.0043	1.1e+05
$Z(1250, 1500) \to \tau^+\tau^-$	301047	450	0.0014	3.2e+05
$Z(1500, 1750) \to \tau^+\tau^-$	301048	350	0.00055	6.4e+05
$Z(1750, 2000) \to \tau^+\tau^-$	301049	235	0.00023	1e+06
$Z(2000, 2250) \to \tau^+\tau^-$	301050	450	0.0001	4.3e+06
$Z(2250, 2500) \to \tau^+\tau^-$	301051	350	4.9e-05	7.1e+06
$Z(2500, 2750) \to \tau^+\tau^-$	301052	350	2.4e-05	1.4e+07
$Z(2750, 3000) \to \tau^+\tau^-$	301053	350	1.2e-05	2.8e+07
$Z(3000, 3500) \to \tau^+\tau^-$	301054	350	1e-05	3.5e+07
$Z(3500, 4000) \to \tau^+\tau^-$	301055	400	2.9e-06	1.4e+08
$Z(4000, 4500) \to \tau^+\tau^-$	301056	315	9e-07	3.5e+08
$Z(4500, 5000) \to \tau^+\tau^-$	301057	350	2.8e-07	1.2e+09
$Z(> 5000) \to \tau^+\tau^-$	301058	350	1.3e-07	2.8e+09

TABLE 9.6: The MC samples for the $Z \to \tau^+\tau^-$ background. For each dataset, the physics process (including the mass range in GeV where appropriate), the ATLAS MC run number, the number of generated events, the cross section times branching ratio and the equivalent integrated luminosity ($L_{\text{int}} = \frac{N_{evt}}{\sigma B}$) are listed.

Process	Dataset ID	N_{evt} [$\times 10^3$]	Generator σB [pb]	k-factor	L_{int} [fb^{-1}]
		Diboson			
$ZZ \to \ell\ell\ell\ell$	364250	17842	1.3	–	1.4e+04
$WZ \to \ell\ell\ell\nu$	364253	15537	4.6	–	3.4e+03
$VV \to \ell\ell\nu\nu$	364254	14996	13	–	1.2e+03
$WZ \to \ell\nu\nu\nu$	364255	5999	3.2	–	1.9e+03
$W^+W^- \to \ell\nu qq$	363360	7188	25	–	2.9e+02
$W^+W^- \to qq\ell\nu$	363359	7194	25	–	2.9e+02
$WZ \to \ell\nu qq$	363489	7180	11	–	6.3e+02
$WZ \to qq\ell\ell$	363358	5400	3.4	–	1.6e+03
$ZZ \to qq\ell\ell$	363356	5400	2.2	–	2.5e+03
		Top			
$t\bar{t} \to \ell X$	410501	59993	4.0e+02	1.14	1.5e+02
t-channel $t \to \ell X$	410011	5000	44	1.0094	1.1e+02
t-channel $\bar{t} \to \ell X$	410012	4998	26	1.0193	1.9e+02
s-channel Wt	410013	5000	34	1.054	1.5e+02
s-channel $W\bar{t}$	410014	4968	34	1.054	1.5e+02

TABLE 9.7: The MC samples for the top and diboson backgrounds. For each dataset, the physics process, the ATLAS MC run number, the number of generated events, the cross section times branching ratio, the applied k-factor (as described in section 6.3) and the equivalent integrated luminosity ($L_{\text{int}} = \frac{N_{evt}}{\sigma B}$) are listed.

9.4 Determination of the Multijet Background

The Standard Model background due to misidentified (or "fake") leptons arising from QCD initiated processes is poorly described by MC. It is therefore necessary to model this background using data-driven methods. The method chosen for this analysis is the *Matrix Method* (MM). For the electron channel, the main source of these misidentified leptons is jets which contains pions, with subsequent decays to W bosons.

9.4.1 The Matrix Method

The Matrix Method gives an estimate of the contribution of misidentified leptons to the signal selection. This is achieved by loosening some of the identification criteria for electrons and then measuring the efficiency for these objects to pass the signal, or 'tight', selection. Efficiencies for real (ϵ_R) and fake (ϵ_F) electrons are defined as:

$$\epsilon_R = \frac{N_{tight}^{real}}{N_{loose}^{real}} \quad \text{and} \quad \epsilon_F = \frac{N_{tight}^{fake}}{N_{loose}^{fake}} \tag{9.7}$$

respectively, where $N_{tight}^{real}/N_{tight}^{fake}$ are the number of real/fake electrons passing the signal selection and $N_{loose}^{real}/N_{loose}^{fake}$ are the number of real/fake leptons passing the loosened selection. A technical description of the calculation of these efficiencies follows in section 9.4.2.

Though the numbers of events arising from real (N_R) and fake (N_F) leptons are truth quantities which cannot be directly accessed, the numbers of events in the loose selection which pass (N_T) and fail (N_L) the signal selection are measurable. The real and fake efficiences connect these quantities via the matrix:

$$\underbrace{\begin{pmatrix} N_T \\ N_L \end{pmatrix}}_{\text{Truth}} = \begin{pmatrix} \epsilon_R & \epsilon_F \\ 1-\epsilon_R & 1-\epsilon_F \end{pmatrix} \underbrace{\begin{pmatrix} N_R \\ N_F \end{pmatrix}}_{\text{Measurable}} \quad . \tag{9.8}$$

For the estimation of the multijet background, the pertinent information is in the first line of this matrix:

$$\overbrace{N_T}^{\text{signal selection}} = \underbrace{\epsilon_R N_R}_{\text{contribution from real electrons}} + \overbrace{\epsilon_F N_F}^{\text{contribution from fake electrons}} \ , \tag{9.9}$$

where the last term, the number of fake leptons passing the signal selection, is the desired quantity. Inverting matrix 9.8 gives an equation for the truth quantities:

$$\begin{pmatrix} N_R \\ N_F \end{pmatrix} = \frac{1}{\epsilon R(1-\epsilon F) - \epsilon F(1-\epsilon R)} \begin{pmatrix} 1-\epsilon_F & -\epsilon_F \\ \epsilon_R - 1 & \epsilon_R \end{pmatrix} \begin{pmatrix} N_T \\ N_L \end{pmatrix} \ . \tag{9.10}$$

Inserting equation 9.9 gives:

$$\epsilon_F N_F = \frac{\epsilon_F}{\epsilon_R - \epsilon_F} \left[\epsilon_R(N_L + N_T) - N_T\right] \ , \tag{9.11}$$

where only measurable quantities (N_T & N_L) and efficiencies (ϵ_R & ϵ_F) are required. It follows (through insertion of equation 9.9) that two weights are calculated and applied to electrons which pass the loosened and tight selections:

$$\text{loose weight} = \frac{\epsilon_F}{\epsilon_R - \epsilon_F}(\epsilon_R) \qquad \text{and} \qquad \text{tight weight} = \frac{\epsilon_F}{\epsilon_R - \epsilon_F}(\epsilon_R - 1) \ , \tag{9.12}$$

respectively. The fake and real efficiencies depend on kinematic properties such as p_{T} and η of the electrons and are therefore parametrised as a function of these variables in order to account for these dependencies.

9.4.2 Real and Fake Efficiency Calculation

The data driven background estimate is calculated on an event-by-event basis. As mentioned above, fake and real efficiencies are calculated using tight and loose selections. The tight selection is the same as the signal selection outlined in section 9.1. For the loose selection, all objects have to pass the signal selection except for the *Tight* likelihood (for $p_{\mathrm{T}} < 145$ GeV) or *Medium* likelihood (for $p_{\mathrm{T}} > 145$ GeV) identification and isolation criteria. Instead, the likelihood *Medium* ($p_{\mathrm{T}} < 145$ GeV) or *Loose* ($p_{\mathrm{T}} > 145$ GeV) criteria are applied, respectively. These selections are very similar to those used at trigger level for these regions.

Since only signal electrons are added to the $E_{\mathrm{T}}^{\mathrm{miss}}$ calculation, the $E_{\mathrm{T}}^{\mathrm{miss}}$ value for events passing the loose selection can differ depending on whether the selected electron also passes the signal selection. This means that in some cases, the signal selection may not be a subset of the loose selection as the candidate may end up in a different bin for variables such as the m_T or $E_{\mathrm{T}}^{\mathrm{miss}}$. In order to address this, a dedicated $E_{\mathrm{T}}^{\mathrm{miss}}$ constructed using all leptons passing the loosened selection, as well as the signal selection, is used for the computation of the multijet background.

The real efficiency is obtained by counting real electron candidates which pass the loose or tight selection. This is estimated using CCDY MC with additional truth matching ($\Delta R < 0.2$) in order to ensure that only real electrons are used. Since there is a p_{T} and η dependency for the real efficiencies, a two-dimensional binning based on these variables is used. The real efficiency as a function of η and p_T is shown in figure 9.10. It lies roughly between 90% and 99%. The efficiencies are p_{T}-binned in three regions which are motivated by the detector geommetry: the barrel ($|\eta| < 1.36$), endcap with trt ($1.52 < |\eta| < 2.01$) and endcap without trt ($2.01 < |\eta| < 2.47$).

The fake efficiency cannot be reliably calculated using MC, therefore data is used. In order to obtain a fake enriched sample, referred to as the multijet *control region* (CR), various cuts are applied to suppress real electrons arising from W and Z bosons. These are:

- Cut events with $E_{\mathrm{T}}^{\mathrm{miss}} < 60$ GeV (referred to as the “$E_{\mathrm{T}}^{\mathrm{miss}}$ veto”).

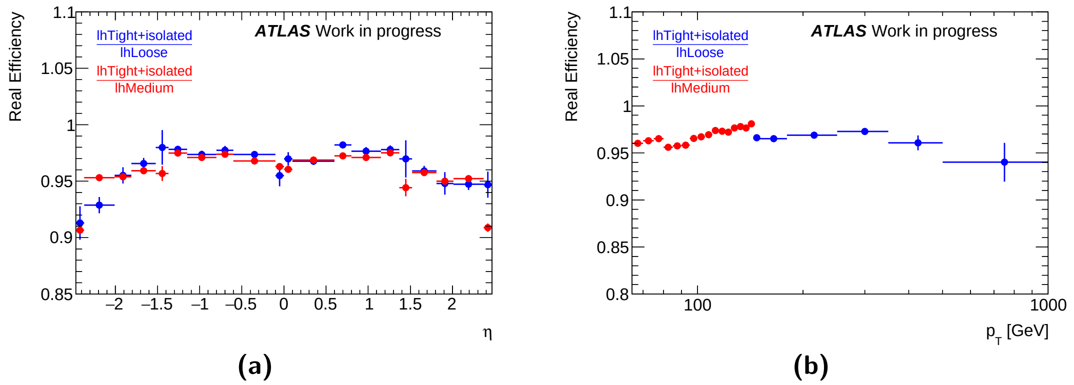

FIGURE 9.10: Real efficiencies for the Tight/Loose and Tight/Medium scenarios parametrised in (a) p_{T} and (b) η.

- Cut events with > 1 *Medium* likelihood electron with $p_T > 20$ GeV.
- Cut events with pairs of *Loose* likelihood electrons with $p_T > 20$ GeV and $|m_{ee} - m_Z| < 20$ GeV (referred to as the "Z veto").

All other applied cuts are the same as signal selection excluding the $E_{\mathrm{T}}^{\mathrm{miss}}$ and m$_T$ cuts. Dilution from real electrons after applying these cuts is estimated using MC - contributions from each MC sample are subtracted from the calculation of the fake rate from data. The fake efficiencies as a function of p_{T}, η, $E_{\mathrm{T}}^{\mathrm{miss}}$ and $\Delta\phi_{e,E_{\mathrm{T}}^{\mathrm{miss}}}$ are shown in figure 9.11. These are all variables which fake efficiencies can be binned in, though in practice the efficiencies are only 2D-binned in p_{T} and $|\Delta\phi_{e,met}|$ for the multijet background estimation, due to lack of statistics.

9.4.3 Multijet Validation Region

In order to test the validity of the predictions made by the matrix method, kinematic distributions for a multijet validation region are monitored. The $E_{\mathrm{T}}^{\mathrm{miss}}$ and m$_T$ cuts are released for this region (with all other tight selections applied), due to the fact that the multijet contribution is significantly higher at low $E_{\mathrm{T}}^{\mathrm{miss}}$. Various kinematic distributions for this region are shown in figure 9.12. Generally, these distributions show good modelling of the multijet background. In the low mass region of the missing

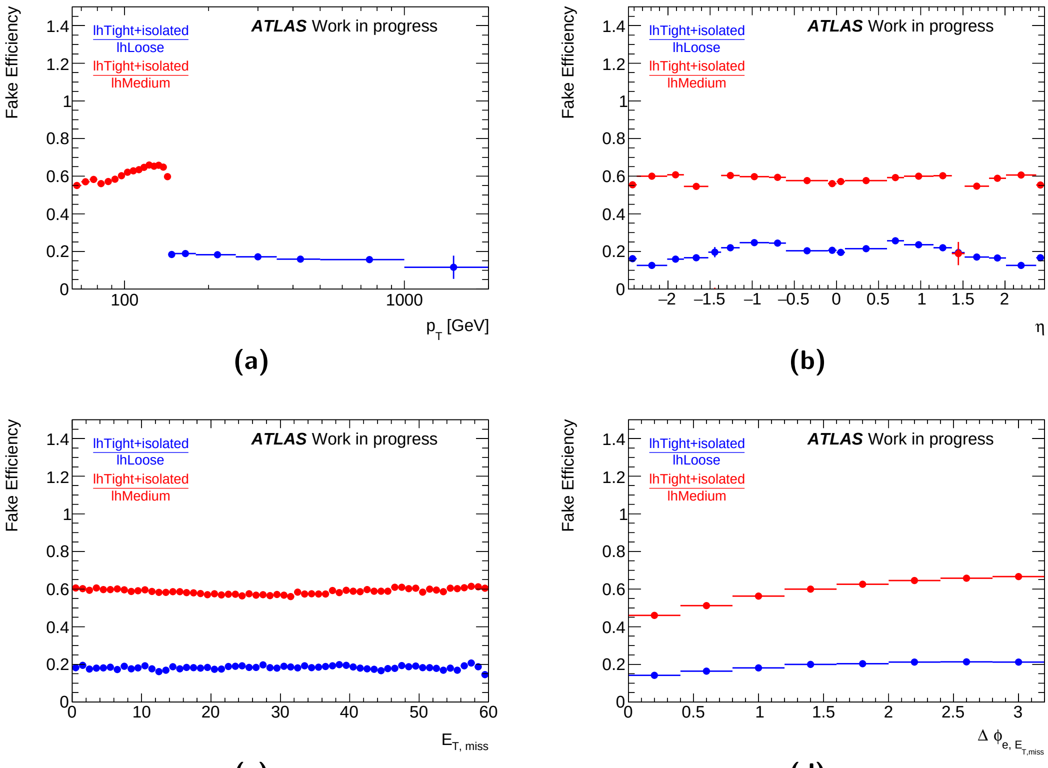

FIGURE 9.11: Fake efficiencies for the Tight/Loose and Tight/Medium scenarios parametrised in (a) p_{T}, (b) η, (c) $E_{\mathrm{T}}^{\mathrm{miss}}$ and (d) $\Delta\phi_{e,E_{\mathrm{T}}^{\mathrm{miss}}}$.

energy distribution, the excess of data is thought to be attributed to problems with the jet energy scale and missing energy resolution (see section 9.8).

9.4.4 Systematic Uncertainties

The largest source of systematic uncertainty for the multijet background arises from the determination of the fake efficiencies. The cuts which define the multijet CR in which these efficiencies are determined are therefore varied in order to quantify the uncertainty. Another source of systematic uncertainty is the subtraction of contamination from real electrons. This is quantified by releasing the Z veto. An uncertainty based on varying the real electron dilution up and down by 5% (referred to as "minDil" and "plDil") is also applied, since the dilution with real candidates is normalised to the integrated luminosity of the data, which has a measured uncertainty $\lesssim 5\%$. The residual $E_{\mathrm{T}}^{\mathrm{miss}}$

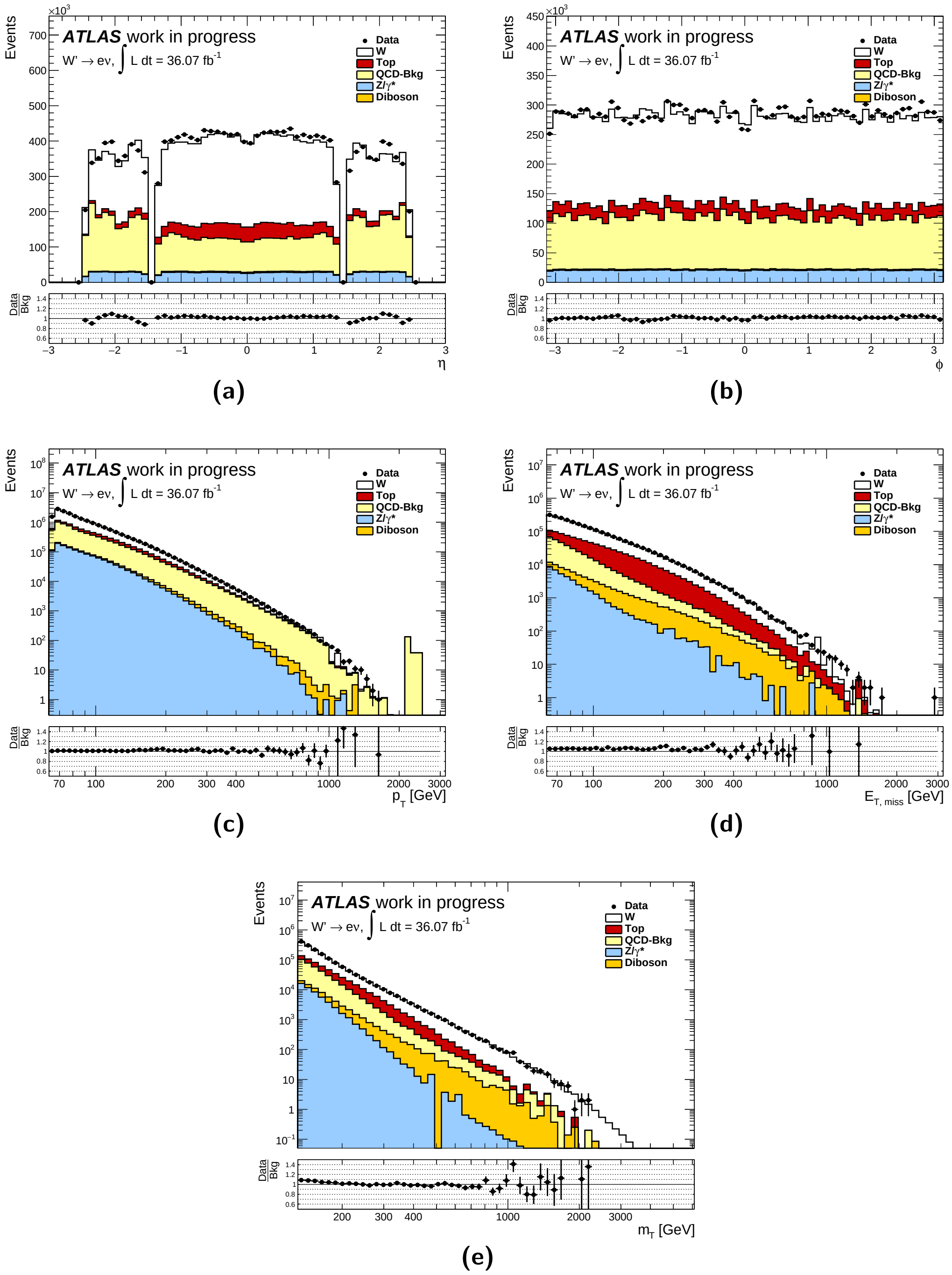

FIGURE 9.12: The (a) η, (b) ϕ, (c) p_{T}, (d) $E_{\mathrm{T}}^{\mathrm{miss}}$, and (e) m_T distributions for the multijet validation region.

dependency of the fake efficiencies is also counted as a source of systematic uncertainty, quantified by varying the $E_{\mathrm{T}}^{\mathrm{miss}}$ region in which the efficiencies are calculated to:

- $E_{\mathrm{T}}^{\mathrm{miss}} < 20$ GeV (referred to as "MET20").
- 20 GeV or $< E_{\mathrm{T}}^{\mathrm{miss}} < 60$ GeV (referred to as "20MET60").

Figure 9.13 shows the nominal p_{T} and η distributions of the fake efficiencies along with coloured lines representing the shifted efficiencies corresponding to the various sources of systematic uncertainties.

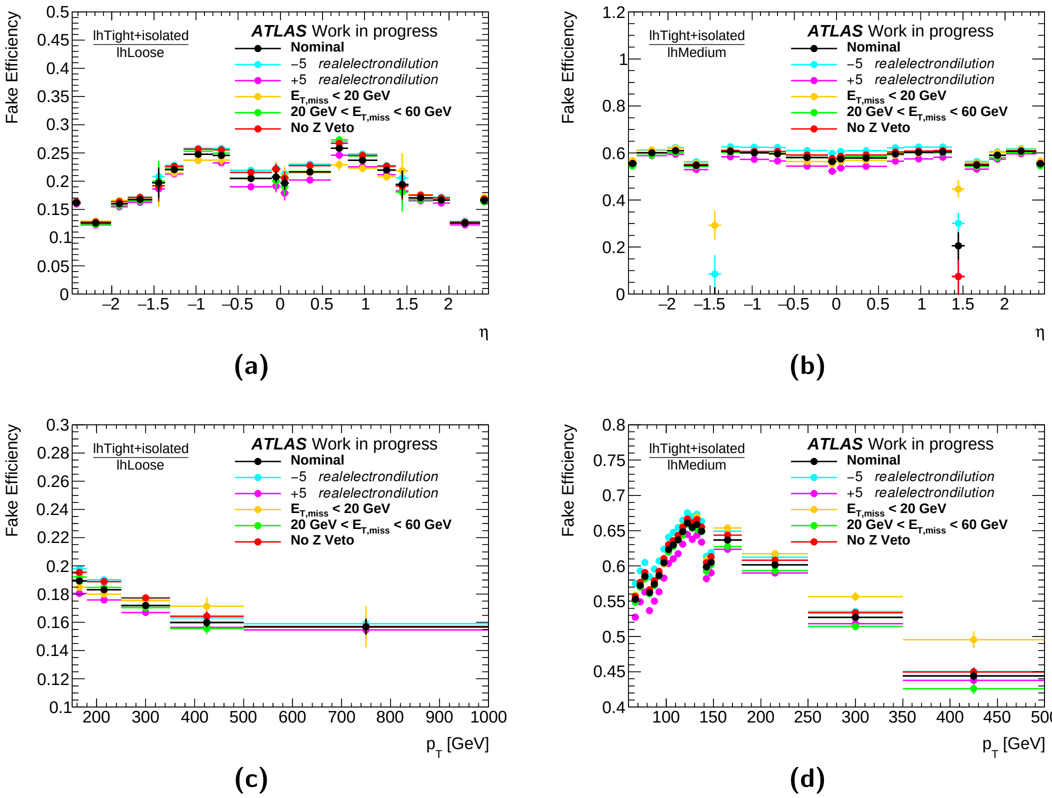

FIGURE 9.13: Fake efficiencies for the Tight/Loose and Tight/Medium scenarios parametrised in η and p_{T}. The black points show the nominal fake efficiency values while the different colours represent the shifted values obtained by changing the multijet control region cuts (see section 9.4.4).

Figure 9.14 shows the impact of the individual (and summed) sources of systematic uncertainty arising from the multijet background estimate on the total background estimate for the W' signal region as a function of transverse mass. The effect of changing the $E_{\mathrm{T}}^{\mathrm{miss}}$ cut is the most significant. There is also a systematic uncertainty arising from the need to extrapolate the multijet background estimate to high masses, which will be discussed in section 9.6.

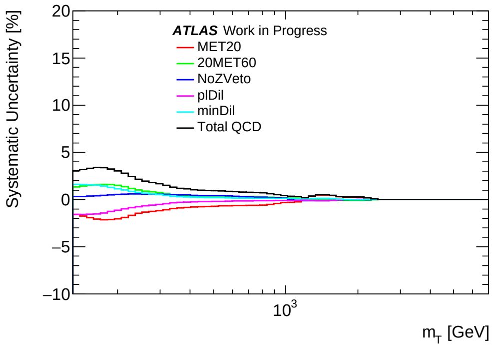

FIGURE 9.14: The effect of the systematic uncertainties arising from the multijet background determination on the total background in the signal region. The coloured lines indicate the various systematic shifts associated with changes to multijet control region cuts, while the black line gives the quadratic sum of these shifts, which is symmetrised to give the upper and lower uncertainty for this background.

9.5 Corrections Applied to MC & Data

As well as scaling the MC samples by the luminosity (from equation **??**) and the k-factors outlined in section 6.3, additional scale factors are applied in order to reflect the current conditions during data-taking. Other corrections include:

Electron Energy Correction¶

The only correction applied to electrons in data is the energy scale correction. Energies are corrected to values which are provided by the ATLAS electron/gamma group [213], obtained using calibrations based on the Z peak [214]. The same tool is used to smear the electron energy in MC in order to reproduce the resolution observed in data.

Pileup Reweighting‖

The MC samples are scaled by a factor which corrects the μ-distributions in data and MC in such a way that pile-up-dependent observables (such as track-related variables) are better described [171].

¶Using ElectronPhotonFourMomentumCorrectionTool-02-03-08.

‖Using PileupReweighting-00-04-08.

Electron Efficiency Corrections[**]

The electron trigger, reconstruction, identification and isolation efficiencies (some of which are explained in section 7.1) measured in data are compared to the efficiencies simulated in the MC using η and $E_{\mathrm{T}}^{\mathrm{miss}}$ dependent distributions. In order to correct for this, a weight corresponding to each of these efficiencies is calculated using the product of the data/MC ratio η and $E_{\mathrm{T}}^{\mathrm{miss}}$ and applied to each MC event. These weights are supplied by the electron/gamma working group.

Jet Energy Scale Calibration[††]

Jet energy scale calibration is applied to the jets in both data and MC which are used to calculate the $E_{\mathrm{T}}^{\mathrm{miss}}$.

Muon Momentum Corrections[‡‡]

Muon momentum corrections are applied to the muons which are used for the additional lepton veto outlined in section 9.1.

[**] Using ElectronEfficiencyCorrection-00-02-05.
[††] Using JetCalibTools-00-04-78.
[‡‡] Using MuonMomentumCorrections-01-00-60.

9.6 Background Extrapolation

Since the top, diboson and multijet backgrounds are not modelled using mass-binned samples, they suffer from low statistics at high mass. In order to address this and provide adequate statistics across the whole m_T spectrum, a fit-based extrapolation is used. The extrapolation is achieved by fitting using two functional forms (based on functions used in the search for di-jet resonances [215] and the 8 TeV dilepton resonance search [165]) and comparing the results. The two functions used are:

$$\frac{dN}{dm_T} = a \cdot m_T^{b+c\,\log(m_T)} \tag{9.13}$$

and

$$\frac{dN}{dm_T} = \frac{a}{\left(m_T + b\right)^c}, \tag{9.14}$$

where a, b and c are free parameters determined by the fits. Several fits are performed using both functions with various start and end points for the fit range. For top and diboson samples, the fit with the best $\frac{\chi^2}{N_{d.o.f}}$ is taken as the central value for the background estimate, while the envelope of all other fits is taken as the systematic uncertainty for the extrapolation. For the multijet background, fits are selected if they satisfy:

$$Q = \frac{1}{N_{\text{bins}}} \sum_{b>b_s}^{N_b^{\text{est}} \neq 0} \frac{\left(N_b^{\text{est}} - N_b^{\text{fit}}\right)^2}{\sigma_b^2} < 1.5, \tag{9.15}$$

where b_s is the stitching bin (the point from which the fit is used to describe the background), N_b^{est} and N_b^{fit} are the numbers of entries in the given bin according to the matrix method and the fit, respectively, and σ_b is the uncertainty for the given bin. The fit with the lowest value of Q is taken as the central value for the background estimate and all other qualifying fits form the envelope which is taken as the uncertainty.

Fits which have been performed on the top background are shown in figure 9.15. The starting point of the fit range was varied from 200 GeV to 300 GeV in steps of 25 GeV. The end point of the fit was varied from 900 GeV to 1300 GeV in steps of 40 GeV. The extrapolated background was stitched to the MC background at m_T= 900 GeV.

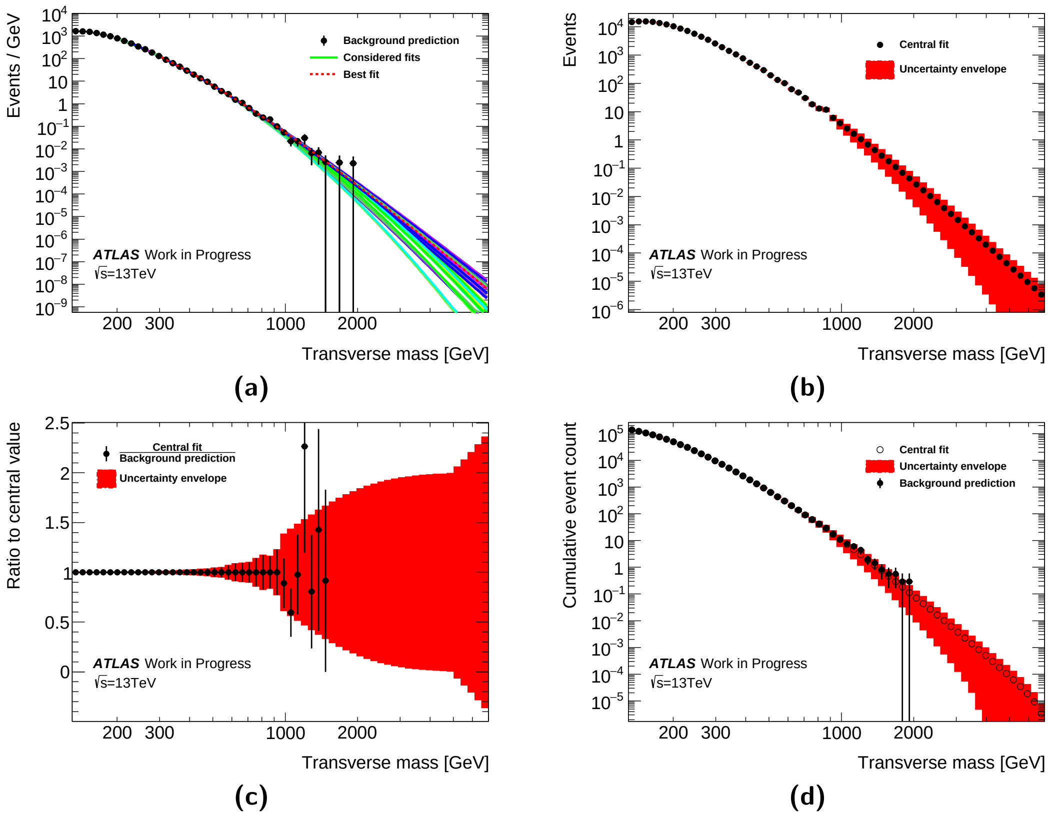

FIGURE 9.15: Results of fitting and extrapolating the top background. Figure (a) shows the full set of individual fits while figure (b) shows the central fit with its uncertainty. Figure (c) shows the ratio of the MC prediction to the central value and figure (d) shows the comparison of the MC prediction to the fit result in terms of the cumulative (integrated in the tail) distribution.

Fits which have been performed on the diboson background are shown in figure 9.16. The starting point of the fit range was varied from 160 GeV to 260 GeV in steps of 20 GeV. The end point of the fit was varied from 800 GeV to 1100 GeV in steps of 25 GeV. The extrapolated background was stitched to the MC background at m_T= 800 GeV.

Fits which have been performed on the multijet background are shown in figure 9.17. The starting point of the fit range was varied from 300 GeV to 400 GeV in steps of

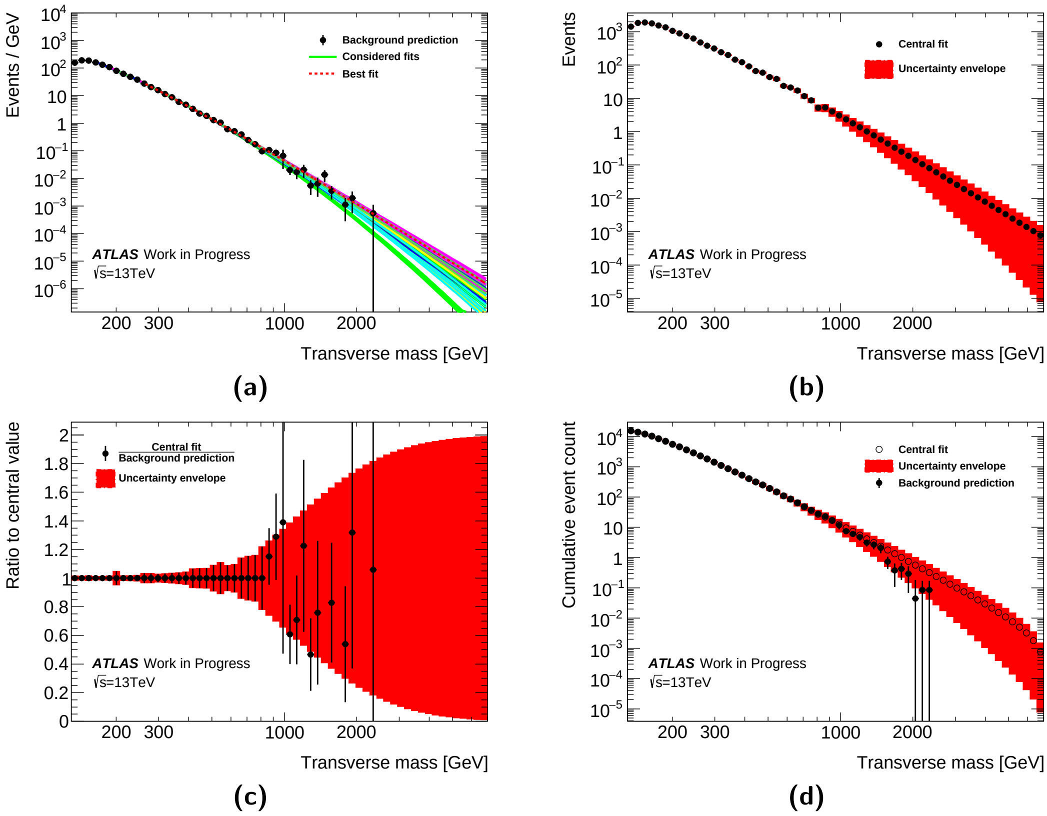

FIGURE 9.16: Results of fitting and extrapolating the diboson background. Figure (a) shows the full set of individual fits while figure (b) shows the central fit with its uncertainty. Figure (c) shows the ratio of the MC prediction to the central value and figure (d) shows the comparison of the MC prediction to the fit result in terms of the cumulative (integrated in the tail) distribution.

20 GeV. The end point of the fit was varied from 800 GeV to 1000 GeV in steps of 20 GeV. The extrapolated background was stitched to the MC background at m_T= 1000 GeV.

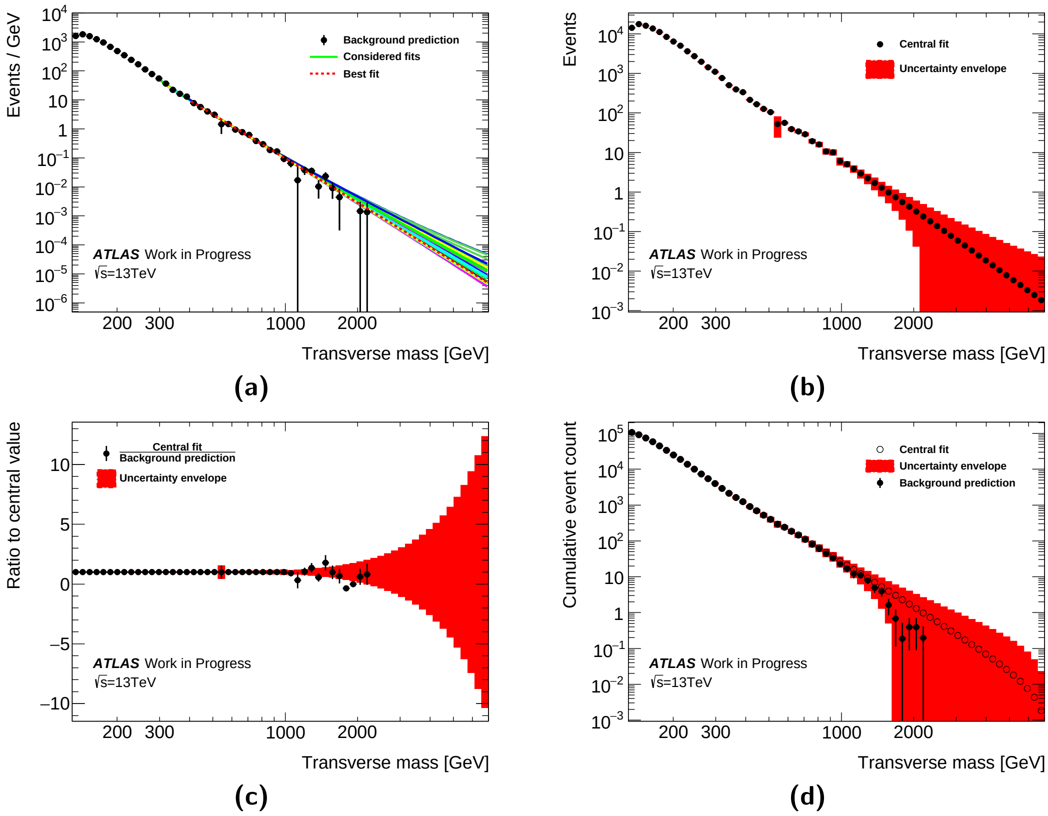

FIGURE 9.17: Results of fitting and extrapolating the multijet background. Figure (a) shows the full set of individual fits while figure (b) shows the central fit with its uncertainty. Figure (c) shows the ratio of the data driven estimate to the central value and figure (d) shows the comparison of the data driven estimate to the fit result in terms of the cumulative (integrated in the tail) distribution.

9.7 Acceptance Times Efficiency

The acceptance, $\mathcal{A}$, sometimes referred to as the acceptance times efficiency, describes the fraction of generated particles within the fiducial range of the detector which pass all selections, taking into account detector efficiency effects. It is calculated as:

$$\mathcal{A} = \mathcal{A}_{\text{geometry}}\epsilon = \frac{N_{\text{generated,cut}}}{N_{\text{generated,all}}} \times \frac{N_{\text{reconstructed,cut}}}{N_{\text{generated,cut}}} = \frac{N_{\text{reconstructed,cut}}}{N_{\text{generated,all}}}, \tag{9.16}$$

where $\mathcal{A}_{\text{geometry}}$ is the geometrical acceptance (or fraction of generated events $N_{\text{generated,all}}$ which survive kinematic cuts) and ϵ is the efficiency (or number of reconstructed events after kinematic cuts divided by number of generated events after kinematic cuts). The acceptance times efficiency for $W' \to e\nu$ as a function of pole mass is shown in figure 9.18. It sharply rises to a peak of 85% (at 1.75 TeV) followed by a gradual decline with increasing pole mass. This plot is produced by calculating the acceptance times efficency for the W' flat signal sample reweighted to pole masses from 150 GeV to 6000 GeV.

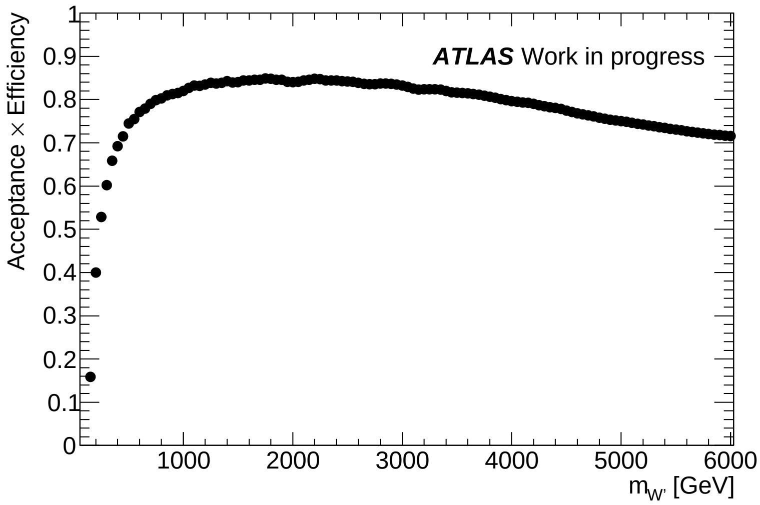

FIGURE 9.18: Total signal acceptance times efficiency as a function of SSM W' pole mass for the electron channel.

9.8 Data-Monte Carlo Comparisons

After running the full analysis chain, including applying the signal selection criteria and scaling the generated Monte Carlo to the luminosity of the measured data, plots can be produced comparing the data and MC distributions of various kinematic variables.

Figure 9.19 shows distributions of some of the important kinematic variables for the selected W' candidates - namely the electron p_{T}, the missing transverse energy, the electron η and the electron ϕ. In each of these plots lower panels show the ratios of data to the total SM background estimate, with coloured bands indicating the systematic and statistical uncertainties for the background. These plots generally show a good agreement between the data and MC+MM prediction. In the lower end of the $E_{\mathrm{T}}^{\mathrm{miss}}$ distribution there is a visible excess in the data which is attributed to problems with the jet energy scale and missing energy resolution.

Figure 9.20 shows the final signal region distribution for the search variable, the transverse mass. As with the previous plots, the middle panel shows the ratio of data/MC+MM with bands for the systematic and statistical uncertainties of the SM background. Similarly to the $E_{\mathrm{T}}^{\mathrm{miss}}$ distribution, an excess is observed in the data at lower values of transverse mass, while the rest of the spectrum shows a generally good agreement. An additional lower panel shows this ratio after pulls on the systematic uncertainties are applied as part of the statistical analysis (which will be discussed in detail in chapter 11). In this panel, after the statistical fit, the data/MC+MM agreement is improved through the application of pulls of the systematic uncertainties. Figure 9.21 is the cumulative m_T distribution, produced in order to more clearly show the data/MC+MM agreement in the high-m_T tail.

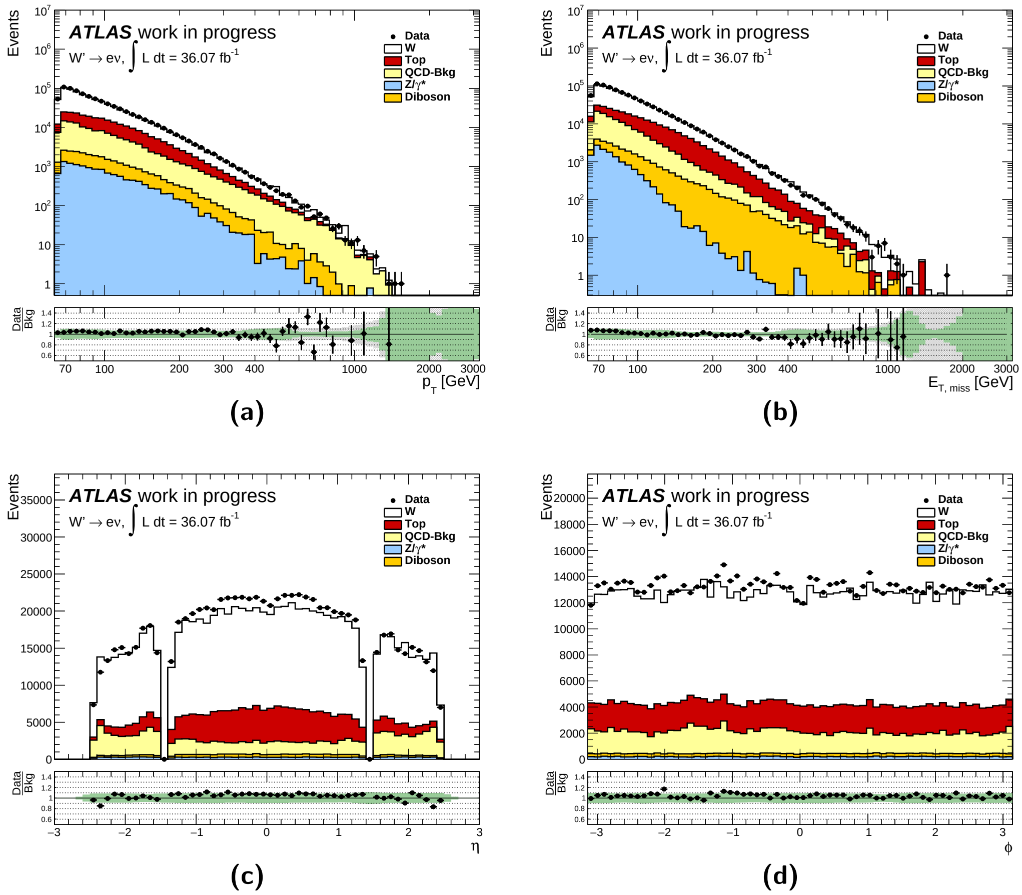

(a) (b) (c) (d)

FIGURE 9.19: Distributions of (a) p_T, (b) $E_{\mathrm{T}}^{\mathrm{miss}}$, (c) η and (d) ϕ after the full selection. The bottom panel in each plot shows the ratio of data to MC with systematic uncertainty bands shown in green and statistical uncertainty shown in grey (hashed).

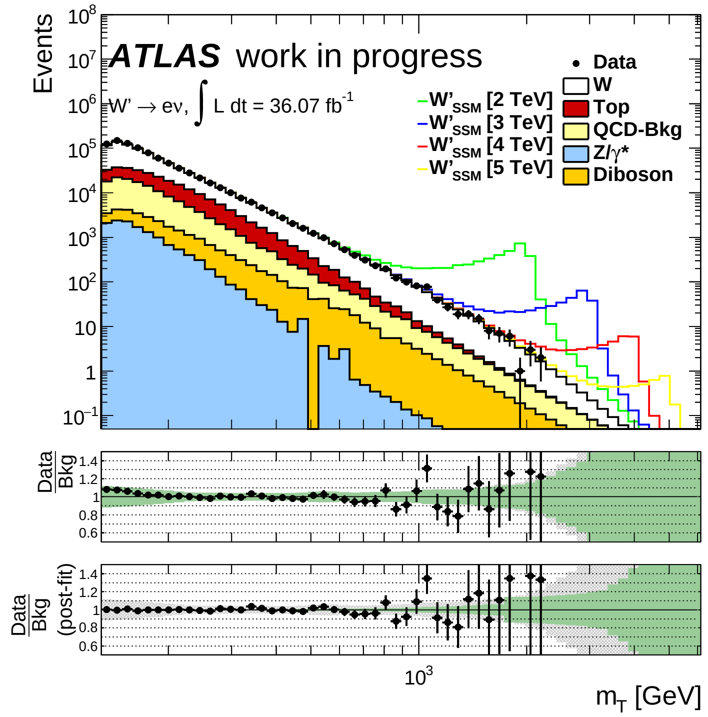

FIGURE 9.20: The transverse mass distribution after the full selection. The bottom two panels show the ratio of data to MC with systematic uncertainty bands with shown in green and statistical uncertainty shown in grey (hashed). The bottom panel is a post-fit ratio which accounts for pulls on the nuisance parameters.

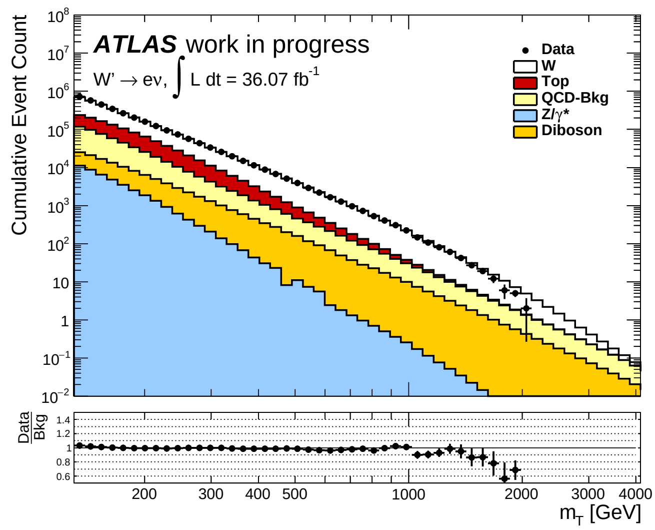

FIGURE 9.21: The cumulative transverse mass distribution after the full selection. For each bin, the content is obtained as the integral of all bins to its right.

Chapter 10

Systematic Uncertainties

In order to perform a full statistical analysis of the results from this analysis, the relevant systematic uncertainties must be understood and quantified. These uncertainties arise from both experimental and theoretical sources. In this chapter, the systematic uncertainties accounted for in this analysis are described. Systematic uncertainties which have an effect of $< 3\%$ on the total background/signal are considered to be negligible.

10.1 Experimental Uncertainties

Electron Efficiencies

The electron scale factors provided by the ATLAS electron/gamma working group [213] outlined in section 9.5 come with associated systematic uncertainties obtained by varying the tag-and-probe selection (e.g. identification requirements of the tag electron, window of the Z-peak or variation of the background model). These uncertainties are propagated to the signal region and are are provided seperately for each of the reconstruction, identification, trigger and isolation scale factors. Further details of these systematic uncertainties can be found in [216].

Electron Resolution

Differences between MC and data in the electron energy resolution are quantified by smearing the electron energies in MC. These uncertainties are again provided by the ATLAS electron gamma working group. The full correlation model for this uncertainty consists of several nuisance parameters where multiple effects have been decorrelated in η bins. For this analysis, a simple correlation model is used, providing one nuisance parameter for the electron energy resolution. In this simplified model, all the effects are considered to be fully correlated in η and are summed in quadrature. Details of this method can be found in [214].

Electron Energy Scale

The effect of varying the uncertainty for electron energy scale up and down is checked, constituting the systematic uncertainty. This is achieved with MC, since higher statistics are available compared to data. The full correlation model consists of 60 nuisance parameters where many effects have been decorrelated in η-bins. For this analysis, a simplified correlation model is used, providing one nuisance parameter for the electron energy scale (denoted EG_SCALE_ALL). In this simplified model, all effects are considered to be fully correlated in η and are summed in quadrature. Details of this method can be found in [214].

Jet Energy Scale & Resolution

Jet energy scale and resolution uncertainties enter the analysis through the $E_{\mathrm{T}}^{\mathrm{miss}}$ calculation, where calibrated jets are used. These uncertainties are provided by the ATLAS Jet/$E_{\mathrm{T}}^{\mathrm{miss}}$ working group [192, 217]. A reduced set of uncertainties with three nuisance parameters is adopted. This reduced set simplifies the correlations between the different sources of the jet energy scale uncertainty. This source of uncertainty is found to be negligible. No nominal resolution smearing is applied and the recommendation at the time of this analysis is to use the smearing as a systematic uncertainty (denoted JET_JER_SINGLE_NP).

$E_{\mathrm{T}}^{\mathrm{miss}}$ Energy Scale & Resolution

Uncertainties for the $E_{\mathrm{T}}^{\mathrm{miss}}$ scale and resolution are also provided by the Jet/$E_{\mathrm{T}}^{\mathrm{miss}}$ working group [191]. They are provided as a set of three systematics; two corresponding to the parallel and perpendicular resolution* (denoted MET_SoftTrk_ResoPara and

*With respect to an axis defined by the transverse momentum of $Z \to \mu\mu$ decays used for $E_{\mathrm{T}}^{\mathrm{miss}}$ scale determination, as outlined in [218].

MET_SoftTrk_ResoPerp, respectively) and one corresponding to the scale uncertainty (denoted MET_SoftTrk_ScaleUp). They enter the analysis through the soft term in the calculation of the $E_{\mathrm{T}}^{\mathrm{miss}}$. The uncertainties cover differences between data and MC and are only applied to the MC estimate. The $E_{\mathrm{T}}^{\mathrm{miss}}$ calculation is also impacted by uncertainties associated with jet, electron and muon momentum, which are accounted for by providing modified objects to the MET construction tool.

Pile-up

The pileup reweighting scale factor outlined in section 9.5 comes with an associated uncertainty (denoted PRW_DATASF).

Luminosity

As outlined in section 5.8, a systematic shift of 3.2% is applied in order to account for the uncertainty in the Luminosity measurement.

10.2 Theoretical/Background Modelling Uncertainties

CCDY/NCDY Backgrounds

The PDF uncertainty for the CT14NNLO PDF set for eigenvectors with a non-negligible effect (as described in section 8.1 and denoted LPX_KFACTOR_PDF_EW1–7) and PDF choice uncertainty with respect to the NNPDF3.0 prediction (as described in section 8.5, denoted LPX_KFACTOR_REDCHOICE_NNPDF30) are applied to the Drell-Yan backgrounds. The α_S uncertainty (as described in section 8.6) is not taken into account since its effect is found to be negligible. The uncertainty on the electroweak corrections used are also applied. These are estimated by comparing the additive (equation 6.4) and factorised (equation 6.3) schemes. The additive approach is used for the central value while the difference to the factorised approach is taken as the uncertainty (denoted LPX_KFACTOR_PDF_EW)

Top/Diboson Backgrounds

Theoretical uncertainties for the top and diboson backgrounds alter the total background estimate by a neglible amount and are therefore neglected. Both of these backgrounds have sizable uncertainties arising from the extrapolations (section 9.6), which are taken into account (denoted TTST_extrapolation and DB_extrapolation, respectively).

Multijet Background

As outlined in section 9.4.4, systematic uncertainties arise from the data-driven multijet background estimate. There is also an uncertainty due to the extrapolation of this backgrounf, as described in section 9.6 (denoted QCD_extrapolation).

10.3 Summary

Figure 10.1 shows the distributions of the relative systematic uncertainties as a function of the transverse mass, split into experimental, theoretical and extrapolation components. Experimental and theoretical uncertainties (including extrapolation uncertainties and QCD uncertainties for the relevant background sources) are applied to the background while only experimental uncertainties are applied to the signal. Additional plots showing the η, ϕ, p_{T} and $E_{\mathrm{T}}^{\mathrm{miss}}$ dependencies of these relative uncertainties can be found in appendix B. At high mass ($>$ 4 TeV), the dominant sources of systematic uncertainty are the QCD background estimate (including extrapolation) and the PDF choice uncertainty.

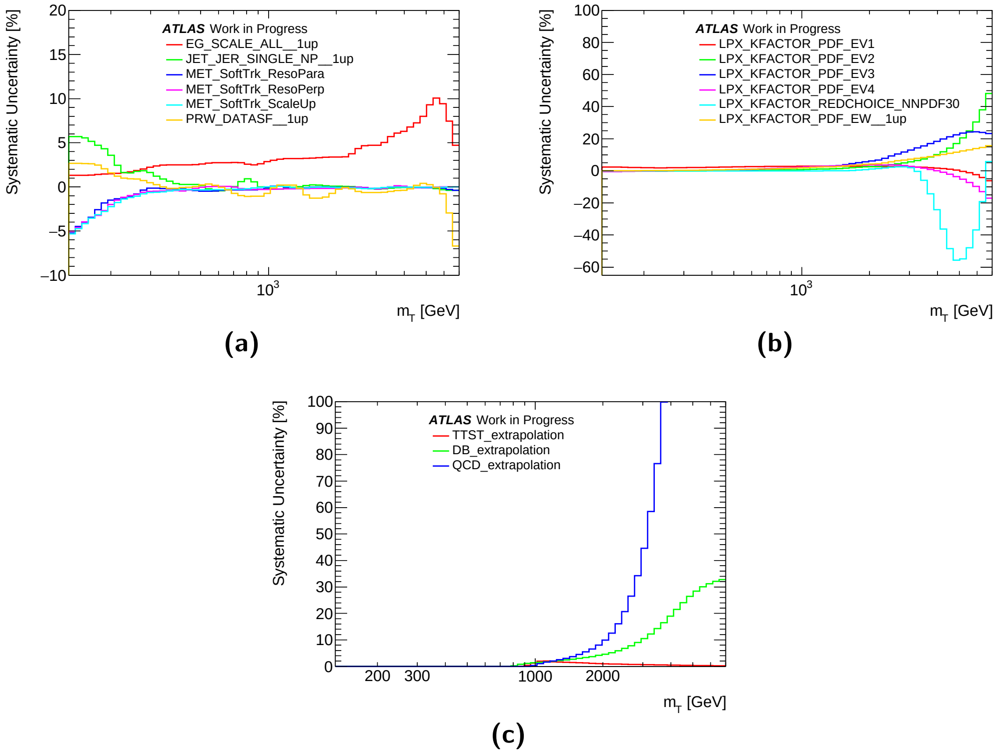

FIGURE 10.1: Transverse mass distributions of the relative systematic uncertainties on the background yield. The systematics are divided into three categories: (a) experimental, (b) theoretical and (c) extrapolation.

Chapter 11

Statistical Interpretation

When searching for a new BSM signal, statistical techniques must be adopted in order to confirm whether observations are consistent with expectations. *Hypothesis tests* are introduced to discriminate between the so-called *null* (H_0) and *alternative* (H_1) hypotheses and select one in favour of the other based on the experimental observations. These hypotheses can have different meanings depending on the type of statistical analysis. If the goal is to calculate the significance of an observed excess for discovery, the null hypothesis is defined as the expectation solely from known SM processes (i.e. background only) while the alternative hypothesis is defined as the expectation from both the known SM and new signal BSM processes (i.e. signal plus background). Conversely, in the case of ruling out/excluding a potential new signal, these definitions are switched. In the absence of an excess over the Standard Model for the observed data presented in this thesis, the statistical analysis focuses on setting exclusion limits.

Since there is a discrete number of observed events, the experimental outcome of the search may be described using Poisson statistics [219]. The probability, or *likelihood* ($\mathcal{L}$), for a Poisson-distributed variable with *expectation value* $\mu s+b$ to take the observed value N is:

$$P(N|\mu s+b) = \mathcal{L}(\mu s+b) = \frac{(\mu s+b)^N e^{-(\mu s+b)}}{N!}, \tag{11.1}$$

where μ, also referred to as the *parameter of interest* (POI), is defined the signal strength given by the ratio of the observed and expected (SM) cross-sections:

$$\mu = \frac{\sigma_{obs}}{\sigma_{SM}}. \tag{11.2}$$

A value of $\mu = 0$ would correspond to a background-only hypothesis while a value of $\mu = 1$ would correspond to the nominal signal hypothesis. In the W' search, σ is taken to be the total cross section for W' production and decay to the electron **or** muon final state individually. This is referred to as the cross section times branching ratio, σB.

Since the analysis presented in this thesis describes the data using a spectrum of transverse mass bins, a multi-bin statistical approach is required. For each channel k^*, each bin l has its own expectation value, denoted here as μ_{kl}. Additionally, this expected value may be shifted by nuiance parameters, $\boldsymbol{\theta}$, which describe the relevant systematic uncertainties:

$$\mu_{kl} \rightarrow \mu'_{kl} = \mu_{kl}\left(1 + \sum_{i=1}^{N_{sys}} \theta_i \epsilon_{ikl}\right), \tag{11.3}$$

where ϵ_{ikl} is the size of the systematic effect for uncertainty i in bin l of channel k. It follows that each bin of each channel has its own likelihood which must be multiplied in order to give the total likelihood:

$$\mathcal{L}(\sigma, \boldsymbol{\theta}) = P(N|\sigma, \boldsymbol{\theta}) = \prod_{k=1}^{N_{chan}} \prod_{l=1}^{N_{bins}} \frac{\mu_{kl}'^{N_{kl}} e^{-\mu'_{kl}}}{N_{kl}!} \prod_{i=1}^{N_{sys}} f(\theta_i), \tag{11.4}$$

where the $f(\theta_i)$ indicates either a *prior* probability density function or a constraint (depending on the type of statistical analysi) which is chosen to describe the nuisance parameters. The number of expected signal and background events can also be defined through probability density functions, which can be interpereted differently depending on whether one adopts a *Bayesian* or *frequentist* statistical method. The former is historically used for the W' and Z' analyses, while the latter is used in most other ATLAS analyses (including the diboson anlayses which are part of the combination described in part V). In this chapter, both statistical methods are outlined. In the

[*] Though the main analysis in this thesis is only concerned with one channel, it is useful to outline how a multi-channel statistical analysis is performed for the combination in part V.

frequentist case two methods are presented; one using a set of *pseudo-experiments* and the other using an approximation built on a set of *asymptotic* formulae. Results obtained using both of these versions of the frequentist framework for the $W' \to e\nu$ search are presented and compared to results from the standard Bayesian approach.

11.1 Bayesian Limit Setting

Bayesian inference involves calculating probabilities based on an existing degree of belief in a certain outcome. Bayes' theorem is used to revise the probability for a hypothesis using new data. According to this theorem, the *posterior* probability of observing event A given that B is true ($P(B) \neq 0$), $P(A|B)$ is:

$$P(A|B) = \frac{P(B|A)P(A)}{P(B)}, \tag{11.5}$$

where, $P(A)$ is the *prior* probability, or the initial degree of belief in A and $P(A|B)$ is the conditional probability, or likelihood, which is the degree of belief in B given that A is true. The $P(B)$ term is sometimes referred to as the *marginal likelihood* and is the same for all considered hypotheses (since there is no dependence on A).

In this analysis, we are concerned with calculating the probability density of the parameter of interest, the signal cross section, given the observed data. This is given in Bayes' theorem as:

$$p(\mu|N) = \frac{P(N|\mu)p(\mu)}{P(N)} = \frac{\mathcal{L}(\mu)p(\mu)}{P(N)}, \tag{11.6}$$

where p denotes probability density and N contains the numbers of observed event counts in all bins of the relevant channels. The denominator, $P(N)$, is determined using the normalisation condition:

$$\int_0^\infty p(\mu|N)d\mu = 1. \tag{11.7}$$

Dependence on nuisance parameters, $\boldsymbol{\theta}$, can be included in equation 11.6, which then takes the form:

$$p(\mu, \boldsymbol{\theta}|N) = \frac{P(N|\mu, \boldsymbol{\theta})p(\mu, \boldsymbol{\theta})}{P(N)}. \tag{11.8}$$

Though the nuisance parameters are associated with Gaussian prior probabilities, a log-normal description of these parameters is implemented through their relationship to the signal and background yields. This is motivated by the fact that a log-normally distributed random variable only takes positive real values [220] (while a Gaussian-distributed variable can be negative). The implementation of the log-normal prior is evident in the calculation for the number of expected signal events for bin l of channel k (s_{kl}):

$$s_{kl}(\mu, \boldsymbol{\theta}) = \overline{s_{kl}}(\mu) \exp\left(\sum_{i=1}^{N_{\mathrm{sys}}} \mathrm{sgn}[(\delta s_{kl})_i]\, \theta_i \sqrt{\ln\left[1 + \left(\frac{(\delta s_{kl})_i}{\overline{s_{kl}}}\right)^2\right]}\right), \tag{11.9}$$

where δs_{kl} is the systematic uncertainty on s_{kl} due to source i and $\overline{s_{kl}}$ is the central value defined as:

$$\overline{s_{kl}}(\mu) = L_{\mathrm{int}} \sigma A_k \epsilon_{kl}, \tag{11.10}$$

with L_{int} denoting the total integrated luminosity, A_k denoting the total acceptance times efficiency for signal events in channel k to pass the event selection and ϵ_{kl} denoting the fraction of surviving events which are in bin l. The quantity $\frac{(\delta s_{kl})_i}{\overline{s_{kl}}}$ represents the relative shift in s_{kl} which is induced by one standard deviation variation of the i^{th} nusance parameter. The exponential function in equation 11.9 leads to the log-normal description of the signal contribution (with the i^{th} nuisance parameter described by a Gaussian prior). In this implementation, the log-normal distribution is required to have the same ratio of standard deviation to mean value as a Gaussian prior. Additionally, the sign (sgn) of $(\delta s_{kl})_i$ is included in order to maintain correlations (and anti-correlations) between fluctuations of θ with fluctiations of the yield. The expected number of background events for bin l of channel k is:

$$b_{kl}(\boldsymbol{\theta}) = \overline{b_{kl}}(\mu)\left(1 + \sum_{i=1}^{N_{sys}} \theta_i \frac{(\delta b_{kl})_i}{\overline{b_{kl}}}\right), \tag{11.11}$$

where $\overline{b_{kl}}$ is the central value of b_{kl} and $\frac{(\delta b_{kl})_i}{\overline{b_{kl}}}$ is the relative shift in b_{kl} associated with systematic uncertainties.

A limit on the signal cross section in the Bayesian analysis is obtained by calculating the posterior for the parameter of interest and nuisance parameters in equation 11.8 and integrating, or *marginalising*, over all nuisance parameters in order to obtain the "marginalised" posterior for μ alone. The prior takes a product form with a Gaussian description of the nuisance parameters:

$$p(\mu, \boldsymbol{\theta}) = p(\mu) \prod_{i=1}^{N_{sys}} \phi(\theta_i), \tag{11.12}$$

where ϕ represents the standard normal probability density function. The cross section prior is taken to be flat (i.e. zero for $\mu < 0$ and constant for $\mu \geqslant 0$). For $\mu \geqslant 0$ the posterior probability takes the form:

$$p(\mu|N) = \int p(\mu, \boldsymbol{\theta}|N) d\boldsymbol{\theta} = N \int \prod_{k=1}^{N_{chan}} \prod_{l=1}^{N_{bin}} \frac{\mu_{kl}'^{N_{kl}} e^{-\mu_{kl}'}}{N_{kl}!} \prod_{i=1}^{N_{sys}} \phi(\theta_i) d\boldsymbol{\theta}, \tag{11.13}$$

where N is the normalization constant determined by equation 11.7. This marginalisation integral is performed using Markov Chain MC (MCMC) [221, 222] sampling in the Bayesian Analysis Toolkit (BAT) [223]. This form of sampling involves scanning the complicated probability distributions arising from many parameters using random walks to points with higher probabilities. The more 'steps' that are performed by the MCMC, the closer the simulated distribution is to converging on the real posterior probability function.

The upper limit μ_{up} on the POI (cross section) at credibility level (CL) $1 - \delta$ is given by:

$$\int_{\mu_{up}}^{\infty} p(\mu|N) d\mu = \delta, \tag{11.14}$$

meaning the posterior probability is δ above this cross section. The expected limit and corresponding upper and lower bands are calculated by sampling the distribution of the cross section limit for a number of background-only pseudo-experiments and taking the median value (as well as the 68% and 95% quantiles). For each pseudo-experiment, sample values are generated for all of the nuisance parameters according to their Gaussian priors and the "observed" count for each bin is generated according to the Poisson distribution with expectation value $b_{kl}(\boldsymbol{\theta})$ for the generated sample values of the nuisance parmeters. These counts are treated as the actual data and the cross section limit is calculated accordingly.

Equations 11.9, 11.10 and 11.11 introduce the required inputs for the Bayesian statistical analysis, namely the integrated luminosity (L_{int}), the acceptance (A_k) and signal shapes (ϵ_{kl}), the background estimates ($\overline{b_{kl}}$) and the signal and background systematic variations ($\frac{(\delta s_{kl})_i}{s_{kl}}$ and $\frac{(\delta b_{kl})_i}{\overline{b_{kl}}}$).

11.2 Frequentist Limit Setting

The frequentist analysis undertaken here follows recommendations outlined in [224]. In frequentist probability, an experiment can be considered as one of an infinite sequence of possible repetitions of that experiment where each repetition is capable of producing statistically independent results. In the frequentist framework, a numerical value which represents the dataset, known as the test statistic t_μ, is defined such that it distinguishes between the null and alternative hypotheses (or, in the case of no alternative hypothesis, characterises the null hypothesis). It is often based on a likelihood ratio $\lambda(\mu)$, such as:

$$t_\mu = -2\ln\lambda(\mu) \qquad \text{where} \qquad \lambda(\mu) = \frac{H_{\text{null}}}{H_{\text{alt}}} = \frac{\mathcal{L}\big(\mu, \hat{\hat{\boldsymbol{\theta}}}_\mu\big)}{\mathcal{L}\big(\hat{\mu}, \hat{\boldsymbol{\theta}}\big)}, \tag{11.15}$$

where, as before, μ is the POI and $\boldsymbol{\theta}$ represents the nuisance parameters. A hat represents the Maximum Likelihood Estimator (MLE), while a double hat represents the constrained, or conditional, MLE, i.e. the MLE of $\boldsymbol{\theta}$ at fixed μ. In other words, $\hat{\hat{\boldsymbol{\theta}}}_\mu$ denotes the value of $\boldsymbol{\theta}$ which maximises $\mathcal{L}$ for the specified μ value. The denominator is the maximised, or unconditional, likelihood function. Since the POI in the case of this analysis is a physical quantity which must take a positive value, a boundary $\mu \geqslant 0$ is implemented. This constraint is included in the definition of the alternative test statistic, which is denoted $\widetilde{t_\mu}$:

$$\widetilde{t_\mu} = -2 \ln \widetilde{\lambda}(\mu) \qquad \text{where} \qquad \widetilde{\lambda}(\mu) = \begin{cases} \frac{\mathcal{L}\left(\mu, \hat{\hat{\boldsymbol{\theta}}}_\mu\right)}{\mathcal{L}\left(\hat{\mu}, \hat{\boldsymbol{\theta}}\right)} & \hat{\mu} \geqslant 0 \\ \frac{\mathcal{L}\left(\mu, \hat{\hat{\boldsymbol{\theta}}}_\mu\right)}{\mathcal{L}\left(0, \hat{\hat{\boldsymbol{\theta}}}(0)\right)} & \hat{\mu} < 0 \end{cases}, \tag{11.16}$$

meaning that for non-physical values of μ, the parameter of interest is assigned a value of zero. In the case of establishing upper limits on the parameter of interest, the test statistic $\widetilde{q_\mu}$ is introduced:

$$\widetilde{q_\mu} = \begin{cases} -2 \ln \widetilde{\lambda}(\mu) & \hat{\mu} \leqslant \mu \\ 0 & \hat{\mu} > \mu \end{cases}, \tag{11.17}$$

where $\hat{\mu} > \mu$ is set to zero to ensure that upward fluctuations of the signal do not serve as evidence against the signal hypothesis.

This test statistic is quantified for different input values of the parameter of interest and compared to to the observed value of this statistic, q_{obs}, taken from data. This allows either the confirmation of the null hypothesis or rejection of it in favour of the alternative hypothesis. Figure 11.1 shows distributions of the test statistic for the null $f(q|b)$ and alternative $f(q|s+b)$ hypotheses for two tested values of μ obtained through 100,000 pseudo-experiments (or *toys*) for the $W' \rightarrow e\nu$ analysis presented in this thesis. The q_{obs} value is also shown on these plots as a dotted line.

For exclusion in this framework, confidence levels (CL) for the null (b) and alternative ($s+b$) hypotheses are defined:

$$CL_b = \frac{\int_{\text{min}}^{q_{\text{obs}}} f(q|b)}{\int_{\text{min}}^{\text{max}} f(q|b)} \qquad CL_{s+b} = \frac{\int_{\text{min}}^{q_{\text{obs}}} f(q|s+b)}{\int_{\text{min}}^{\text{max}} f(q|s+b)}, \tag{11.18}$$

where “min” and “max” refer to the lowest and highest values of the test statistic for the relevant distribution. Exclusion is then based on the value of the confidence level

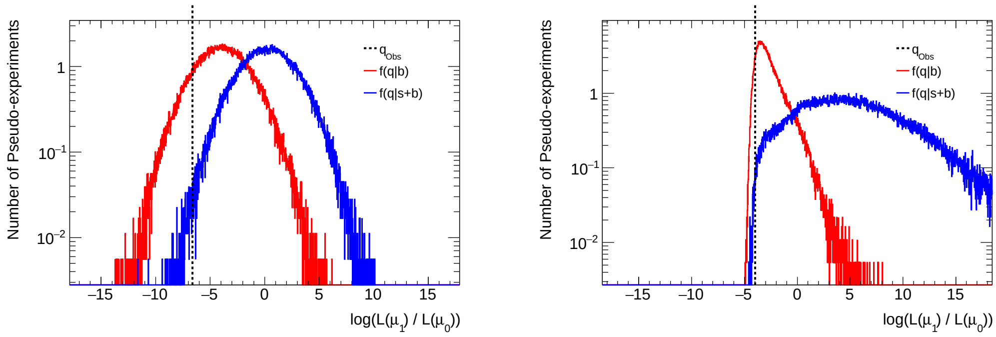

(a) **(b)**

FIGURE 11.1: Distributions of the test statistic for the null (red) and alternative (blue) hypotheses for two different tested values of signal strength μ obtained through 100,000 pseudo-experiments for different W' masses. The dotted lines show the observed value of the test statistic, q_{obs}. Figure (a) is for a W' mass of 750 GeV while figure (b) is for a W' mass of 5000 GeV. The distributions in the former are approximately gaussian, reflecting the high statistics in this region, while those in the latter exhibit Poisson-like behaviour, reflecting a low number of expected signal and background events.

for the signal, CL_s [225], defined using these two as:

$$CL_s = \frac{CL_{s+b}}{CL_b}. \tag{11.19}$$

This method is used in order to avoid ruling out scenarios which the analysis is not sensitive to (since a zero value for the POI is allowed). The value of CL_s is calculated for a range[†] of tested values of μ, with the point where $CL_s < 0.05$ giving the exclusion limit, i.e. any μ values below this point are excluded. Expected limits are obtained by calculating these CL values using an *Asimov dataset*, which replaces the alternative hypothesis. This dataset is constructed such that it represents the expected results obtained from a series of hypotheses using the distributions of the search parameter, representing the expected background without statistical fluctuations for a typical experiment. It is defined such that when one uses it to evaluate the estimators for all parameters, these are consistent with the true parameter values. Figure 11.2 shows an example of a distribution of p-value vs. μ for a mass point of the $W' \to e\nu$ analysis with a line drawn at $CL_s = 0.05$ to indicate the cross section limit for this mass.

[†]The process of choosing this range is outlined in appendix G.

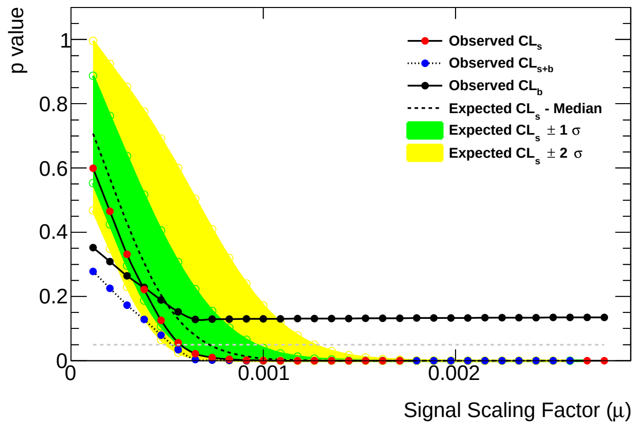

FIGURE 11.2: An example of the distribution of p-values for all tested values of μ for a W' mass of 750 GeV. Lines corresponding to CL_b, CL_{s+b} and CL_s are shown, as well as expected bands for CL_s. A dotted line indicates the point where the p-value is equal to 0.05.

11.2.1 Using Asymptotic Calculations

In addition to employing pseudo-experiments in order to perform the frequentist statistical analysis, asymptotic formulae (as described in [226]) are also used. These formulae are adopted by many analyses in the ATLAS community, motivated by the lesser computational requirements of this approach. The asymptotic formulae, built upon the theorems of Wilks [227] and Wald [228], allow one to calculate the significance for data as well as the full sampling distribution of the significance under different signal hypotheses without the use of pseudo-experiments. The asymptotic approximation assumes that distributions of the test statistic are Gaussian, meaning that in the case of Poisson-like distributions due to low statistics (as in figure 11.1(b)) limits obtained through this approximation may be optimistic. For this reason, limits obtained using asymptotic calculations are insufficient for the W' analysis, with its steeply falling statistics at very high mass. Asymptotic calculations are still prominently used to perform tests for the combination in part V since they are much less time consuming and computationally expensive than pseudo-experiments. Additionally, the inclusion of other channels in the combination gives a statistics boost at high mass, making the asymptotic assumption more valid.

11.3 Treatment of Monte Carlo Statistical Uncertainty

The integrated luminosity of the data collected in 2015+2016 is significantly larger than the integrated luminosity of the MC background samples. As a result, the statistical uncertainty of the background in the low mass region is larger than the statistical uncertainty of the data, i.e. the square root of the number of events (or width of the corresponding Poisson distribution). This MC statistical uncertainty has a non-negligible impact on the results of the statistical analysis and must therefore be taken into account. Though this uncertainty is smaller than other sources of systematic uncertainty, the fact that it is uncorrelated between all of the transverse mass bins means that it has a large overall impact. The relative uncertainty is found to be greatest for the first 25 bins (up to 600 GeV in transverse mass for the electron channel). Above this point the statistical uncertainty of the data is significantly larger than that of the MC.

In the Bayesian analysis, the standard approach would be to add a nuisance parameter θ_i for each bin corresponding to the uncertainty $\frac{(\delta b_{kl})_i}{b_{kl}} = \frac{(\delta b_{kl})_{stat}}{b_{kl}}$ for the given bin and $\frac{(\delta b_{kl})_i}{b_{kl}} = 0$ for all other bins. However, this was found to be time consuming, since it involves running the MCMC with an additional nuisance parameter for each of the 60 transverse mass bins. In order to avoid this, an approximation is adopted, whereby the likelihood (equation 11.4) is modified for all of the bins with non-negligible MC statistical uncertainty. This modification involves the assumption that statistics are sufficiently high to approximate the Poisson distribution of the likelihood as a Gaussian and is described in more detail in appendix F of [229].

In order to be consistent with the Bayesian statistical tools, a MC statistical error is also applied to the lowest 25 m_T bins in the frequentist analysis. This is achieved by splitting the signal and background into two regions - the lowest 25 m_T bins and the remaining bins. The MC statistical uncertainty is then only applied to the region corresponding to the lowst 25 bins following a Barlow-Beeston [230] "lite"[‡] approach, where each bin of the total background has 2 nuisance parameters corresponding to the

[‡] As opposed to the full method where each individual background component would have $2n_{\text{bins}}$ nuisance parameters.

up and down MC statistical error. The frequentist results shown in the main body of this thesis do not include this statistical error, since it was not implemented in time to produce results with pseudo-experiments. In order to be consistent, results obtained through asymptotic calculations are also shown without this implemented. This leads to some disagreement with the Bayesian results in the lower mass range. The $W' \to e\nu$ results from asymptotic calculations with the MC statistical uncertainty implemented are shown in appendix D, with comparison plots to the BAT result illustrating the improved agreement.

11.4 Results

Limits on μ (the cross section) obtained from the various statistical tools are multiplied by the cross section times branching fraction for $W' \to e\nu$ in order to present lower limits on the W' transverse mass. Figure 11.3 shows the limits vs. mass obtained using both pseudo-experiments and asymptotic calculations in the frequentist framework, as well as comparisons of these results to the Bayesian limits which were published in [231]. Observed and expected curves (with sigma bands in the case of the latter) are shown, along with the "theory" curve corresponding to the cross section times branching fraction for the SSM $W' \to e\nu$ process (with its own error bands arising from PDF uncertainties). Masses below the point where the observed and expected limits meet this theory curve are excluded. A notable feature of figure 11.3 is the difference in the sigma bands for the expected limit between the two frequentist approaches. This is related to the assumption of Gaussian cumulative distribution functions for the background-only hypothesis in the asymptotic approximation. In the case of Gaussian distributions, the sigma bands are symmetric about the central expected limit value. However, in practice, limits are not Gaussian (and not symmetric), meaning that the upper and lower sigma bands are not necessarily symmetric. This effect is more manifest in the high-mass tail, where statistics are low and distributions are less Gaussian. Narrow bands are expected in the case of high numbers of frequentist pseudo-experiments, since these are generated under the best-fit background hypothesis with systematics fit to their background-only best fit values, causing them to converge towards the median expected value.

Generally, there is good agreement between the frequentist and Bayesian frameworks. At higher masses the breakdown of the asymptotic assumption is clear, as the limits obtained using asymptotic calculations are up to $\sim 20\%$ lower than those from BAT and frequentist pseudo-experiments, leading to a more optimistic (higher) mass exclusion limit. For lower masses, differences can be attributed to the lack of implementation of the MC statistical uncertainty in the frequentist tools. As previously stated, results obtained using asymptotic calculations with this source of uncertainty included can be found in appendix D, where comparisons to the Bayesian result show an improved agreement. Due to time constraints, no such result is shown using pseudo-experiments.

The observed and expected lower mass exclusion limits obtained through each of the statistical frameworks are quoted in table 11.1. As previously stated, the exclusions obtained using asymptotic calculations are much higher than those obtained through the other two tested methods which, especially for the expected limit, are in good agreement. In the nominal frequentist approach, W' masses below 5.12 TeV are excluded.

	$\mathbf{m}_{W'}$ **lower limit [TeV]**	
Decay	**Expected**	**Observed**
$W'_{SSM} \rightarrow e\nu_{(100{,}000\ \text{PE})}$	5.07	5.12
$W'_{SSM} \rightarrow e\nu_{(\text{Asymptotics})}$	5.21	5.39
$W'_{SSM} \rightarrow e\nu_{(\text{Published BAT})}$	5.09	5.22

Table 11.1: Lower mass limits obtained through frequentist (both with pseudo-experiments and asymptotic formulae) and Bayesian frameworks.

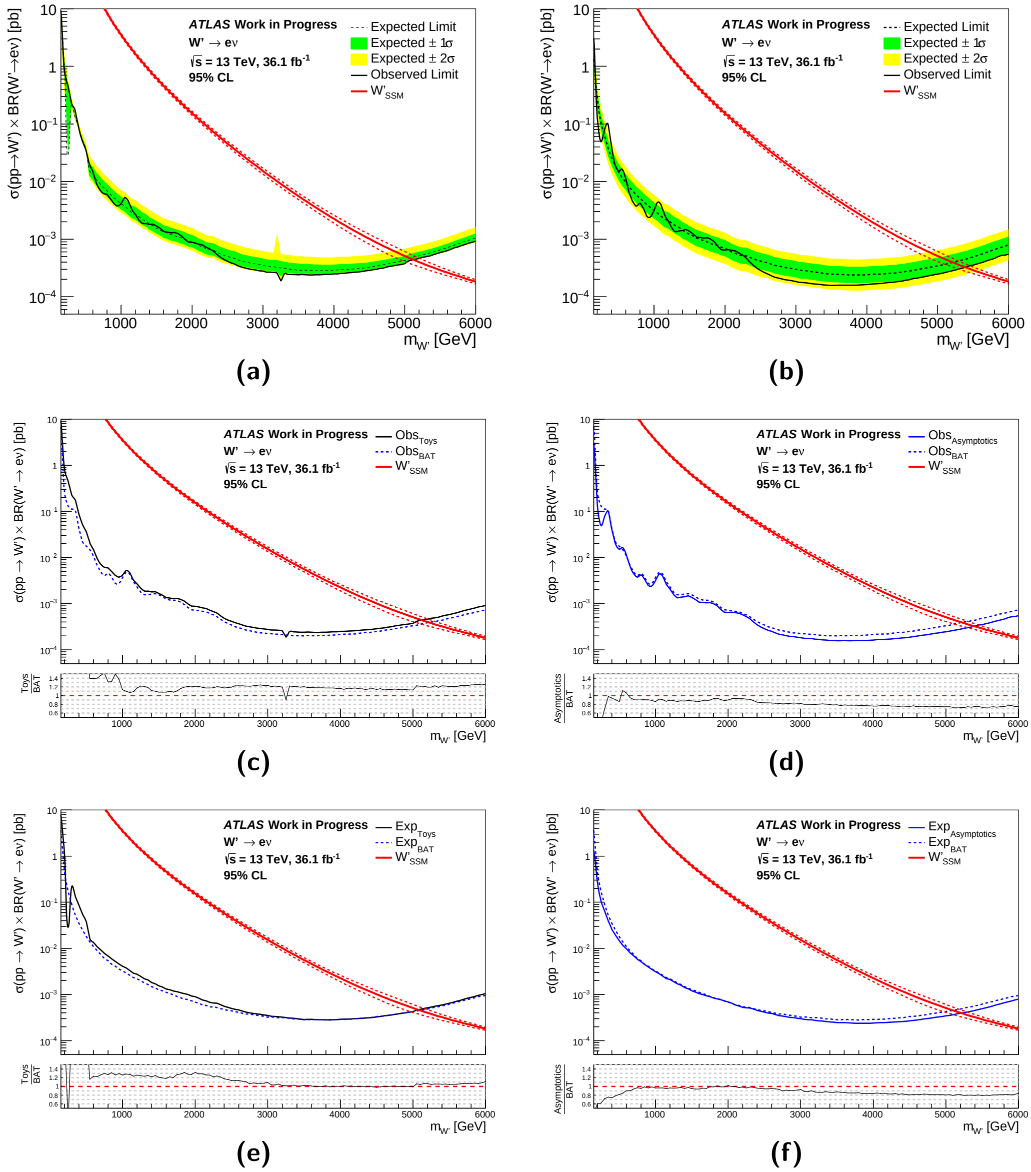

FIGURE 11.3: Limits for the $W' \to e\nu$ analysis with all systematic uncertainties accounted for. Figure (a) shows the frequentist limits obtained using 100,000 pseudo-experiments while figure (b) shows the frequentist limits obtained using asymptotic calculations. Figures (c) and (d) show direct comparisons of the observed limits obtained using BAT to the results from pseudo-experiments and asymptotic calculations, respectively. Similarly, figures (e) and (f) show comparisons of the expected limtis obtained using BAT to the results from the pseudo-experiments and asymptotic calculations, respectively. The red bands on these plot indicate the cross section times branching fraction for the process with errors corresponding to the PDF uncertainty.

Part V

Reinterpretation: $W'/Z'/VV/VH$ Combination

Chapter 12

Motivation & Statistical Tool Validation

In this chapter, the motivation for reinterpreting the $W' \to \ell\nu$ search results detailed in this thesis in a new model and combining with $Z' \to \ell\ell$ and diboson channels are outlined. Since the diboson searches adopt a distinct statistical approach to that used for W'/Z' (frequentist rather than Bayesian), the latter must be moved to a compatible statistical framework (as described in chapter 11) in order to facilitate the combination of results. This chapter documents the validation of the new statistical tools.

12.1 Combining Dilepton and Diboson Analyses

Following the publications of the almost model-independent $W' \to \ell\nu$ [231] and $Z' \to \ell\ell$ [206] analyses, the next natural step is to reinterpret these results in the context of a more specific model. As outlined in section 3.2, the HVT model predicts two charged W' bosons and an uncharged Z' boson, with many available channels such as diboson final states. This means that, in addition to adapting the searches to apply to this more physical model, the W'/Z' results can be combined. Additionally, these results may be combined with those from searches for diboson (VV and VH) resonances*. This

*Combined limits in the context of the HVT model have only previously been set using the searches for VV resonances [232].

reinterpretation is a powerful method to establish improved constraints on couplings for heavy gauge bosons which have only previously been set indirectly (e.g. at the *ee* collider, LEP [233]). The dilepton and diboson channels each provide access to several coupling factors for interactions of heavy resonances to SM particles, meaning their combination probes a wide expanse of parameter space which is not fully accessible to any of the individual analyses. Though a specific Heavy Vector Triplet model has been chosen as the context for this combination, the methodology developed in the process may be applied to any given explicit model, and could pave the way for combinations of other results between channels and experiments.

12.2 Validation of Frequentist Statistical Tools

Prior to using the frequentist statistical framework for obtaining combination results, these tools were run on the SSM inputs in order to compare obtained limits to those from the Bayesian tools. In this chapter, direct comparisons of these results are shown for each of the W' and Z' channels. The inputs used for these checks are the published W' and Z' results for the full 2015 and 2016 datasets presented in [231] and [206], respectively. Due to time constraints, the frequentist results shown here do not include the application of MC statistical errors (as outlined in section 11.3) for the pertinent mass bins. As a result, there is some disagreement visible for this region between the frequentist and Bayesian results presented here which has since been addressed.

12.2.1 W' Results

Figures 12.1 and 12.2 show the limits obtained for the $W' \to \mu\nu$ channel and the combined $W' \to \ell\nu$, respectively, with all systematic uncertainties taken into account using both pseudo-experiments and asymptotic calculations. In each of these plots, the red curve representing the SSM theory cross section times branching ratio indicate the mass limit. Direct comparisons of the observed and expected curves to those obtained using BAT are also shown. The $W' \to e\nu$ channel validation is not shown here, since this can be found in section 11.4. The agreement with BAT is generally good for both approaches. For low masses, the disagreement arising from the lack of MC statistical error for the frequentist tools is apparent. At higher masses ($\gtrsim 2$ TeV) where statistics become low, the expected curves (e.g. figure 12.1(f) for the muon channel) clearly show that the asymptotic calculations are insufficent and disagree with the Bayesian result.

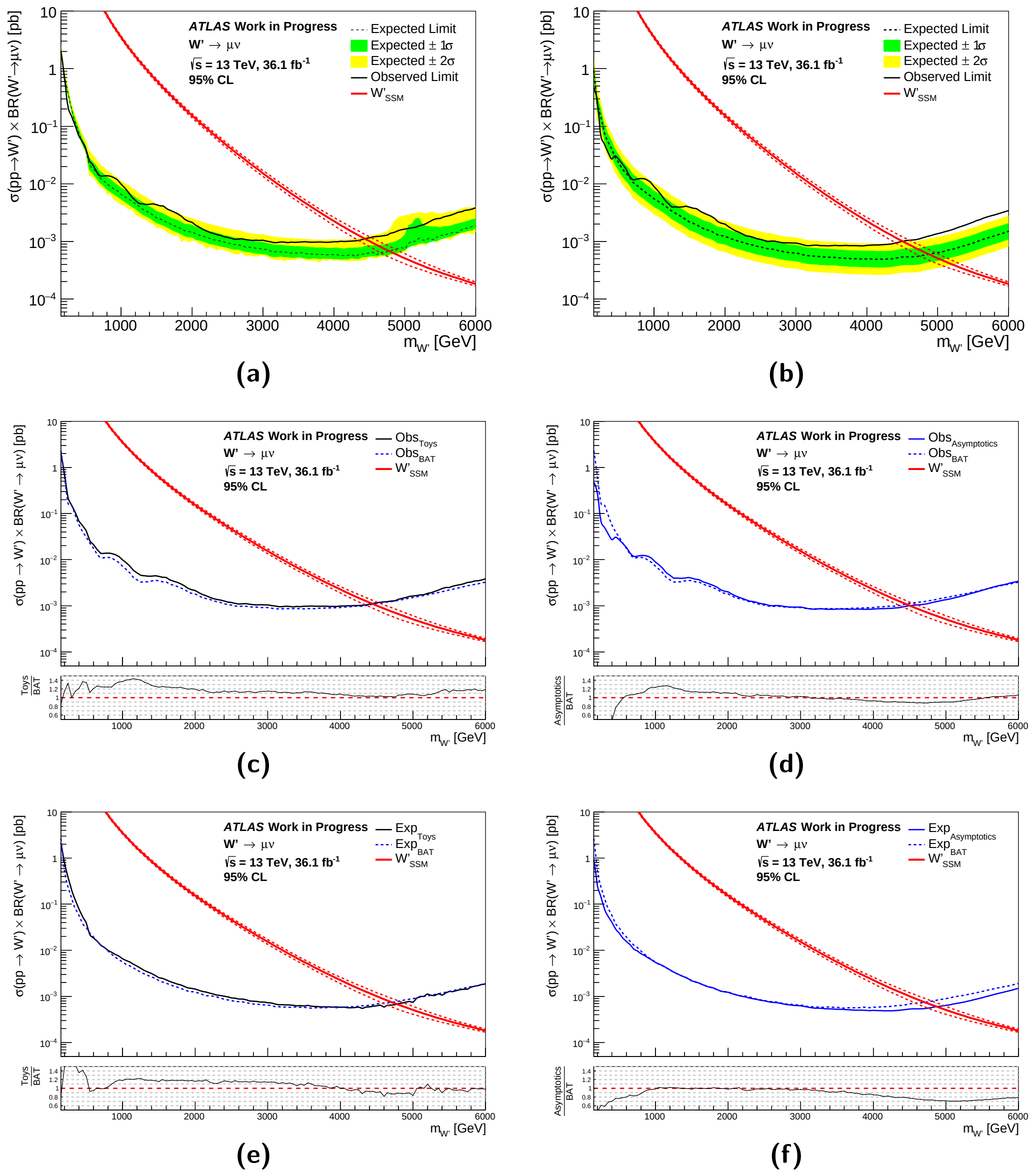

FIGURE 12.1: Limits for the $W' \rightarrow \mu\nu$ channel with all systematic uncertainties accounted for. Figure (a) shows the limit obtained using 5000 pseudo-experiments while figure (b) shows the limit obtained using asymptotic calculations. Figures (c) and (d) show direct comparisons of the observed limits obtained using BAT to the results from pseudo-experiments and asymptotic calculations, respectively. Similarly, figures (e) and (f) show comparisons of the expected limtis obtained using BAT to the results from the pseudo-experiments and asymptotic calculations, respectively.

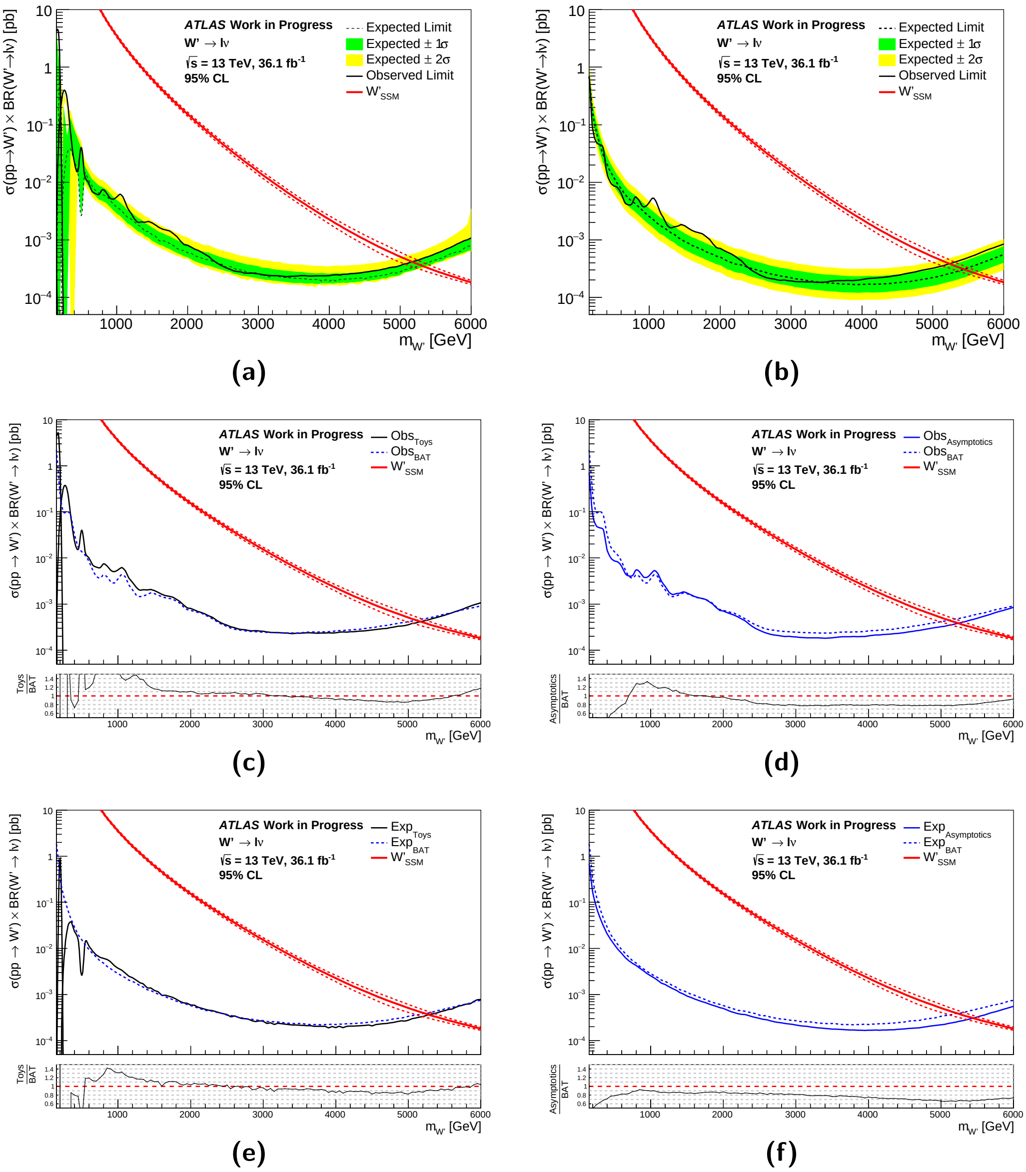

FIGURE 12.2: Limits for the $W' \to \ell\nu$ channel with all systematic uncertainties accounted for. Figure (a) shows the limit obtained using 10000 pseudo-experiments while figure (b) shows the limit obtained using asymptotic calculations. Figures (c) and (d) show direct comparisons of the observed limits obtained using BAT to the results from pseudo-experiments and asymptotic calculations, respectively. Similarly, figures (e) and (f) show comparisons of the expected limtis obtained using BAT to the results from the pseudo-experiments and asymptotic calculations, respectively.

12.2.2 Z' Results

Figures 12.3, 12.4 and 12.5 show the limits calculated for the $Z' \to ee$, $Z' \to \mu\mu$ and combined $Z' \to \ell\ell$ channels, respectively. All systematic uncertainties are taken into account and results obtained using both pseudo-experiments and asymptotic calculations are shown, including comparisons to results obtained using BAT. Theory curves corresponding to the SSM as well as an E_6 GUT model (as outlined in section 3.2 and [92]) are overlaid to indicate the lower mass exclusion limits. For the electron channel there is a clear feature at high mass for the asymptotic calculations, with the observed limit lying outside of the expected uncertainty bands which show a steep upwards inflection. The effect also propagates to the combined $Z' \to \ell\ell$ result, manifesting in a less extreme feature. This has since been attributed to the treatment of systematic uncertainties (see section 13.3), with studies presented in appendix H. Specifically, in the case of the $Z' \to ee$ channel, the uncertainty on the multijet background reaches 1000% at 6 TeV and can therefore lead to a negative number of events. Figure H.1 shows the frequentist results and comparisons to Bayesian results when no systematic uncertainties are taken into account, where no such feature is visible. For the original Bayesian analysis this uncertainty was symmetrised and described with a log-normal prior. A temporary measure of constraining this uncertainty to -10% to 500% for masses above 4 TeV negates the effect that this has on final limits. Figure H.2 shows the limits obtained using asymptotic calculations after this solution is implemented. The problem arises from the use of Gaussian priors for the systematic uncertainties in the frequentist framework. In future iterations of this analysis, this may be addressed through the use of more appropriate priors in a similar manner to the log-normal approach used in the Bayesian analysis. In the main body of this thesis, due to time constraints and desire to show consistent results for the two frequentist approaches used, results shown do not include a fix for this systematic shift. As detailed in section H.1 of the appendix, this systematic has a negligible effect for the combination due to the truncation of the mass spectrum which is applied to the samples (see section 13.2).

Aside from this high mass problem for the electron channel, as well as some disagreements at low mass due to the lack of treatment of MC statistical errors (though these are less pronounced than in the W' case), the agreement between the frequentist and Bayesian tools is generally good. As with W', the asymptotic calculations clearly prove insufficient at higher masses due to steeply falling statistics.

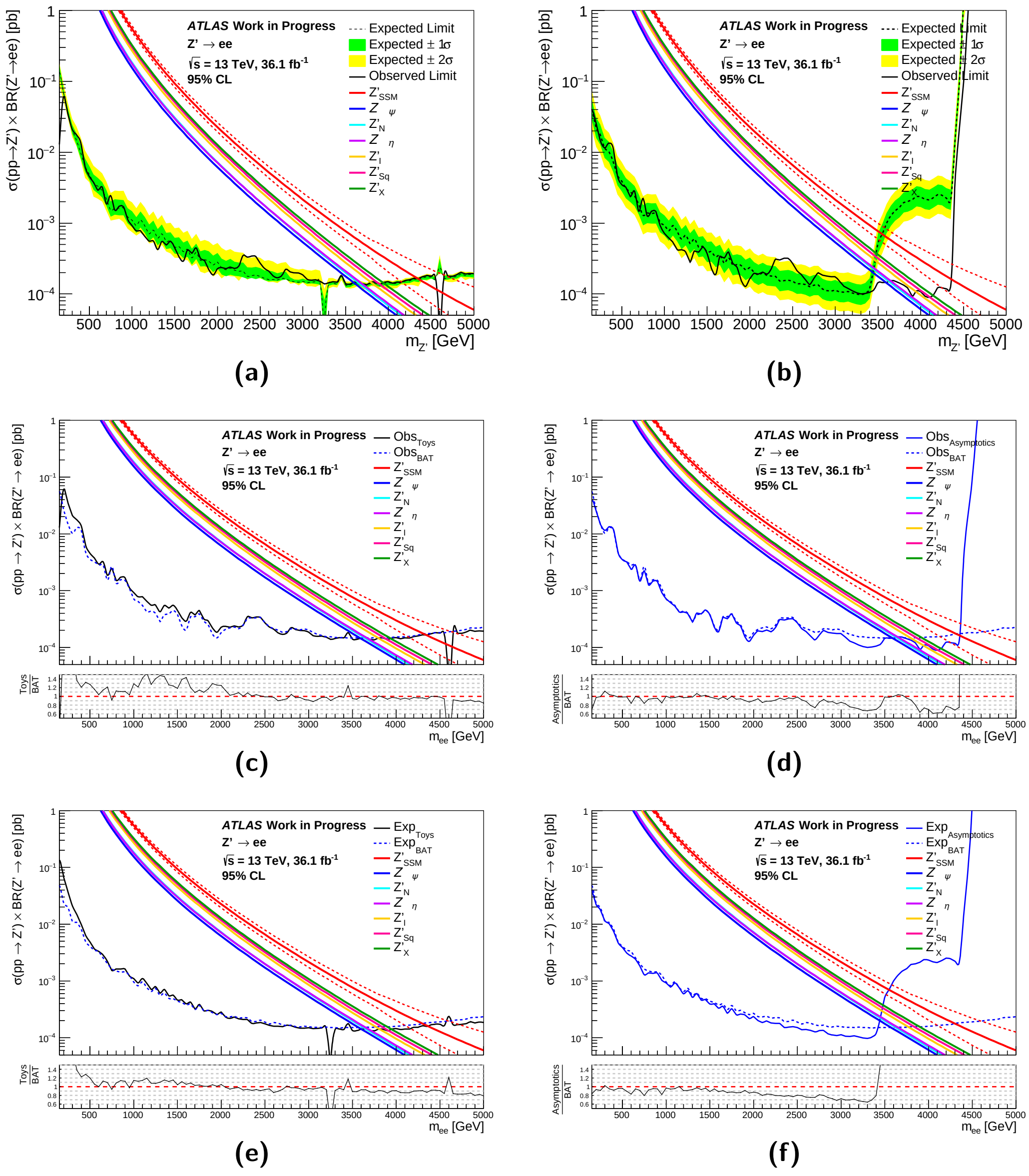

FIGURE 12.3: Limits for the $Z' \to ee$ channel with all systematic uncertainties accounted for. Theory curves corresponding to the SSM as well as the 6 excitations of the E_6 GUT model are overlaid. Figure (a) shows the limit obtained using 5000 pseudo-experiments while figure (b) shows the limit obtained using asymptotic calculations. Figures (c) and (d) show direct comparisons of the observed limits obtained using BAT to the results from pseudo-experiments and asymptotic calculations, respectively. Similarly, figures (e) and (f) show comparisons of the expected limtis obtained using BAT to the results from the pseudo-experiments and asymptotic calculations, respectively.

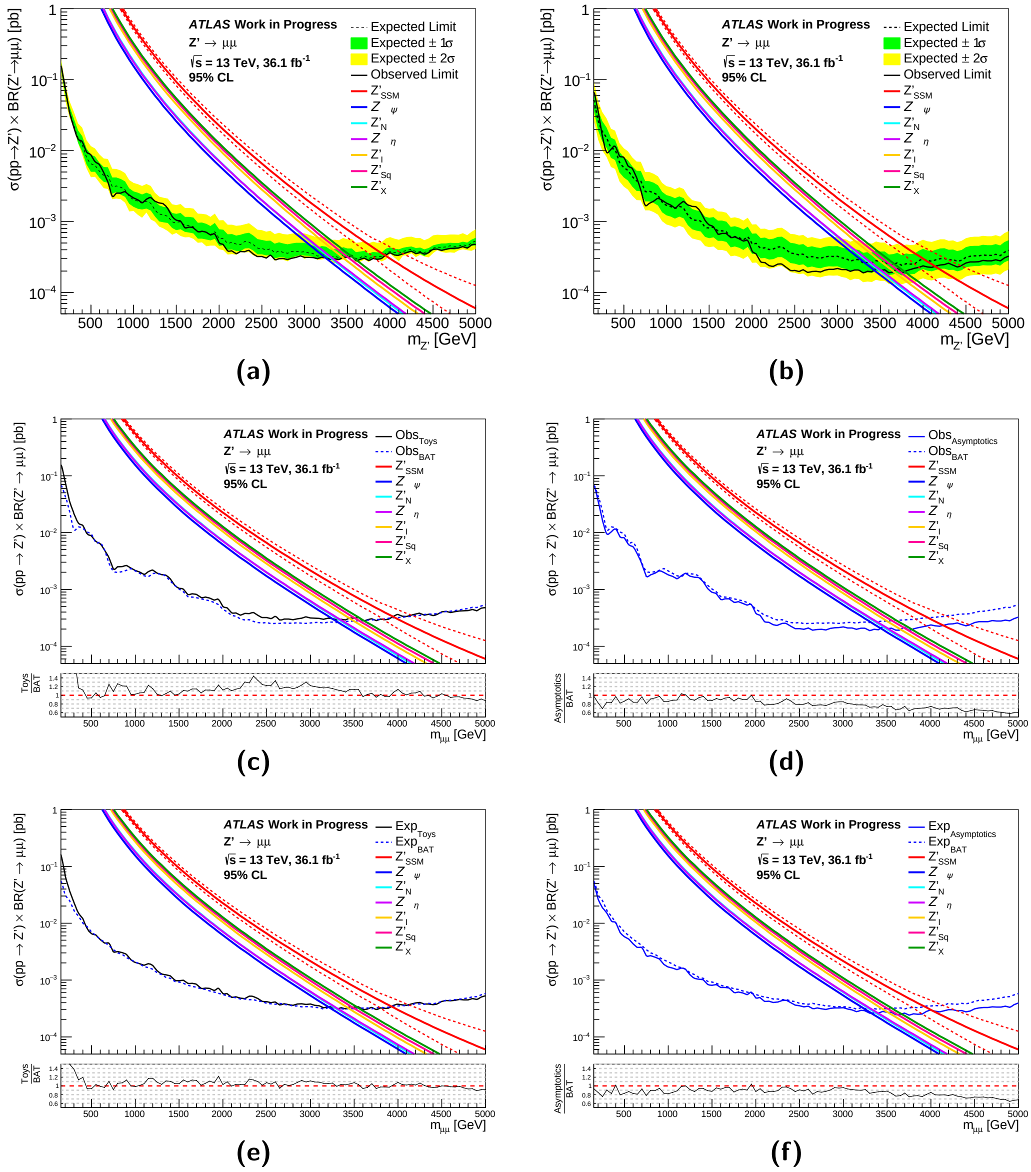

FIGURE 12.4: Limits for the $Z' \to \mu\mu$ channel with all systematic uncertainties accounted for. Theory curves corresponding to the SSM as well as the 6 excitations of the E_6 GUT model are overlaid. Figure (a) shows the limit obtained using 5000 pseudo-experiments while figure (b) shows the limit obtained using asymptotic calculations. Figures (c) and (d) show direct comparisons of the observed limits obtained using BAT to the results from pseudo-experiments and asymptotic calculations, respectively. Similarly, figures (e) and (f) show comparisons of the expected limtis obtained using BAT to the results from the pseudo-experiments and asymptotic calculations, respectively.

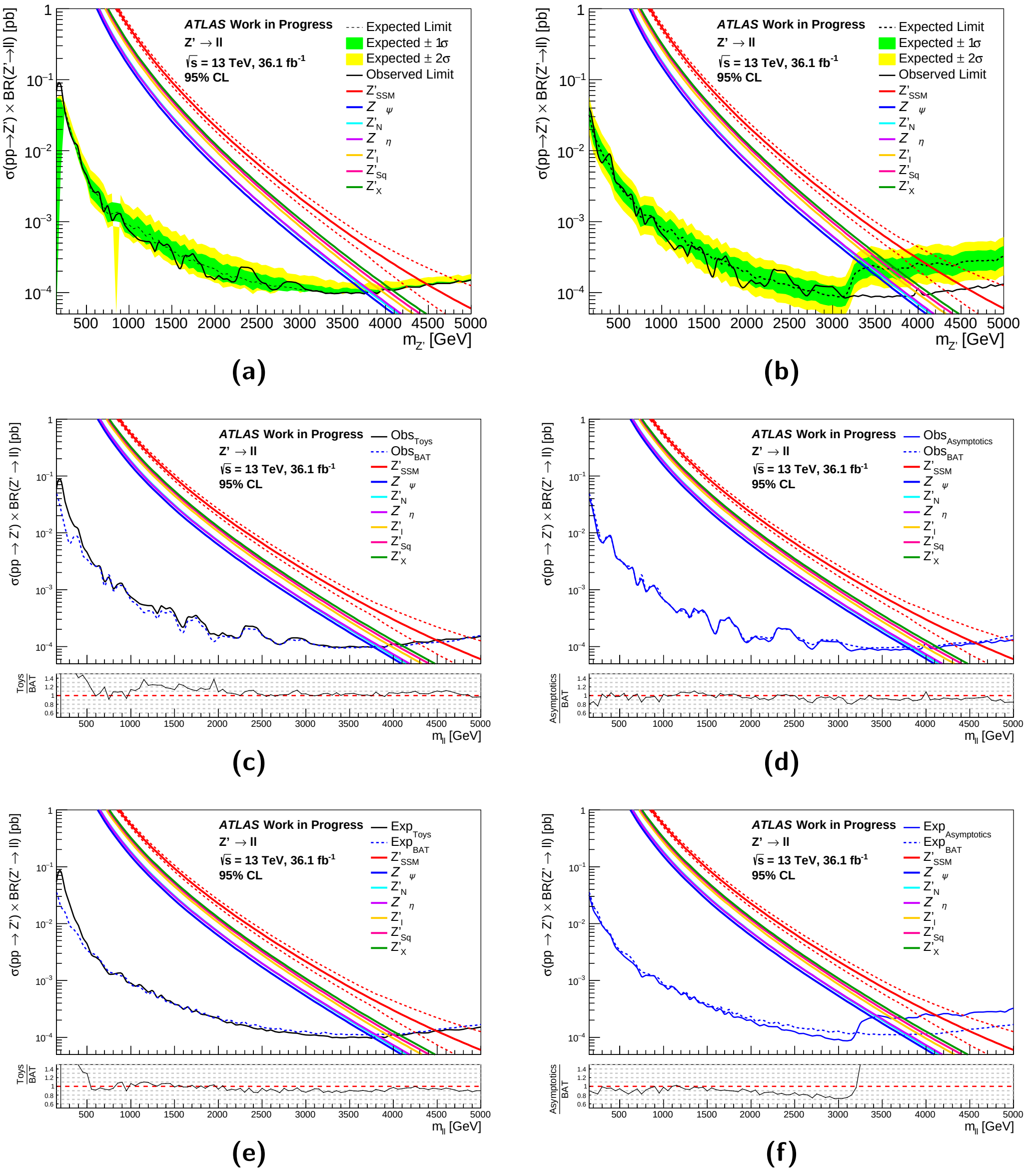

FIGURE 12.5: Limits for the $Z' \to \ell\ell$ channel with all systematic uncertainties accounted for. Theory curves corresponding to the SSM as well as the 6 excitations of the E_6 GUT model are overlaid. Figure (a) shows the limit obtained using 10000 pseudo-experiments while figure (b) shows the limit obtained using asymptotic calculations. Figures (c) and (d) show direct comparisons of the observed limits obtained using BAT to the results from pseudo-experiments and asymptotic calculations, respectively. Similarly, figures (e) and (f) show comparisons of the expected limtis obtained using BAT to the results from the pseudo-experiments and asymptotic calculations, respectively.

12.2.3 Conclusions

Generally, there is a good agreement betwen the results obtained from frequentist and Bayesian frameworks. In the low mass region, there is some disagreement which can be attributed to a different treatment of Monte Carlo statistical errors (see appendix D). These errors will be accounted for in future iterations of this analysis, though they are shown to only impact the limits at lower masses far below the exclusion point. There are also some issues arising from large systematic uncertainties, namely the shift due to the multijet background estimate for the $Z' \rightarrow ee$ channel, which have been understood (appendix H). In the high mass region, the use of pseudo-experiments is clearly more suited to the analysis, since statistics steeply fall, rendering the naive assumption of Gaussian PDFs made in the asymptotic approximation inappropriate. Based on these results, the frequentist framework is considered to be in sufficient enough agreement with the established Bayesian tools to be used for the combination of results. Though pseudo-experiments are used for final results put forward for the full combination, asymptotic calculations are still heavily used for illustrative purposes and cross-checks throughout this thesis since they are much less computationally expensive and still provide a generally good description of the limits up to ~ 2 TeV.

Chapter 13

Method & Results

In this chapter, the methods used to calculate limits in the context of the HVT model are presented. Limits obtained using the frequentist framework are presented for the combined $W' \rightarrow \ell\nu$ and $Z' \rightarrow \ell\ell$ channels ($V' \rightarrow \ell\ell/\ell\nu$). For the individual channels, the discriminating variables are the transverse mass and dileption invariant mass, respectively, and the signal selections are the same as those outlined in [231] and [206]. New signal samples produced in the context of the HVT model are used, while data and background templates are taken directly from these analyses without need for modification, aside from truncation cuts which are applied to all samples (see section 13.2). These combined results, as well as results for the full combination of dilepton and diboson channels, are also presented in this chapter as 2D limits in the g_l, g_q and g_f, g_H coupling planes.

13.1 HVT Signal Samples

Signal templates used for limit setting are produced for HVT A (with $g_V = 1$ as defined in section 3.2) with $g_l = g_q = -0.554$ and $g_H = -0.56$. These signals are produced by reweighting LO Pythia 8 Drell-Yan samples using the same reweighting tool as the analysis described in section 9.2 with updates to include the HVT model with non-zero Higgs couplings (as the reweighting tool originally only used $g_H = 0$). A resonance width of $\frac{\Gamma}{M_{\text{pole}}} \sim 2.5\%$ is chosen in order to be consistent with HVT A and the diboson searches. Studies on the variation of the resonance width on the couplings can be found in [234]. The width is found to have a weak dependence on g_H, with a difference in width between the HVT A coupling point and the point ($g_l = g_q = -0.556, g_H = 0$) of only 0.25%. Inputs with a width of 8% (at $g_l = g_q = 1$) were also tested in order to check the impact of resonance width on the obtained limit. This study, found in appendix E, proved the effect to be negligible. The resultant reweighted distributions were validated against dedicated Pythia 8 and MadGraph5 [235] samples for various W' and Z' pole masses, with results shown in [236] and [237].

13.2 Addressing Interference Effects With Template Truncation

Though the individual W' and Z' analyses neglect interference effects by opting for a narrow width approximation, such effects are non-negligible for this combination in the context of HVT A for both vector bosons. This means that signals shapes may be heavily distorted, with new peak and trough structures replacing the familiar clean peaks at the resonance mass. A full implementation of interference would tradiationally involve providing signal templates both with and without full interference effects for the statistical analysis, using $\sqrt{\mu}$ as the PoI (as explained and exemplified in [238]). However, due to the time consuming nature of this method, as well as some uncertainty as to how results obtained thus could be combined with diboson results which do not include such effects, the approach outlined in [239] was adopted. This method involves applying a cuts to signal and background templates at truth and reconstruction level* on the dilepton/transverse mass:

$$|m_{\ell\ell} - M_{\text{pole}}| < \Delta M \quad \text{and} \quad |m_T - M_{\text{pole}}| < \Delta M \tag{13.1}$$

*In future iterations of this analysis, cuts will only be applied at truth level in order to preserve the side bands about the resonance peak which make the signal and backgorund more distinguishable from each other.

for Z' and W', respectively. Two acceptable *narrow* (*wide*) cut values for the $\ell\ell$ and $\ell\nu$ channels were established:

$$\frac{\Delta M}{\sqrt{M_{\text{pole}}}} = \frac{5(8)}{\sqrt{\text{GeV}}} \quad \text{and} \quad \frac{\Delta M}{\sqrt{M_{\text{pole}}}} = \frac{10(15)}{\sqrt{\text{GeV}}}, \tag{13.2}$$

respectively. The wide window constrains the effect of interference on the signal cross section to be less than 30% while the narrow window constrains to below 15%. The narrow window is preferred, since it leads to a more consevative final result due to the lower signal acceptance in addition to reducing sensitivity to residual interference effects.

Figure 13.1 shows the comparison of the expected limits obtained when performing the statistical analysis using inputs with the wide mass cut window applied both with and without interference effects. The differences observed are larger for lower resonance masses and generally do not exceed 25%. Comparions of results in the case of no interference obtained using wide cuts, narrow cuts and no cuts can be found in appendix F.

13.3 Treatment of Systematic Uncertainties

In order to conduct the full statistical analysis with the combined channels, any correlations or decorellations between the systematic uncertainties which affect each channel must be accounted for. Tables 13.1 and 13.2 list the theoretical and experimental systematic uncertaintes respectively for each channel, as well as the correlations between them. The systematic sources relevant to the $W' \to e\nu$ channel are detailed in chapter 10, while further details of those applied to other channels can be found in the relevant papers ([231] and [206]).

For both W' and Z', all 7 of the eigenvectors† detailed in section 8.1 are used to describe the PDF variation uncertainty in order to be consistent between channels. In the case of Z', systematic uncertainties corresponding to PDF scale variation, α_S uncertainty

†As previously stated, only eigenvectors 1–4 are applied for the W' analysis.

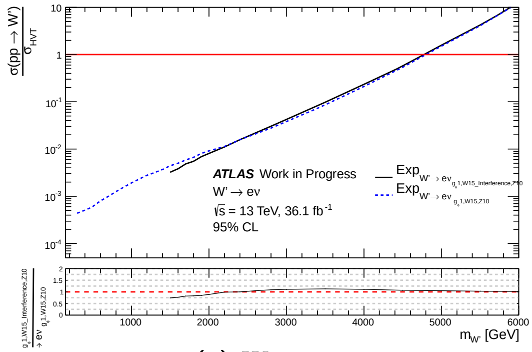

(a) $W \to e\nu$

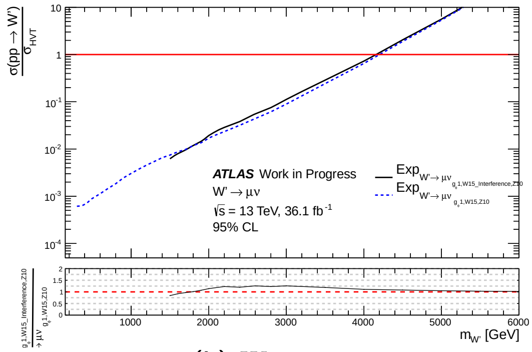

(b) $W \to \mu\nu$

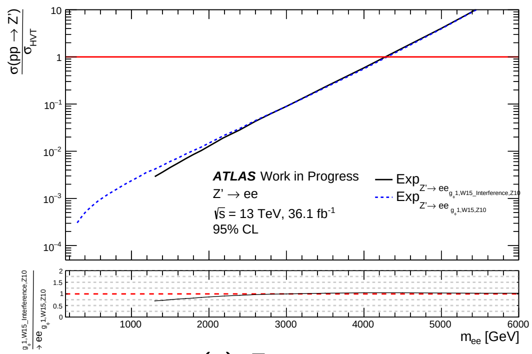

(c) $Z \to ee$

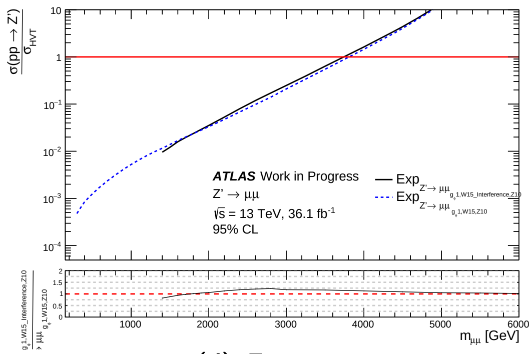

(d) $Z \to \mu\mu$

FIGURE 13.1: Expected limits for each of the W' and Z' channels with the wide mass window cut applied to inputs with (black) and without (blue) interference effects included, obtained using asymptotic calulations. In the case of the limits with interference effects, there are no results for the lower masses as the interference causes bins to have negative entries.

and corrections for photon-induced processes are also applied and are correlated between the electron and muon channels. The uncertainties due to PDF choice and EW corrections are applied to and correlated between all channels. In the case of the latter, scenarios of various correlations[‡] were tested, due to the strong model dependence of EW corrections. None of these alternative configurations proved to have a significant effect on the resultant combined limits [240].

The systematic uncertainty due to beam energy uncertainty was found to be negligible and is therefore not applied for the combination. Details of this uncertainty can be found in appendix C. The pile-up reweighting systematic is only applied to the W' channels, since it is negligible for Z' and therefore not historically applied in this search.

[‡]Uncorrelated between the charged and neutral currents and fully uncorrelated between all bosons and channels.

Uncertainties due to MC statistics are not implemented for the results shown in this thesis, but are found to have a negligible effect on the HVT limits obtained with truncated templates (see section D.1 of the appendix). In future iterations of this analysis, such uncertainties will be applied to the W' channels using the method outlined in section 11.3.

Uncertainties due to the multijet background estimate and extrapolations (used for W')/cross section uncertainties (used for Z') for top and diboson backgrounds are assumed to be uncorrelated between all channels.

	Boson				
Systematic	ee	$\mu\mu$	$e\nu$	$\mu\nu$	Correlated?
PDF Var	BG	BG	BG	BG	Yes
PDF Choice	BG	BG	BG	BG	Yes
PDF Scale	BG	BG	-	-	Yes
α_S	BG	BG	-	-	Yes
Photon-Induced	BG	BG	-	-	Yes
EW Corrections	BG	BG	BG	BG	Yes
$t\bar{t}$ extrap.	BG	BG	BG	BG	No
Diboson extrap	-	-	BG	BG	No
Beam Energy	Sig+BG	Sig+BG	-	-	Dropped
Luminosity	Sig+BG	Sig+BG	Sig+BG	Sig+BG	Yes
Pile-up Reweighting	-	-	Sig+BG	Sig+BG	Yes

TABLE 13.1: Summary of the theoretical uncertainties applied to the signal ("Sig") and backgrounds ("BG") in the W' and Z' analyses, with those correlated between the channels indicated.

13.4 Limit Setting

Limits are set for the HVT inputs for $W' \to \ell\nu$, $Z' \to \ell\ell$ and the combined $V' \to \ell\ell/\ell\nu$. As opposed to presenting results as limits on the signal cross section times BR, they are shown as the ratio of signal cross section to the HVT theory cross section $\frac{\sigma(pp \to V')}{\sigma_{HVT}}$ for model A. This is done to avoid adding model assumptions to the result and to facilitate comparison of the results of individual and combined channels, with a single HVT A theory curve at $\frac{\sigma(pp \to V')}{\sigma_{HVT}} = 1$ indicating the exclusion point (mass points lower than the point at which the limits reach this value are excluded). Limits are created in this way by scaling the inputs to the relevant W' and Z' cross sections. Figure 13.2 shows

	Boson				
Systematic	ee	$\mu\mu$	$e\nu$	$\mu\nu$	Correlated?
Electron ID Eff	Sig+BG	N/A	-	N/A	-
Electron Isolation Eff	Sig+BG	N/A	-	N/A	-
Electron Energy Scale	Sig+BG	N/A	Sig+BG	N/A	Yes
Electron Energy Resolution	Sig	-	-	-	-
Muon Reconstruction Eff	N/A	Sig+BG	N/A	Sig+BG	Yes
Muon Isolation Eff	N/A	Sig+BG	N/A	-	-
Muon Trigger Eff	N/A	-	N/A	Sig+BG	-
Muon ID Eff	N/A	Sig+BG	N/A	Sig+BG	Yes
Muon MS Eff	N/A	Sig+BG	N/A	Sig+BG	Yes
Fake Estimate	BG	-	BG	BG	No
JER	N/A	N/A	Sig+BG	Sig+BG	Yes
MET Para	N/A	N/A	Sig+BG	Sig+BG	Yes
MET Perp	N/A	N/A	Sig+BG	Sig+BG	Yes
MET Scale	N/A	N/A	Sig+BG	Sig+BG	Yes

TABLE 13.2: Summary of the experimental uncertainties applied to the signal ("Sig") and backgrounds ("BG") in the W' and Z' analyses, with those correlated between the channels indeicated.

the final HVT limits from this combination using both asymptotic calculations and 10000 pseudo-experiments. Here, figure 13.2(a) shows the results for $W' \to \ell\nu$, $Z' \to \ell\ell$ and combined $V' \to \ell\ell/\ell\nu$, illustrating the strengthening of the limit achieved through combining channels. The lower mass limits obtained using the pseudo-experiments are presented in table 13.3. For the combined result, the lower mass limit for this model is found to be 4.67 TeV.

	$\mathbf{m_{V'}}$ lower limit [TeV]	
Decay	**Expected**	**Observed**
$Z' \to \ell\ell_{Asym}$	4.39	4.45
$W' \to \ell\nu_{Asym}$	4.63	4.49
$V' \to \ell\nu/\ell\ell_{Asym}$	4.93	4.83
$V' \to \ell\nu/\ell\ell_{Toys}$	4.68	4.67

TABLE 13.3: Lower mass limits (with systematic uncertainties) for the individual W' and Z' using asymptotic calculations and for the combined $V' \to \ell\ell/\ell\nu$ using both asymptotic calculations and 10000 pseudo-experiments.

During the limit setting process, nuisance parameters are shifted in order to find the best fit for the MC to match the distribution of the observed data. The size of these shifts relative to the magnitude of the input systematics in question are referred to as *pulls*. The pulls of the nuisance parameters in the full W'/Z' combination for the

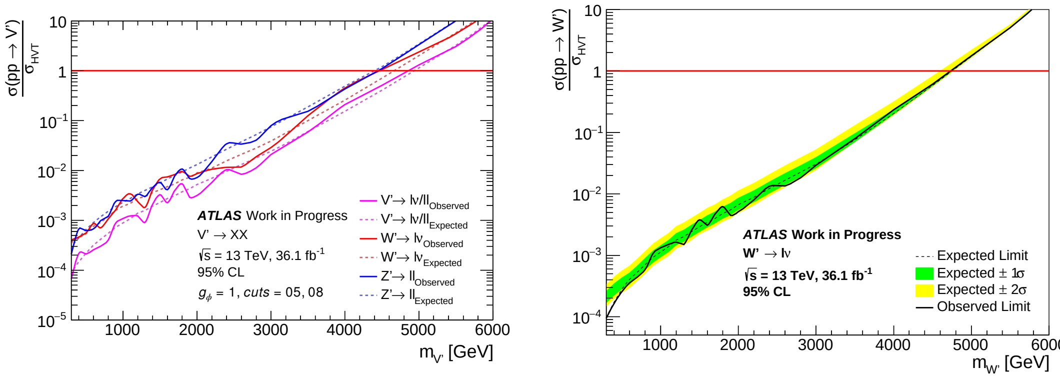

(a) **(b)**

FIGURE 13.2: Frequentist limits on $\frac{\sigma(pp \to V')}{\sigma_{HVT}}$ for V' resonances in the context of HVT A. Figure (a) shows the limits for $W' \to \ell\nu$, $Z' \to \ell\ell$ and the combined $V' \to \ell\ell/\ell\nu$ produced using asymptotic calculations. Figure (b) shows the limit for $V' \to \ell\ell/\ell\nu$ produced using 10000 pseudo-experiments. In each of these plots, the red line at $\frac{\sigma(pp \to V')}{\sigma_{HVT}} = 1$ indicates the HVT A theory line - masses below the point where the limits cross this line are excluded in this model.

1 TeV mass point are shown in figure 13.3. Only the most strongly pulled nuisance parameters are shown for readability. None of the nuisance parameters are significantly pulled, with all shifts lying within the 1σ bands, indicating a good fit.

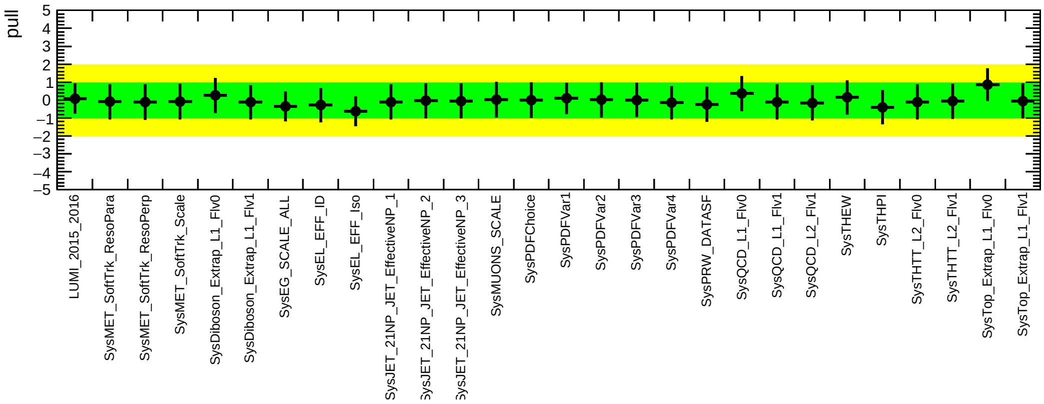

FIGURE 13.3: Pulls of the nuisance parameters for the 1 TeV mass point of the HVT decaying to the $\ell\ell$ and $\ell\nu$ combination. Though some nuisance parameters seem to be repeated, these correspond to the decorrelated systematic variations, with the different variations of characters such as “L1_Flv0” in their names indicating the channels which they are applied to.

13.5 Full Combination With Diboson Channels

In addition to combining the leptonic (dilepton) channels outlined here, results may also be combined with those from searches for VV and VH diboson resonances. While the dilepton channels provide constraints on the coupling strength to quarks and leptons, the diboson channels constrain the coupling strength to quarks and bosons, making these complementary channels for combination. Results from analyses of the following VV final states are added to the combination[§]:

- $WW/WZ \to \ell\nu qq$ [241].
- $WZ \to \ell\nu\ell\ell$ [242].
- $WW/WZ \to qqqq$ [243, 244].
- $WZ \to \ell\nu\ell\ell$ [245].
- $WW \to \ell\nu\ell\nu$ [246].

And results from analyses of the following VH final states are also added:

- $ZH \to \ell\ell bb$ [247]
- $WH \to \ell\nu bb$ [247]
- $ZH \to \nu\nu bb$ [247]
- $WH/ZH \to qqbb$ [248, 249]

Additional details of the diboson results which were prepared for this combination can be found in [250].

13.6 Limits in the Coupling Plane

The limits obtained from the dilepton and diboson analyses in the context of HVT A are used to draw contours in two coupling spaces. The first probes the g_H, g_f plane, assuming common fermionic couplings ($g_f = g_q = g_l$), while the second probes the g_q, g_l plane with fixed $g_H = -0.56$ (the value at HVT model A). While the one-dimensional limits are calculated with fixed ratios of W' to Z' (predicted by the benchmark models

[§]There are no ZZ channels listed here due to the fact that such decays do not occur in the HVT model.

for each mass), for the two-dimensional constraints the signal yields must be paramaterized in such a way that the relative contributions of each signal may vary independently. This is achieved using a set of coupling parameters **g**, modifying the test statistic in equation 11.17 to give:

$$\widetilde{q_\mu}' = -2\ln\frac{\mathcal{L}(\boldsymbol{g},\hat{\hat{\boldsymbol{\theta}}}_{\boldsymbol{g}})}{\mathcal{L}(\hat{\boldsymbol{g}},\hat{\boldsymbol{\theta}}_{\boldsymbol{g}})} \tag{13.3}$$

Limit contours are determined at 95% CL by evaluating this test statistic by normalising signal rates to the cross section times branching predicted by the HVT model for different values of $\boldsymbol{g}$. The parametrisation of the couplings assumes that all signal production proceeds via quark-antiquark annihilation (proportional to g_q^2) and that the final state decays are proportional to g_H^2 and g_l^2 for the diboson and dilepton channels, respectively.

The constraints on the two considered coupling planes are shown in figure 13.4. In all of these plots, the parameters for HVT model A and model B are shown. The range of considered couplings is generally limited to $g_f < 0.8$ in order to remain in the region where resonances are relatively narrow $\left(\frac{\Gamma}{M_{pole}} < 5\%\right)$ - this ensures that widths which would exceed the resolution of discriminating variables used for the searches (and break the narrow width approximation) are not considered. This range is indicated on the plots by a shaded grey area.

Figures 13.4(a) and 13.4(b) show the constraints on the g_f vs. g_H and g_l vs. g_q planes, respectively for the combined dilepton channels. In the former, the lack of sensitivity to the Higgs coupling for these channels is evident, while in the latter there is a strong sensitivty to both quark and lepton couplings. It may be noted that these constraints become stronger as the Higgs coupling approaches zero, since in this scenario alternative decay modes are restricted. The constraints for these channels are weakened as g_f, g_q and g_l tend to zero, since the production of the resonances are subsequently decreased.

Figures 13.4(c) and 13.4(d) show the constraints on the g_f vs. g_H and g_l vs. g_q planes, respectively for the combined $VV + VH$ channels. In the former, the constraints are strongest at large values of both couplings and become insensitive as the couplings approach zero, symptomatic of the fact that the resonance couplings to VV and VH

tend to zero as the coupling to Higgs reaches zero, as well as the fact that the production of the resonance tends to zero with decreasing g_f. In the latter, the lack of sensitivity to the coupling to leptons is evident. There is no contour drawn at 5 TeV in this plane, since there is no sensitivity for this mass point in the tested range of couplings.

Figure 13.4(e) shows the g_f vs. g_H constraints for the full combination of $VV + VH$+Dilepton channels. The visible feature around $g_H = 0$ may be attributed to the observed best-fit minimum shifting away from $g_H,\ g_f = 0$, which creates a less stringent constraint in the direction of ther shift and a stronger constraint in the opposite direction. Figure 13.4(f) shows the g_q and g_l constraints for the full combination.

Figure 13.5 shows the same constraints with indirect limits from EW precision measurements, such as LEP results [233], overlaid. It should be noted that these indirect limits already exclude the $\frac{\Gamma}{M_{pole}} > 5\%$ region. These comparisons clearly show that the stringent limits obtained from the combination outlined here improve the indirect limits in almost all areas of the considered planes, aside from the region of low g_q and high g_l. This is a consequence of the asymmetry of the limits from EW precision measreuments, which is related to interference effects.

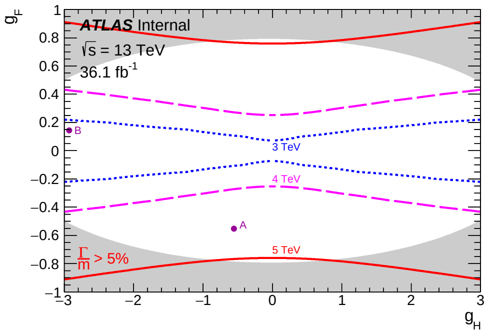

(a) Dilepton: g_f vs. g_H

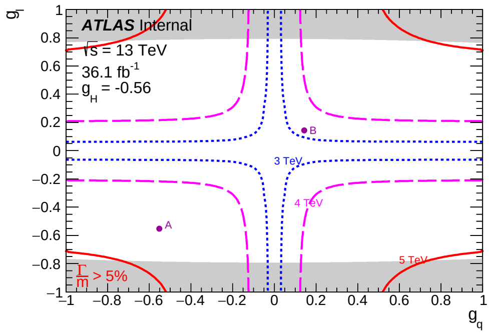

(b) Dilepton: g_l vs. g_q

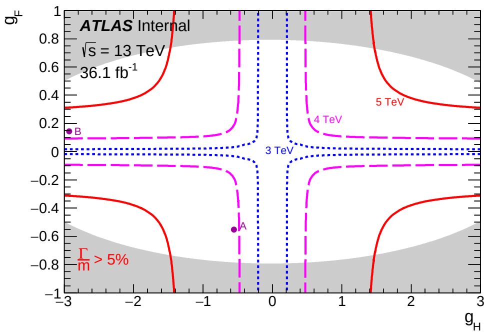

(c) VV+VH: g_f vs. g_H

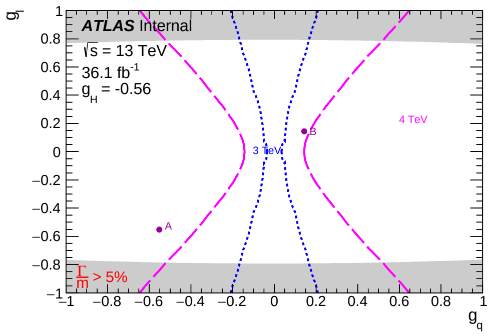

(d) VV+VH: g_l vs. g_q

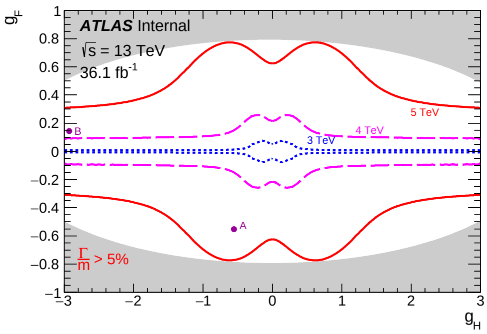

(e) VV+VH+Dilepton: g_f vs. g_H

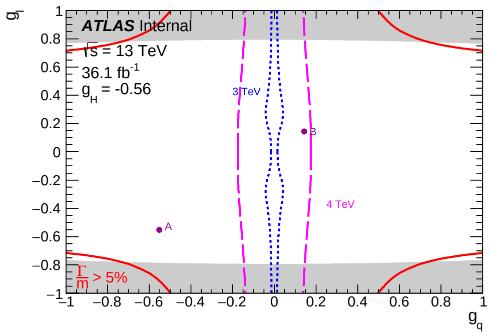

(f) VV+VH+Dilepton: g_l vs. g_q

FIGURE 13.4: The observed 95% CL exclusion contours in HVT parameter space for the dilepton, $VV + VH$ and dilepton+$VV + VH$ combinations. The various curves represent pole mass limits ranging from 3 (blue) to 5 (red) TeV. The areas outside these curves are excluded. The grey shaded area corresponds to the range where $\frac{\Gamma}{M_{pole}} > 5\%$. The parameters for HVT models A and B are also shown. Figures (a) and (b) show $g_l = g_q = g_f$ vs. g_H and g_l vs. g_q for fixed $g_H = -0.56$ (HVT A) for the dilepton combination. Figures (c) and (d) show $g_l = g_q = g_f$ vs. g_H and g_l vs. g_q for fixed $g_H = -0.56$ (HVT A) for the $VV + VH$ combination. Figures (e) and (f) show $g_l = g_q = g_f$ vs. g_H and g_l vs. g_q for fixed $g_H = -0.56$ (HVT A) for the full combination of VV, VH and dilepton results.

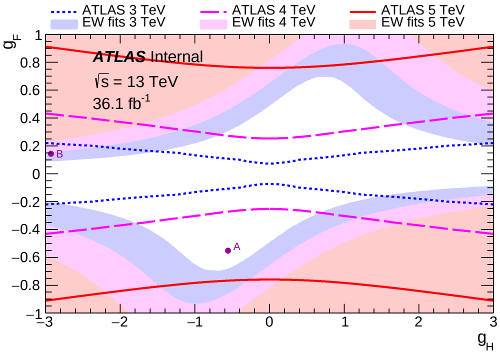

(a) Dilepton: g_f vs. g_H

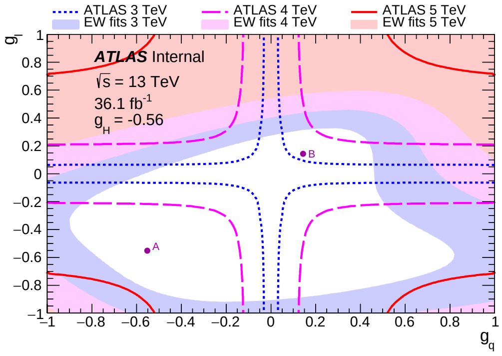

(b) Dilepton: g_l vs. g_q

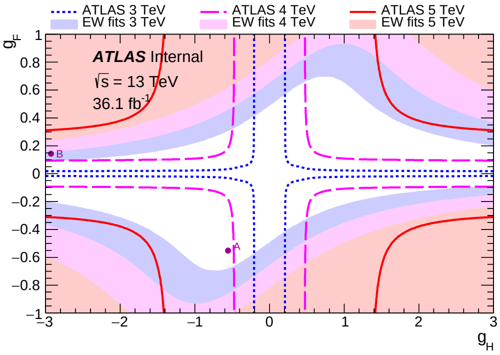

(c) VV+VH: g_f vs. g_H

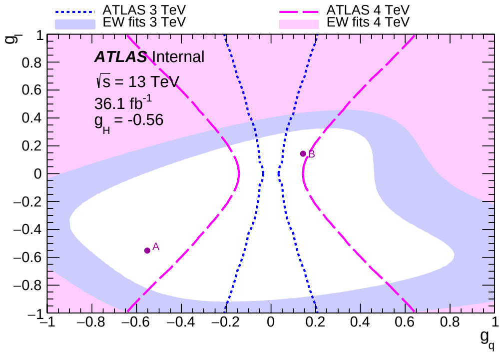

(d) VV+VH: g_l vs. g_q

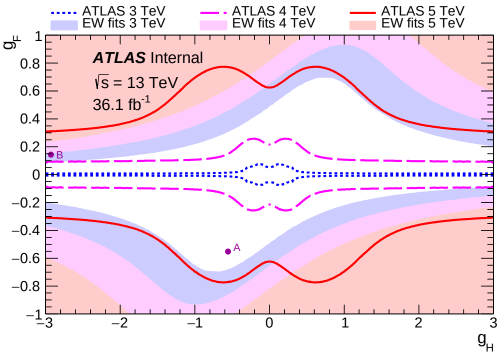

(e) VV+VH+Dilepton: g_f vs. g_H

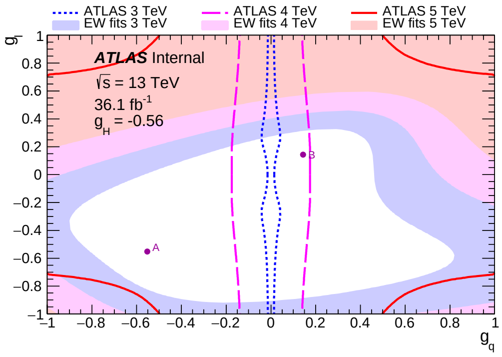

(f) VV+VH+Dilepton: g_l vs. g_q

FIGURE 13.5: The observed 95% CL exclusion contours in HVT parameter space for the dilepton, $VV + VH$ and dilepton+$VV + VH$ combinations. The various curves represent pole mass limits ranging from 3 (blue) to 5 (red) TeV. The areas outside these curves are excluded. The coloured shaded areas correspond to the indirect limits from EW precision measurements [233] for various resonance masses indicated by the different colours (following the same colour scheme as the ATLAS limits). Figures (a) and (b) show $g_l = g_q = g_f$ vs. g_H and g_l vs. g_q for fixed $g_H = -0.56$ (HVT A) for the dilepton combination. Figures (c) and (d) show $g_l = g_q = g_f$ vs. g_H and g_l vs. g_q for fixed $g_H = -0.56$ (HVT A) for the $VV + VH$ combination. Figures (e) and (f) show $g_l = g_q = g_f$ vs. g_H and g_l vs. g_q for fixed $g_H = -0.56$ (HVT A) for the full combination of VV, VH and dilepton results.

Part VI

Conclusions & Auxiliary Material

Chapter 14

Conclusions

This thesis describes a search for new heavy charged W' bosons in the context of the SSM using 36.1 fb^{-1} of $\sqrt{s} = 13$ TeV data taken with the ATLAS detector during the 2015+2016 runs of the LHC. The analysis uses the transverse mass as the search variable, searching in the region 150 GeV $<$ m$_T$ $<$ 6000 GeV. Expected W' signal shapes are produced using a single MC sample which is reweighted to a range desired pole masses spanning the entire considered mass spectrum. The SM expectation for the spectrum is described using Monte Carlo samples for various sources of irreducible background, the most dominant being charged current Drell-Yan production. A state-of-the-art description of these Drell-Yan processes is obtained by scaling the MC prediction to the best current theory knowledge. The background arising from fake electrons is estimated using data-driven methods.

In this thesis, novel techniques for quantifying the uncertainties associated with higher-order correction factors for the neutral and charged current Drell-Yan process are outlined. This includes the uncertainty envelopes for all modern available PDF sets, which become larger and more distinct from each other at the TeV scale where they are no longer informed by measurements. A new frequentist statistical framework is also introduced, with results compared to those obtained using the Bayesian tools historically used by the W' and Z' analyses.

Upon comparing the data to the expected background, no significant excess above the SM is observed. Using the new statistical tools, a 95% CL frequentist lower mass limit is set on the W'_{SSM} at 5.12 TeV. The work presented here is included in the 2017 paper [231] published by the ATLAS collaboration.

A reinterpretation of these results, as well as those obtained from the similar Z' analysis [206], in the context of a Heavy Vector Triplet model is also presented. Combined $V' \rightarrow \ell\ell/\ell\nu$ resonances with masses below 4.67 TeV are excluded at 95% CL. These 'dilepton' channels are also combined with results from searches for diboson resonances. The dilepton channels access couplings to quarks and leptons while the diboson channels probe couplings to fermions and Higgs, exposing their complimentarity. HVT limits from each of the contributing channels are used to inform the creation of contours in two coupling planes, giving a set of 2D limits for the final combination. These are compared to indirect limits obtained from EW precision measurements, proving to be more stringent over most of the tested parameter space. The work presented here is set to be included in an upcoming paper.

Appendix A

Event Yields & Average Pileup

Figure A.1 shows the average yield for each run of the 2015 and 2016 data with the average pileup $\langle\mu\rangle$ overlaid. The increase in yield for the 2016 runs is clearly mirrored by the distribution of $\langle\mu\rangle$, indicating a connection between the two.

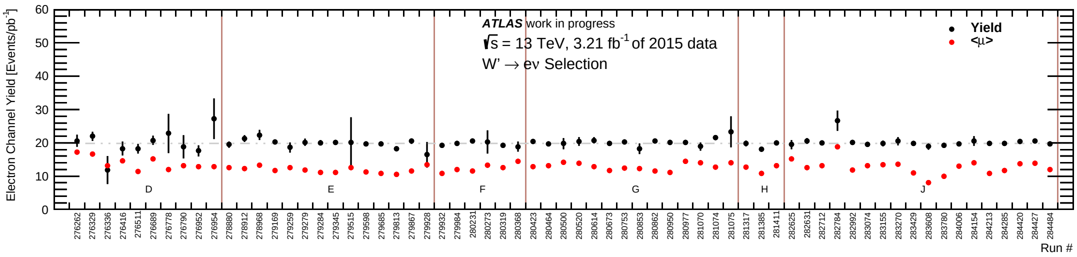

(a) 2015

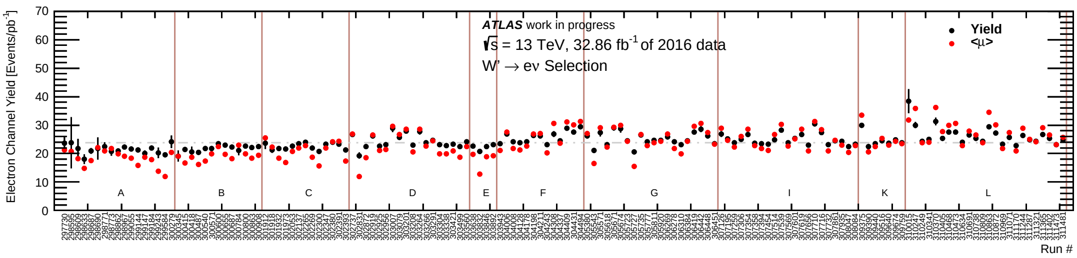

(b) 2016

FIGURE A.1: Electron channel yields for each run of (a) 2015 and (b) 2016 data with the average pile-up ($\langle\mu\rangle$) per run overlayed.

Appendix B

Systematic Uncertainties

Additional distributions illustrating the dependences of the various sources of systematic uncertainties considered for the W' analysis in electron p_{T}, electron η, electron ϕ and $E_{\mathrm{T}}^{\mathrm{miss}}$ are presented here.

Figure B.1 shows the impact of the systematic uncertainties associated with the multijet background estimate on the total background yield. The black lines in these plots are calculated as the quadratic sum of all of the individual sources of uncertainty arising from the data driven background.

Figures B.2 and B.3 show the impact of the experimental and theoretical uncertainties on the total background estimate, respectively.

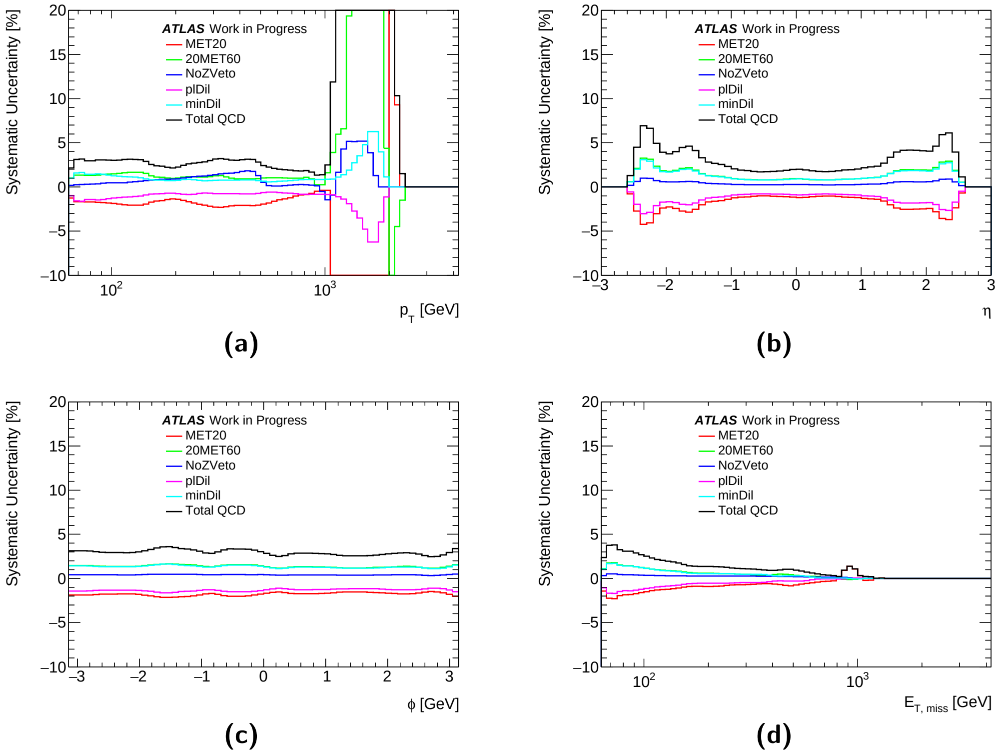

FIGURE B.1: The (a) electron p_{T}, (b) electron η, (c) electron ϕ and (d) $E_{\mathrm{T}}^{\mathrm{miss}}$ dependences of the systematic uncertainties associated with the multijet background estimate (as outlined in section 9.4.4) on the total background yield.

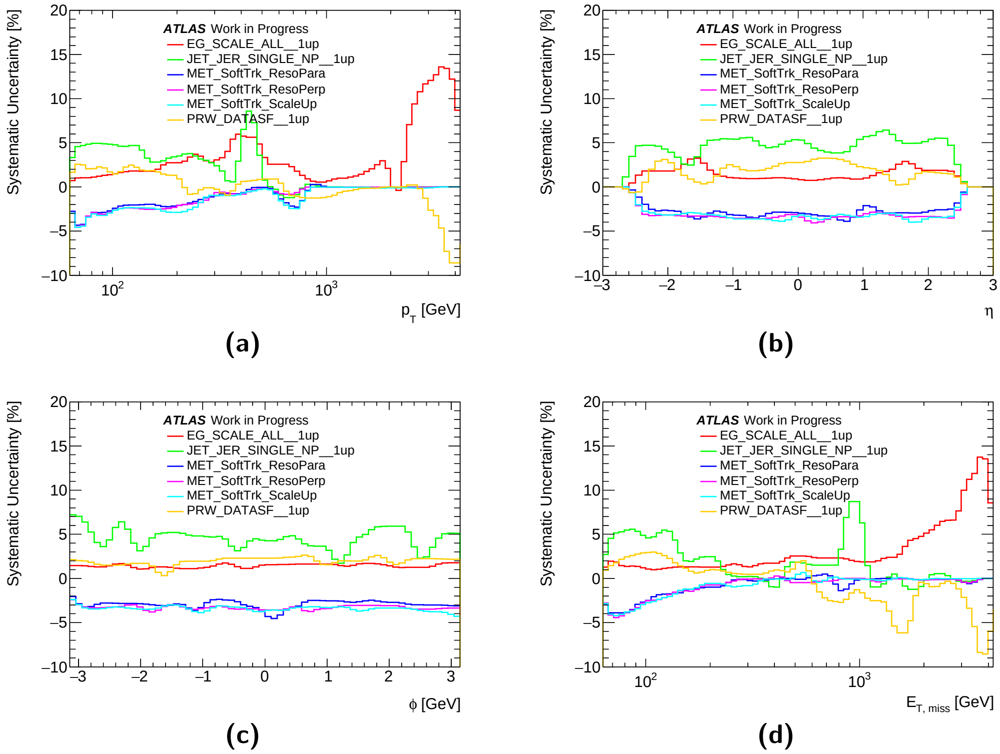

FIGURE B.2: The (a) electron p_{T}, (b) electron η, (c) electron ϕ and (d) $E_{\mathrm{T}}^{\mathrm{miss}}$ dependences of the experimental systematic uncertainties (as outlined in section 10.1) on the background yield.

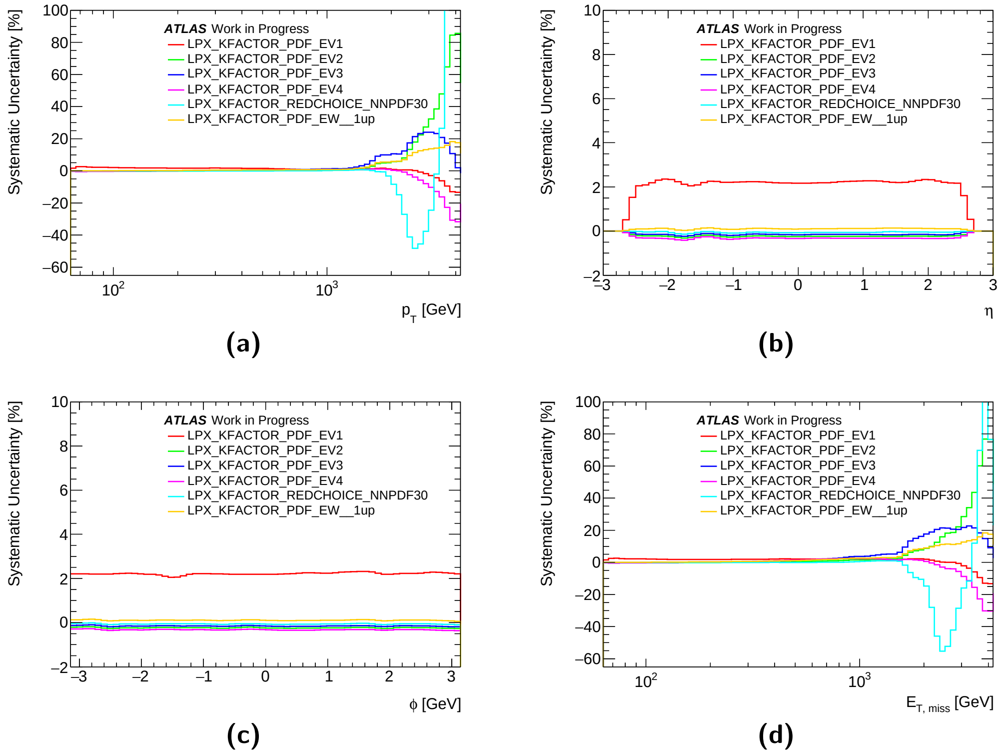

FIGURE B.3: The (a) electron p_{T}, (b) electron η, (c) electron ϕ and (d) $E_{\mathrm{T}}^{\mathrm{miss}}$ dependences of the theoretical systematic uncertainties (as outlined in section 10.2) on the background yield.

Appendix C

Beam Uncertainty

Uncertainty in the measurement of beam energy is calculated using the nominal beam energy of 13 TeV with up and down variations of $\pm$ 0.65% for both proton beams. The decision to use a variation of 0.65% was based on the assumption that the fractional uncertainty for 13 TeV is the same as that for 8 TeV [251] in the absence of more recent studies [252]. Beam uncertainties are calculated using VRAP 0.9 with CT14 NNLO as the nominal PDF set with a dependence on the invariant generated mass (before QED FSR). Uncertainty in the beam energy is symmetric and is determined as:

$$\Delta = \pm 100 \times \frac{down - up}{down + up}. \tag{C.1}$$

As of March 2017, the fractional beam uncertainty has been reduced to 0.1% [253]. This is small enoughto be considered negligible for the W' and Z' searches. This improvement can be attributed to the introduction of proton-lead runs from 2013, since the revolution frequency (RF) measurements of protons and lead which are used for calculating this uncertainty can be simultaneously measured. This development eradicates the need to correct for time-dependent effects, such as ground movements, which the LHC is subject to.

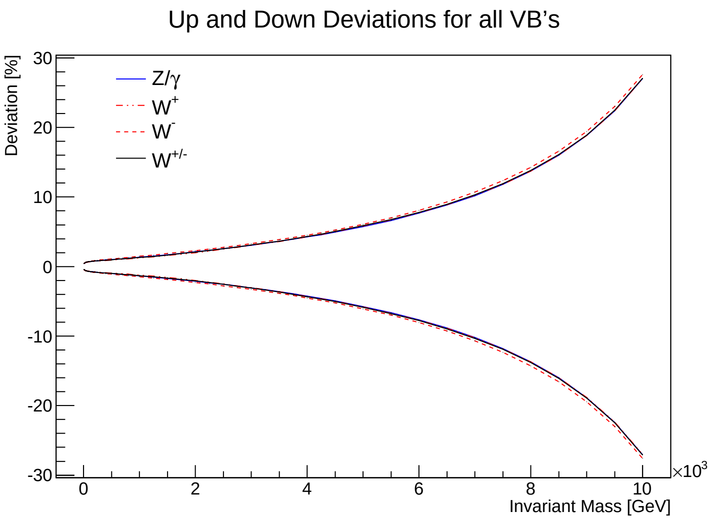

FIGURE C.1: up and down beam uncertainties for W^+, W^-, Z and combined W.

Appendix D

Inclusion of Monte Carlo Statistical Errors

The effect of implementing the MC statistical error treatment outlined in section 11.3 is presented here. Figure D.1 shows the ratios of the observed and expected limits obtained using asymptotic calculations (frequentist) and BAT for the SSM W' search. The agreement at lower mass is visible when compared with figures 11.3(d) and 11.3(f), which did not include treatment of the MC statistical uncertainty for the frequentist result.

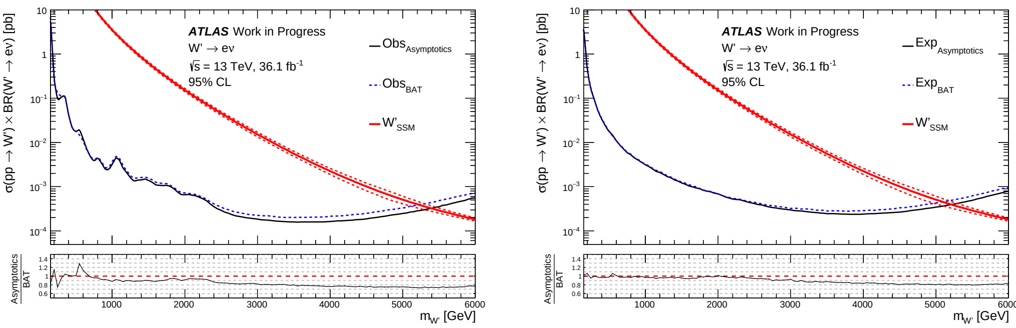

(a) Observed $W' \to e\nu$ **(b)** Expected $W' \to e\nu$

FIGURE D.1: Comparison of (a) observed and (b) expected limits obtained using asymptotic frequentist calculations (black, solid) and BAT (blue, dotted) where MC statistical errors are fully implemented.

D.1 Impact on HVT Limits

Figure D.2 shows the combined HVT W'/Z' observed and expected limits. The blue dotted lines give the limits obtained without treatment of the MC statistical error, while the black lines give the limits obtained with the treatment outlined in section 11.3 implemented. In each of the plots, a lower panel gives the ratio of these limits. The inclusion of MC statistical errors clearly makes a large difference at lower masses $\leqslant$ 2 TeV. At higher masses (most importantly, near the exclusion limits) there is not much of an effect. This uncertainty treatment will be implemented in future iterations of this analysis, though, due to time constraints, the studies presented in this thesis do not include it.

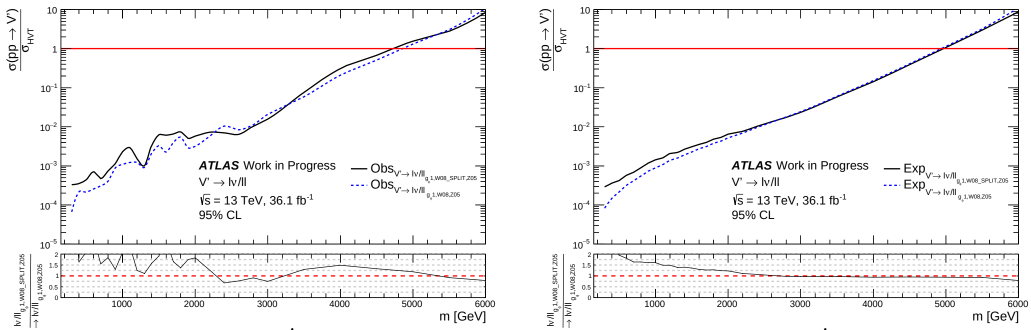

(a) Observed $V' \to \ell\ell/\ell\nu$ **(b)** Expected $V' \to \ell\ell/\ell\nu$

FIGURE D.2: Comparison of the combined HVT W'/Z' (a) observed and (b) expected limits obtained both with (black, solid) and without (blue, dotted) the inclusion of MC statistical errors.

Appendix E

Resonance Width Studies for the W'/Z' Combination

The impact of using wide and narrow resonances on the HVT W'/Z' limits is presented here. For narrow resonances, a width of 2.5% is used with coupling parameters $g_l = g_q = -0.554$, $g_H = -0.55969$, while for wide resonances a width of 8% is used with coupling parameters $g_l = g_q = 1$, $g_H = -0.55969$. The different template cuts described in section 13.2 are also tested. Figure E.1 shows the observed (solid) and expected (dotted) limits obtained using wide (red) and narrow (blue) resonances for both of the different template cuts. The wide cuts lead to more conservative limits for lower masses $\leqslant 2$ TeV, though only minor differences are observed at higher masses.

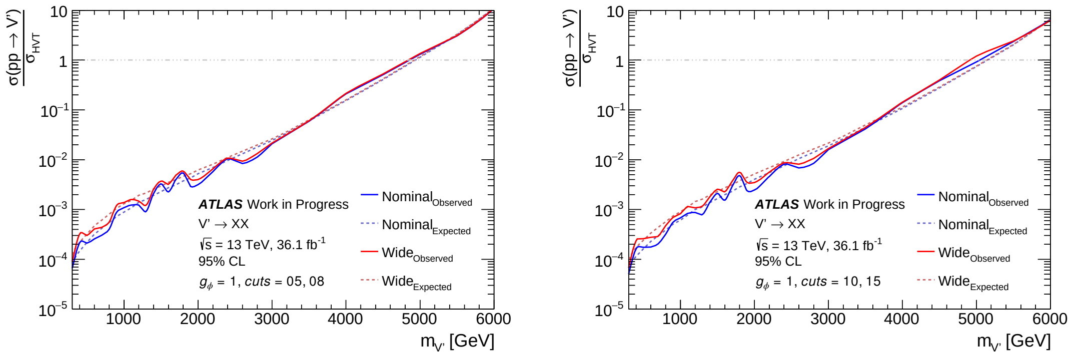

(a) Z cut = 5, W cut = 8 **(b)** Z cut = 10, W cut = 15

FIGURE E.1: The observed (dotted) and expected (solid) limits obtained using resonance widths of 2.5% (blue) and 8% (red) obtained using (a) narrow and (b) wide template truncation cuts.

Appendix F

Study of Wide and Narrow Mass Window Cuts for Signal Templates

The impact of using the wide or narrow signal template cuts outlined in section 13.2 is presented here. Figure F.1(a) shows the observed (solid line) and expected (dotted line) HVT W'/Z' limits obtained using wide (red) and narrow (blue) template cuts. The different cuts lead to a 25-50% difference in the observed limits, with the narrow cuts giving more conservative limits.

Table F.1 gives the lower mass exclusion limits for the W'/Z' combination obtained using wide and narrow cuts. The expected limits for the narrow cuts are 0.2 TeV lower than those obtained using wide cuts.

	$\mathbf{m_{W'}}$ **lower limit [TeV]**	
Cut Level	**Expected**	**Observed**
Narrow	4.90	4.80
Wide	5.10	5.03

Table F.1: Lower mass limits obtained through frequentist (both with pseudo-experiments and asymptotic formulae) and Bayesian frameworks.

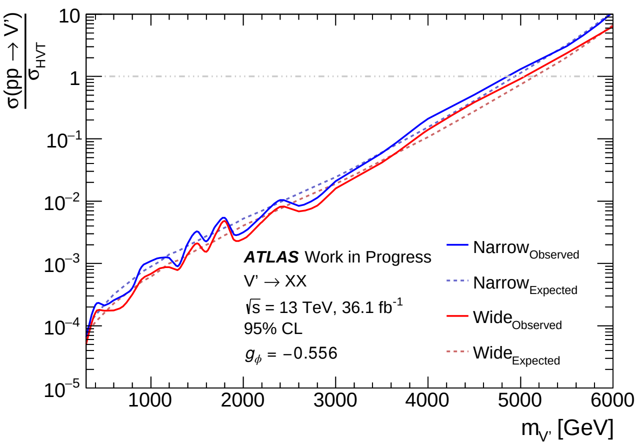

(a) Observed $V' \to \ell\ell/\ell\nu$

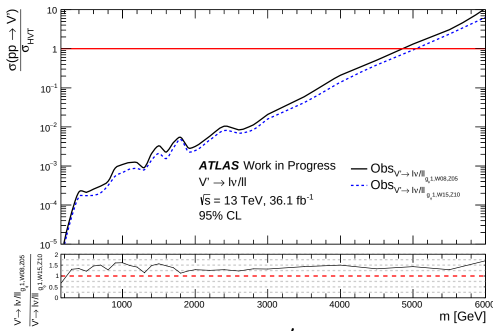

(b) Observed $V' \to \ell\ell/\ell\nu$

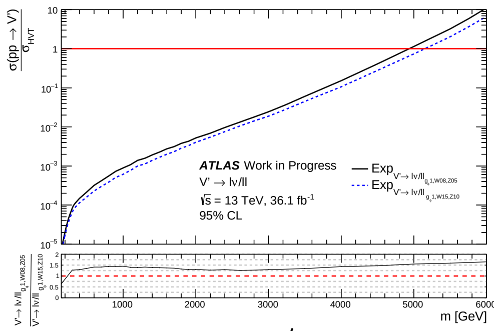

(c) Expected $V' \to \ell\ell/\ell\nu$

FIGURE F.1: Comparisons of combined HVT W'/Z' limits obtained using both wide and narrow template truncation cuts. Figure (a) shows the observed (solid) and expected (dotted) limits for both the wide (red) and narrow (blue) cuts overlaid . Figures (a) and (b) show the observed and expected limits, respectively, with the limits obtained using the narrow cuts shown in black (solid) and the limits obtained using wide cuts shown in blue (dotted). In the latter two plots, the lower panels give the ratio of the limits obtained using the different cuts.

Appendix G

Choice of Scale Factor Range

The method for choosing μ values (scale factors) for setting frequentist limits using pseudo-experiments is outlined here. The ranges are informed by fits performed on the observed limits obtained using asymptotic calculations. A number of μ values is then chosen for each mass point, with a lower (sfLo) and upper (sfHi) guess based on this observed limit. There are then 30 different scale factor values tested, separated by: $\mathrm{sfStep} = \frac{\mathrm{sfHi}-\mathrm{sfLo}}{30}$

For SSM limits the scale factor ranges are:
for m $\geqslant$ 500 GeV :
$\mathrm{sfLo} = 5e^{-11}$
$\mathrm{sfHi} = 5e^{-8}$
for m $\leqslant$ 5000 :
$\mathrm{sfLo} = \mathrm{Exp}_{\mathrm{asymptotics}} - \left(3 \times \frac{\mathrm{Exp}_{\mathrm{asymptotics}}}{5}\right)$
$\mathrm{sfHi} = \mathrm{Exp}_{\mathrm{asymptotics}} + \left(31 \times \frac{\mathrm{Exp}_{\mathrm{asymptotics}}}{5}\right)$
for m $>$ 5000: $\mathrm{sfLo} = \mathrm{Exp}_{\mathrm{asymptotics}} - \left(2 \times \frac{\mathrm{Exp}_{\mathrm{asymptotics}}}{4}\right)$
$\mathrm{sfHi} = \mathrm{Exp}_{\mathrm{asymptotics}} + \left(34 \times \frac{\mathrm{Exp}_{\mathrm{asymptotics}}}{4}\right)$

For HVT limits the scale factor ranges are:
for m $\geqslant$ 500 GeV :

$$\text{sfLo} = 1e^{-3}$$

$$\text{sfHi} = 1$$

for m $\leqslant 1000$:

$$\text{sfLo} = 1e^{-4}$$

$$\text{sfHi} = 1e^{-1}$$

for m $\leqslant 5000$:

$$\text{sfLo} = \text{Exp}_{\text{asymptotics}} - \left(3 \times \frac{\text{Exp}_{\text{asymptotics}}}{5}\right)$$

$$\text{sfHi} = \text{Exp}_{\text{asymptotics}} + \left(31 \times \frac{\text{Exp}_{\text{asymptotics}}}{5}\right)$$

for m > 5000: $\text{sfLo} = \text{Exp}_{\text{asymptotics}} - \left(2 \times \frac{\text{Exp}_{\text{asymptotics}}}{4}\right)$

$$\text{sfHi} = \text{Exp}_{\text{asymptotics}} + \left(34 \times \frac{\text{Exp}_{\text{asymptotics}}}{4}\right)$$

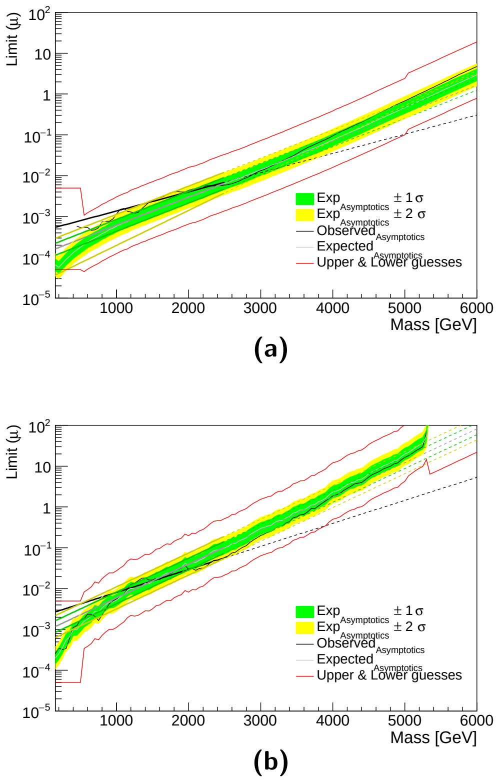

FIGURE G.1: The HVT limits for (a) $W' \to \ell\nu$ and (b) $Z' \to \ell\ell$ with lines representing the upper and lower μ ranges (shown in red) overlaid. As before, the black solid line gives the observed limit while the grey line and shaded yellow and green bands indicate the expected limit with its uncertainty. The dotted lines of the same colour indicate the extrapolated fits which are performed to these limits in order to inform the μ guesses.

Appendix H

Treatment of Multijet Systematic Uncertainties for the $Z' \to ee$ Channel

The impact of applying the fix described in section 12.2.2 for the large systematic uncertainties for the $Z' \to ee$ channel is outlined here. Figure H.1 shows the comparisons of frequentist and Bayesian limits for the $Z' \to ee$ channel without the inclusion of systematic uncertainties. Clearly, the strange features in the results obtained using asymptotic calculations with systematics included (figure 12.3) are not visible here, confirming that the problem arises through inclusion of the systematics.

Figure H.2 shows the limits obtained using asymptotic calculations after taking measures to address the large systematic shifts for the multijet background estimate. The strange features that were previously observed are no longer present.

H.1 Impact on HVT Limits

Figure H.3 shows the observed and expected W'/Z' HVT limits (with the nominal narrow template truncation cuts) obtained before (black, solid) and after (blue, dotted)

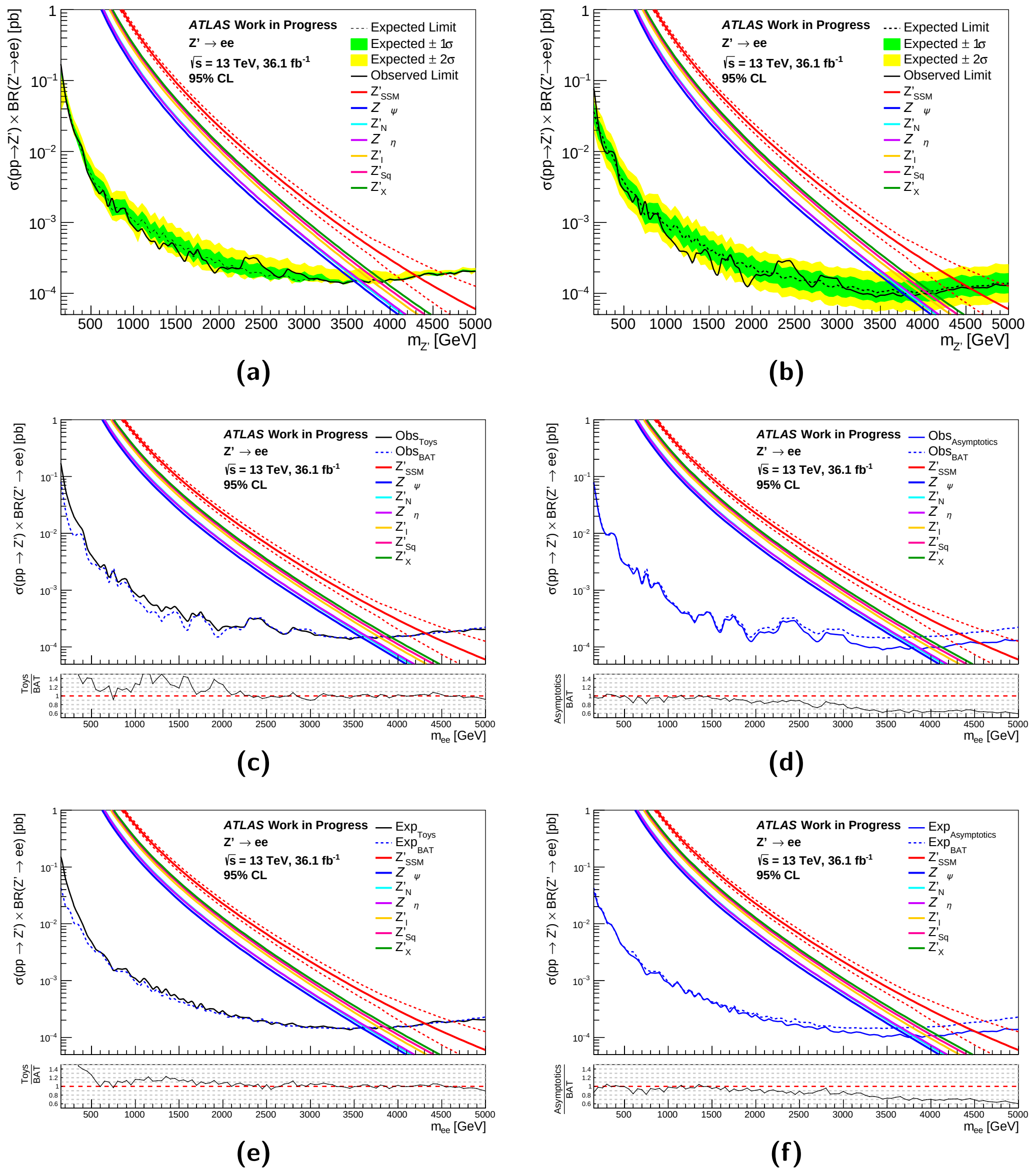

FIGURE H.1: Limits for the $Z' \to ee$ channel without the inclusion of systematic uncertainties. Figure (a) shows the limit obtained using 5000 pseudo-experiments while figure (b) shows the limit obtained using asymptotic calculations. Figures (c) and (d) show direct comparisons of the observed limits obtained using BAT to the results from pseudo-experiments and asymptotic calculations, respectively. Similarly, figures (e) and (f) show comparisons of the expected limtis obtained using BAT to the results from the pseudo-experiments and asymptotic calculations, respectively.

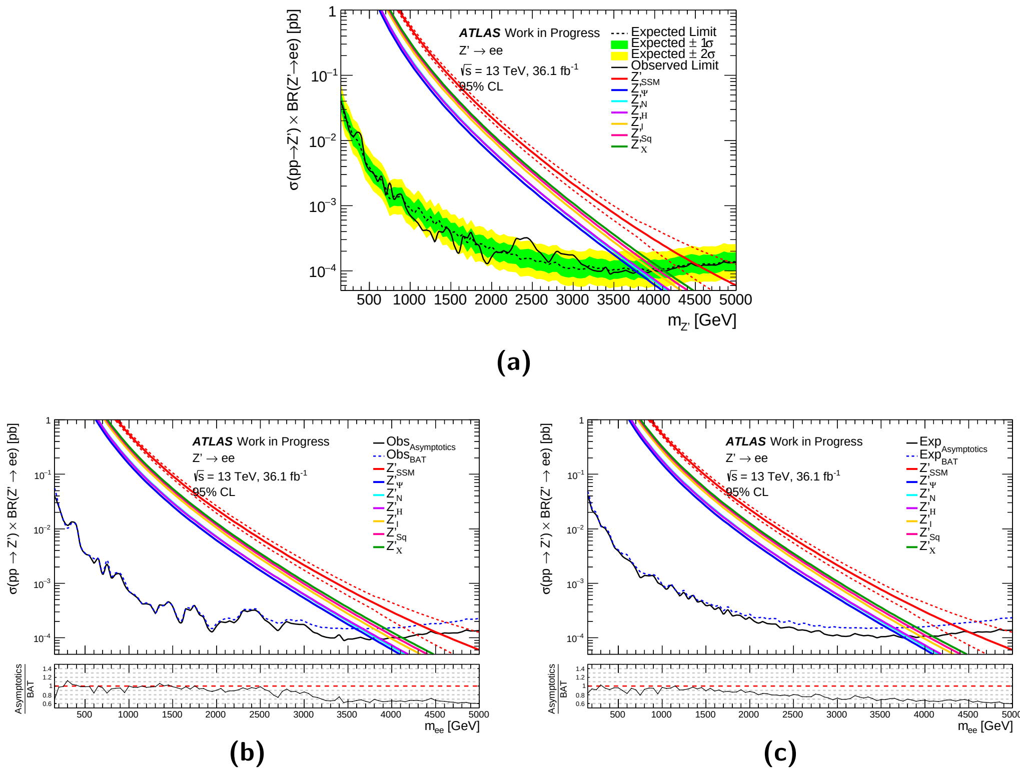

FIGURE H.2: Limits for the $Z' \to ee$ channel with all systematic uncertainties accounted for with an additional measure taken to avoid issues arising from the multijet systematics, performed using asymptotic calculations. Figure (a) shows the observed and expected limit bands. Figures **??** and (c) show the comparisons of observed and expected limits, respectively to those obtained using BAT.

applying the fix outlined in section 12.2.2 for the large multijet systematics for the $Z' \to ee$ channel. Clearly, the combined HVT limits using truncated templates are not affected by the large multijet background systematics, therefore applying the fix makes no difference to the final limits.

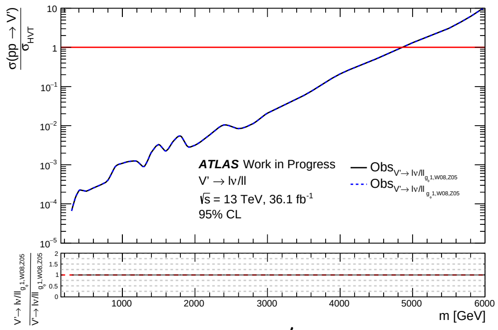

(a) Observed $V' \to \ell\ell/\ell\nu$

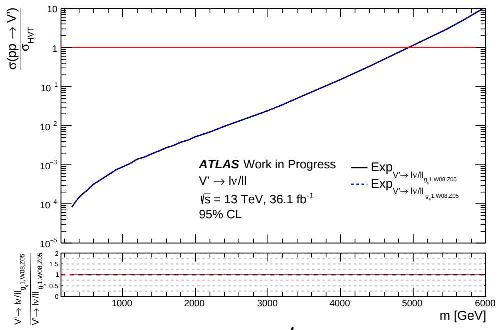

(b) Expected $V' \to \ell\ell/\ell\nu$

FIGURE H.3: The combined W'/Z' HVT limits before (black, solid) and after (blue, dotted) applying the fix for the large multijet systematics for the $Z' \to ee$ channel. In each of the plots, the lower panel shows the ratio of the limits obtained before and after the fix.

List of Figures

List of Tables

Bibliography

[1] ATLAS Collaboration, *Observation of a new particle in the search for the Standard Model Higgs boson with the ATLAS detector at the LHC*, Phys. Lett. B **716** (2012) p. 1, arXiv: `1207.7214 [hep-ex]`.

[2] CMS Collaboration, *Observation of a new boson at a mass of 125 GeV with the CMS experiment at the LHC*, Phys. Lett. B **716** (2012) p. 30, arXiv: `1207.7235 [hep-ex]`.

[3] ATLAS Collaboration, *Evidence for the spin-0 nature of the Higgs boson using ATLAS data*, Phys. Lett. B **726** (2013) p. 120, arXiv: `1307.1432 [hep-ex]`.

[4] ATLAS and CMS Collaborations, *Measurements of the Higgs boson production and decay rates and constraints on its couplings from a combined ATLAS and CMS analysis of the LHC pp collision data at* $\sqrt{s} = 7$ *and 8 TeV*, JHEP **08** (2016) p. 045, arXiv: `1606.02266 [hep-ex]`.

[5] "The LEP Electroweak Working Group", URL: `http://lepewwg.web.cern.ch/LEPEWWG/stanmod/`.

[6] Paul Langacker, *The Standard Model and Beyond*, Taylor & Francis, 2017.

[7] M Peskin and D Schroeder, *An Introduction To Quantum Field Theory*, (1995).

[8] G. Münster and G Bergner, "Gauge Theories of the Strong and Electroweak Interactions", Notes by B. Echtermeyer, Univeristy of Münster, 2011, URL: `https://www.uni-muenster.de/Physik.TP/archive/fileadmin/lehre/skripte/muenster/Gauge-theories.pdf`.

[9] Antonio Pich, "The Standard Model of Electroweak Interactions", *Proceedings, High-energy Physics. Proceedings, 18th European School (ESHEP 2010): Raseborg, Finland, June 20 - July 3, 2010*, [,1(2012)], 2012 p. 1, arXiv: `1201.0537 [hep-ph]`, URL: `http://inspirehep.net/record/1083304/files/arXiv:1201.0537.pdf`.

[10] A Banfi, C Englert, B Maitre D adn Pecjack, and P Dauncey, "Lecture Notes for the 2015 HEP School for Experimental High Energy Physics Students", 2015.

[11] Emmy Noether and M. A. Tavel, *Invariant Variation Problems*, (2005), eprint: `arXiv:physics/0503066`.

[12] C. et al. Patrignani, Chin. Phys C **40** (2016).

[13] W. Heisenberg, *Über den anschaulichen Inhalt der quantentheoretischen Kinematik und Mechanik*, Zeitschrift für Physik **43** (1927) p. 172, ISSN: 0044-3328, URL: `https://doi.org/10.1007/BF01397280`.

[14] Hideki Yukawa, *On the Interaction of Elementary Particles I*, Proc. Phys. Math. Soc. Jap. **17** (1935) p. 48, [Prog. Theor. Phys. Suppl.1,1(1935)].

[15] O. W. Greenberg, *Spin and Unitary-Spin Independence in a Paraquark Model of Baryons and Mesons*, Phys. Rev. Lett. **13** (20 1964) p. 598, URL: `https://link.aps.org/doi/10.1103/PhysRevLett.13.598`.

[16] M. Y. Han and Y. Nambu, *Three-Triplet Model with Double* SU(3) *Symmetry*, Phys. Rev. **139** (4B 1965) B1006, URL: `https://link.aps.org/doi/10.1103/PhysRev.139.B1006`.

[17] C. N. Yang and R. L. Mills, *Conservation of Isotopic Spin and Isotopic Gauge Invariance*, Phys. Rev. **96** (1954).

[18] C. S. Wu, E. Ambler, R. W. Hayward, D. D. Hoppes, and R. P. Hudson, *Experimental Test of Parity Conservation in Beta Decay*, Phys. Rev. **105** (4 1957) p. 1413, URL: `https://link.aps.org/doi/10.1103/PhysRev.105.1413`.

[19] R. P. Feynman and M. Gell-Mann, *Theory of the Fermi Interaction*, Phys. Rev. **109** (1 1958) p. 193, URL: `https://link.aps.org/doi/10.1103/PhysRev.109.193`.

[20] E. C. G. Sudarshan and R. E. Marshak, *Chirality Invariance and the Universal Fermi Interaction*, Phys. Rev. **109** (5 1958) p. 1860, URL: `https://link.aps.org/doi/10.1103/PhysRev.109.1860.2`.

[21] F. J. Hasert et al., *Observation of Neutrino Like Interactions Without Muon Or Electron in the Gargamelle Neutrino Experiment*, Phys. Lett. **46B** (1973) p. 138.

[22] G. Arnison et al., *Experimental Observation of Isolated Large Transverse Energy Electrons with Associated Missing Energy at* $\sqrt{s} = 540$ *GeV*, Phys. Lett. **122B** (1983) p. 103, [,611(1983)].

[23] G. Arnison et al., *Experimental Observation of Lepton Pairs of Invariant Mass Around 95 GeV/*c^2 *at the CERN SPS Collider*, Phys. Lett. **126B** (1983) p. 398.

[24] S. L. Glashow, *Partial Symmetries of Weak Interactions*, Nucl. Phys. **22** (1961) p. 579.

[25] Abdus Salam, *Weak and Electromagnetic Interactions*, Conf. Proc. **C680519** (1968) p. 367.

[26] Steven Weinberg, *A Model of Leptons*, Phys. Rev. Lett. **19** (1967) p. 1264.

[27] M. Gell-Mann,
The interpretation of the new particles as displaced charge multiplets,
Il Nuovo Cimento (1955-1965) **4** (1956) p. 848, ISSN: 1827-6121,
URL: `https://doi.org/10.1007/BF02748000`.

[28] Tadao Nakano and Kazuhiko Nishijima, *Charge Independence for V-particles**,
Progress of Theoretical Physics **10** (1953) p. 581, eprint: `/oup/backfile/content_public/journal/ptp/10/5/10.1143/ptp.10.581/2/10-5-581.pdf`,
URL: `+%20http://dx.doi.org/10.1143/PTP.10.581`.

[29] Makoto Kobayashi and Toshihide Maskawa,
CP-Violation in the Renormalizable Theory of Weak Interaction,
Progress of Theoretical Physics **49** (1973) p. 652, eprint: `/oup/backfile/content_public/journal/ptp/49/2/10.1143/ptp.49.652/2/49-2-652.pdf`,
URL: `+%20http://dx.doi.org/10.1143/PTP.49.652`.

[30] Ziro Maki, Masami Nakagawa, and Shoichi Sakata,
Remarks on the Unified Model of Elementary Particles,
Progress of Theoretical Physics **28** (1962) p. 870, eprint: `/oup/backfile/content_public/journal/ptp/28/5/10.1143/ptp.28.870/2/28-5-870.pdf`,
URL: `+%20http://dx.doi.org/10.1143/PTP.28.870`.

[31] F. Englert and R. Brout,
Broken Symmetry and the Mass of Gauge Vector Mesons,
Phys. Rev. Lett. **13** (9 1964) p. 321,
URL: `https://link.aps.org/doi/10.1103/PhysRevLett.13.321`.

[32] P.W. Higgs, *Broken symmetries, massless particles and gauge fields*,
Physics Letters **12** (1964) p. 132, ISSN: 0031-9163, URL:
`http://www.sciencedirect.com/science/article/pii/0031916364911369`.

[33] Peter W. Higgs, *Broken Symmetries and the Masses of Gauge Bosons*,
Phys. Rev. Lett. **13** (16 1964) p. 508,
URL: `https://link.aps.org/doi/10.1103/PhysRevLett.13.508`.

[34] Peter W. Higgs, *Spontaneous Symmetry Breakdown without Massless Bosons*,
Phys. Rev. **145** (4 1966) p. 1156,
URL: `https://link.aps.org/doi/10.1103/PhysRev.145.1156`.

[35] G. S. Guralnik, C. R. Hagen, and T. W. B. Kibble,
Global Conservation Laws and Massless Particles,
Phys. Rev. Lett. **13** (20 1964) p. 585,
URL: `https://link.aps.org/doi/10.1103/PhysRevLett.13.585`.

[36] Wim de Boer, "The Discovery of the Higgs Boson with the CMS Detector and its Implications for Supersymmetry and Cosmology",
Time and Matter 2013 (TAM2013) Venice, Italy, 2013,
arXiv: `1309.0721 [hep-ph]`, URL:
`http://inspirehep.net/record/1252561/files/arXiv:1309.0721.pdf`.

[37] CMS Collaboration, *Study of the Mass and Spin-Parity of the Higgs Boson Candidate Via Its Decays to Z Boson Pairs*,
Phys. Rev. Lett. **110** (2013) p. 081803, arXiv: `1212.6639 [hep-ex]`.

[38] Sidney D Drell and Tung-Mow Yan, *Partons and their applications at high energies*, Annals of Physics **66** (1971) p. 578, ISSN: 0003-4916, URL: `http://www.sciencedirect.com/science/article/pii/0003491671900716`.

[39] John M. Campbell, J. W. Huston, and W. J. Stirling, *Hard Interactions of Quarks and Gluons: A Primer for LHC Physics*, Rept. Prog. Phys. **70** (2007) p. 89, arXiv: `hep-ph/0611148 [hep-ph]`.

[40] S.D Drell and J.D Walecka, *Electrodynamic processes with nuclear targets*, Annals of Physics **28** (1964) p. 18, ISSN: 0003-4916, URL: `http://www.sciencedirect.com/science/article/pii/0003491664901411`.

[41] W.B. Atwood et al., *Inelastic electron scattering from hydrogen at 50 and 60*, Physics Letters B **64** (1976) p. 479, ISSN: 0370-2693, URL: `http://www.sciencedirect.com/science/article/pii/0370269376901271`.

[42] J. D. Bjorken, *Asymptotic Sum Rules at Infinite Momentum*, Phys. Rev. **179** (5 1969) p. 1547, URL: `https://link.aps.org/doi/10.1103/PhysRev.179.1547`.

[43] Richard Phillips. Feynman, *Photon-hadron interactions [by] R. P. Feynman*, English, W. A. Benjamin Reading, Mass, 1972 xvi, 282 p. ISBN: 0805325107 0805325115.

[44] Richard Phillips Feynman, *The behaviour of hadron collisions at extreme energies*, (1969).

[45] Richard P. Feynman, *Very High-Energy Collisions of Hadrons*, Phys. Rev. Lett. **23** (24 1969) p. 1415, URL: `https://link.aps.org/doi/10.1103/PhysRevLett.23.1415`.

[46] David J. Gross and Frank Wilczek, *Ultraviolet Behavior of Non-Abelian Gauge Theories*, Phys. Rev. Lett. **30** (26 1973) p. 1343, URL: `https://link.aps.org/doi/10.1103/PhysRevLett.30.1343`.

[47] H. David Politzer, *Reliable Perturbative Results for Strong Interactions?*, Phys. Rev. Lett. **30** (26 1973) p. 1346, URL: `https://link.aps.org/doi/10.1103/PhysRevLett.30.1346`.

[48] The H1 Collaboration, *Measurement and QCD analysis of neutral and charged current cross sections at HERA*, The European Physical Journal C - Particles and Fields **30** (2003) p. 1, ISSN: 1434-6052, URL: `https://doi.org/10.1140/epjc/s2003-01257-6`.

[49] The ZEUS Collaboration, *Measurement of the neutral current cross-section and F(2) structure function for deep inelastic e + p scattering at HERA*, Eur. Phys. J. **C21** (2001) p. 443, arXiv: `hep-ex/0105090 [hep-ex]`.

[50] The BCDMS Collaboration, *A High Statistics Measurement of the Deuteron Structure Functions F2 (X, Q^2) and R From Deep Inelastic Muon Scattering at High Q^2*, Phys. Lett. **B237** (1990) p. 592.

[51] The New Muon Collaboration, *Measurement of the proton and the deuteron structure functions, F2(p) and F2(d)*, Phys. Lett. **B364** (1995) p. 107, arXiv: `hep-ph/9509406 [hep-ph]`.

[52] S. Mandelstam, *Determination of the Pion-Nucleon Scattering Amplitude from Dispersion Relations and Unitarity. General Theory*, Phys. Rev. **112** (4 1958) p. 1344, URL: `https://link.aps.org/doi/10.1103/PhysRev.112.1344`.

[53] H. Schellman, "Learn hadron collider physics in 3 days", *Physics in D ¿= 4. Proceedings, Theoretical Advanced Study Institute in elementary particle physics, TASI 2004, Boulder, USA, June 6-July 2, 2004*, 2004 p. 359.

[54] L. A. Harland-Lang, A. D. Martin, P. Motylinski, and R. S. Thorne, *Parton distributions in the LHC era: MMHT 2014 PDFs*, The European Physical Journal C **75** (2015), arXiv: 1412.3989, ISSN: 1434-6044, 1434-6052, URL: `http://arxiv.org/abs/1412.3989`.

[55] V. N. Gribov and L. N. Lipatov, *Deep inelastic e p scattering in perturbation theory*, Sov. J. Nucl. Phys. **15** (1972) p. 438, [Yad. Fiz.15,781(1972)].

[56] Guido Altarelli and G. Parisi, *Asymptotic Freedom in Parton Language*, Nucl. Phys. **B126** (1977) p. 298.

[57] Yuri L. Dokshitzer, *Calculation of the Structure Functions for Deep Inelastic Scattering and e+ e- Annihilation by Perturbation Theory in Quantum Chromodynamics.*, Sov. Phys. JETP **46** (1977) p. 641, [Zh. Eksp. Teor. Fiz.73,1216(1977)].

[58] Robin Devenish and Amanda Cooper-Sarkar, *Deep Inelastic Scattering*, Oxford University Press, 2004.

[59] S Farry, "Electroweak Physics at LHCb", vol. 273275, 2016 p. 2181.

[60] M. Goncharov et al., *Precise measurement of dimuon production cross-sections in muon neutrino Fe and muon anti-neutrino Fe deep inelastic scattering at the Tevatron*, Phys. Rev. **D64** (2001) p. 112006, arXiv: `hep-ex/0102049 [hep-ex]`.

[61] O. Samoylov et al., *A Precision Measurement of Charm Dimuon Production in Neutrino Interactions from the NOMAD Experiment*, Nucl. Phys. **B876** (2013) p. 339, arXiv: `1308.4750 [hep-ex]`.

[62] A. Kayis-Topaksu et al., *Measurement of charm production in neutrino charged-current interactions*, New J. Phys. **13** (2011) p. 093002, arXiv: `1107.0613 [hep-ex]`.

[63] S. Alekhin et al., *Determination of Strange Sea Quark Distributions from Fixed-target and Collider Data*, Phys. Rev. **D91** (2015) p. 094002, arXiv: `1404.6469 [hep-ph]`.

[64] ATLAS Collaboration, *Precision measurement and interpretation of inclusive W^+, W^- and Z/γ^* production cross sections with the ATLAS detector*, Eur. Phys. J. C **77** (2017) p. 367, arXiv: `1612.03016 [hep-ex]`.

[65] C. L. Bennett et al., *Nine-Year Wilkinson Microwave Anisotropy Probe (WMAP) Observations: Final Maps and Results*, (2012), eprint: `arXiv:1212.5225`.

[66] Planck Collaboration et al., *Planck 2013 results. I. Overview of products and scientific results*, (2013), eprint: `arXiv:1303.5062`.

[67] J. Beringer et al., *Review of Particle Physics*, Phys. Rev. D **86** (1 2012) p. 010001, URL: `https://link.aps.org/doi/10.1103/PhysRevD.86.010001`.

[68] Matts Roos, *Dark Matter: The evidence from astronomy, astrophysics and cosmology*, (2010), eprint: `arXiv:1001.0316`.

[69] Yonit Hochberg, Eric Kuflik, Tomer Volansky, and Jay G. Wacker, *Mechanism for Thermal Relic Dark Matter of Strongly Interacting Massive Particles*, Phys. Rev. Lett. **113** (2014) p. 171301, arXiv: `1402.5143 [hep-ph]`.

[70] Chris Quigg, *Cosmic Neutrinos*, (2008), eprint: `arXiv:0802.0013`.

[71] P. J. E. Peebles and Bharat Ratra, *The Cosmological Constant and Dark Energy*, (2002), eprint: `arXiv:astro-ph/0207347`.

[72] “Running of Coupling”, URL: `http://scienceblogs.com/startswithabang/files/2013/05/running_coupling.gif`.

[73] A. D. Sakharov, *Violation of CP Invariance, c Asymmetry, and Baryon Asymmetry of the Universe*, Pisma Zh. Eksp. Teor. Fiz. **5** (1967) p. 32, [Usp. Fiz. Nauk161,61(1991)].

[74] Cheng-Wei Chiang, Neil D. Christensen, Gui-Jun Ding, and Tao Han, *Discovery in Drell-Yan processes at the LHC*, Phys. Rev. D **85** (1 2012) p. 015023, URL: `https://link.aps.org/doi/10.1103/PhysRevD.85.015023`.

[75] Elena Accomando et al., *Interference effects in heavy W'-boson searches at the LHC*, Phys. Rev. **D85** (2012) p. 115017, arXiv: `1110.0713 [hep-ph]`.

[76] Jogesh C. Pati and Abdus Salam, *Lepton number as the fourth ”color”*, Phys. Rev. D **10** (1 1974) p. 275, URL: `https://link.aps.org/doi/10.1103/PhysRevD.10.275`.

[77] J. L. Hewett and T. G. Rizzo, *Probing new gauge boson couplings via three-body decays*, Phys. Rev. **D47** (1993) p. 4981, arXiv: `hep-ph/9206221 [hep-ph]`.

[78] Rabindra N. Mohapatra and Jogesh C. Pati, *Left-right gauge symmetry and an ”isoconjugate” model of* CP *violation*, Phys. Rev. D **11** (3 1975) p. 566, URL: `https://link.aps.org/doi/10.1103/PhysRevD.11.566`.

[79] R. N. Mohapatra, J. C. Pati, and L. Wolfenstein, *Superweak model of* CP *violation in unified gauge theories*,

Phys. Rev. D **11** (11 1975) p. 3319,
URL: `https://link.aps.org/doi/10.1103/PhysRevD.11.3319`.

[80] G. Senjanovic and R. N. Mohapatra, *Exact left-right symmetry and spontaneous violation of parity*, Phys. Rev. D **12** (5 1975) p. 1502, URL: `https://link.aps.org/doi/10.1103/PhysRevD.12.1502`.

[81] R. N. Mohapatra, Frank E. Paige, and D. P. Sidhu, *Symmetry breaking and naturalness of parity conservation in weak neutral currents in left-right symmetric gauge theories*, Phys. Rev. D **17** (9 1978) p. 2462, URL: `https://link.aps.org/doi/10.1103/PhysRevD.17.2462`.

[82] Mariana Frank, Alper Hayreter, and Ismail Turan, *Production and Decays of W_R bosons at the LHC*, Phys. Rev.D **83** (2011) p. 035001, arXiv: `1010.5809 [hep-ph]`.

[83] Shrihari Gopalakrishna, Tao Han, Ian Lewis, Zong-guo Si, and Yu-Feng Zhou, *Chiral Couplings of W' and Top Quark Polarization at the LHC*, Phys. Rev. **D82** (2010) p. 115020, arXiv: `1008.3508 [hep-ph]`.

[84] Miha Nemevsek, Fabrizio Nesti, Goran Senjanovic, and Yue Zhang, *First Limits on Left-Right Symmetry Scale from LHC Data*, Phys. Rev. **D83** (2011) p. 115014, arXiv: `1103.1627 [hep-ph]`.

[85] Alessio Maiezza, Miha Nemevsek, Fabrizio Nesti, and Goran Senjanovic, *Left-Right Symmetry at LHC*, Phys. Rev. **D82** (2010) p. 055022, arXiv: `1005.5160 [hep-ph]`.

[86] R. N. Mohapatra and J. C. Pati, *"Natural" left-right symmetry*, Phys. Rev. D **11** (9 1975) p. 2558, URL: `https://link.aps.org/doi/10.1103/PhysRevD.11.2558`.

[87] Manfred Lindner, Tommy Ohlsson, and Gerhart Seidl, *See-saw Mechanisms for Dirac and Majorana Neutrino Masses*, (2001), eprint: `arXiv:hep-ph/0109264`.

[88] Edward E. Boos, Viacheslav E. Bunichev, Maxim A. Perfilov, Mikhail N. Smolyakov, and Igor P. Volobuev, *The specificity of searches for W', Z' and γ' coming from extra dimensions*, JHEP **06** (2014) p. 160, arXiv: `1311.5968 [hep-ph]`.

[89] T. Kaluza, *Zum Unitätsproblem der Physik*, Sitzungsberichte der Königlich Preußischen Akademie der Wissenschaften (Berlin), Seite p. 966-972 (1921) p. 966.

[90] Oskar Klein, *Quantentheorie und fünfdimensionale Relativitätstheorie*, Zeitschrift für Physik **37** (1926) p. 895, ISSN: 0044-3328, URL: `https://doi.org/10.1007/BF01397481`.

[91] Oskar Klein, *The Atomicity of Electricity as a Quantum Theory Law*, Nature **118** (1926), URL: `http://dx.doi.org/10.1038/118516a0`.

[92] David London and Jonathan L. Rosner, *Extra gauge bosons in* E_6, Phys. Rev. D **34** (5 1986) p. 1530, URL: `https://link.aps.org/doi/10.1103/PhysRevD.34.1530`.

[93] Paul Langacker, *The physics of heavy* $Z^{'}$ *gauge bosons*, Rev. Mod. Phys. **81** (3 2009) p. 1199, URL: `https://link.aps.org/doi/10.1103/RevModPhys.81.1199`.

[94] Tao Han, Heather E. Logan, Bob McElrath, and Lian-Tao Wang, *Phenomenology of the little Higgs model*, Phys. Rev. **D67** (2003) p. 095004, arXiv: `hep-ph/0301040 [hep-ph]`.

[95] N. Arkani-Hamed, A. G. Cohen, E. Katz, and A. E. Nelson, *The Littlest Higgs*, JHEP **07** (2002) p. 034, arXiv: `hep-ph/0206021 [hep-ph]`.

[96] Steven Weinberg, *Implications of dynamical symmetry breaking*, Phys. Rev. D **13** (4 1976) p. 974, URL: `https://link.aps.org/doi/10.1103/PhysRevD.13.974`.

[97] Leonard Susskind, *Dynamics of spontaneous symmetry breaking in the Weinberg-Salam theory*, Phys. Rev. D **20** (10 1979) p. 2619, URL: `https://link.aps.org/doi/10.1103/PhysRevD.20.2619`.

[98] Alexander Belyaev et al., *Technicolor Walks at the LHC*, Phys. Rev. **D79** (2009) p. 035006, arXiv: `0809.0793 [hep-ph]`.

[99] Christopher T. Hill and Elizabeth H. Simmons, *Strong dynamics and electroweak symmetry breaking*, Phys. Rept. **381** (2003) p. 235, [Erratum: Phys. Rept.390,553(2004)], arXiv: `hep-ph/0203079 [hep-ph]`.

[100] P. H. Frampton, *Chiral dilepton model and the flavor question*, Phys. Rev. Lett. **69** (20 1992) p. 2889, URL: `https://link.aps.org/doi/10.1103/PhysRevLett.69.2889`.

[101] F. Pisano and V. Pleitez, *SU(3)*$\bigotimes$*U(1) model for electroweak interactions*, Phys. Rev. D **46** (1 1992) p. 410, URL: `https://link.aps.org/doi/10.1103/PhysRevD.46.410`.

[102] J. M. Cabarcas, J. Duarte, and J. -Alexis Rodriguez, *Charged lepton mixing processes in 331 Models*, Int. J. Mod. Phys. **A29** (2014) p. 1450015, arXiv: `1310.1407 [hep-ph]`.

[103] Pierre Fayet, *Supersymmetry and Weak, Electromagnetic and Strong Interactions*, Phys. Lett. **64B** (1976) p. 159.

[104] Puneet Batra, Antonio Delgado, David E. Kaplan, and Timothy M. P. Tait, *The Higgs mass bound in gauge extensions of the minimal supersymmetric standard model*, JHEP **02** (2004) p. 043, arXiv: `hep-ph/0309149 [hep-ph]`.

[105] Duccio Pappadopulo, Andrea Thamm, Riccardo Torre, and Andrea Wulzer, *Heavy Vector Triplets: Bridging Theory and Data*, JHEP **09** (2014) p. 060, arXiv: `1402.4431 [hep-ph]`.

[106] J. de Blas, J. M. Lizana, and M. Pérez-Victoria, *Combining searches of Z' and W' bosons*, JHEP **01** (2013) p. 166, arXiv: `1211.2229 [hep-ph]`.

[107] V. Barger, W. Y. Keung, and Ernest Ma, *Gauge model with light W and Z bosons*, Phys. Rev. D **22** (3 1980) p. 727, URL: `https://link.aps.org/doi/10.1103/PhysRevD.22.727`.

[108] Roberto Contino, David Marzocca, Duccio Pappadopulo, and Riccardo Rattazzi, *On the effect of resonances in composite Higgs phenomenology*, JHEP **10** (2011) p. 081, arXiv: `1109.1570 [hep-ph]`.

[109] Oliver Sim Brüning et al., *LHC Design Report*, CERN, 2004, URL: `https://cds.cern.ch/record/782076`.

[110] ATLAS Collaboration, *ATLAS:Detector and physics performance technical design report. Volume 1*, (1999).

[111] ATLAS Collaboration, *ATLAS:Detector and physics performance technical design report. Volume 2*, (1999).

[112] CMS Collaboration, *The CMS experiment at the CERN LHC*, JINST **3** (2008) S08004.

[113] CMS Collaboration, *CMS Physics Technical Design Report, Volume II: Physics Performance*, J. Phys G **34** (2007) p. 995.

[114] A. Augusto Alves Jr. et al., *The LHCb Detector at the LHC*, JINST **3** (2008) S08005.

[115] Betty Bezverkhny Abelev et al., *Performance of the ALICE Experiment at the CERN LHC*, Int. J. Mod. Phys. **A29** (2014) p. 1430044, arXiv: `1402.4476 [nucl-ex]`.

[116] Christine Lefèvre, "The CERN accelerator complex. Complexe des accélérateurs du CERN", 2008, URL: `https://cds.cern.ch/record/1260465`.

[117] *Impact of the Crossing Angle on Luminosity Asymmetries at the LHC in 2016 Proton Proton Physics Operation*, vol. 2035, 2017.

[118] D Nisbet, "LHC Operation in 2016", LHC Performance Workship, Chamonix, 2017, URL: `https://indico.cern.ch/event/580313/contributions/2359285/attachments/1396590/2135891/Operation_in_2016_v1_1.pdf`.

[119] ATLAS Collaboration, *ATLAS: letter of intent for a general-purpose pp experiment at the large hadron collider at CERN*, (1992), URL: `https://cds.cern.ch/record/291061`.

[120] ATLAS Collaboration, *The ATLAS Experiment at the CERN Large Hadron Collider*, JINST **3** (2008) S08003.

[121] ATLAS Collaboration, *ATLAS inner detector: Technical Design Report, 1*, Technical Design Report ATLAS, CERN, 1997, URL: `https://cds.cern.ch/record/331063`.

[122] ATLAS Collaboration, *ATLAS inner detector: Technical Design Report, 2*, Technical Design Report ATLAS, CERN, 1997, URL: `https://cds.cern.ch/record/331064`.

[123] ATLAS Collaboration, *ATLAS calorimeter performance: Technical Design Report*, Technical Design Report ATLAS, CERN, 1996, URL: `https://cds.cern.ch/record/331059`.

[124] ATLAS Collaboration, *ATLAS liquid-argon calorimeter: Technical Design Report*, Technical Design Report ATLAS, CERN, 1996, URL: `https://cds.cern.ch/record/331061`.

[125] ATLAS Collaboration, *ATLAS tile calorimeter: Technical Design Report*, Technical Design Report ATLAS, CERN, 1996, URL: `https://cds.cern.ch/record/331062`.

[126] ATLAS Collaboration, *ATLAS muon spectrometer: Technical Design Report*, Technical Design Report ATLAS, CERN, 1997, URL: `https://cds.cern.ch/record/331068`.

[127] ATLAS Collaboration, *Expected Performance of the ATLAS Experiment - Detector, Trigger and Physics*, (2009), arXiv: `0901.0512 [hep-ex]`.

[128] Norbert Wermes and G Hallewel, *ATLAS pixel detector: Technical Design Report*, Technical Design Report ATLAS, CERN, 1998, URL: `https://cds.cern.ch/record/381263`.

[129] Karolos Potamianos, *The upgraded Pixel detector and the commissioning of the Inner Detector tracking of the ATLAS experiment for Run-2 at the Large Hadron Collider*, PoS **EPS-HEP2015** (2015) p. 261, arXiv: `1608.07850 [physics.ins-det]`.

[130] Ripellino G., *The alignment of the ATLAS Inner Detector in Run 2*, ATL-INDET-PROC **2016-003** (2016).

[131] The Atlas Collaboration, *The ATLAS Pixel Insertable B-layer (IBL)*, Nuclear Instruments and Methods in Physics Research A **650** (2011) p. 45, arXiv: `1012.2742 [physics.ins-det]`.

[132] The ATLAS Collaboration, *ATLAS Insertable B-Layer Technical Design Report*, CERN-LHCC-2010-013 **ATLAS-TDR-19** (2010).

[133] Y. Takubo, *The Pixel Detector of the ATLAS experiment for the Run2 at the Large Hadron Collider*, JINST **10** (2015) p. C02001, arXiv: `1411.5338 [physics.ins-det]`.

[134] The ATLAS Collaboration, *The ATLAS semiconductor tracker end-cap module*, Nucl. Instrum. Meth. **A575** (2007) p. 353.

[135] ATLAS TRT Group, “”TRT Public Results”, `https://twiki.cern.ch/twiki/bin/view/AtlasPublic/TRTPublicResults`.

[136] ATLAS Collaboration, *ATLAS central solenoid: Technical Design Report*, Technical Design Report ATLAS, CERN, 1997, URL: `https://cds.cern.ch/record/331067`.

[137] ATLAS Collaboration, *ATLAS level-1 trigger: Technical Design Report*, Technical Design Report ATLAS, CERN, 1998, URL: `https://cds.cern.ch/record/381429`.

[138] Peter Jenni, Marzio Nessi, Markus Nordberg, and Kenway Smith, *ATLAS high-level trigger, data-acquisition and controls: Technical Design Report*, Technical Design Report ATLAS, CERN, 2003, URL: `https://cds.cern.ch/record/616089`.

[139] Peter Jenni and Marzio Nessi, “ATLAS Forward Detectors for Luminosity Measurement and Monitoring”, tech. rep. CERN-LHCC-2004-010. LHCC-I-014, revised version number 1 submitted on 2004-03-22 14:56:11: CERN, 2004, URL: `https://cds.cern.ch/record/721908`.

[140] V Cindro et al., *The ATLAS beam conditions monitor*, JINST **3** (2008) P02004, URL: `https://cds.cern.ch/record/1094819`.

[141] S. van der Meer, *Calibration of the Effective Beam Height in the ISR*, (1968).

[142] ATLAS Luminosity Group, “”ATLAS Luminosity Recommendations””, `https://twiki.cern.ch/twiki/bin/viewauth/Atlas/LuminosityForPhysics#2016_13_TeV_proton_proton_final`.

[143] ATLAS Collaboration, *Search for New Particles in Two-Jet Final States in 7 TeV Proton–Proton Collisions with the ATLAS Detector at the LHC*, Phys. Rev. Lett. **105** (2010) p. 161801, arXiv: `1008.2461 [hep-ex]`.

[144] ATLAS Luminosity Taskforce, “”Luminosity Public Results””, `https://twiki.cern.ch/twiki/bin/view/AtlasPublic/LuminosityPublicResultsRun2`.

[145] Stefan Höche, “Introduction to parton-shower event generators”, *Proceedings, Theoretical Advanced Study Institute in Elementary Particle Physics: Journeys Through the Precision Frontier: Amplitudes for Colliders (TASI 2014): Boulder, Colorado, June 2-27, 2014*, 2015 p. 235, arXiv: `1411.4085 [hep-ph]`, URL: `http://inspirehep.net/record/1328513/files/arXiv:1411.4085.pdf`.

[146] V. V. Sudakov, *Vertex parts at very high-energies in quantum electrodynamics*, Sov. Phys. JETP **3** (1956) p. 65, [Zh. Eksp. Teor. Fiz.30,87(1956)].

[147] Torbjorn Sjostrand, “Monte Carlo Generators”, *High-energy physics. Proceedings, European School, Aronsborg, Sweden, June 18-July 1, 2006*, 2006

p. 51, arXiv: `hep-ph/0611247 [hep-ph]`,
URL: `http://weblib.cern.ch/abstract?CERN-LCGAPP-2006-06`.

[148] Johan Alwall et al., *Comparative study of various algorithms for the merging of parton showers and matrix elements in hadronic collisions*, Eur. Phys. J. **C53** (2008) p. 473, arXiv: `0706.2569 [hep-ph]`.

[149] Simone Alioli, Paolo Nason, Carlo Oleari, and Emanuele Re, *A general framework for implementing NLO calculations in shower Monte Carlo programs: the POWHEG BOX*, JHEP **06** (2010) p. 043, arXiv: `1002.2581 [hep-ph]`.

[150] Torbjörn Sjöstrand et al., *An Introduction to PYTHIA 8.2*, Comput. Phys. Commun. **191** (2015) p. 159, arXiv: `1410.3012 [hep-ph]`.

[151] Marco Guzzi et al., *CT10 parton distributions and other developments in the global QCD analysis*, (2011), arXiv: `1101.0561 [hep-ph]`.

[152] ATLAS Collaboration, *Measurement of the Z/γ^* boson transverse momentum distribution in pp collisions at $\sqrt{s} = 7$ TeV with the ATLAS detector*, JHEP **09** (2014) p. 145, arXiv: `1406.3660 [hep-ex]`.

[153] J. Pumplin et al., *New generation of parton distributions with uncertainties from global QCD analysis*, JHEP **07** (2002) p. 012, arXiv: `hep-ph/0201195`.

[154] D. J. Lange, *The EvtGen particle decay simulation package*, Nucl. Instrum. Meth. A **462** (2001) p. 152.

[155] N. Davidson, T. Przedzinski, and Z. Was, *PHOTOS Interface in C++: Technical and Physics Documentation*, (2010), arXiv: `1011.0937 [hep-ph]`.

[156] Pierre Artoisenet, Rikkert Frederix, Olivier Mattelaer, and Robbert Rietkerk, *Automatic spin-entangled decays of heavy resonances in Monte Carlo simulations*, JHEP **03** (2013) p. 015, arXiv: `1212.3460 [hep-ph]`.

[157] Torbjorn Sjöstrand, Stephen Mrenna, and Peter Z. Skands, *PYTHIA 6.4 Physics and Manual*, JHEP **05** (2006) p. 026, arXiv: `hep-ph/0603175`.

[158] Peter Zeiler Skands, *Tuning Monte Carlo Generators: The Perugia Tunes*, Phys. Rev. D **82** (2010) p. 074018, arXiv: `1005.3457 [hep-ph]`.

[159] T. Gleisberg, Stefan. Höche, F. Krauss, M. Schönherr, S. Schumann, et al., *Event generation with SHERPA 1.1*, JHEP **02** (2009) p. 007, arXiv: `0811.4622 [hep-ph]`.

[160] Tanju Gleisberg and Stefan Höche, *Comix, a new matrix element generator*, JHEP **12** (2008) p. 039, arXiv: `0808.3674 [hep-ph]`.

[161] Fabio Cascioli, Philipp Maierhofer, and Stefano Pozzorini, *Scattering Amplitudes with Open Loops*, Phys. Rev. Lett. **108** (2012) p. 111601, arXiv: `1111.5206 [hep-ph]`.

[162] Steffen Schumann and Frank Krauss, *A Parton shower algorithm based on Catani-Seymour dipole factorisation*, JHEP **03** (2008) p. 038, arXiv: `0709.1027 [hep-ph]`.

[163] Stefan Höche, Frank Krauss, Marek Schönherr, and Frank Siegert, *QCD matrix elements + parton showers: The NLO case*, JHEP **04** (2013) p. 027, arXiv: 1207.5030 [hep-ph].

[164] U Klein, *Les Houches 2013: Physics at TeV Colliders: Standard Model Working Group Report Chapter III.2*, arXiv:1405.1067 [hep-ph] (2014), arXiv: 1405.1067, URL: http://arxiv.org/abs/1405.1067.

[165] ATLAS Collaboration, *Search for high-mass dilepton resonances in pp collisions at $\sqrt{s} = 8$ TeV with the ATLAS detector*, Phys. Rev. D **90** (2014) p. 052005, arXiv: 1405.4123 [hep-ex].

[166] Uta Klein, private communication.

[167] G. Duckeck et al., *ATLAS computing: Technical design report*, (2005).

[168] S. Agostinelli et al., *GEANT4: A Simulation toolkit*, Nucl. Instrum. Meth. **A506** (2003) p. 250.

[169] ATLAS Collaboration, *The ATLAS Simulation Infrastructure*, Eur. Phys. J. C **70** (2010) p. 823, arXiv: 1005.4568 [hep-ex].

[170] The Atlas Collaboration, *Simulation of Pile-up in the ATLAS Experiment*, Journal of Physics: Conference Series **513** (2014) p. 022024, URL: http://stacks.iop.org/1742-6596/513/i=2/a=022024.

[171] ATLAS Luminosity Taskforce, “”ATLAS Pileup Reweighting””, https://twiki.cern.ch/twiki/bin/view/AtlasProtected/PileupReweighting.

[172] Walter Lampl et al., *Calorimeter Clustering Algorithms: Description and Performance*, ATL-LARG-PUB-2008-002, 2008, URL: https://cds.cern.ch/record/1099735.

[173] T Cornelissen et al., “Concepts, Design and Implementation of the ATLAS New Tracking (NEWT)”, tech. rep. ATL-SOFT-PUB-2007-007. ATL-COM-SOFT-2007-002, CERN, 2007, URL: https://cds.cern.ch/record/1020106.

[174] T G Cornelissen et al., “Updates of the ATLAS Tracking Event Data Model (Release 13)”, tech. rep. ATL-SOFT-PUB-2007-003. ATL-COM-SOFT-2007-008, CERN, 2007, URL: https://cds.cern.ch/record/1038095.

[175] A Salzburger, S Todorova, and M Wolter, “The ATLAS Tracking Geometry Description”, tech. rep. ATL-SOFT-PUB-2007-004. ATL-COM-SOFT-2007-009, CERN, 2007, URL: https://cds.cern.ch/record/1038098.

[176] ATLAS Collaboration, *Electron efficiency measurements with the ATLAS detector using 2012 LHC proton–proton collision data*, Eur. Phys. J. C **77** (2017) p. 195, arXiv: 1612.01456 [hep-ex].

[177] ATLAS Collaboration, *Improved electron reconstruction in ATLAS using the Gaussian Sum Filter-based model for bremsstrahlung*, ATLAS-CONF-2012-047, 2012, URL: https://cds.cern.ch/record/1449796.

[178] T G Cornelissen et al., *The global 2 track fitter in ATLAS*, Journal of Physics: Conference Series **119** (2008) p. 032013, URL: `http://stacks.iop.org/1742-6596/119/i=3/a=032013`.

[179] ATLAS Collaboration, *Electron efficiency measurements with the ATLAS detector using the 2015 LHC proton–proton collision data*, ATLAS-CONF-2016-024, 2016, URL: `https://cds.cern.ch/record/2157687`.

[180] ATLAS Collaboration, *Electron reconstruction and identification efficiency measurements with the ATLAS detector using the 2011 LHC proton–proton collision data*, Eur. Phys. J. C **74** (2014) p. 2941, arXiv: `1404.2240 [hep-ex]`.

[181] ATLAS ElectronGamma Working Group, “”Egamma Group Electron Efficiency Results””, `https://atlas.web.cern.ch/Atlas/GROUPS/PHYSICS/PLOTS/EGAM-2016-002`, 2016.

[182] ATLAS Collaboration, *Measurement of the muon reconstruction performance of the ATLAS detector using 2011 and 2012 LHC proton–proton collision data*, Eur. Phys. J. C **74** (2014) p. 3130, arXiv: `1407.3935 [hep-ex]`.

[183] Ryan Atkin, *Review of jet reconstruction algorithms*, Journal of Physics: Conference Series **645** (2015) p. 012008, URL: `http://stacks.iop.org/1742-6596/645/i=1/a=012008`.

[184] Matteo Cacciari, Gavin P. Salam, and Gregory Soyez, *The Anti-k(t) jet clustering algorithm*, JHEP **04** (2008) p. 063, arXiv: `0802.1189 [hep-ph]`.

[185] ATLAS Collaboration, *Jet energy scale measurements and their systematic uncertainties in proton–proton collisions at $\sqrt{s} = 13$ TeV with the ATLAS detector*, (2017), arXiv: `1703.09665 [hep-ex]`.

[186] ATLAS Collaboration, *Expected photon performance in the ATLAS experiment*, ATL-PHYS-PUB-2011-007, 2011, URL: `https://cds.cern.ch/record/1345329`.

[187] ATLAS Collaboration, *Measurements of the photon identification efficiency with the ATLAS detector using 4.9 fb^{-1} of pp collision data collected in 2011*, ATLAS-CONF-2012-123, 2012, URL: `https://cds.cern.ch/record/1473426`.

[188] ATLAS Collaboration, *Identification and energy calibration of hadronically decaying tau leptons with the ATLAS experiment in pp collisions at $\sqrt{s} = 8$ TeV*, Eur. Phys. J. C **75** (2015) p. 303, arXiv: `1412.7086 [hep-ex]`.

[189] ATLAS Collaboration, *Reconstruction, Energy Calibration, and Identification of Hadronically Decaying Tau Leptons in the ATLAS Experiment for Run-2 of the LHC*, ATL-PHYS-PUB-2015-045, 2015, URL: `https://atlas.web.cern.ch/Atlas/GROUPS/PHYSICS/PUBNOTES/ATL-PHYS-PUB-2015-045`.

[190] ATLAS Collaboration, *Performance of missing transverse momentum reconstruction with the ATLAS detector in the first proton–proton collisions at $\sqrt{s} = 13$ TeV*, ATL-PHYS-PUB-2015-027, 2015, URL: `https://cds.cern.ch/record/2037904`.

[191] ATLAS Collaboration, *Expected performance of missing transverse momentum reconstruction for the ATLAS detector at $\sqrt{s} = 13$ TeV*, ATL-PHYS-PUB-2015-023, 2015, URL: `https://cds.cern.ch/record/2037700`.

[192] ATLAS Collaboration, *Jet Calibration and Systematic Uncertainties for Jets Reconstructed in the ATLAS Detector at $\sqrt{s} = 13$ TeV*, ATL-PHYS-PUB-2015-015, 2015, URL: `https://cds.cern.ch/record/2037613`.

[193] ATLAS Collaboration, *Tagging and suppression of pileup jets with the ATLAS detector*, ATLAS-CONF-2014-018, 2014, URL: `https://cds.cern.ch/record/1700870`.

[194] ATLAS Collaboration, *Data-Quality Requirements and Event Cleaning for Jets and Missing Transverse Energy Reconstruction with the ATLAS Detector in Proton–Proton Collisions at a Center-of-Mass Energy of $\sqrt{s} = 7$ TeV*, ATLAS-CONF-2010-038, 2010, URL: `https://cds.cern.ch/record/1277678`.

[195] Sayipjamal Dulat et al., *New parton distribution functions from a global analysis of quantum chromodynamics*, Physical Review D **93** (2016), arXiv: 1506.07443, ISSN: 2470-0010, 2470-0029, URL: `http://arxiv.org/abs/1506.07443`.

[196] The NNPDF Collaboration et al., *Parton distributions for the LHC Run II*, Journal of High Energy Physics **2015** (2015), arXiv: 1410.8849, ISSN: 1029-8479, URL: `http://arxiv.org/abs/1410.8849`.

[197] Jon Butterworth et al., *PDF4LHC recommendations for LHC Run II*, Journal of Physics G: Nuclear and Particle Physics **43** (2016) p. 023001, arXiv: 1510.03865, ISSN: 0954-3899, 1361-6471, URL: `http://arxiv.org/abs/1510.03865`.

[198] H1 and ZEUS Collaborations, *Combination of measurements of inclusive deep inelastic $e^{\pm}p$ scattering cross sections and QCD analysis of HERA data*, Eur. Phys. J. **C75** (2015) p. 580, arXiv: `1506.06042 [hep-ex]`.

[199] S. Alekhin, J. Bluemlein, and S. Moch, *The ABM parton distributions tuned to LHC data*, Physical Review D **89** (2014), arXiv: 1310.3059, ISSN: 1550-7998, 1550-2368, URL: `http://arxiv.org/abs/1310.3059`.

[200] Pedro Jimenez-Delgado and Ewald Reya, *Delineating parton distributions and the strong coupling*, Physical Review D **89** (2014), arXiv: 1403.1852, ISSN: 1550-7998, 1550-2368, URL: `http://arxiv.org/abs/1403.1852`.

[201] ATLAS Collaboration, *Precision measurement and interpretation of inclusive W^+, W^- and Z/γ^* production cross sections with the ATLAS detector*, Eur. Phys. J. **C77** (2017) p. 367, arXiv: `1612.03016 [hep-ex]`.

[202] "Source Code of VRAP 0.9", `http://www.slac.stanford.edu/~lance/Vrap`.

[203] Jun Gao and Pavel Nadolsky, private communication, 2016.

[204] Kurt Brendlinger, Rob Fletcher, Sarah Heim, Joe Kroll, and Joey Reichert, "d_0 in the likelihood", `https://indico.cern.ch/event/386865/contributions/1817961/attachments/772633/1059655/egd0_SarahHeim_04152015.pdf`.

[205] ATLAS Collaboration, *Selection of jets produced in* 13 *TeV proton–proton collisions with the ATLAS detector*, ATLAS-CONF-2015-029, 2015, URL: `https://cds.cern.ch/record/2037702`.

[206] ATLAS Collaboration, *Search for heavy resonances decaying to a Z boson and a photon in pp collisions at $\sqrt{s} = 13$ TeV with the ATLAS detector*, Phys. Lett. B **764** (2017) p. 11, arXiv: `1607.06363 [hep-ex]`.

[207] ATLAS Collaboration, *Search for new particles in events with one lepton and missing transverse momentum in pp collisions at $\sqrt{s} = 8$ TeV with the ATLAS detector*, JHEP **09** (2014) p. 037, arXiv: `1407.7494 [hep-ex]`.

[208] ATLAS Collaboration, "W' Flat Template Reweighting (ATLAS Internal Web page)", `https://twiki.cern.ch/twiki/bin/view/AtlasProtected/WprimeFlatTemplate#Re_weighting_Back_to_Resonance_p`.

[209] Torbjorn Sjöstrand, Stephen Mrenna, and Peter Z. Skands, *A Brief Introduction to PYTHIA 8.1*, Comput. Phys. Commun. **178** (2008) p. 852, arXiv: `0710.3820 [hep-ph]`.

[210] Richard D. Ball et al., *Parton distributions with LHC data*, Nucl. Phys. **B867** (2013) p. 244, arXiv: `1207.1303 [hep-ph]`.

[211] Particle Data Group, *Review of Particle Physics Chapter 49: Resonances*, Chin. Phys. **C40** (2017).

[212] M.V. Chizhov and I.R. Boyko, "Presentation: Optimal Template for W^*", `https://indico.cern.ch/event/180082/contributions/302831/attachments/238956/334537/templateWstarOptimal.pdf`.

[213] ATLAS ElectronGamma Working Group, `https://twiki.cern.ch/twiki/bin/viewauth/AtlasProtected/ElectronGamma`.

[214] ATLAS Collaboration, *Electron and photon energy calibration with the ATLAS detector using LHC Run 1 data*, Eur. Phys. J. C **74** (2014) p. 3071, arXiv: `1407.5063 [hep-ex]`.

[215] ATLAS Collaboration, *Search for new phenomena in dijet events using* 37 *fb*$^{-1}$ *of pp collision data collected at $\sqrt{s} = 13$ TeV with the ATLAS detector*, (2017), arXiv: `1703.09127 [hep-ex]`.

[216] ATLAS Collaboration, *Electron efficiency measurements with the ATLAS detector using the 2012 LHC proton–proton collision data*, ATLAS-CONF-2014-032, 2014, URL: `https://cds.cern.ch/record/1706245`.

[217] ATLAS Collaboration, *A method for the construction of strongly reduced representations of ATLAS experimental uncertainties and the application thereof to the jet energy scale*, ATL-PHYS-PUB-2015-014, 2015, URL: `https://cds.cern.ch/record/2037436`.

[218] Morad Aaboud et al., *Performance of missing transverse momentum reconstruction with the ATLAS detector using proton-proton collisions at $\sqrt{s}$ = 13 TeV*, (2018), arXiv: `1802.08168 [hep-ex]`.

[219] S.D. Poisson, *Recherches sur la probabilité des jugements en matière criminelle et en matière civile: précédées des règles générales du calcul des probabilités*, Bachelier, 1837, URL: `https://books.google.co.uk/books?id=uB8OAAAAQAAJ`.

[220] M.K Bugge, "Studies of choice of prior for the W' statistical analysis", `https://indico.cern.ch/event/446479/contributions/1110066/attachments/1156633/1662947/presentasjon.pdf`, `https://indico.cern.ch/event/402802/contributions/955483/attachments/806979/1105881/presentasjon.pdf`.

[221] N. Metropolis, A. W. Rosenbluth, M. N. Rosenbluth, A. H. Teller, and E. Teller, *Equation of State Calculations by Fast Computing Machines*, JCP **21** (1953) p. 1087.

[222] W. K. Hastings, *Monte Carlo sampling methods using Markov chains and their applications*, Biometrika **57** (1970) p. 97, eprint: `http://biomet.oxfordjournals.org/cgi/reprint/57/1/97.pdf`, URL: `http://biomet.oxfordjournals.org/cgi/content/abstract/57/1/97`.

[223] Allen Caldwell, Daniel Kollar, and Kevin Kroeninger, *BAT - The Bayesian Analysis Toolkit*, (2008), eprint: `arXiv:0808.2552`.

[224] The ATLAS Statistics Forum, "Frequentist Limit Recommendation", `https://indico.cern.ch/event/126652/contributions/1343592/attachments/80222/115004/Frequentist_Limit_Recommendation.pdf`, 2011.

[225] Alexander L. Read, *Presentation of search results: The CL(s) technique*, J. Phys. **G28** (2002) p. 2693, [,11(2002)].

[226] Glen Cowan, Kyle Cranmer, Eilam Gross, and Ofer Vitells, *Asymptotic formulae for likelihood-based tests of new physics*, Eur. Phys. J. **C71** (2011) p. 1554, [Erratum: Eur. Phys. J.C73,2501(2013)], arXiv: `1007.1727 [physics.data-an]`.

[227] S. S. Wilks, *The Large-Sample Distribution of the Likelihood Ratio for Testing Composite Hypotheses*, The Annals of Mathematical Statistics **9** (1938) p. 60, ISSN: 00034851, URL: `http://www.jstor.org/stable/2957648`.

[228] Abraham Wald, *Tests of Statistical Hypotheses Concerning Several Parameters When the Number of Observations is Large*, Transactions of the American Mathematical Society **54** (1943) p. 426, ISSN: 00029947, URL: `http://www.jstor.org/stable/1990256`.

[229] Magnar Kopangen Bugge et al., "Search for new particles in the charged lepton plus missing transverse energy final state using pp collisions at $\sqrt{s} = 13$ TeV in the ATLAS detector", tech. rep. ATL-COM-PHYS-2016-1405, CERN, 2016, URL: `https://cds.cern.ch/record/2217650`.

[230] Roger Barlow and Christine Beeston, *Fitting using finite Monte Carlo samples*, Computer Physics Communications **77** (1993) p. 219, ISSN: 0010-4655, URL: `http://www.sciencedirect.com/science/article/pii/001046559390005W`.

[231] ATLAS Collaboration, *Search for a new heavy gauge boson resonance decaying into a lepton and missing transverse momentum in* 36 fb^{-1} *of pp collisions at* $\sqrt{s} = 13$ *TeV with the ATLAS experiment*, (2017), arXiv: `1706.04786 [hep-ex]`.

[232] ATLAS Collaboration, *Search for heavy resonances decaying to a W or Z boson and a Higgs boson in final states with leptons and b-jets in* 36.1 fb^{-1} *of pp collision data at* $\sqrt{s} = 13$ *TeV with the ATLAS detector*, ATLAS-CONF-2017-055, 2017, URL: `https://cds.cern.ch/record/2273871`.

[233] F. del Aguila, J. de Blas, and M. Pérez-Victoria, *Electroweak Limits on General New Vector Bosons*, JHEP **09** (2010) p. 033, With contours produced with updated fits by Jorge de Blas, arXiv: `1005.3998 [hep-ph]`.

[234] P Falke and T Hryn′ova, "Reinterpretation of the Z' generic limits for the HVT model", `https://indico.cern.ch/event/650669/contributions/2653681/attachments/1493643/2322923/Presentation_HVT.pdf`.

[235] Johan Alwall, Michel Herquet, Fabio Maltoni, Olivier Mattelaer, and Tim Stelzer, *MadGraph 5 : Going Beyond*, JHEP **06** (2011) p. 128, arXiv: `1106.0522 [hep-ph]`.

[236] Y Takubo and P Falke, "Development of reweighting tool for W'/Z'", `https://indico.cern.ch/event/632029/contributions/2555626/attachments/1444674/2225285/wprime1670413.pdf`, `https://indico.cern.ch/event/689157/contributions/2829843/attachments/1577493/2491516/wprime171219.pdf`.

[237] P Falke and D Hayden, "Signal templates from Pythia and signal reweighting", `https://indico.cern.ch/event/632029/contributions/2555625/attachments/1444112/2224817/ZpSignalTemplates_Dan_Peter.pdf`.

[238] Janna Katharina Behr, Jike Wang, Klaus Mönig, and Yu-heng Chen, "Search for heavy Higgs bosons A/H decaying to a top-quark pair in pp collisions at $\sqrt{s}$=8 TeV with the ATLAS detector: Supporting documentation for 8 TeV paper", tech. rep. ATL-COM-PHYS-2016-1179, Supporting note for EXOT-2016-04: CERN, 2016, URL: `https://cds.cern.ch/record/2209529`.

[239] Elena Accomando, Diego Becciolini, Alexander Belyaev, Stefano Moretti, and Claire Shepherd-Themistocleous, *Z' at the LHC: Interference and Finite Width Effects in Drell-Yan*, JHEP **10** (2013) p. 153, arXiv: `1304.6700 [hep-ph]`.

[240] E Kay, "Electroweak Uncertainty Study for the W'/Z' Combination", `https://indico.cern.ch/event/695170/contributions/2850351/attachments/1583140/2502008/EkayUpdate16-01-18.pdf`.

[241] Ossama AbouZeid et al., "Search for diboson resonance in the $\ell\nu qq$ final state in pp collisions at $\sqrt{s} = 13$ TeV with the ATLAS detector", tech. rep. ATL-COM-PHYS-2016-1488, CERN, 2016, URL: `https://cds.cern.ch/record/2225969`.

[242] "Search for resonant WZ Production in the fully leptonic final state in Proton-Proton Collisions at $\sqrt{s} = 13$ TeV with the ATLAS Detector", tech. rep. ATLAS-EXOT-2016-11-002, CERN, 2018, URL: `https://cds.cern.ch/record/2313171`.

[243] Reina Camacho Toro et al., "Search for diboson resonances with jets in 36.7 fb $^{-1}$ of pp collisions at $\sqrt{s} = 13$ TeV with the ATLAS detector", tech. rep. ATL-COM-PHYS-2016-1490, CERN, 2016, URL: `https://cds.cern.ch/record/2225991`.

[244] The ATLAS Collaboration, *Search for diboson resonances with boson-tagged jets in pp collisions at $\sqrt{s} = 13$ TeV with the ATLAS detector*, Phys. Lett. **B777** (2018) p. 91, arXiv: `1708.04445 [hep-ex]`.

[245] Joany Manjarres Ramos et al., "Search for resonant $WZ \to lll$ production in proton-proton collisions at $\sqrt{s} = 13$ TeV with the ATLAS detector", tech. rep. ATL-COM-PHYS-2016-514, CERN, 2016, URL: `https://cds.cern.ch/record/2152365`.

[246] João Barreiro Guimarães da Costa et al., "Search for a high mass Higgs boson in the $H \to WW \to \ell\nu\ell\nu$ channel in pp collisions at $\sqrt{s}$=13 TeV with the ATLAS detector", tech. rep. ATL-COM-PHYS-2016-1671, CERN, 2016, URL: `https://cds.cern.ch/record/2233660`.

[247] Spyridon Argyropoulos et al., "Search for resonances decaying to a W or Z boson and a Higgs boson in the $\nu\nu bb$, $\ell\nu bb$ and $\ell\ell bb$ final states with $\sqrt{s} = 13$ TeV ATLAS data in the context of models with 2 Higgs doublets or additional heavy vector triplets", tech. rep. ATL-COM-PHYS-2016-479, CERN, 2016, URL: `https://cds.cern.ch/record/2151842`.

[248] Gustaaf Brooijmans et al., "Supporting document for the search for new resonances decaying to a W/Z boson and a Higgs boson in $q\bar{q}^{(\prime)}b\bar{b}$ final states", tech. rep. ATL-COM-PHYS-2016-1480, CERN, 2016, URL: `https://cds.cern.ch/record/2225577`.

[249] The ATLAS Collaboration, *Search for heavy resonances decaying to a W or Z boson and a Higgs boson in the $q\bar{q}^{(\prime)}b\bar{b}$ final state in pp collisions at $\sqrt{s} = 13$ TeV with the ATLAS detector*, Phys. Lett. **B774** (2017) p. 494, arXiv: `1707.06958 [hep-ex]`.

[250] Ossama AbouZeid et al., "VV/VH and Dilepton combination", tech. rep. ATL-COM-PHYS-2017-986, CERN, 2017, URL: `https://cds.cern.ch/record/2272170`.

[251] J Wenninger, "Energy Calibration of the LHC Beams at 4 TeV", tech. rep. CERN-ATS-2013-040, CERN, 2013, URL: `https://cds.cern.ch/record/1546734`.

[252] Jamie Boyd and Joerg Wenninger, private communication, 2016.

[253] Jorg Wenninger and Ezio Todesco, "Large Hadron Collider momentum calibration and accuracy", tech. rep. CERN-ACC-2017-0007, CERN, 2017, URL: `https://cds.cern.ch/record/2254678`.